

International Journal of

Rotating Machinery

Special Issue

Advances in Measurement Techniques for Turbomachinery Flow, Heat Transfer, and Acoustics

Guest Editors: Nekkanti Sitaram, Giovanni Maria Carlomagno, Takayuki Matsunuma,
and Mark McQuilling



**Advances in Measurement Techniques for
Turbomachinery Flow, Heat Transfer,
and Acoustics**

International Journal of Rotating Machinery

**Advances in Measurement Techniques for
Turbomachinery Flow, Heat Transfer,
and Acoustics**

Guest Editors: Nekkanti Sitaram, Giovanni Maria Carlomagno,
Takayuki Matsunuma, and Mark McQuilling



Copyright © 2015 Hindawi Publishing Corporation. All rights reserved.

This is a special issue published in “International Journal of Rotating Machinery.” All articles are open access articles distributed under the Creative Commons Attribution License, which permits unrestricted use, distribution, and reproduction in any medium, provided the original work is properly cited.

Editorial Board

S. Acharya, USA
Abdollah A. Afjeh, USA
Hyeong J. Ahn, Korea
Ryoichi S. Amano, USA
Forrest E. Ames, USA
Luis S. Andres, USA
Jerome Antoni, France
S. V. Apte, USA
Farid Bakir, France
Hans J. Bauer, Germany
Dieter E. Bohn, Germany
Gerard BOIS, France
C. E. Brennen, USA
Mustafa Canakci, Turkey
G. M. Carlomagno, Italy
L. Chen, China
M. K. Chyu, USA
A. Corsini, Italy
Ningsheng Feng, Australia
David P. Fleming, USA
Koji Fujimoto, Japan
Luis Gato, Portugal
G. A. Gerolymos, France
J Paul Gostelow, UK
Chunill Hah, USA
Eric J. Hahn, Australia
Awatef Hamed, USA

J-C. Han, USA
Hiroshi Hayami, Japan
Robert C. Hendricks, USA
Hooshang Heshmat, USA
D. T. Hountalas, Greece
Zuohua Huang, China
Norihiko Iki, Japan
Tariq Iqbal, Canada
Takuzo Iwatsubo, Japan
David Japikse, USA
Yasutomo Kaneko, Japan
Funazaki Ken-ichi, Japan
Tong Seop Kim, Korea
Spyros A. Kinnas, USA
Ching-Pang Lee, USA
Shigenao Maruyama, Japan
H.H. Masjuki, Malaysia
Fabian Mauss, Germany
David U. Mba, UK
Jiun-Jih Miao, Taiwan
Akira Murata, Japan
Agnes Muszynska, USA
V. T. Nagaraj, USA
Razi Nalim, USA
Eddie Y. K. Ng, Singapore
Osamu Nozaki, Japan
Yutaka Ohta, Japan

Takanari Okamura, Japan
Yoji Okita, Japan
Ion Paraschivoiu, Canada
Raul Payri, Spain
Paolo Pennacchi, Italy
Sergio Preidikman, USA
Richard B. Rivir, USA
T. Sattelmayer, Germany
Jerzy T. Sawicki, USA
Meinhard T. Schobeiri, USA
Enrico Sciubba, Italy
Terrence W. Simon, USA
ONKAR SINGH, India
Seung Jin Song, Korea
Toyotaka Sonoda, Japan
Ken-Ichiro Takeishi, Japan
Hamid A. Toliyat, USA
Wei Tong, USA
Yoshinobu Tsujimoto, Japan
Ting Wang, USA
Bernhard Weigand, Germany
Dave Wisler, USA
S. L. K. Wittig, Germany
K. Yamaguchi, Japan
Yasuyuki Yokono, Japan
Saburoou Yuasa, Japan

Contents

Advances in Measurement Techniques for Turbomachinery Flow, Heat Transfer, and Acoustics, Nekkanti Sitaram, Giovanni Maria Carlomagno, Takayuki Matsunuma, and Mark McQuilling
Volume 2015, Article ID 716241, 2 pages

A Time Efficient Adaptive Gridding Approach and Improved Calibrations in Five-Hole Probe Measurements, Jason Town and Cengiz Camci
Volume 2015, Article ID 376967, 14 pages

Detection of Rotor Forced Response Vibrations Using Stationary Pressure Transducers in a Multistage Axial Compressor, William L. Murray III and Nicole L. Key
Volume 2015, Article ID 198534, 10 pages

Conjugate Heat Transfer Study of Combined Impingement and Showerhead Film Cooling Near NGV Leading Edge, Dileep Chandran and Bhamidi Prasad
Volume 2015, Article ID 315036, 13 pages

Experimental Investigation of Factors Influencing Operating Rotor Tip Clearance in Multistage Compressors, Reid A. Berdanier and Nicole L. Key
Volume 2015, Article ID 146272, 13 pages

Some Experimental Investigations on Gas Turbine Cooling Performed with Infrared Thermography at Federico II, T. Astarita, G. Cardone, L. de Luca, and G. M. Carlomagno
Volume 2015, Article ID 890414, 16 pages

Effect of Chamfer Angle on the Calibration Curves of Five Hole Probes, Nekkanti Sitaram and Kancherla Srikanth
Volume 2014, Article ID 704315, 11 pages

A Miniature Four-Hole Probe for Measurement of Three-Dimensional Flow with Large Gradients, Raviraj Jangir, Nekkanti Sitaram, and Ct Gajanan
Volume 2014, Article ID 297861, 12 pages

Editorial

Advances in Measurement Techniques for Turbomachinery Flow, Heat Transfer, and Acoustics

**Nekkanti Sitaram,¹ Giovanni Maria Carlomagno,²
Takayuki Matsunuma,³ and Mark McQuilling⁴**

¹*IIT Madras, Chennai 600036, India*

²*University of Naples Federico II, Piazzale Tecchio 80, 80125 Naples, Italy*

³*National Institute of Advanced Industrial Science and Technology (AIST), 1-2-1 Namiki, Tsukuba, Ibaraki 305-8564, Japan*

⁴*Parks College of Engineering, Aviation, and Technology, Saint Louis University, St. Louis, MO 63103, USA*

Correspondence should be addressed to Nekkanti Sitaram; nsitaram.iitm@gmail.com

Received 11 March 2015; Accepted 11 March 2015

Copyright © 2015 Nekkanti Sitaram et al. This is an open access article distributed under the Creative Commons Attribution License, which permits unrestricted use, distribution, and reproduction in any medium, provided the original work is properly cited.

Flow in turbomachines is highly three-dimensional and complex. The flow may be incompressible or compressible subsonic/supersonic or mixed flow. The flow is further complicated by high temperatures of working fluids. Large gradients of pressure, velocity, angle, temperature, and density in all directions and with time occur in most of turbomachinery. Two-phase flow is also encountered in many turbomachines. Although CFD is being extensively used to predict flow in turbomachines, it is essential that CFD results must be validated experimentally. A wide variety of measurement techniques are required starting with simple performance measurements to most complex measurements in the rotating blade rows of turbomachines. Substantial advances are being made in different techniques used for turbomachinery flow, heat transfer, and acoustics measurements. The present special issue addresses these advances for the use of researchers in academia, industry, and R&D laboratories.

This special issue compiles various original research articles that describe advanced measurement techniques and their application to different types of measurements in turbomachines. J. Town and C. Camci developed a time efficient adaptive gridding approach for use with a subminiature five-hole probe in an axial flow turbine. Their approach increases the possible number of measurement points in a two-hour period by 160%. Flow structures behind the NGV measurement plane are identified with high spatial resolution and reduced uncertainty. R. Jangir et al. developed a subminiature

four-hole probe with minimum spatial errors. Measurements made with this probe, a conventional five-hole probe and a miniature pitot probe across a calibration section, demonstrated that the errors due to gradient and surface proximity for this probe are considerably reduced compared to the five-hole probe. N. Sitaram and K. Srikanth addressed the effect of chamfer angle on the calibration curves of a large five-hole probe. They concluded that five-hole probe with a chamfer angle of 30° has larger operating range, while five-hole probe with a chamfer angle of 50° has increased sensitivity.

T. Astarita et al. summarized their experience in using IR thermography for convective heat transfer coefficient measurements in gas turbine cooling applications. D. Chandran and B. Prasad used IR thermography on the leading edge region of a typical gas turbine NGV, cooled by a combination of impingement and showerhead film cooling. They found good agreement between computational and experimental results. W. L. Murray III and N. L. Key developed data processing techniques needed to detect rotor blade vibration in a forced response condition from stationary fast response pressure transducers to allow for detection of rotor vibration from transient data and lead to techniques for vibration monitoring in gas turbines. They used these techniques to detect engine order resonant response of an embedded bladed disk in a three-stage intermediate speed axial compressor. R. A. Berdanier and N. L. Key measured circumferential variation of compressor rotor tip clearance using capacitance probe

instrumentation in the same compressor at different loading levels and at several compressor operating speeds. They found that thermal variations and centrifugal effects related to rotational speed changes affect clearance heights relative to the assembled configuration.

It is hoped that this special issue will provide useful information to wide readership from academia, industry, and research establishments and inspire development of new and more efficient measurement techniques for use in turbomachinery and other complex aerodynamics flows.

Acknowledgments

We thank the authors for their contributions. We are grateful to the reviewers who helped us during the reviewing process and selection of the papers.

*Nekkanti Sitaram
Giovanni Maria Carlomagno
Takayuki Matsunuma
Mark McQuilling*

Research Article

A Time Efficient Adaptive Gridding Approach and Improved Calibrations in Five-Hole Probe Measurements

Jason Town and Cengiz Camci

Turbomachinery Aero-Heat Transfer Laboratory, Department of Aerospace Engineering, The Pennsylvania State University, University Park, PA 16802, USA

Correspondence should be addressed to Cengiz Camci; cxcl1@psu.edu

Received 25 July 2014; Revised 6 November 2014; Accepted 8 November 2014

Academic Editor: Nekkanti Sitaram

Copyright © 2015 J. Town and C. Camci. This is an open access article distributed under the Creative Commons Attribution License, which permits unrestricted use, distribution, and reproduction in any medium, provided the original work is properly cited.

Five-Hole Probes (FHP), being a dependable and accurate aerodynamic tool, are an excellent choice for measuring three-dimensional flow fields in turbomachinery. To improve spatial resolution, a subminiature FHP with a diameter of 1.68 mm is employed. High length to diameter ratio of the tubing and manual pitch and yaw calibration cause increased uncertainty. A new FHP calibrator is designed and built to reduce the uncertainty by precise, computer controlled movements and reduced calibration time. The calibrated FHP is then placed downstream of the nozzle guide vane (NGV) assembly of a low-speed, large-scale, axial flow turbine. The cold flow HP turbine stage contains 29 vanes and 36 blades. A fast and computer controllable traversing system is implemented using an adaptive grid method for the refinement of measurements in regions such as vane wake, secondary flows, and boundary layers. The current approach increases the possible number of measurement points in a two-hour period by 160%. Flow structures behind the NGV measurement plane are identified with high spatial resolution and reduced uncertainty. The automated pitch and yaw calibration and the adaptive grid approach introduced in this study are shown to be a highly effective way of measuring complex flow fields in the research turbine.

1. Introduction

Five-Hole Probes are used to determine the three components of the mean velocity vector, local total pressure, and local static pressure [1]. They work by selectively comparing pressure data from five ports on the probe. According to Treaster and Yocum [2], by comparing the pressure differences between these ports, flow velocity magnitude, pitch angle, yaw angle, total pressure, and static pressure can be simultaneously determined. However, this method is found to work in a range of $\pm 30^\circ$ of pitch and yaw angle. A method is suggested by Ostowari and Wentz [3] to increase the range to $\pm 85^\circ$ by using a nulling method of the probe. However, nulling is not always possible, especially in the tight clearances and rotating machinery such as the flows internal to a turbine research rig. Norwack attempts to increase the range at which a FHP may be used by developing a long, spherical probe [4]. The useable range of the probe is increased to $\pm 65^\circ$, but the increased size makes it hard to incorporate in many cases.

Correction methods by interpolation to find the necessary coefficients have been implemented through a variety of

methods. A curve fitting approach is used by Treaster and Yocum [2] and Weiz [5]. The curve fitting approach takes into account the fact that the data taken by each port is in a different location. By using an orthogonal grid, the data is curve-fitted across the measurement region and interpolated to the center port of measurement. Reichert and Wendt suggest another method of data reduction for the FHP [6]. This method replaces the pitch and yaw angles with unit vectors and develops a Taylor series based approach to find flow parameters.

Dominy and Hodson studied the effects of Reynolds number extensively. Their study showed how probe design could affect Reynolds number related errors [7]. Treaster and Yocum [2] also covered this feature and suggested that calibration should be made at the expected Reynolds number or a correction factor must be used. Methods for the detection of abnormalities in the probe are suggested by Morrison et al. [8]. These suggestions aid in the identification of probe damage and flow alignment issues.

Investigations into the effect of near-wall measurements with Five-Hole Probes were carried out by Treaster and

Yocum [2] and Lee and Yoon [9]. They have concluded that measurements should be taken at least two probe diameters away from the wall. Closer distance causes blockage by the probe and acceleration of the flow, leading to greater uncertainty in the measurement. If it is necessary to operate closer than this distance, Lee and Yoon provide guidelines to make such measurements [9].

A FHP might also be used in place of laser Doppler anemometers for wake measurements, Brophy et al. [10]. The main application of the FHP would be in location where it would be difficult to use a laser, such as the rotating frame of reference in a turbine or in geometrically difficult situations to reach flow zones. Sitaram et al. have performed a detailed study on which type of probe to use within the rotating frame of a single stage compressor research rig at the Pennsylvania State University [11]. Town and Camci presented their early observations about using a subminiature Five-Hole Probe in an axial flow turbine rig in [12].

There are many recent studies on the development of FHP based aerodynamic measurement systems. Pisasale and Ahmed [13] presented a theoretical calibration approach for a FHP for highly three-dimensional flows. They also worked on a novel method for extending the calibration range of FHPs for highly three-dimensional flows [14]. Development of a functional relationship between port pressures and flow properties for the calibration and application of a multihole probe to highly three-dimensional flow was a topic of investigation in their 2004 paper [15]. Multihole probes can also be used in the determination of skin friction coefficient in turbulent flows, Lien and Ahmed [16].

The present paper presents significant improvements in FHP based aerodynamic measurements in four significant areas. The specific approach reduces the elapsed calibration time of a typical Five-Hole Probe from 3 hours down to 65 minutes for a (9×9) carpet map of pitch and yaw coefficients because of the unique properties of the new computer controlled calibration mechanism. A second major improvement is in the spatial resolution of measurements in selected high gradient areas such as the boundary layers, wakes, tip vortices, and secondary flow dominated flow zones. The third important property of the present approach is in the improved accuracy of the measurements because of an improved calibration system, the use of more accurate positioning of the probe, the use of highly improved present day transducers, and a careful selection of tubing. Finally, the current approach reduces turbine facility run-time significantly. The new system increases the number of data points that can be collected in a two-hour period from 366 points to 868 points, an increase of 160%.

2. Symbols

AFTRF: Axial Flow Turbine Research Facility

$C_{P,pitch}$: Pitch coefficient

$$\frac{(P_5 - P_4)}{(P_1 - \bar{P})} \quad (1)$$

$C_{P,static}$: Static pressure coefficient

$$\frac{(\bar{P} - P_{static})}{(P_1 - \bar{P})} \quad (2)$$

$C_{P,total}$: Total pressure coefficient

$$\frac{(P_1 - P_{total})}{(P_1 - \bar{P})} \quad (3)$$

$C_{P,yaw}$: Yaw coefficient

$$\frac{(P_2 - P_3)}{(P_1 - \bar{P})} \quad (4)$$

DAQ: Data acquisition device

\bar{P} : Average value of outside pressure points (Pa)

$$\frac{(P_2 + P_3 + P_4 + P_5)}{(4)} \quad (5)$$

P_1 : Pressure point 1, Figure 1

P_2 : Pressure point 2, Figure 1

P_3 : Pressure point 3, Figure 1

P_4 : Pressure point 4, Figure 1

P_5 : Pressure point 5, Figure 1

P_S : Static pressure at defined location (Pa)

P_T : Total pressure at defined location (Pa)

P_{static} : Local FHP measured static pressure (Pa)

P_{total} : Local FHP measured total pressure (Pa)

V_1 : Transducer voltage measured at point 1, Figure 1

V_2 : Transducer voltage measured at point 2, Figure 1

V_3 : Transducer voltage measured at point 3, Figure 1

V_4 : Transducer voltage measured at point 4, Figure 1

V_5 : Transducer voltage measured at point 5, Figure 1

V : Absolute velocity magnitude (m/s)

c : Calibration constant (Pa/V)

exit: Measurement location downstream of rotor

inlet: Measurement location upstream of NGV

local: Measurement location in intraspaces at specific point

r : Radius to probe traverser track

u : Velocity component in the probe relative x -direction (m/s)

v : Velocity component in the probe relative y -direction (m/s)

w : Velocity component in the probe relative z -direction (m/s)

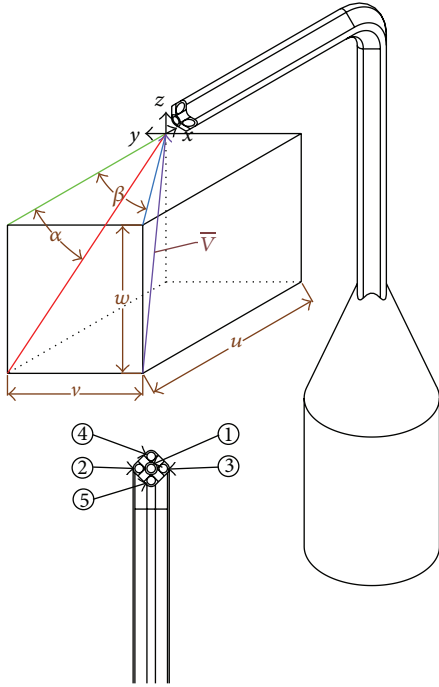


FIGURE 1: Isometric view of a subminiature Five-Hole Probe with velocity vector, positive angles, and positive velocity components and probe port number assignments.

- x : Distance of traverser from probe parallel to ground (zero) location
- z : Zero voltage measurement (V)
- α : Probe relative pitch angle ($^{\circ}$)
- β : Probe relative yaw angle ($^{\circ}$)
- θ : Desired measurement azimuthal angle
- ρ : Density (kg/m^3).

3. Material and Methods

3.1. Objectives. First of the specific objectives is the reduction of elapsed calibration time of a typical FHP for use in the AFTRF from three hours down to about an hour for a (9×9) carpet map of pitch and yaw coefficient. A second major objective is in the improvements in the spatial resolution of measurements in selected high gradient areas such as boundary layers, wakes, tip vortices, and secondary flow dominated zones. The third important objective of the present approach is in the improved accuracy of the measurements. The final objective is about significantly reducing the AFTRF turbine facility run-time for a selected FHP measurement effort.

3.2. Calibration Hardware. A flowchart for the acquisition of calibration data is shown in Figure 2. The commands, interface, and data logging at the computer level are written in LabVIEW. The 16-bit A/D converter system (DAQ) is made by Measurement Computing Corporation (MCC model USB-1608FS). It can obtain 200 k samples per second, interfaces through USB, and has an accuracy of ± 0.68 mV at

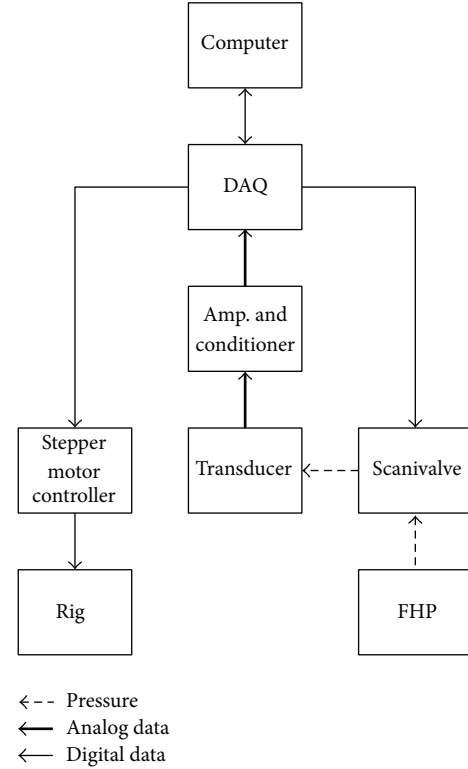


FIGURE 2: Calibration block diagram for Five-Hole Probe measurements.

an input range of ± 1 V. The 16-bit capabilities are essential to help reduce measurement uncertainty during the calibration and measurements.

The pressure is measured by a Validyne DP15 low pressure transducer with a 3500 Pa diaphragm. The transducer's accuracy is rated at 0.25%, (± 3.5 Pascal) of the full-scale measurement. Only one transducer is used to measure all five ports; its reference port is left open to atmosphere, and efforts are made to isolate the transducer thermally, electronically, and mechanically. Using one transducer for all five ports eliminates the bias errors coming from individual transducer zero values.

The transducer is connected to a Scanivalve Corp. 48-channel mechanical pressure selector. The specific electrical commands to step and reset the scanner are provided by the digital output D/A of the DAQ. The mechanical scanning approach with one transducer reduces measurement uncertainty by canceling out any thermal shift and calibration error the transducer might measure. It also reduces the total cost of the system but comes up with increased measurement time for the calibrations and measurements.

Previously employed methods of pitch and yaw calibration were applied by hand. To increase the accuracy of movements and decrease the total time taken for a complete calibration map, computer actuated rotary tables for pitch and yaw movements are used. Two different rotary tables are used, both provided by Velmex Inc. The larger of the two, model B4800TS, is used to change the pitch angle. For each

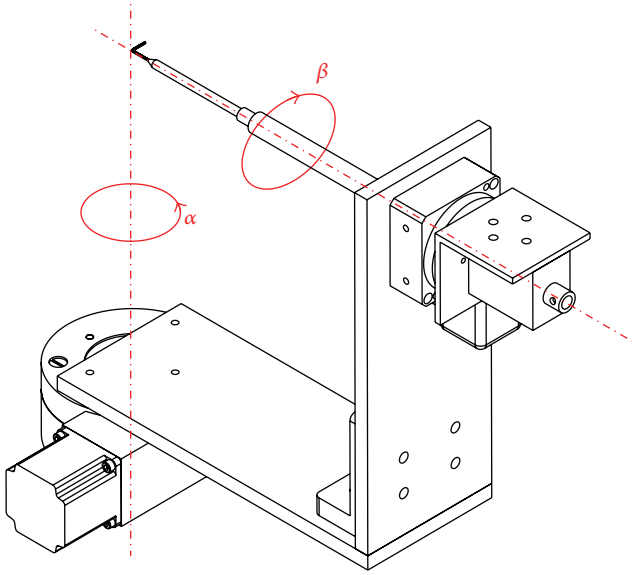


FIGURE 3: Calibrator design with pitch (α) and yaw (β) movements.

half step it moves 0.0125° . A second table, model B5990TS, is used to for yaw adjustments. For each half step it moves 0.010° .

The calibration rig shown in Figure 3 is designed to minimize movement of the probe tip in the direction normal to the outlet of the wind tunnel. The design intent is to keep the probe tip as near the intersection of the pitch and yaw axes as possible. This reduces the arm length of the probe and its displacement within the calibration jet.

A subminiature FHP shown in Figure 1 is designed and created on site using five hypodermic needles. It has a square cross-section with one hole in the center surrounded by four others located above, below, left, and right of the center. All sides of the probe have been beveled to a 45° angle, leaving the center port in a normal plane to the flow. The specific hypodermic needles reduce the size of the probe to a maximum diameter of 1.68 mm at the tip. The inherently small diameter of hypodermic tubing and the long length of tubing lead to a very large length to diameter ratio. Subminiature FHPs usually require relatively long settling and data acquisition times. However, the small tip size increases the spatial resolution of the measurements and allows the probe to be inserted into the complex internal flow areas of most turbomachinery passages. An additional Pitot probe is also used to measure the calibration tunnel's free jet axial velocity, total pressure, and static pressure.

The calibration facility, shown in Figure 4, consists of an open loop wind tunnel with an axial blower, a diffused housing with multiple screens, a plenum chamber, a high area ratio circular nozzle, a circular to square transition nozzle, and a section of constant cross-sectional duct. The compressor is 45.7 cm in diameter and is driven by a variable speed motor rated up to 7.5 kW. The tests are performed in the free jet just outside the constant cross-sectional duct. Free jet velocities are continuously adjustable via an AC inverter up to

28 m/s. Turbulent flow characteristics in the test section can be adjusted to turbulence intensity values between 0.5% and 1.2% by the use of calibrated screens and biplane turbulence promoters. Details of the test section flow quality can be found in Wiedner [1], Kuisoon et al. [17, 18], and Camci and Rizzo [19].

3.3. Calibration Technique. A modified version of the calibration/reduction technique of a nonnulling FHP used by Treaster and Yocum [2] is used in this paper. The main difference between the two methods is in the way pitch and yaw angles are defined. Figure 1 defines the positions of the holes, the coordinate system for the probe, the positive angles of the probe, and the positive velocity components. In this configuration, being positioned on the probe facing the incoming flow, a positive pitch value would occur when the flow was coming from below the probe (nose up). Positive yaw value would occur when the flow is coming from the left (nose right). The only manual input into the calibration sequence is the initial hand positioning of the probe at zero pitch, zero yaw angles. The calibration grid uses an improved 81-point (9×9) configuration with more data points in the nonlinear region near the maximum acceptance range of the probe ($\pm 30^\circ$). Calibration maps for coefficients of yaw, pitch, total pressure, and static pressure are calculated directly from the measurements of the FHP and Pitot probe as shown in Figures 8, 9, and 10. In most earlier studies, the carpet maps were limited to a 49-point (7×7) configuration or less. One of the main concerns with calibrating a FHP is producing a high quality map with reduced absolute error. One concern is about instant changes in calibration flow quality that can be caused by laboratory disturbances or unwanted air currents. Another source of error can occur when the probe is first aligned with the flow. The probe is initially aligned by hand and is prone to human error. Only one transducer is used to sample pressure from all pressure measurement points. Five input channels to the rotary pressure scanner are required for the FHP ports and two input channels are needed for the Pitot probe documenting the total pressure and static pressure in the test section.

Using a single transducer for all seven pressure measurements during calibration measurably increased the elapsed time for a calibration. However, this approach significantly reduces calibration error. Equation (6) states that pressure is a function of the measured voltage V_n , the zero z , and a calibration factor c . Since the zero and the calibration factor are for only one transducer, they can be considered constant for all pressure measurements. The analysis will only take $C_{P,\text{total}}$ from (3) into consideration, though it can be done with any of the other pressure coefficient equations. Substitution of (6) into (3) results in (7). Since c is in every term, canceling it out leads to (8). The result of canceling out the z term in the numerator and simplifying the z term in the denominator is shown in (9). Finally, the z term in the denominator is cancelled out and the result is shown in (10). The result shows that when calculating $C_{P,\text{total}}$, or for that matter any of the C_P values, the zero and calibration factors cancel out. Thus, using one transducer eliminates the source of error that could be

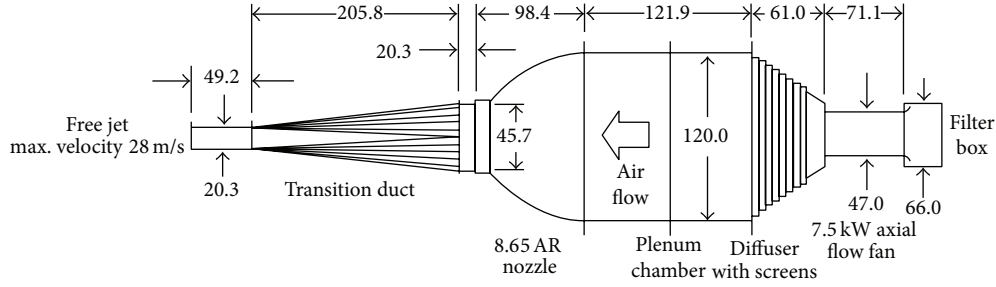


FIGURE 4: Calibration wind tunnel, dimensions in centimeters (not to scale).

caused by a typical calibration of a transducer and incorrect zeroing procedure. Consider

$$P_n = (V_n - z)c, \quad (6)$$

$$\begin{aligned} C_{P,\text{total}} &= ((V_1 - z)c - (V_T - z)c) \\ &\times \left((V_1 - z)c - \frac{(V_2 - z)c + (V_3 - z)c + (V_4 - z)c + (V_5 - z)c}{4} \right)^{-1}, \end{aligned} \quad (7)$$

$$\begin{aligned} C_{P,\text{total}} &= ((V_1 - z) - (V_T - z)) \\ &\times \left((V_1 - z) - \frac{(V_2 - z) + (V_3 - z) + (V_4 - z) + (V_5 - z)}{4} \right)^{-1}, \end{aligned} \quad (8)$$

$$C_{P,\text{total}} = \frac{V_1 - V_T}{(V_1 - z) - (V_2 + V_3 + V_4 + V_5 - 4z)/4}, \quad (9)$$

$$C_{P,\text{total}} = \frac{V_1 - V_T}{V_1 - (V_2 + V_3 + V_4 + V_5)/4}. \quad (10)$$

3.4. Calculating Unknown Flow Variables. A FORTRAN code developed in-house is the traditional method of data reduction in the measurements of a FHP. The recent fully automated LabVIEW implementation of the same analytical calibration/reduction procedure is shown to produce identical results or better when compared to our past manual calibration/reduction system. Input to the code requires the current ambient temperature (T), absolute static pressure (P_S), and the five pressures as measurements of the FHP. The program then determines the pitch angle α through a series of linear interpolations. The interpolation scheme calls $C_{P,\text{pitch}}$ to be calculated for each possible pitch angle in the 81-point carpet map where there are nine possible pitch angles at a constant $C_{P,\text{yaw}}$. A second interpolation calculates the value of pitch angle by using the measured value of $C_{P,\text{pitch}}$. Yaw angle β is calculated in a similar interpolation scheme. This interpolation scheme calls $C_{P,\text{yaw}}$ to be calculated for

each possible yaw angle at a constant $C_{P,\text{pitch}}$. The next interpolation calculates the exact value of yaw angle by using the measured value of $C_{P,\text{yaw}}$. A calibration chart used to visualize the data of the interpolations of pitch and yaw angle can be found in Figure 8.

Pitch and yaw angles are used for the interpolation of $C_{P,\text{total}}$ and $C_{P,\text{static}}$. The interpolation works similarly to pitch and yaw interpolation. First, α is held constant and an array of $C_{P,\text{total}}$ or $C_{P,\text{static}}$ is found with an array of β . The previously found value of β is then used to calculate $C_{P,\text{total}}$ and $C_{P,\text{static}}$, respectively. The charts used for the calculation of $C_{P,\text{total}}$ and $C_{P,\text{static}}$ can be found in Figures 9 and 10. Hence,

$$P_{\text{total}} = P_1 - C_{P,\text{total}}(P_1 - \bar{P}), \quad (11)$$

$$P_{\text{static}} = \bar{P} - C_{P,\text{static}}(P_1 - \bar{P}), \quad (12)$$

$$V = \left[\frac{2(P_T - P_S)}{\rho} \right]^{1/2}, \quad (13)$$

$$u = V \cdot \cos \alpha \cdot \cos \beta, \quad (14)$$

$$v = V \cdot \sin \beta, \quad (15)$$

$$w = V \cdot \sin \alpha \cdot \cos \beta. \quad (16)$$

Equation (3) can be rewritten to solve for total and static pressure. The results are shown in (11) and (12). Pitch and yaw angles are the first values found in the data reduction and are known. Definitions of velocity components with conventions are given in Figure 1 and derivations are in (14), (15), and (16).

3.5. Axial Flow Turbine Research Facility. The Axial Flow Turbine Research Facility at Pennsylvania State University currently consists of a single stage state-of-the-art HP turbine with 29 nozzle guide vanes (NGV) and 36 rotor blades. Figure 5 shows a cross-sectional view of the AFTRF. Flow enters through the inlet bellmouth and accelerates through the NGV. A detailed explanation of the design and characteristics of the AFTRF can be found in Lakshminarayana et al. [20].

The recent probe traverser as shown in Figures 5 and 6 is a modification of a previous design used in the AFTRF. In the previous design, circumferential movements were achieved by a belt system. The flexible belt system had noticeable play in it, and the new system replaces the belts

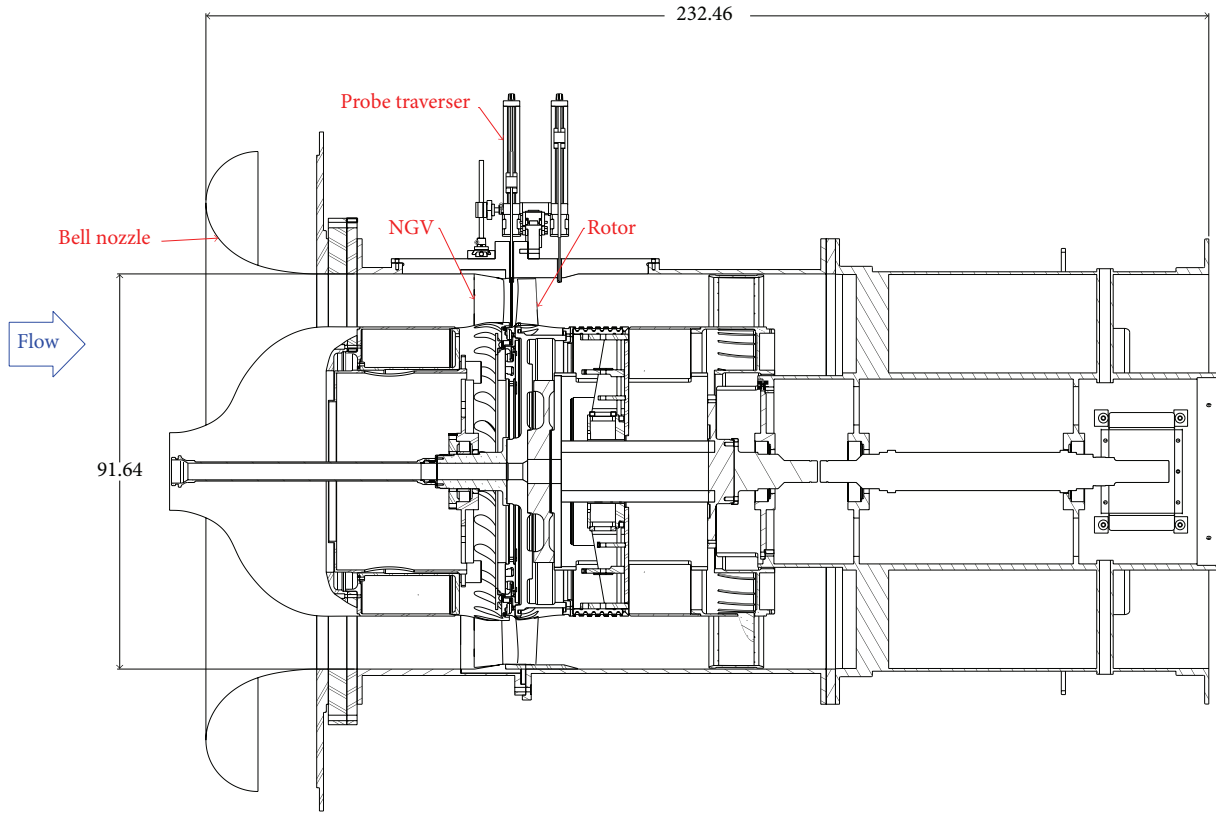


FIGURE 5: Axial Flow Turbine Research Facility (AFTRF) cutaway (dimensions in cm).

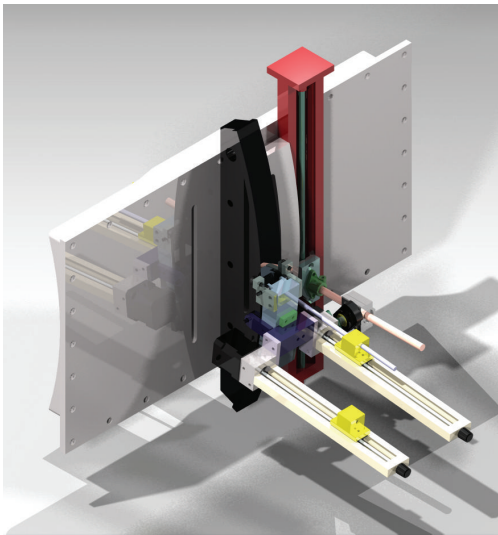


FIGURE 6: Probe traverser attached to the AFTRF instrumentation window, isometric view.

with a precision built linear traverser shown in red. Replacing the belt system with a traverser greatly increases the accuracy and reduces the play of the system. There are two radial traversers that are connected to the trolley (light blue), and the probe holders are shown in yellow. It is designed with two radial traversers so that the system could take measurements

in locations in between the NGV and rotor (intraspace), or downstream of the rotor. The new traversing system also includes improvements to the stepper motor drivers, which helps the traverser to move much faster than previously.

A cylindrical coordinate system is used within the AFTRF. Movements of the trolley could be translated to azimuthal position by calculation of arc length. Equation (17) is the result of the calculation to find the distance the traverser must move to change to a particular azimuthal angle θ . All distances are derived from a zero angle; the probe is parallel to the normal of the traverser. The radius r is the distance to the surface of the track that the trolley rides upon. The final variable, x , is the distance that the traverser must move from the zero position. To move from 1° to 2° , x is calculated for both cases and the values are subtracted to find the correct distance:

$$x = \frac{r \cdot \tan \theta}{\sqrt{\tan^2 \theta + 1}} \quad (17)$$

Data is acquired by a modular National Instruments CompactDAQ system. The module used to measure the analog signals of the Validyne DP-15 pressure transducers is a 32-channel, 16-bit NI 9205 data acquisition system. Rotor speed measurements are obtained from a high resolution MIL-spec optical encoder from BAE Systems (Model H25) encoder attached to the rotor. A Velmex VXM drives the stepper motors. All data logging, traverser movements, data analysis,

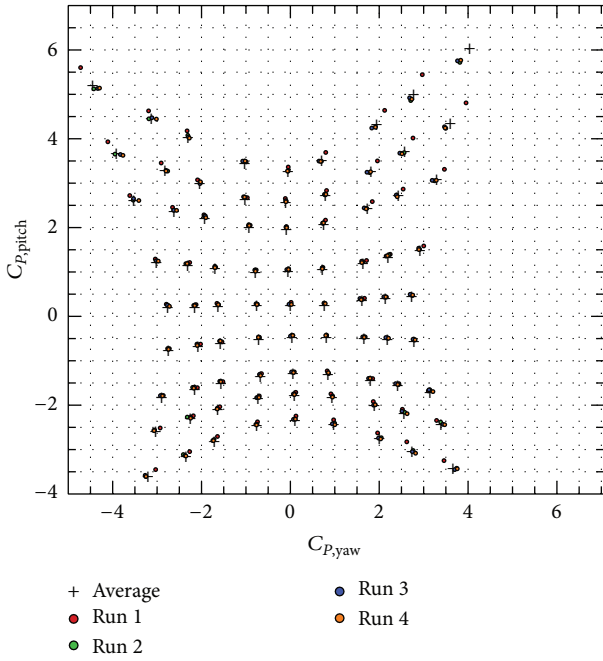


FIGURE 7: Average values (crosses) with data spread of four runs (points).

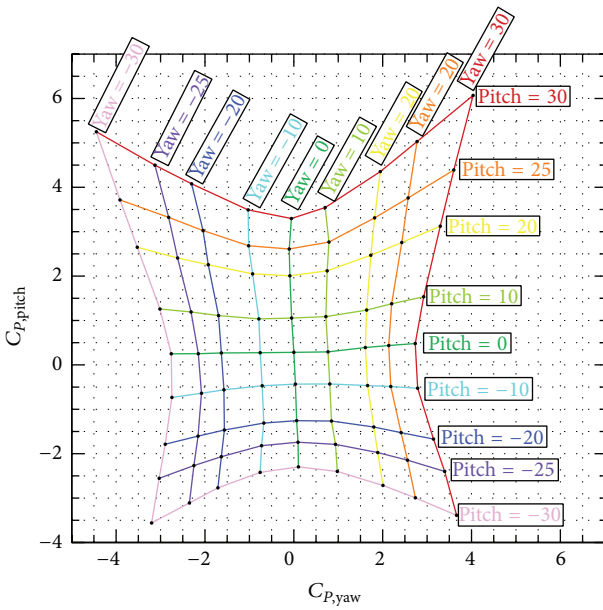


FIGURE 8: Coefficient of yaw and pitch with lines of constant pitch or yaw angles, 81 (9 × 9) points.

and data recording are completed by a custom LabVIEW script.

Although a conventional Scanivalve mechanical pressure scanner was used in the calibration of the FHP measurements for the improved calibration accuracy, our current AFTRF FHP measurements are performed using state-of-the-art electronic pressure scanners. Thirty-two-channel ZOC22b units from Scanivalve Corporation were employed in most

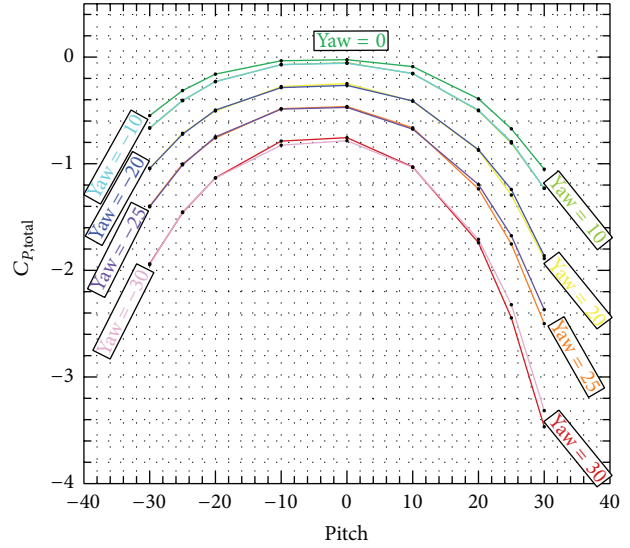


FIGURE 9: Pitch and coefficient of total pressure with lines of constant yaw, 81 (9 × 9) points.

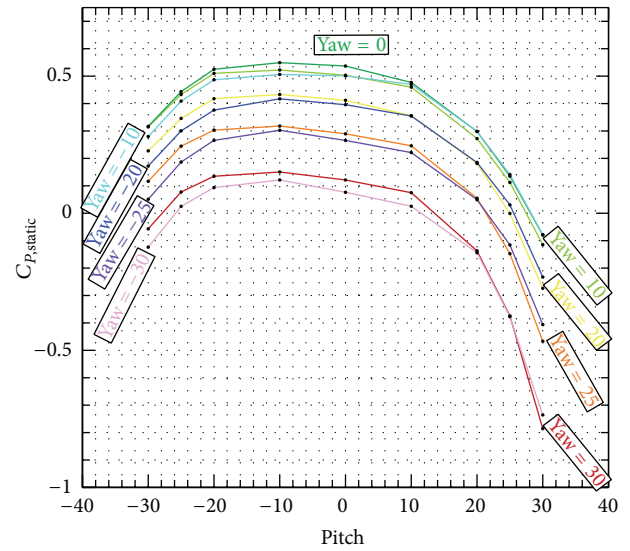


FIGURE 10: Pitch and coefficient of static pressure with lines of constant yaw, 81 (9 × 9) points.

of the turbine runs for faster operation and better thermal stability of the measurements.

Calculation of density in our FHP based calibrations and actual measurements require a measurement of local temperature. A K type thermocouple based probe is employed in our temperature measurements throughout the AFTRF. The thermocouple signal is referenced/amplified and converted into engineering units in a custom NI-9213 thermocouple processing unit. Our final temperature measurement accuracy for calibrations and AFTRF is estimated to be around $\pm 0.15^\circ\text{C}$.

Fluid flow through the AFTRF varies in velocity to the extent that a probe calibrated for the inlet could not be used

TABLE 1: Predicted midspan flow speeds and locations.

Location	Inlet	Intraspace	Absolute exit	Relative exit
Midspan velocity (m/s)	16.15	66.30	20.05	66.88

in the intraspace or rotor exit relative frame locations but could be used in the rotor exit absolute frame of reference. Table 1 covers the values of midspan velocity in meters per second. Present measurements are performed in the intraspace location, so the probe is calibrated at about 66 m/s.

4. Results

4.1. Five-Hole Probe Calibration. The carpet map as shown in Figure 7 was obtained four times in subsequent runs in an effort to establish the repeatability of the calibration process. The center of each cross represents the average value, while the four points surrounding each cross represent the data collected from each run. Nearly all points within the $\pm 20^\circ$ range have good grouping and are close to the average value. In the outlying regions of the calibration, those greater than $\pm 20^\circ$, the grouping is not as tight and initial alignment errors are exacerbated. The star shaped carpet map shown in Figure 7 is not perfectly symmetrical because a dimensionally perfect and symmetrical FHP is very difficult to manufacture because of the probe's small size and the inherent machining imperfections.

Calculations of $C_{P,\text{pitch}}$ and $C_{P,\text{yaw}}$ are found directly through (4) and (1). The results are used to interpolate pitch and yaw angle values with the help of the data presented in Figure 8 that is a typical averaged carpet map produced by the current automated calibration approach. Figure 9 presents the variation in $C_{P,\text{total}}$ with respect to pitch and yaw angle. Interpolation is done to find $C_{P,\text{total}}$ using the pitch and yaw found in the previous section. Similarly, Figure 10 provides $C_{P,\text{static}}$ as a function of pitch and yaw. $C_{P,\text{static}}$ can be recovered from the FHP measurements using the previously found pitch and yaw angles.

Previous design of calibration called for the probe to be moved by hand. One of the major advantages of the current computer automated system is stepper motor driven movements. No longer relying on human movement allows for a much greater degree of accuracy. The stepper motor controller can move the turntables in steps as fine as 0.0125° . Once the initial zero pitch and zero yaw position are defined at the start of each run, the computer driven mechanism can move to a new position with excellent spatial resolution and accuracy.

Calibrations of a FHP by manual pitch and yaw angle adjustments are long and arduous tasks. Previously, a 49-point map in a manual calibration effort took at least three hours to complete since a high quality adjustment of each pitch and yaw angle required great care. When the design was changed to the current automated system, a 49-point map took 65 minutes, and an 81-point map took 100 minutes. Further reduction in elapsed time is seen if multiple transducers are used, at the cost of previously mentioned accuracy

improvements with the single transducer approach. An 81-point grid with multiple transducers takes approximately 22 minutes to complete. Ensemble averaging from four individually obtained carpet maps can also be very easily obtained in the current computer driven system in a time efficient manner. Ensemble averaging is an excellent way of removing some of the error originating from initial alignment of the probe. Paying attention to properly recording the transducer zero voltages just before a turbine run starts is an effective way of improving accuracy in the multiple transducer approach.

The method of attachment of a FHP to the pitch and yaw calibrator is extremely critical. The style and quality of the mechanical attachment influence the movement of the probe and the value of the calibration. Large swings and displacements can produce large errors in the calibration from spatial nonuniformity, turbulence decay, or shear layer mixing. The calibrator in Figure 3 shows a design where the probe's tip is located near the intersection of the pitch and yaw rotational axes. The improved design makes the calibration more accurate and reduces the uncertainties.

Due to the nature of the design of the probe, the initial alignment must be performed by hand. This is because of the small size and unforeseen defects that make nulling the probe unfeasible. However, a few techniques are developed in order to increase the initial alignment accuracy. First, a plumb bob is used to align the calibrator base so that it is parallel to the exit of the wind tunnel. This helps to insure that the probe will be held normal to the exit of the wind tunnel and parallel to the streamlines in the pitch direction. Yaw angle alignment is done with the help of a visible, horizontal laser beam. Placing a piece of paper over the exit of the tunnel allows for comparison of the shape of the shadow of the probe. The shadow is then brought to its minimum size by making small adjustments with the yaw stepper motor. These two alignments are done at the beginning of every run.

An uncertainty analysis is prepared for the total pressure, the static pressure, and velocity as defined by (11), (12), and (13). An adaptation of a method set forth by Taylor [21] is used. Equation (18) is an example of the total pressure uncertainty estimates. The other variables follow the same processes but are not presented for brevity:

$$\begin{aligned} \delta P_T &= \left[\left(\delta P_1 \frac{\delta P_T}{\delta P_1} \right)^2 + \left(\delta P_2 \frac{\delta P_T}{\delta P_2} \right)^2 + \left(\delta P_3 \frac{\delta P_T}{\delta P_3} \right)^2 \right. \\ &\quad \left. + \left(\delta P_4 \frac{\delta P_T}{\delta P_4} \right)^2 + \left(\delta P_5 \frac{\delta P_T}{\delta P_5} \right)^2 \right. \\ &\quad \left. + \left(\delta C_{P,\text{total}} \frac{\delta P_T}{\delta C_{P,\text{total}}} \right)^2 \right]^{1/2}, \end{aligned} \quad (18)$$

$$\delta P_1 = \delta P_2 = \delta P_3 = \delta P_4 = \delta P_5 = \pm 5 \text{ Pa}, \quad (19)$$

$$\delta C_{P,\text{total}} = \pm \frac{1}{2} (C_{P,\text{total max}} - C_{P,\text{total min}}). \quad (20)$$

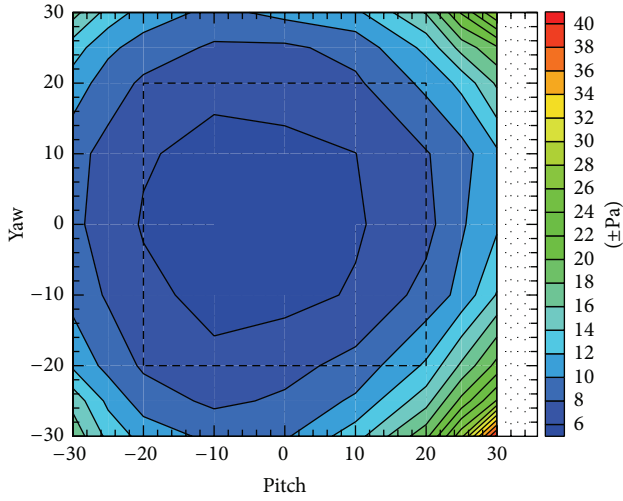


FIGURE 11: Total pressure uncertainty at 20 m/s, 81 (9 × 9) points (in terms of ±Pa).

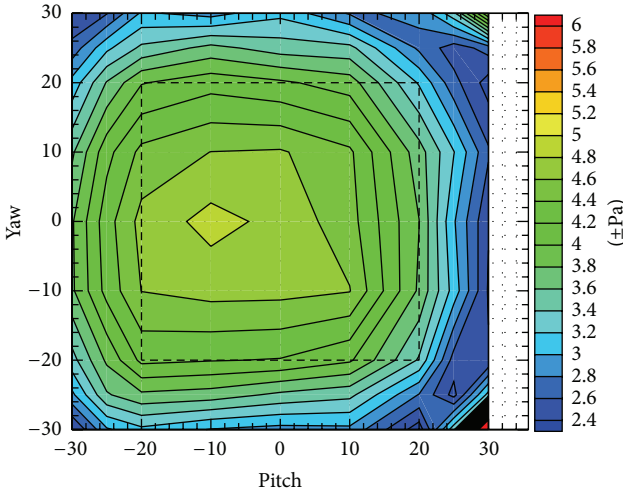


FIGURE 12: Static pressure uncertainty at 20 m/s, 81 (9 × 9) points (in terms of ±Pa).

Accuracy of the transducer is approximately ±3.5 Pa. Due to additional equipment and the high length to diameter ratio of connecting tubes, the accuracy decreased to ±5 Pa. This is expressed in (19). The uncertainty of the total pressure coefficient needs to be estimated using (20).

Total pressure uncertainty is shown in Figure 11 where the most accurate region of the measurement is located slightly to the left of the zero pitch, zero yaw location. This is due to small defects that are asymmetries in the probe tip shape. The 30° pitch, -30° yaw location sees a much larger variation in total pressure. The dashed box represents a ±20° region that is to help identify the range for which the probe is most accurate. When taking measurements, the incidence angle of the flow to the probe is kept within this region.

Static pressure uncertainty at 20 m/s is shown in Figure 12. The uncertainty results are not symmetric due to imperfections in the probe. The uncertainty near the center

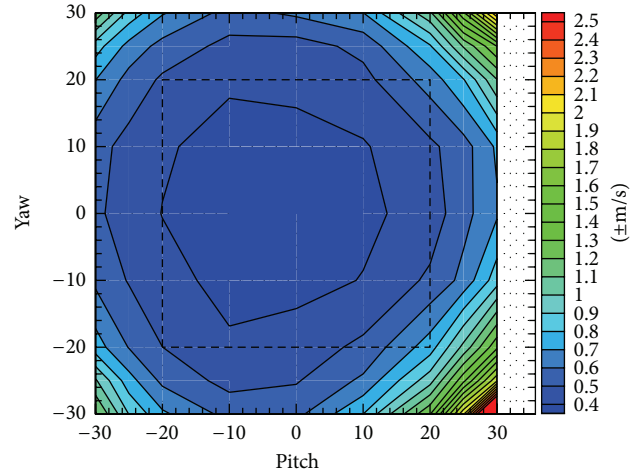


FIGURE 13: Velocity uncertainty at 20 m/s, 81 (9 × 9) points (in terms of ±m/s).

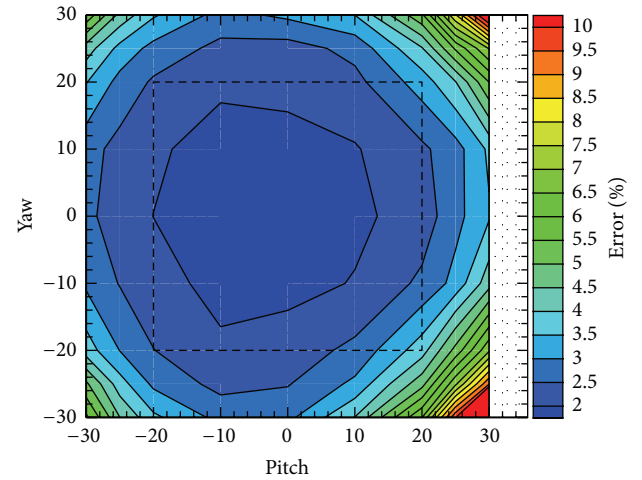


FIGURE 14: Velocity percent error at 20 m/s, 81 (9 × 9) points (in terms of percentage from baseline).

is larger. This is most likely because of the way the static pressure is calculated. The probe measures greater pressure when it is aligned to flow leading to an increase in uncertainty through greater measurement variability. When the probe is taking measurements near the maximum range, some of the pressure measurements decrease and the overall uncertainty is reduced.

Velocity uncertainty shown in Figure 13 has a minimum to the left of center. It reaches a maximum uncertainty greater than ±2.5 m/s at pitch 30° and yaw -30°. Uncertainty in the recommended ±20° range is below ±0.8 m/s.

Figure 14 represents the relative velocity uncertainty. The smallest error is located to the left of center in the map, while the largest error is located near the edges. At pitch 30°, yaw -30°, the error is greater than 10%. Within the dashed box range of ±20° no error is found to be greater than 4%. The estimated error in the range of ±10° is about 2% of the calibration tunnel velocity.

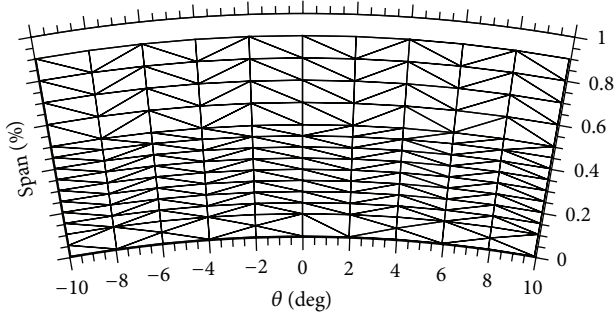


FIGURE 15: Initial measurement grid, 165 points.

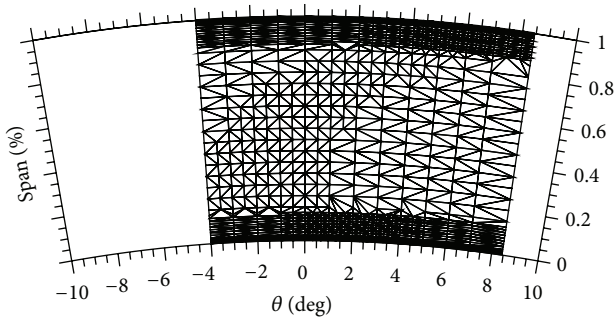


FIGURE 16: Refined measurement grid, 868 points.

The preceding figures determine that the most ideal operation of this probe would be within the $\pm 20^\circ$ range that is defined by the dashed box. A pitch and yaw range of $\pm 30^\circ$ is also possible. However, the elevated measurement uncertainty should be carefully evaluated in this range.

4.2. AFTRF Intraspace Five-Hole Probe Measurement Results.

The new traverser greatly reduced the amount of time it takes to move from one point to another. The maximum allowable testing period for the AFTRF was about two hours. In older previous experiments performed in the AFTRF, a 336-point mesh was used with the same sampling time for each measurement point. This mesh would take approximately two hours to complete and could not handle adaptive gridding. Improvements in the traversing system increased the number of points that are measured in a two-hour period to 868. The adaptive mesh and traverser improvements increased the number of points taken by nearly 160% over the previously used meshing techniques for the same two-hour test.

The addition of the adaptive grid approach into the mesh generation allows fine measurements in locations of greater interest and large gradients. The iterative process that is done for the adaptive gridding is currently manual. The initial grid of 165 points is shown in Figure 15. This grid is refined in areas of wake, boundary layer, and endwall vortices until the grid becomes what is shown in Figure 16. The refined grid of Figure 16 allows for less time to be spent in regions of

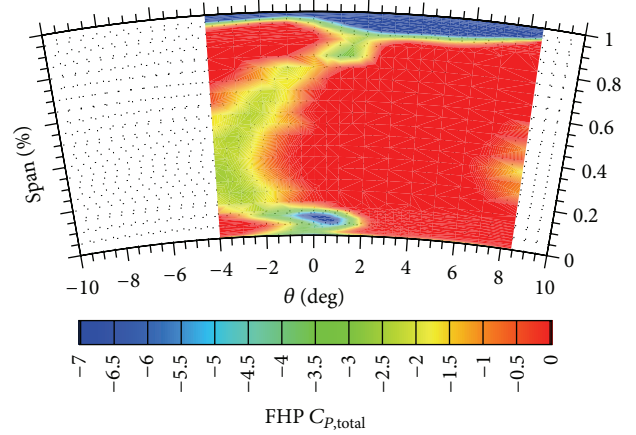


FIGURE 17: FHP coefficient of total pressure, intraspaces.

less variation and more time spent in large gradient areas. Consider

$$C_{P,\text{total}} = \frac{P_{T,\text{local}} - P_{T,\text{inlet}}}{(1/2) \rho V_{\text{inlet}}^2}, \quad (21)$$

$$C_{P,\text{static}} = \frac{P_{S,\text{local}} - P_{T,\text{inlet}}}{(1/2) \rho V_{\text{inlet}}^2}. \quad (22)$$

Coefficient of total pressure as defined by (21) for one vane pitch (12.41°) is shown in Figure 17. In this figure, the more negative values “going toward blue” indicate greater total pressure loss. The boundary layer near the hub is very small. The probe at the zero span location is currently behind a backward facing step which reduces size of the boundary layer. The passage vortex of the hub centered in the blue region is in the range of θ , from -1° to 1° , and span 0.05 to 0.10. The vane wake is the yellow region of the total pressure loss that curves through the measurement plane. Above 90% span, the uncertainty is increased as the probe is nearing the slot. This slot is used to access the intraspaces measurement plane and the boundary layer can be seen along with the casing passage vortex.

Coefficient of static pressure measured by the FHP in the intraspaces of the AFTRF as defined by (22) is shown in Figure 18. One can see the effects the secondary flows in Figures 17 and 18. The highest static pressure can be found near the hub; the lowest static pressure is found near the casing. The casing has greater uncertainty because the measurements are taken near the instrumentation slot. Static pressure over the midspan varies from being values of -23 to values of -28 .

Velocity magnitude measured by the FHP is shown in Figure 19. The highest velocity is found near the hub and velocity is reduced near the casing. The blue region in Figure 17 identified as the hub passage vortex appears here as a yellow deficit zone in velocity in the same location. Inspection can make out the outline of the vane wake, but it is not as clear as the hub passage vortex. Velocities are the lowest near the casing. This is an area of increased uncertainty due to its proximity to the instrumentation slot. The casing passage vortex and boundary layer can be identified.

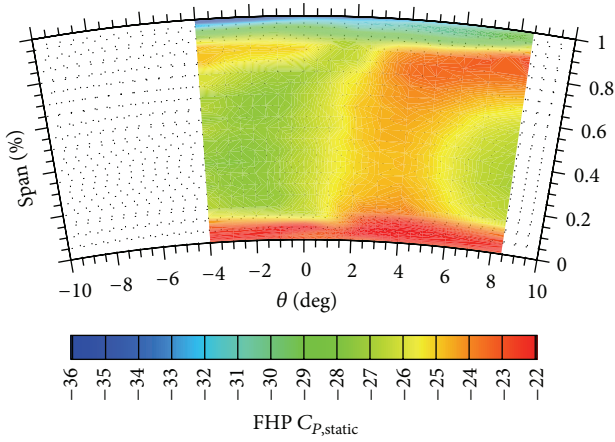


FIGURE 18: FHP coefficient of static pressure, intraspacer.

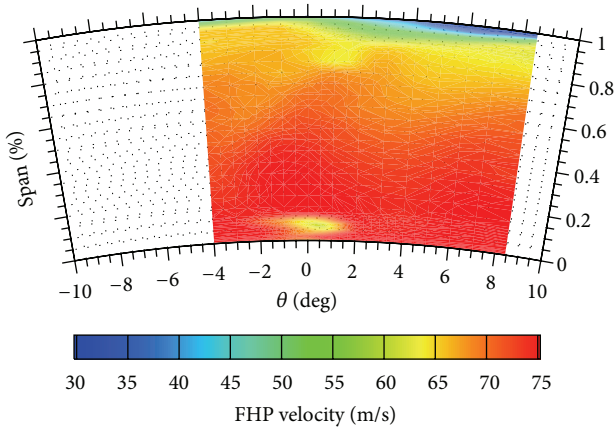


FIGURE 19: FHP velocity measurement, intraspacer.

Since local velocity is known at each measurement location, mass averaging can be performed with the FHP results. This is achieved by taking the entire measurement area, partitioning it into slices of constant radius, and then finding the mass average of each slice of constant radius. Mass averaged total and static pressure are reported in Figure 20. The effect of the hub passage vortex is seen in the five to ten percent span region causing a higher static pressure and a lower total pressure. For much of the span the total pressure remains near zero, while static pressure is becoming greater as it moves toward the casing. Near the casing total and static pressure measurements converge due to loss from the casing boundary layer, passage vortex, and the increased uncertainty of the instrumentation slot.

Figure 21 shows the pitch angle measured by the FHP. In this case, a positive pitch angle means the flow is moving radially toward the center of the test rig, or from the casing to the hub. Here, the effects of the backward facing step can be seen as an increased alpha near the hub. The entire passage shows the flow is moving from the casing toward the hub as shown in Figure 20. Interference from the instrumentation slot results in flow moving radially toward the hub near 100% span.

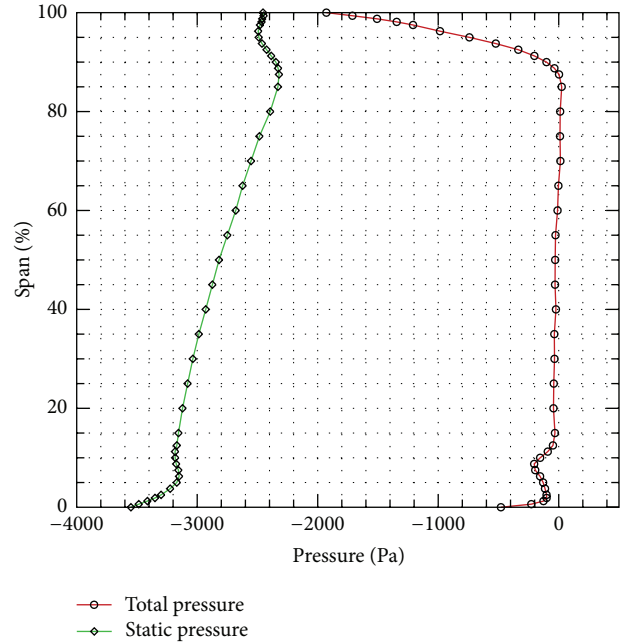


FIGURE 20: Mass averaged FHP measured total and static pressure, intraspacer.

Mass averaged yaw angle is shown in Figure 22. The effect of the hub passage vortex is seen near 5% span as a quick increase and decrease in yaw angle. Near 100% span, a yaw angle decrease is seen from the casing boundary layer and casing passage vortex. Increased uncertainty in this region is due to the instrumentation slot.

The mass averaged components of velocity are shown in Figure 23. Azimuthal velocity β is the largest component of velocity. The fluid out of the NGV is highly swirled. A reduction in this velocity from the hub passage vortex can be seen from five to ten percent. Velocity near the casing boundary layer, casing passage vortex, and instrumentation slot locally reduces the azimuthal component of velocity. A nearly constant and very small magnitude radial velocity is shown over the entire span, signifying the flow is moving toward the hub from the casing. Axial velocity is the highest near the hub passage vortex, slowly changes over the whole span, and then quickly drops in the presence of the casing boundary layer and instrumentation slot. The velocity magnitude closely follows the azimuthal component. The effects of the hub passage vortex can be found from five to ten percent, and the casing effects are also shown as a reduction in velocity.

5. Conclusions

A subminiature Five-Hole Probe is calibrated using a newly designed automated pitch and yaw calibration system and an overview of various recent FHP implementations is given. The automated system reduces the amount of time for an 81-point (9×9) carpet map calibration from three hours to 65 minutes.

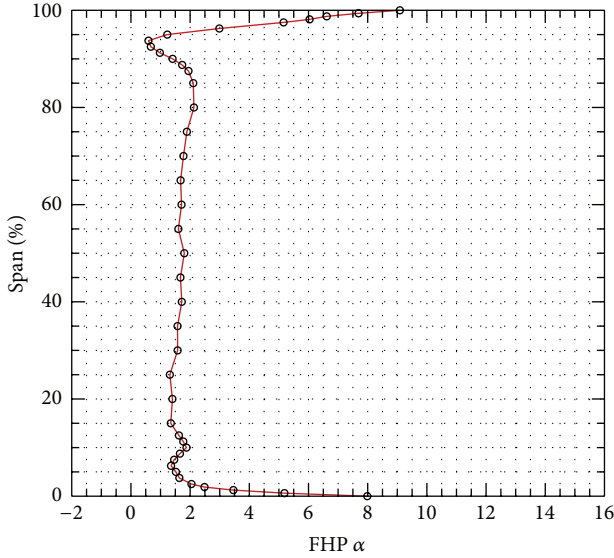


FIGURE 21: Mass averaged FHP measured pitch (α) angle, intraspacer.

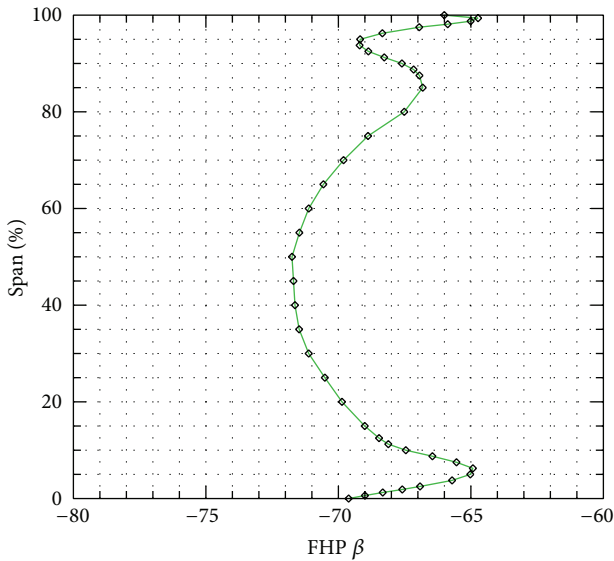


FIGURE 22: Mass averaged FHP measured yaw (β) angle, intraspacer.

Ensemble averaging of multiple runs measurably reduces the uncertainty of FHP calibrations in carpet maps. Uncertainty is further reduced by realigning the probe at a zero pitch, zero yaw position with the help of a laser level and plumb bob for each calibration run.

Using only one transducer during calibration reduces calibration uncertainty by eliminating the zero and calibration terms.

The fully automated pitch and yaw calibrator is designed to reduce uncertainty caused by streamwise displacement of the probe by keeping the tip of the probe close to the intersection of the pitch and yaw rotational axis. The pitch and yaw calibrator uses state-of-the-art mechanical components, stepper motors, indexers, and computer controls to provide

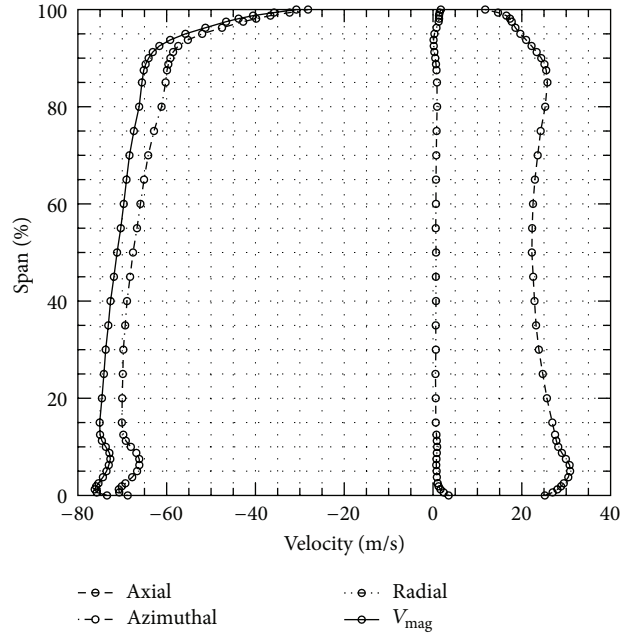


FIGURE 23: Mass averaged FHP measured velocity components, intraspacer.

incremental angular changes in reduced time duration when compared to the conventional manual calibrator.

An uncertainty analysis is completed on the FHP calibration data. Within a $\pm 20^\circ$ range total pressure uncertainty is found to be less than ± 12 Pa, static pressure uncertainty is less than ± 5 Pa, and velocity uncertainty is less than ± 1 m/s (4%).

A calibrated probe is placed into a large-scale axial turbine research rig. The research rig AFTRF has a recently modified probe traverser, state-of-the-art stepper motor drivers, pressure transducers, and programming approach. The new traverser replaces the old belt driven traverser with a mechanical system operated by a few linear translation stages. The new traversing system allows for effective adaptive gridding with much higher spatial resolution and position accuracy when compared to the belt driven system. The new system has increased the number of data points that can be collected in a two-hour turbine run period from 336 points to 868 points, an increase of approximately 160%. Current system parameters are monitored in real-time using a graphical user interface allowing for ease of tracking and monitoring the results of the test.

The current adaptive grid definition is proved to the computer by the user in a manual manner. However, the present system also allows a fully automatic/adaptive grid definition starting from a coarse grid measurement. The present system has capabilities to detect large and small gradients of measured quantities in a relatively coarse grid. The computerized approach can define the new time optimized adaptive grid without human intervention. Experiments of this fully automated measurement grid generation system are underway.

The current approach provides a much needed mass averaged flow measurement system since it can provide all

three components of the velocity vector over an area of interest with improved accuracy.

The calibrated probe currently maps the flow field behind the NGV using the new traversing system along one vane pitch and full span. Typical NGV passage exit flow structures such as vane wake, boundary layer, and passage vortex within the field are identified. The adaptive gridding method allows for measurements locations in these flow structures to be increased, while areas of smaller gradients are coarser. This leads to a reduction in the amount of time required to measure one entire vane passage.

The present paper presents significant improvements in FHP based aerodynamic measurements in four significant areas. The specific approach reduces the elapsed calibration time of a typical Five-Hole Probe. A second major improvement is in the spatial resolution of measurements in selected high gradient areas. The third important property of the present approach is in the improved accuracy of the measurements. Finally, the current approach reduces turbine facility run-time significantly.

Conflict of Interests

The authors declare that there is no conflict of interests regarding the publication of this paper.

Acknowledgments

The authors acknowledge the financial support provided for Jason Town by the Department of Aerospace Engineering at Penn State University. Cengiz Camci also acknowledges the support generously provided to him by TUBITAK, The Scientific and Technological Research Council of Turkey, during his sabbatical leave at Istanbul Technical University. Mr. Rick Auhl, Mark Catalano, and Kirk Hellen of Aerospace Engineering at Penn State provided significant technical expertise during the construction and execution of the experiments. The Five-Hole Probe construction at the subminiature scale would not have been possible without Mr. Harry Houtz's technical contributions.

References

- [1] B. G. Wiedner, *Passage Flow Structure and its Influence on Endwall Heat Transfer in a 90° Turning Duct*, The Pennsylvania State University, University Park, Pa, USA, 1994.
- [2] A. L. Treaster and A. M. Yocum, "The calibration and application of five-hole probes," *ISA Transactions*, vol. 18, no. 3, pp. 23–34, 1979.
- [3] C. Ostowari and W. H. Wentz, "Modified calibration techniques of a five-hole probe for high flow angles," *Experiments in Fluids*, vol. 3, no. 1, pp. 166–168, 1983.
- [4] C. F. R. Nowack, "Improved calibration method for a five-hole spherical Pitot probe," *Journal of Physics E: Scientific Instruments*, vol. 3, no. 1, pp. 21–26, 1970.
- [5] J. P. Weiz, *An Algorithm for Using the Five-Hole Probe in the Non-Nullled Mode*, The Applied Research Laboratory of the Pennsylvania State University, University Park, Pa, USA, 1980.
- [6] B. A. Reichert and B. J. Wendt, *A New Algorithm for Five-Hole Probe Calibration and Data Reduction and Its Application to a Rake-Type Probe*, ASME-FED, 1993.
- [7] R. G. Dominy and H. P. Hodson, "Investigation of factors influencing the calibration of five-hole probes for three-dimensional flow measurements," *Journal of Turbomachinery*, vol. 115, no. 3, pp. 513–519, 1993.
- [8] G. L. Morrison, M. T. Schobeiri, and K. R. Pappu, "Five-hole pressure probe analysis technique," *Flow Measurement and Instrumentation*, vol. 9, no. 3, pp. 153–158, 1998.
- [9] S. W. Lee and T. J. Yoon, "An investigation of wall-proximity effect using a typical large-scale five-hole probe," *Korean Society of Mechanical Engineers International Journal*, vol. 3, no. 13, pp. 273–285, 1999.
- [10] M. C. Brophy, A. L. Treaster, D. R. Stinebring, and J. P. Weiz, "Optimization of a five-hole probe wake measuring system," Technical Memorandum 87-156, Applied Research Laboratory, The Pennsylvania State University, University Park, Pa, USA, 1980.
- [11] N. Sitaram, B. Lakshminarayana, and A. Ravindranath, "Conventional probes for the relative flow measurement in a rotor blade passage," in *Proceedings of the Joint Fluids Engineering Gas Turbine Conference and Products Show*, New Orleans, La, USA, March 1980.
- [12] J. Town and C. Camci, "Sub-miniature five-hole probe calibration using a time efficient pitch and yaw mechanism and accuracy improvements," in *Proceedings of the ASME International Gas Turbine Conference*, ASME GT-46391, Vancouver, Canada, 2011.
- [13] A. J. Pisasale and N. A. Ahmed, "Theoretical calibration for highly three-dimensional low-speed flows of a five-hole probe," *Measurement Science and Technology*, vol. 13, no. 7, pp. 1100–1107, 2002.
- [14] A. J. Pisasale and N. A. Ahmed, "A novel method for extending the calibration range of five-hole probe for highly three-dimensional flows," *Flow Measurement and Instrumentation*, vol. 13, no. 1-2, pp. 23–30, 2002.
- [15] A. J. Pisasale and N. A. Ahmed, "Development of a functional relationship between port pressures and flow properties for the calibration and application of multihole probes to highly three-dimensional flows," *Experiments in Fluids*, vol. 36, no. 3, pp. 422–436, 2004.
- [16] S. J. Lien and N. A. Ahmed, "An examination of suitability of multi-hole pressure probe technique for skin friction measurement in turbulent flow," *Flow Measurement and Instrumentation*, vol. 22, no. 3, pp. 215–224, 2011.
- [17] K. Kuisoon, B. G. Wiedner, and C. Camci, "Turbulent flow and endwall heat transfer analysis in a 90° turning duct and comparisons with measured data—part II: influence of secondary flow, vorticity, turbulent kinetic energy, and thermal boundary conditions on endwall heat transfer," *International Journal of Rotating Machinery*, vol. 8, no. 2, pp. 125–140, 2002.
- [18] K. Kuisoon, B. G. Wiedner, and C. Camci, "Turbulent flow and endwall heat transfer analysis in a 90° turning duct and comparisons with measured data. Part I. Influence of Reynolds number and streamline curvature on viscous flow development," *International Journal of Rotating Machinery*, vol. 8, no. 2, pp. 109–123, 2002.
- [19] C. Camci and D. H. Rizzo, "Secondary flow and forced convection heat transfer near endwall boundary layer fences in a 90° turning duct," *International Journal of Heat and Mass Transfer*, vol. 45, no. 4, pp. 831–843, 2001.

- [20] B. Lakshminarayana, C. Camci, I. Halliwell, and M. Zaccaria, "Design and development of a turbine research facility to study rotor-stator interaction effects," *International Journal of Turbo & Jet Engines*, vol. 13, no. 3, pp. 155–172, 1996.
- [21] J. R. Taylor, *An Introduction to Error Analysis the Study of Uncertainties and Physical Measurements*, University Science Books, Sausalito, Calif, USA, 1997.

Research Article

Detection of Rotor Forced Response Vibrations Using Stationary Pressure Transducers in a Multistage Axial Compressor

William L. Murray III and Nicole L. Key

Purdue University, 500 Allison Road, West Lafayette, IN 47907, USA

Correspondence should be addressed to Nicole L. Key; nkey@purdue.edu

Received 23 July 2014; Revised 31 October 2014; Accepted 3 November 2014

Academic Editor: Mark McQuilling

Copyright © 2015 W. L. Murray III and N. L. Key. This is an open access article distributed under the Creative Commons Attribution License, which permits unrestricted use, distribution, and reproduction in any medium, provided the original work is properly cited.

Blade row interactions in turbomachinery can lead to blade vibrations and even high cycle fatigue. Forced response conditions occur when a forcing function (such as impingement of stator wakes) occurs at a frequency that matches the natural frequency of a blade. The objective of this research is to develop the data processing techniques needed to detect rotor blade vibration in a forced response condition from stationary fast-response pressure transducers to allow for detection of rotor vibration from transient data and lead to techniques for vibration monitoring in gas turbines. This paper marks the first time in the open literature that engine-order resonant response of an embedded bladed disk in a 3-stage intermediate-speed axial compressor was detected using stationary pressure transducers. Experiments were performed in a stage axial research compressor focusing on the embedded rotor of blisk construction. Fourier waterfall graphs from a laser tip timing system were used to detect the vibrations after applying signal processing methods to uncover these pressure waves associated with blade vibration. Individual blade response was investigated using cross covariance to compare blade passage pressure signatures through resonance. Both methods agree with NSMS data that provide a measure of the exact compressor speeds at which individual blades enter resonance.

1. Introduction

Blade row interactions in turbomachinery can lead to blade vibrations and even high cycle fatigue. Forced response conditions occur when the frequency of the forcing function matches the frequency of the blade vibration mode. Forcing functions include the viscous wakes shed from upstream blade rows and the potential fields generated by the upstream and downstream blade rows. It is impossible to remove all resonant crossings from the entire operating range of a multistage axial compressor, and thus, it is important to detect blade vibration to ensure it is within proper limits and to bring to light unexpected engine-order resonant conditions. Since recent turbomachinery designs have moved toward higher pressure ratios and integrally bladed rotors (IBRs), aerodynamic forcing environments have grown in strength and mechanical system damping has decreased. It is now more important than ever to develop robust, dependable methods to detect, characterize, and help mitigate potential vibrational issues before they can have disastrous effects.

Common techniques for detecting blade vibration include strain gauges or tip timing probes. Strain gauge techniques can be employed in a number of ways, but the most common technique involves mounting strain gauges on the blades, and when rotor vibrations are considered, a slip-ring is needed to transmit the signals from the strain gauges to the recording equipment. This measurement is easier if, instead, the strain gauges are mounted to stationary hardware, such as a stator vane or used in a cascade experiment, as done by Freund et al. [1]. Tip timing systems, or nonintrusive stress measurement systems, (NSMS) utilize a set (typically 8) of light probes that are arranged in an optimal configuration to detect a particular vibrational mode. Thus, they are limited in the quantity modes that can be measured, and if there is little deflection in the outer part of the blade for the mode of interest, they will not provide any useful information.

Some researchers have also used pressure transducers to study blade vibrations. Pressure transducers can be mounted either on a stationary part of the machine, most often

the casing endwall as in the work conducted by Baumgartner et al. [2], or they can be mounted onto the rotating hardware, for example Gill and Capece [3], where the signal would be transmitted through a slip ring device to a recorder. When measuring rotor vibrations in the stationary reference frame, the vibration frequency will be Doppler shifted as discussed by Mengle [4] and Kurkov [5].

The acoustic environment inside of an operating compressor is noisy and usually dominated by flow physics unrelated to compressor vibration. Baumgartner et al. [2] used a single hot film downstream of the tip of a vibrating rotor blade and some casing-mounted pressure transducers to investigate rotating stall and flutter vibration of rotating blades. They found that the spectral magnitudes of the instability and vibration were significantly smaller in amplitude than the spectral magnitude related to blade passing frequency. Kurkov [5] showed that the spectrum of the signal obtained when the blade was not vibrating could be subtracted from the spectrum of the pressure signal measured during the forced response vibration to view the frequency spectrum of forced response. This method has also been employed by Mengle [4] in his attempt to remove integral engine order frequencies from observed spectra of a rotating compressor blade. Kurkov [5] was able to take an average frequency response of 16 revolutions of data without vibration and subtract that frequency spectrum from the vibratory response spectrum.

Rotating stall and flutter have been studied extensively in the realm of aeromechanics. These non-EO vibrations tend to have larger vibration amplitudes and correspondingly larger pressure wave amplitudes, making them easier to measure with pressure transducers. Leichtfuss et al. [6] measured non-engine-order stall flutter spectral signatures with stationary Kulite pressure transducers. Schoenenborn and Breuer [7] measured torsional vibration and flutter of blades during surge and were able to detect aeroacoustic signatures from unsteady pressure transducers related to blade motion relatively easily. They were also able to relate the pressure measurements to NSMS tip timing blade deflection data.

The development of techniques that allow pressure transducers to detect forced response during compressor operation as a real-time diagnostic tool or simply as a backup to more complex vibration detection instrumentation is valuable. Pressure fluctuations due to engine order (EO) vibrations such as forced response are typically smaller in comparison to pressure fluctuations due to non-EO vibrations (such as those associated with flutter, rotating stall, and buffeting), making forced response detection difficult. Additionally, forced response pressure fluctuations are Doppler shifted to blade pass frequencies (and their harmonics), which are already heavily influenced by aerodynamics even when the blades are not vibrating, making the identification of forced response pressure components difficult.

The authors are not aware of any open literature that discusses directly measured engine-order forced response through the use of stationary pressure transducers in an experimental compressor facility, as the amplitudes of the acoustic waves are generally very small in comparison to

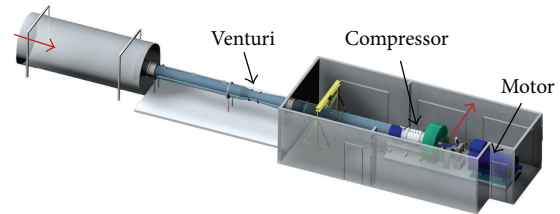


FIGURE 1: Layout of the Purdue 3-Stage Axial Compressor Research Facility.

other flow field features. Most research conducted to this point has been focused on flow measurements associated with nonintegral engine order vibrations, such as stall, flutter, surge, or acoustic resonances. Fridh et al. [8] measured the spectral component of forced response from partial admission inlet distortion in a turbine using pressure transducers in a rotating reference frame. They were able to detect resonance at Campbell diagram crossings with strain gauge and pressure transducer data. However, the strain gauge data provided more detailed spectral data on the response characteristics of important Campbell crossings compared to the pressure data. Therefore, the objective of this paper is to show how embedded rotor vibrations associated with forced response have been detected with stationary Kulite pressure transducers and describe in detail the important aspects of the instrumentation and data processing techniques that made this possible. This paper marks the first time in the open literature that engine-order resonant response has been measured in a compressor using stationary pressure transducers.

2. Materials and Methods

The Purdue Three-Stage Research Compressor is a unique research facility that models the rear stages of a high-speed compressor, matching Mach number and Reynolds number to aircraft engine operating conditions. The facility is conducive to detailed flow measurements in the pitch wise direction because each vane row can be individually indexed past stationary probes. There is a significant and measurable total pressure rise per stage, and blade heights are 50.8 mm, allowing sufficient space for detailed flow measurements without probe blockage issues.

The facility layout is shown in Figure 1. Unconditioned ambient air is drawn into a large settling chamber. Air enters the inlet duct through a bellmouth, which is followed by a series of flow straighteners. An ASME-standard long-form Venturi flow meter installed in the inlet ducting measures the mass flow rate through the compressor. Following an additional length of insulated ducting inside the test cell, a nosecone directs the flow into the annulus of the compressor. The compressor has a constant-area annulus with a 609.6 mm outer diameter. After passing through the compressor, the air encounters a sliding-annulus throttle and exhausts to atmosphere through a collector. The compressor is driven by a 1 MW AC motor with a variable frequency drive. The motor

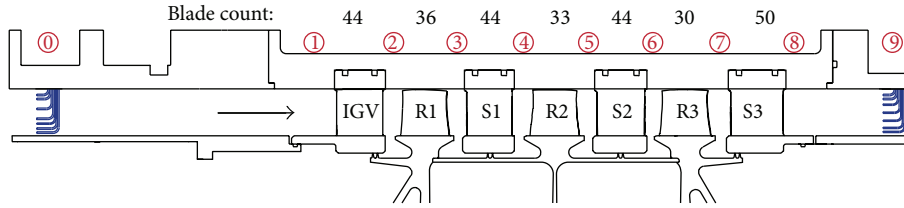


FIGURE 2: A cross-section of the flow path including data acquisition stations.

is connected to a speed-increasing gearbox via a gear coupling to provide the compressor design speed of 5,000 RPM.

The compressor consists of an inlet guide vane (IGV) row followed by three stages, Figure 2. The compressor features IBRs with rotor counts of 36 for Rotor 1, 33 for Rotor 2, and 30 for Rotor 3. The rotors are attached to a drum in a fixed configuration. The shrouded stator rows have similar vane counts of 44 except for S3, which has 50 vanes. The vane rings are split into two halves and installed in the split casing. Steady compressor performance is measured with 7-element Kiel head total pressure and total temperature rakes. The overall compressor total pressure ratio is measured with rakes positioned at Stations 0 and 9.

Figure 3 shows the Campbell diagram for Rotor 2. With 44 vanes upstream in Stator 1 and 44 vanes downstream in Stator 2, the 44 engine order excitation of the first torsion (1T) vibratory mode is the Campbell diagram crossing studied in this research. The frequency of the 1T mode is 2700 Hz, and the 44EO excitation of the R2 1T vibratory mode occurs near 3700 RPM (74% speed). Also shown is the first torsion mode shape and nodal line as calculated by Fulayter [9] using a finite element analysis.

Tip timing data were acquired to characterize the Rotor 2 1T vibratory response to the 44EO excitation by measuring the rotor tip deflection. These measurements can be used to compare the results obtained with the new data processing technique developed for the pressure sensors. The Agilis nonintrusive stress measurement system (NSMS) consists of 8 fiber-based optical probes, laser and detector boxes, and an NI 5112 ADC data acquisition chassis. The laser module generates a signal that is sent to each of the 8 probes that shine down on the passing blades. The casing-mounted probes also have a sensing optical cable that transmits the reflection of the blade tips to a photo detector and a pulse-to-digital converter. The converter has a digital clock to track the time of the blade passing and relate it to a 1/rev shaft signal. The timing of each blade arrival and the correlation of arrival times over all 8 sensors allow the measurement of the amplitude and phase of vibration for each blade.

The resolution of the tip timing measurements is a function of the counter timer board clock speed, the rotor tip diameter, and the rotor tip speed. With a sampling period of 2 microseconds, the resolution of the tip timing data near the 1T vibratory resonance of Rotor 2 is about 0.009 mils. Since it is unsafe to operate at the resonance speed due to potential fatigue and failure of the vibrating rotor, the data are acquired during a transient speed change through the resonant condition, and the sweep rate is an important

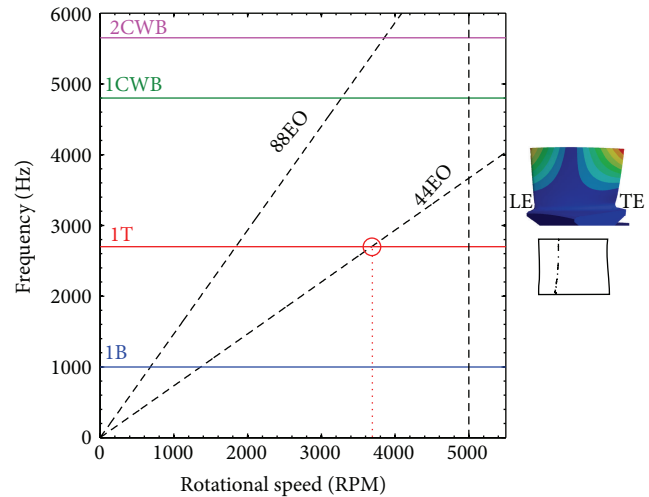


FIGURE 3: Campbell diagram for Rotor 2 including mode shape and nodal line for the 1T vibratory mode.

parameter. As suggested by von Flotow [10], the critical sweep rate is defined as the ratio of the half-power bandwidth acquired over 3 vibration cycles. For the 1T resonance of Rotor 2, the critical sweep rate is around 15 rpm/s. Also, the control of the compressor drive system was programmed such that the compressor speed would have a constant acceleration rate through the resonant condition, and thus, this aspect of the experiment was fully controlled. Sweep rates as low as 2.2 RPM/s were utilized.

The steady loading of the compressor was adjusted using the throttle. Two loading conditions were considered: nominal loading (NL) and high loading (HL). Figure 4 shows the compressor performance map including two speedlines: 68% and 80% corrected speed. These speedlines bound the resonant condition studied. Each point on the speedline represents the area-averaged pressure ratio as determined from a vane traverse every 5% passage to include the effects of the vane wakes. The mass flow rate has been normalized by the stall flow rate at 68% corrected speed. The total pressure ratio is the overall compressor total pressure ratio. The operating lines were created by quickly scanning the pressure rakes and flow meter while accelerating the compressor through resonant speed, and thus, they are not area-averaged quantities.

The pressure measurements were acquired from the downstream vane which was instrumented for a different research project. The sensors were Kulite LQ-062 pressure

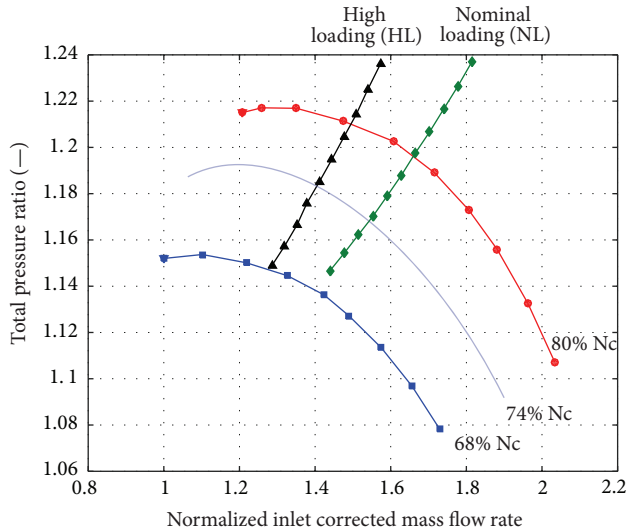


FIGURE 4: Compressor operating map including operating lines.

transducers with a range of 0–5 psig. The key aspect that made these sensors useful in blade vibration detection is that they had no screen, and this resulted in a high frequency response, as much as 100–150 kHz per manufacturer's specifications. Other sensors in the facility with lower frequency response did not capture the same phenomenon. To briefly describe the installation of these sensors, a removable S2 passage that could be sent to Kulite for sensor installation was fabricated, Figure 5. The part was constructed of 17-4 PH stainless steel and EDM cut into 3 segments. The vanes of the removable passage were machined to accommodate a total of 16 transducers, 8 on each vane. They were positioned at 50% span and 80% span, and axial positions include 10%, 20%, 30%, and 40% chord on the pressure side of one blade and the suction side of another. The sensors were clustered as close as possible to the leading edge, and RTV was used to back fill the pockets drilled for the sensors.

Figure 6 shows a diagram of the location of the pressure transducers installed in Stator 2 with respect to the flowpath. Because of space restrictions, a single vane could not support transducers on both the pressure side and suction side. Thus, a passage was instrumented, with the transducers measuring a particular flow passage. This arrangement was also favored because RTV was used to backfill the pocket, and thus, the RTV did not affect the pressure measurements since measurements were not made on the same surface with the RTV treatment.

Figure 7 shows photographs of the removable Stator 2 insert with the Kulite pressure transducers installed. The wires are fed through a hole in the casing and the vane row is not traversed when this passage is installed. In the photograph on the right, the RTV on the suction side of the top vane is visible. The unsteady pressure on the pressure side of the top vane is measured. Also, some of the holes for the pressure measurements on the suction side of the bottom vane are visible.

The excitation signal and amplification for the Kulites were provided by a Precision Filter 28000 chassis with

quantity 4, 28118 full bridge amplification cards, each capable of amplifying 8 channels. Data were digitized with an NI PXI-1073 chassis with two 16-channel NI PXIE-6358 cards, with a total bandwidth of 1.25 MS/s per channel for all 32 channels simultaneously sampled. The transducers were calibrated with a calibration chamber, Figure 8, constructed from 15.24 cm cast aluminum pipe that was 15.24 cm long with caps on each end. The stator was installed in the chamber by a short piece of threaded rod that was threaded into one of the machined and tapped threads in the shroud of the stator. The LEMO connectors were fed out of two holes drilled in one of the end caps and sealed with silicone sealant. The heat shrink used on the outside of each of the wires was also sealed at each end with silicone to keep air from leaking through the heat shrink and out of the calibration chamber. The slope of the calibration for the installed stator sensors was as much as 25% different from the values quoted by Kulite for the sensors prior to installation in the stator highlighting the need for calibration.

3. Results and Discussion

Since this is a research compressor that operates at lower pressure levels than an actual gas turbine compressor, the pressure waves associated with blade vibration are expected to be small. To assess the ability of the available pressure instrumentation to detect the blade vibration, a simple analysis was performed. LINSUB, a linear, flat plate cascade, aeromechanics solver created by Whitehead [11], was used to predict the expected pressure amplitude due to the vibration of Rotor 2 for this forced response condition. It outputs the absolute and fluctuating components of the flow field (such as lift, pressure, and moments) related to bending, torsion, chord wise bending, and wakes/gusts. In this case, it is of interest to calculate the unsteady pressure waves traveling upstream and downstream from a blade vibrating in torsion. Based on the compressor geometry and previously measured flow conditions near resonance, LINSUB predicted an upstream-traveling pressure component of 292.3 Pa and a downstream-propagating pressure wave of amplitude 584.7 Pa.

The typical uncertainty of the Kulite pressure transducers model LQ-062 is $\pm 0.1\%$ of the full range of the transducer, which corresponds to ± 34.5 Pa. (The manufacturer provides a typical and maximum uncertainty, where the maximum is $\pm 0.5\%$.) This uncertainty does not include any uncertainty or noise introduced by connectors, cables, Precision Filter amplifier equipment, or the PXI analog-to-digital conversion. By including these effects, the largest resulting uncertainty in the Kulite pressure measurements amounts to approximately ± 175.8 Pa. This was calculated considering that the Precision Filter 28118 amplifier cards have an accuracy of $\pm 0.1\%$ of full scale range and the PXI-6358/6356 A/D converters have an uncertainty of 0.012% full scale.

The LINSUB analysis is 1D, and thus serves as an approximation of the expected pressure amplitudes due to rotor vibration. Nonetheless, the results indicate that at these compressor speeds, the pressure waves due to resonance are small. However, if signal processing techniques can be



FIGURE 5: Vane ring modification for accommodation of Kulite sensors.

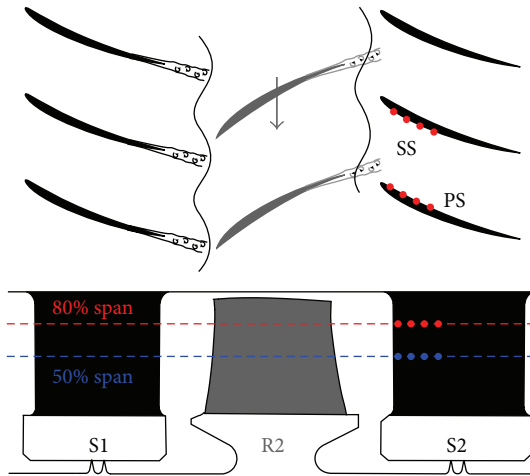


FIGURE 6: Top-down and side view of Stator 2 with installed pressure transducers.

developed to identify the blade vibration effects at these low compressor speeds, then vibrations in actual compressors which operate at higher speeds should be easier to detect.

To detect these small pressure waves generated by the vibrations of Rotor 2, several data processing methods were investigated. The most difficult issue was the removal of background noise and pressure information that was not pertinent to the blade vibration. Additionally, data handling algorithms to manage the large volumes of unsteady binary data were developed.

The Kulite pressure transducers are in the stationary reference frame, but the vibrating rotor is in the relative reference frame, and thus, the frequency of vibration as measured by the transducer will be shifted due to the relative motion between the rotor and the transducer. Mengle [4] showed that since the rotor is spinning at a rotation rate, Ω , the vibration frequency of the blades, ω , will be Doppler shifted to a different frequency, ω' , based on nodal diameter, ND, and wave number, m , in (1).

$$\omega' = \omega + (ND + mB) \Omega. \quad (1)$$

The nodal diameter can either be determined from the NSMS data or from the difference between stator vanes and rotor blades, since the frequency of vibration is an engine-order (EO) forced response, in this case, as shown in

$$ND = N_{\text{Stator Vanes}} - N_{\text{Rotor Blades}} = 44 - 33 = 11. \quad (2)$$

Because of blisk mistuning, the approximate band of blade response varies over a range of 2700–2735 Hz, as measured with NSMS. By choosing m values of $-2, -1, 0, 1,$ and 2 , the first few wave modes will be captured. These should be the highest responding modes. When the frequency of interest is associated with an engine-order forced response vibration, the Doppler shift will always shift the forced response to multiples of the blade pass frequency. Therefore, the signal processing challenge is to determine changes in the 33/rev frequency (and higher harmonics) in the spectrum. This may prove difficult because as the compressor rotational speed increases, changes in the strength of these components of the signal will also be associated with aerodynamic changes. However, if a spike in the higher harmonics of the signal is visible only in a RPM band where rotor vibration is known to occur (as measured with the tip timing data), then it will confirm that the pressure sensors detected rotor vibration.

An effective way to analyze the change in the pressure spectrum with time is with Fourier transform waterfall graphs. A cartoon explaining the construction of these graphs is shown in Figure 9. The pressure data from the sensors are recorded as the compressor rotational speed is increased at a constant rate through the speed corresponding to the first torsion vibratory mode. First, the pressure data from a particular channel are divided up into separate compressor revolutions using the use of the once-per-revolution signal from the compressor shaft. Simply dividing the data by each revolution is effectively square windowing the signal, which can introduce unwanted artifacts into the frequency spectrum, and thus, a Kaiser window was applied to each revolution. A Kaiser window allows a high resolution between two frequency components that are separated greatly in amplitude but closely related by frequency. This windowing technique allows for the detection of small components of the IT signal that are Doppler shifted to a frequency slightly different than blade pass frequency due to individual blade mistuning. It also allows for a cleaner waterfall plot, resolving features due to a better resolution in frequency.

After windowing the revolution of data, a Fourier transform is performed, and the frequency is normalized by the rotor blade pass frequency. This normalization is important because it connects the spectral magnitudes to blade pass events rather than to physical compressor speeds, which are constantly changing through the sweep. Pressure fluctuations will occur with the blade passing events due to rotor wakes impinging on the downstream vane row. Thus, a significant magnitude in the spectral component associated with blade pass frequency will always be present. To reduce this effect in the hopes of identifying the small pressure waves associated



FIGURE 7: Photographs of the removable Stator 2 insert with pressure transducers installed.

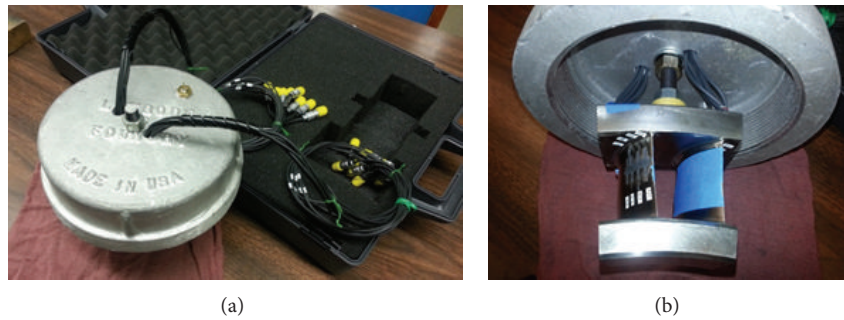


FIGURE 8: Calibration chamber setup for the vane-mounted pressure transducers.

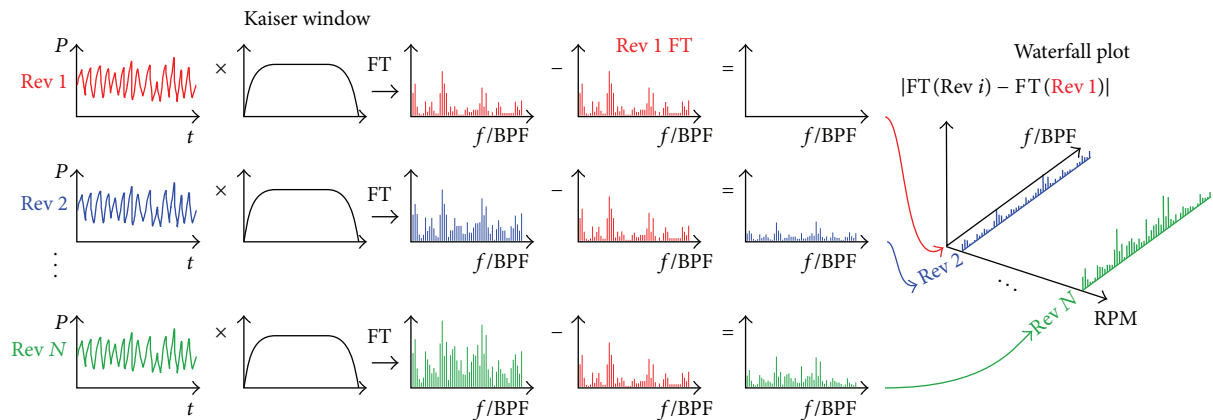


FIGURE 9: Data processing strategy for generating waterfall graphs.

with the resonant vibration, the spectral magnitudes measured at the beginning of the sweep (3670 rpm) are subtracted from the spectra at all successive revolutions. Then, these reduced spectra are assembled to create the resulting waterfall graph. This provides a snapshot of several thousand Fourier transforms, allowing trends to be easily identified. This also allows for easy comparison of the changes in amplitude of a given frequency band as the compressor accelerates through resonance.

Figure 10 shows the waterfall graph constructed from data acquired at nominal loading. The labels on the right show particular blade pass frequencies and their harmonics. Recall the blade counts decrease by 3 (Rotor 1 has 36 blades, Rotor 2

has 33, and Rotor 30 has 30). The 44EO excitation of the Rotor 2 first torsion vibration should occur at Rotor 2 blade pass frequency (33/rev) or its harmonics. The 33/rev frequency component is, for the most part, nonexistent. Also, the 66/rev tends come and go. However, the 99/rev either is nonexistent or appears and disappears in conjunction with resonance. There are also other frequencies present, namely, responses at 30/rev, 36/rev, higher order harmonics of these frequencies (which correspond to R1 and R3 blade pass frequencies). This is due to the pressure transducers picking up the destructive and constructive interference of R1 and R3. The manner in which the reflected multiples of these blades pass frequency harmonics is transmitted through the compressor and could

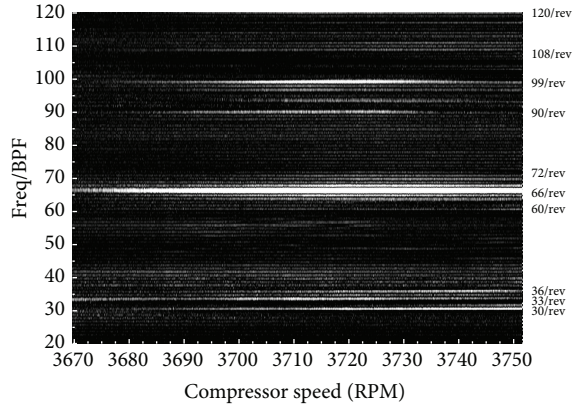


FIGURE 10: Waterfall graph at nominal loading.

be indicative of resonance, perhaps even R3 resonance which occurs in the speed range of 3705–3805 RPM.

Figure 11 shows the amplitude of the 99/rev response (taken to be the sum of the amplitudes in the frequency band between 98.5/rev and 99.5/rev), and the response grows and decays as a function of compressor speed. For comparison to NSMS data, Figure 12 shows the RPM band of the Rotor 2 resonant response. Each blade has its own natural frequency, and the results from all 33 blades are overlaid. One graph shows the results at nominal loading and the other at high loading. The mean loading does not change the frequency of the response, but it does change the amplitude of the response. The compressor speeds (or frequency) of the 1T response ranges from approximately 3700 to 3730 RPM. The range at which the 99/rev frequency bands increase in amplitude from the pressure transducer measurements agrees well with the NSMS data.

The 66/rev response grows but then seems to level out as RPM is increased, and this could be attributed to the data processing technique, where the nonvibrating spectrum at the low speed range of the sweep was used to adjust the other spectra, as shown in Figure 9. Therefore, if the spectral magnitudes change because of the change in compressor speed resulting in a change of the aerodynamic interaction of the blade rows, then that would appear in the waterfall graphs as well.

The 33/rev spectral component does not have a significant amplitude, and this is a result of the data processing methods. The blade pass frequency component is large and by subtracting the spectrum from the first revolution off of all subsequent signals, it was sufficient to remove the blade pass component from the other revolutions. The spectral magnitude of blade pass frequency was an order of magnitude higher than the harmonics, and thus, it would be difficult to identify the small pressure fluctuations associated with rotor vibration at this frequency. Therefore, to detect forced response vibration effects from the vane pressure signal, efforts should focus on the higher harmonics of blade pass frequency where the Doppler shifted forced response frequency components are on the same order of magnitude as the amplitudes that occur when the blade is not vibrating.

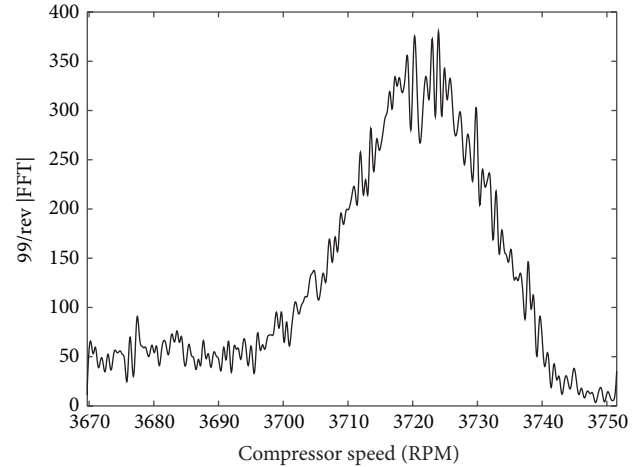


FIGURE 11: The magnitude of the spectral component associated with the 99/rev frequency at nominal loading.

The waterfall graph for the results at high loading is shown in Figure 13. As before, the magnitude of the 99/rev spectral component signal is shown in Figure 14. The increased spectral magnitude of the 99/rev frequency occurs over the same speed range as the NSMS system measured the rotor vibration, as shown in Figure 12. The 33/rev and 66/rev frequencies in the waterfall graph follow the same trends as shown at nominal loading: the 33/rev contribution has been subtracted out and the 66/rev contribution seems to be increasing with compressor speed.

In summary, the frequency domain analysis showed that the pressure transducers did detect the rotor vibration at a Doppler shifted frequency associated with 3rd harmonic of blade pass frequency (99/rev). This waterfall analysis considers the spectrum on a revolution-by-revolution basis. Another way to investigate these data is to focus on a time domain analysis where individual blade pass events are considered, rather than a full revolution of data. The advantage of having NSMS data is the vibration frequency and amplitude of each rotor blade is recorded, and thus, the pressure signals associated with highly responding blades can be investigated. This can be done with a cross correlation which essentially looks for a blade pass event that appears to be different than the others. The pressure trace measured when the blade is vibrating will be different than that measured when the blade is not vibrating, and thus a low correlation value could be an indicator of the forced response event.

Cross correlation and cross covariance are methods of determining the “similarity” or likeness, of two random vectors or signals, denoted by x and y with length N . By varying the offset, m , between the two vectors, a correlation sequence of the two vectors is generated and is a function of the element-by-element product of each point in the vector, as shown in

$$\hat{R}_{xy}(m) = \begin{cases} \sum_{n=0}^{N-m-1} x_{n+m} y_n^*, & m \geq 0 \\ \hat{R}_{yx}^*(-m) & m < 0 \end{cases} \quad (3)$$

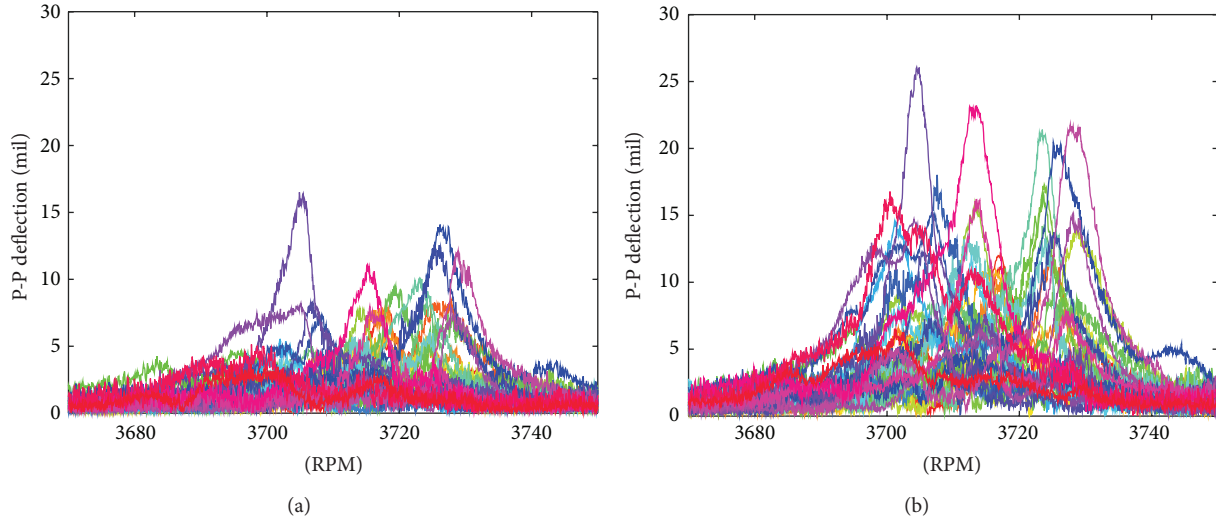


FIGURE 12: NL (a) and HL (b) peak-to-peak deflection of each blade of R2 as recorded by NSMS.

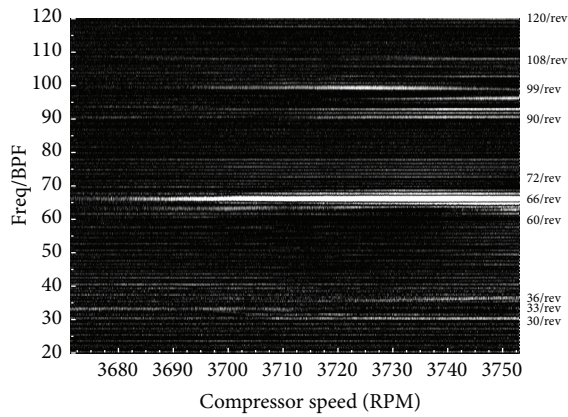


FIGURE 13: Waterfall graph at high loading.

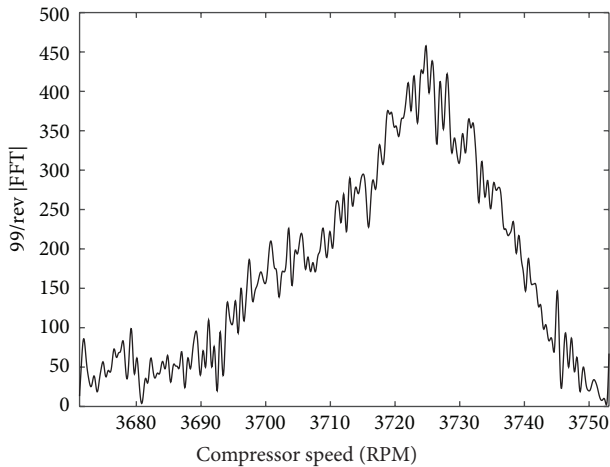


FIGURE 14: The magnitude of the spectral component associated with the 99/rev frequency at high loading.

Cross correlations, however, are not normalized, and since the amplitude of the mean level of pressure continually increases due to the increase in compressor total pressure ratio with increasing speed during the sweep, the transient nature of this experiment renders the cross correlation inappropriate. Therefore, to remove the effects of the magnitude differences, the cross covariance is considered. It is the product of two vectors, which are normalized by their mean, denoted by $(1/N) \sum_{i=0}^{N-1} x_i$ and $(1/N) \sum_{i=0}^{N-1} y_i^*$. The cross covariance, (4), is used since there will be no overall rise in correlation due to the rise in overall compressor pressure ratio. Consider

$$c_{xy}(m) = \begin{cases} \sum_{n=0}^{N-|m|-1} \left(x(n+m) - \left(\frac{1}{N} \sum_{i=0}^{N-1} x_i \right) \right) \\ \quad \times \left(y_n^* - \left(\frac{1}{N} \sum_{i=0}^{N-1} y_i^* \right) \right) & m \geq 0, \\ c_{yx}^*(-m) & m < 0. \end{cases} \quad (4)$$

Figure 15 shows the pressure traces measured on the pressure side of Stator 2 when Blade 26 was passing in front of it. The different traces are shown for different compressor speeds to illustrate how the pressure signal associated with a particular Rotor 2 blade is changing throughout the compressor sweep. The red trace at 3671 RPM is the pressure trace from the 1st full revolution of data to which all successive pressure traces are compared for this analysis. The blue and cyan lines, at 3705 and 3710 RPM, respectively, show pressure traces of the blade in and around resonance, and the 3735 RPM black lines shows the pressure trace near the end of the sweep. This illustrates how much the shape of the pressure signal will change as the compressor pressure ratio increases.

In Figure 16, there is a large drop in cross covariance around 3705 RPM, which corresponds directly to the RPM

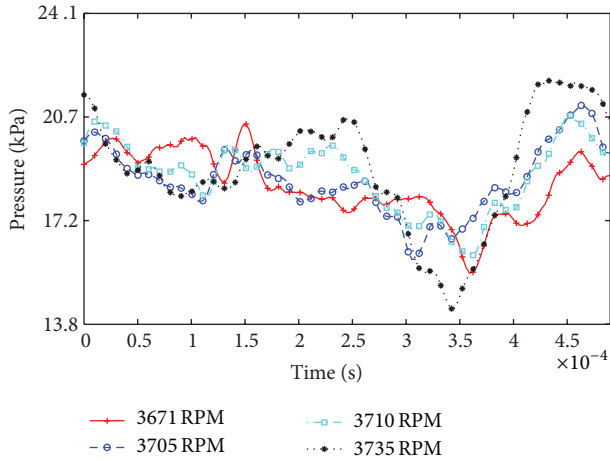


FIGURE 15: Rotor blade passage traces, Blade 26, PS 80% Span 20% Chord, HL.

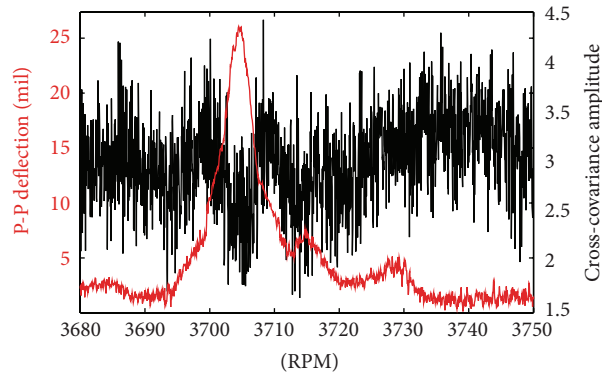


FIGURE 16: Cross covariance and NSMS deflection for Blade 26 at high loading (80% span).

band of maximum displacement in R2 for blade 26 at high loading (refer to Figure 12). Although the drop in covariance amplitude is small in comparison to the revolution-to-revolution changes in covariance amplitude (i.e., the noise in the signal), it is apparent that there is approximately a 30% drop in average covariance amplitude from 3700 to 3705 RPM, and then a corresponding 30% increase at 3705–3710 RPM.

Blade 22 is another high responding blade according to the NSMS data from Figure 12. The cross covariance of the pressure signal acquired at 80% span shows a similar drop in cross covariance, Figure 17. The compressor speed range over which this occurs is roughly equivalent to the speed range for which the NSMS data show that the blade vibration occurs. There is an inherent waviness, or fluctuation, in the overall trend of the cross covariance that is apparent in all sensors regardless of speed, which makes the measurements of cross covariance amplitude drops difficult to compute. Future work is aimed at advanced signal processing techniques to further explore the utility of the cross covariance in identifying rotor vibration.

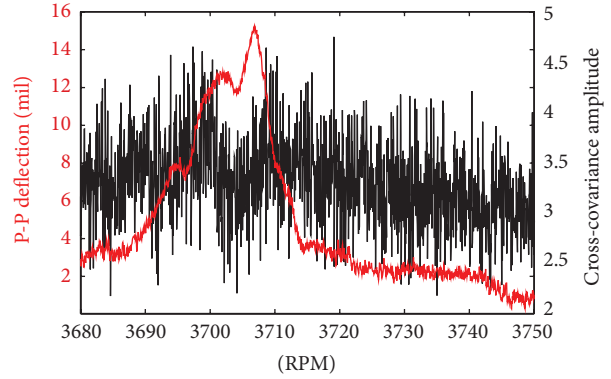


FIGURE 17: Cross Covariance and NSMS deflection for Blade 22.

4. Conclusions

This is the first time in the open literature that measurements of a compressor forced response vibrational mode have been detected with stationary pressure transducers. This paper explains the particular data processing methods used to identify rotor vibration. The data processing was challenging since the data were transient in nature; the compressor was accelerated through the resonant speed as the data were collected to avoid depleting several cycles from the life of the blade. An additional challenge was associated with the fact that forced response rotor vibrations always get Doppler-shifted to a harmonic of blade pass frequency when measured in the absolute reference frame. This makes it difficult to identify the smaller contributions of that spectral magnitude that are associated with vibrations rather than the aerodynamics of the blade passing event. On top of all this, the smaller pressure levels associated with a research compressor result in small-amplitude pressure waves generated when the blade vibrates. Despite all these challenges, the technique was successful.

Detection of engine-order forced response at part speed compressor operation through the use of stationary pressure transducers could have an impact on the way blade vibrations are measured in turbomachinery, as this measurement method is significantly simpler than other advanced vibration measurements, such as rotating instrumentation and/or laser-based tip timing measurements. It can also revolutionize the health monitoring strategy of gas turbine compressors as it can identify high cycle fatigue issues prior to blade failure.

The focus of this research was to interrogate the signals obtained from fast-response pressure transducers while a 3-stage compressor was being accelerated through force response resonant speeds. The 44 engine order excitation of the first torsion vibrational mode of the embedded Rotor 2 was studied. Kulite pressure transducers without screens had enough frequency response to detect the blade vibration. In this experiment, the transducers of this type were installed in the downstream stator vane, but flush-mounting this sensor in the casing over the rotor would

be even more convenient. LINSUB was used to estimate whether the Kulite pressure transducers would be able to detect acoustic signatures from this forced response event, and it showed that the acoustic pressure fluctuations would be slightly higher (3-4 times) than the uncertainty in the Kulite pressure measurement. The amplitude of the pressure wave will increase with compressor rotational speed so while the pressure signature associated with blade vibration may be small in this research vehicle, it could be more significant at actual engine operating conditions rendering this technique perhaps even more effective for higher speed compressor investigations.

Data processing in both the frequency and time domain show that the acoustic signature generated by the vibrating rotor is detectable. Through the calculation of Doppler-shifted vibration frequencies, spectra related to the rotor vibration have been detected in the 3rd harmonic of the rotor blade pass frequency. Additionally, through the use of a cross covariance blade-to-blade similitude analysis, individual blade vibration has been detected and confirmed with NSMS tip timing results.

Future work is aimed at advanced signal processing techniques to further explore the utility of the cross covariance in identifying rotor vibration. In particular, the noise in the cross correlation results must be reduced if this type of signal is to be used in a control loop for compressor operation. Also, close collaboration with sensor manufacturers should be aimed at reducing the cost and increasing the durability of these sensors for implementation in actual gas turbines.

Nomenclature

ω :	Torsional vibration frequency
ω' :	Doppler-shifted torsional vibration frequency
ND:	Nodal diameter
B :	Number of blades
m :	Integer, harmonic number, lag offset
Ω :	Rotational velocity [1/s]
k :	Wave number, spring constant
c_{xy} :	Covariance term
N :	Vector length
\tilde{R}_{xy} :	Cross covariance term
x, y :	Arbitrary vectors.

Conflict of Interests

The authors declare that there is no conflict of interests regarding the publication of this paper.

Acknowledgments

This work was funded by the GUIde IV Consortium, which included NASA, the US Air Force, Rolls-Royce, GE, Pratt & Whitney, Honeywell, Siemens, and Mitsubishi. The authors are grateful to the GUIde IV Consortium for its guidance and financial support of this work. Also, the authors acknowledge Natalie Smith's artistic contribution to the figures.

References

- [1] O. Freund, M. Bartelt, M. Mittelbach, M. Montgomery, D. M. Vogt, and J. R. Seume, "Impact of the flow on an acoustic excitation system for Aeroelastic studies," *ASME Journal of Turbomachinery*, vol. 135, no. 3, Article ID 031033, 2013.
- [2] M. Baumgartner, F. Kameier, and J. Hourmouzaiadis, "Non-engine order blade vibration in a high pressure compressor," in *Proceedings of the ISABE International Symposium on Airbreathing Engines*, Melbourne, Australia, September 1995.
- [3] J. D. Gill and V. R. Capece, "Experimental investigation of flutter in a single stage unshrouded axial-flow fan," in *Proceedings of the 42nd AIAA Aerospace Sciences Meeting and Exhibit*, pp. 7997–8005, Reno, Nev, USA, January 2004.
- [4] V. Mengle, "Acoustic spectra and detection of vibrating rotor blades, including row-to-row interference," in *Proceedings of the AIAA 13th Aeroacoustics Conference*, Tallahassee, Fla, USA, October 1990.
- [5] A. P. Kurkov, "Flutter spectral measurements using stationary pressure transducers," *Journal of Engineering for Power*, vol. 103, no. 2, pp. 461–467, 1981.
- [6] S. Leichtfuss, F. Holzinger, C. Brandstetter, F. Wartzek, and H. P. Schiffer, "Aeroelastic investigation of a transonic research compressor," in *Proceedings of ASME Turbo Expo*, San Antonio, Tex, USA, June 2013.
- [7] H. Schoenenborn and T. Breuer, "Aeroelasticity at reversed flow conditions—part II: application to compressor surge," *Journal of Turbomachinery*, vol. 134, no. 6, Article ID 061031, 8 pages, 2012.
- [8] J. Fridh, B. Laumert, and T. Fransson, "Forced response in axial turbines under the influence of partial admission," *Journal of Turbomachinery*, vol. 135, no. 3, Article ID 041014, pp. 041014-1–041014-9, 2013.
- [9] R. D. Fulayter, *An experimental investigation of resonant response of mistuned fan and compressor rotors utilizing NSMS [Ph.D. dissertation]*, School of Mechanical Engineering, Purdue University, West Lafayette, Ind, USA, 2004.
- [10] A. von Flotow, *Hood Technologies Corporation's Analyze Blade Vibration Software Version 3.3 User Manual*, 2003.
- [11] D. S. Whitehead, "Unsteady two-dimensional linearized subsonic flow in cascades," in *AGARD Manual on Aeroelasticity in Axial-Flow Turbomachines*, vol. 1, pp. 3.24–3.30, 1987.

Research Article

Conjugate Heat Transfer Study of Combined Impingement and Showerhead Film Cooling Near NGV Leading Edge

Dileep Chandran and Bhamidi Prasad

Thermal Turbomachines Laboratory, Department of Mechanical Engineering, Indian Institute of Technology Madras, Chennai 600036, India

Correspondence should be addressed to Bhamidi Prasad; prasad@iitm.ac.in

Received 30 May 2014; Revised 20 September 2014; Accepted 4 October 2014

Academic Editor: Giovanni Carlomagno

Copyright © 2015 D. Chandran and B. Prasad. This is an open access article distributed under the Creative Commons Attribution License, which permits unrestricted use, distribution, and reproduction in any medium, provided the original work is properly cited.

A computational and experimental study is carried out on the leading edge region of a typical gas turbine NGV, cooled by a combination of impingement and showerhead film cooling. A detailed flow and conjugate heat transfer study has revealed the complex flow structure owing to the coolant-mainstream interaction and the influence of vane material thermal conductivity. The local effectiveness values obtained by the computations agreed well with the experimental data from IR thermography. The effect of blowing ratio on the overall effectiveness is found to be strongly dependent on the vane material conductivity. The effect of blowing ratio is also found to be different towards the pressure and suction sides of the stagnation region. However, the overall effectiveness is found to decrease by about 12% and 6% for low and high conducting materials, respectively, with an increase in mainstream Reynolds number from $Re = 4.8 \times 10^5$ to 14.4×10^5 .

1. Introduction

Heat transfer studies related to the leading edge cooling of a nozzle guide vane (NGV) are of great relevance and interest for the design of modern gas turbines, as it is the part mostly exposed to the hot gases. An improper understanding and design of cooling configuration in this region may cause very high thermal stress and may ultimately lead to the failure of the blade. Hence the effects of film hole configuration, blowing ratio, coolant to mainstream density ratio, Reynolds number, and mainstream turbulence intensity on heat transfer near the leading edge have been of immense interest to researchers.

Most of the earlier investigations were reported by comparing the adiabatic effectiveness (η) on the leading edge surface, which is defined as follows:

$$\eta = \frac{T_m - T_{aw}}{T_m - T_c} \quad (1)$$

Here, T_m , T_c , and T_{aw} are the mainstream, coolant, and the adiabatic wall temperatures, respectively. Mehendale and Je-Chin [1] used a cylindrical model with two rows of film holes for studying the effect of Reynolds number and film

hole spacing on the adiabatic effectiveness. They found an increase in effectiveness value with increase in Reynolds number. A similar study was conducted by Ou and Rivir [2, 3] by adding an extra row of film holes at the stagnation region and concluded that the Reynolds number effect is significant at low blowing ratios and high turbulence. The effect of mainstream turbulence was also investigated by Funazaki et al. [4] for cylindrical as well as diffuser holes. They reported a reduction in spanwise effectiveness with increase in turbulence for both holes. Similar investigations were conducted to find the effect of different hole shapes [5, 6], inclinations, and injection angles [7] on the adiabatic effectiveness distribution.

The emphasis on the conjugate heat transfer (CHT) technique is reported in recent studies where a wide variation was found in the temperature distribution over a vane under adiabatic and conjugate conditions [8, 9]. Montomoli et al. [10] carried out CHT calculations on a cylindrical leading edge and prescribed the use of high conductivity material for turbine nozzles. Their model contained two rows of film holes on either side of the stagnation region and a row of impingement holes inside. Moritz et al. [11] used a CHT

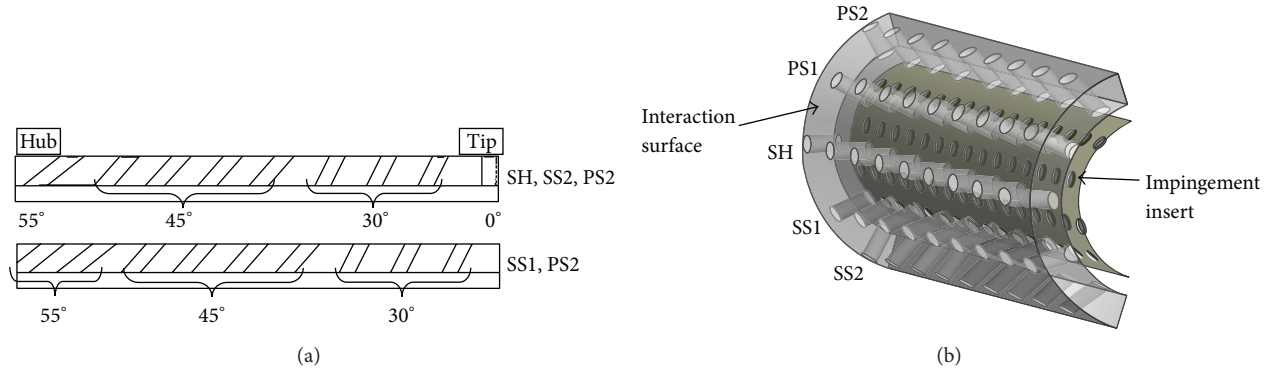


FIGURE 1: (a) Inclination of holes within a row from hub to tip. (b) Solid leading edge with impingement insert.

code developed at their institute and demonstrated that a conjugate calculation technique is suited for predicting three-dimensional thermal load on blades with complex cooling configurations. A key parameter used in CHT calculations is the overall cooling effectiveness (Φ). This variable gives an idea of the actual vane temperature in the nondimensional form by coupling the convective heat transfers due to the external and internal flow field with the conduction in the blade:

$$\Phi = \frac{T_m - T_w}{T_m - T_c} \quad (2)$$

Here T_w is the wall temperature under conjugate condition. The values of adiabatic and overall cooling effectiveness at the leading edge region of a turbine vane with internal impingement cooling were compared by Nathan et al. [12]. They reported that the values of Φ are equivalent to the actual engine values and are higher compared to the adiabatic effectiveness. They prescribed the use of contours of Φ for determining the regions of high thermal gradient.

Even though there are a lot of studies related to leading edge heat transfer, data on parametric studies carried out with conjugate thermal conditions with realistic external and internal cooling configurations are limited. Literature does not throw much light on the effect of some of the key parameters like blowing ratio, Reynolds number, and material conductivity on the overall effectiveness of the leading edge with the conjugate conditions. The present study hence focuses on these aspects by considering a NGV cascade with the leading edge of a typical gas turbine provided with showerhead holes and impingement holes. The parameters investigated in the study include the effect of three different blowing ratios and the effect of three different Reynolds numbers for each blowing ratio on the overall effectiveness of the leading edge made of different thermal conducting materials.

2. Methodology

2.1. Computational Methodology. Studies are conducted on a curved plate having a radius of curvature 21 mm and thickness 5 mm, provided with five rows of 2.85 mm diameter staggered showerhead holes. The middle row of holes (SH)

is at the stagnation region and the other four rows, SS1, SS2, PS1, and PS2, are positioned at +30°, +60°, -30°, and -60°, respectively, from the middle row. Typical to a gas turbine NGV, these holes in each row are varyingly inclined in the spanwise direction from 55° to 0° as shown in Figure 1(a).

The computational domain is a linear cascade as shown in Figure 2(a). The chord length of the blade is 228 mm and the spacing between the blades is maintained at 200 mm. The NGV has a span of 100 mm. To avoid end wall effects, the NGV is extended on either side by 100 mm resulting in a total span of 300 mm. The domain is extended 1.5 times the chord upstream and downstream of the blades.

The computational model consists of two fluid zones and a solid zone. Fluid zone 1 is the mainstream flow and fluid zone 2 is the coolant flow from the impingement holes to the vane rear surface and through the film holes to finally mix with fluid zone 1. The solid zone comprises the leading edge region. The mesh is generated in these zones by the grid generating tool GAMBIT 2.3.16 (Figure 2(b)). A grid independence study is conducted with three meshes, coarse, medium, and fine, which had approximately 1.7 million, 2.54 million, and 3.1 million cells, respectively. The spanwise averaged effectiveness at various streamwise locations is plotted for all three cases as shown in Figure 3.

The medium mesh is found adequate for the present study as the result was almost independent of further grid refinement. A multiblock technique is used and it allows creating separate grids for different parts of the flow domain. The interblock boundaries are virtual and hence have no physical significance. The impingement holes, film holes, and the solid leading edge are meshed with tetrahedral grid and are well refined. On the other hand, the flow domain is meshed with hexahedral grids. A three-dimensional boundary layer with first row height of 0.02 mm and growth factor of 1.2 for 20 rows is provided throughout over the blade surface and over the film hole exits to bring down the y^+ value of the 1st cell below unity.

At the cascade domain inlet and impingement hole inlet, a uniform velocity and temperature boundary condition is specified for the mainstream flow and coolant flow, respectively. The coolant from the inlet impinges on the rear side of the leading edge and then effuses out of the film (showerhead) holes to interact with the mainstream and finally exits

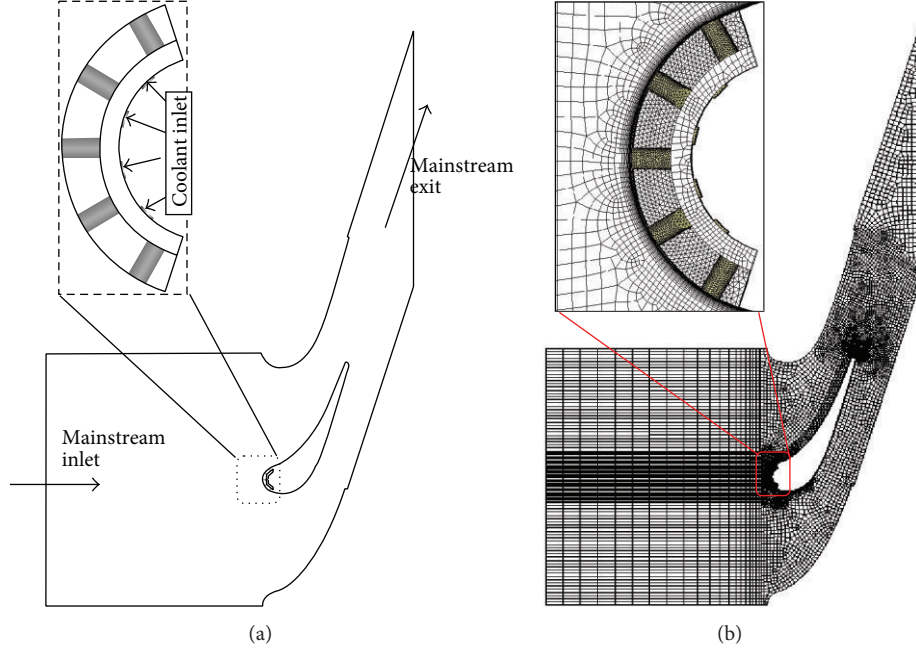


FIGURE 2: (a) Computational domain. (b) Mesh generated in the domain.

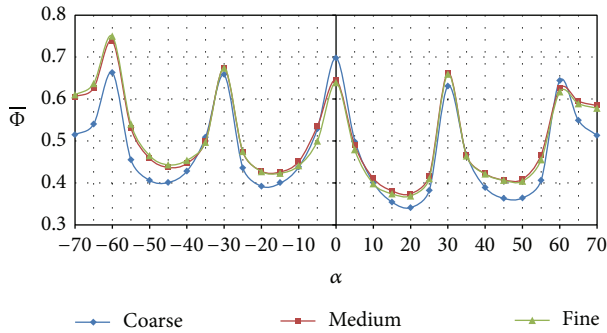


FIGURE 3: Grid independence study.

the domain through a constant pressure outlet. A turbulent intensity of 1% is imposed at the mainstream inlet and 5% at the impingement inlet. A periodic boundary condition is given at the top and bottom wall of the domain so as to generate an infinite cascade model.

Three-dimensional conjugate heat transfer problem is formulated with the following assumptions: (i) the fluid is incompressible, (ii) the fluid properties are constant, (iii) radiation and natural convection are neglected, (iv) viscous dissipation is absent, and (v) the flow is steady. The governing equations used for simulation are the Reynolds averaged continuity, momentum, and the energy equations along with the equations for modeling the turbulence quantities.

Boundary conditions used for the present study are as follows:

- (i) no slip boundary condition at wall, $v_w = 0$;
- (ii) mainstream velocity inlet (v_m) corresponding to different Reynolds numbers and $T = 308$ K;

- (iii) coolant inlet condition, $T = 288$ K, and v_c calculated from blowing ratio ($M = \rho_c v_c / \rho_m v_m$);
- (iv) outlet boundary condition, $P = P_{amb}$ at exit;
- (v) conjugate boundary condition at solid plate,

$$T_s = T_f, \quad k_s \frac{\partial T_s}{\partial y} = k_f \frac{\partial T_f}{\partial y} \quad \text{at wall}; \quad (3)$$

- (vi) adiabatic condition at the other walls,

$$\frac{\partial T_s}{\partial y} = 0 \quad \text{at wall}. \quad (4)$$

The governing equations are solved using the finite volume based Fluent14 solver from the Ansys14 package. The κ - ω SST model is adopted for turbulence modeling. This model was recommended by Panda and Prasad [13], who conducted a combined impingement-film cooling study on a flat plate, where the κ - ω SST model is reported to have predicted the flow interactions very well and matched with their experimental results. A standard pressure interpolation scheme is used. The SIMPLE algorithm is used for pressure-velocity coupling. A second-order upwind scheme is used for momentum and energy and a first-order upwind scheme for κ and ω . The solution is considered to be converged when the maximum residual value is of the order of 10^{-5} for continuity, momentum, and turbulence equations and 10^{-6} for the energy equation. Further, the spanwise averaged effectiveness values at various streamwise locations on the NGV are constantly monitored so that the variation will be within 0.1% for 500 consecutive iterations.

For the present study, two curved plates, one with a lower thermal conductivity (Material A with $k = 0.2$ W/mK) and

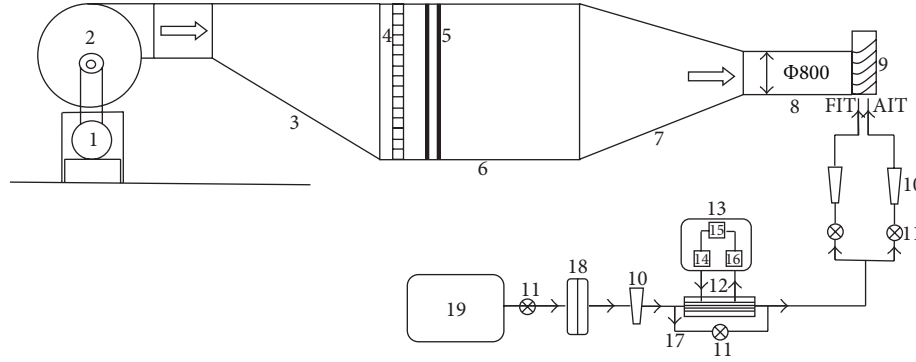


FIGURE 4: Experimental test rig. 1: DC motor 75 kW 1500 rpm, 2: centrifugal air blower $14 \text{ m}^3/\text{s}$, 3: diffuser, 4: honeycomb, 5: mesh, 6: settling chamber, 7: converging duct, 8: test section, 9: cascade, 10: rotameter, 11: flow control valve, 12: heat exchanger, 13: condensing unit, 14: thermostatic expansion valve, 15: condenser, 16: refrigerant compressor, 17: bypass, 18: air dryer, and 19: reciprocating air compressor.

another with a higher thermal conductivity (Material B with $k = 14.9 \text{ W/mK}$), are considered. The effect of blowing ratio is studied at $M = 1, 1.5,$ and 2 by varying the coolant velocity maintaining the mainstream velocity constant. The effect of Reynolds number is studied at each blowing ratio by varying both mainstream and coolant velocity. Reynolds number is varied by $Re_1 = 4.8 \times 10^5$, $Re_2 = 9.6 \times 10^5$, and $Re_3 = 14.4 \times 10^5$ for each blowing ratio and its effect on the overall effectiveness on the leading edge external surface is studied.

2.2. Experimental Methodology. The computational model is validated with the experimental results obtained from the study carried out on a five-vane cascade in the laboratory linear cascade wind tunnel. The center vane in the cascade is instrumented for static pressure and temperature measurements. The cascade and vane dimensions are exactly the same as those of the computational model. The experimental setup is shown in Figure 4. The mainstream air is supplied by a centrifugal blower. A uniform flow is ensured by the honeycomb screens and meshes provided in the settling chamber as shown in the figure. The secondary air is supplied by a reciprocating air compressor and is cooled using a tube-in-tube heat exchanger. The coolant is fed into the two impingement inserts fitted inside the NGV. The coolant impinges on the rear side of the vane and effuses out of the showerhead and film holes.

The two-dimensionality and periodicity of the cascade are established using flow measurements at the inlet and exit of the cascade. A pitot probe is traversed at the inlet of the cascade and a calibrated five-hole pressure probe at the exit. The static pressure on the vane is measured using static taps put at various streamwise locations. The air is bled from these static taps using 2.5 mm brass tubes.

The steady state temperature on the external surface of the NGV made of Material B is measured by infrared thermography using a FLIR A315 camera. The entire leading edge is mapped by placing the camera at three different locations (as shown in Figure 5(b)) so as to bring down the maximum viewing angle, between the camera and the normal surface, below 35° . This is done to avoid any variance in directional emissivity, as previous study [14] has reported that

the emissivity is nearly constant from the normal direction (0°) to 45° . Germanium IR windows are placed on the tunnel walls at all these locations. The camera is connected to the computer using a gigabit Ethernet cable and the FLIR Tools+ software enable triggering, synchronization, and focus of the camera remotely. Various corrections like atmosphere transmission correction, emissivity correction, reflected temperature correction, external windows correction, and optics transmission correction are made before taking the image. In situ calibration of the IR camera is done by simultaneously recording the temperatures obtained from calibrated thermocouples that are stuck at various locations on the NGV. The NGV along with the thermocouples are painted with flat black to achieve uniform emissivity of about 0.97 . The emissivity is then corrected by comparing the IR and thermocouple readings, even though the magnitude of this correction is as low as 0.01 . Lines of equal length are drawn at various streamwise locations on the vane surface. The weighted averages of temperature in all these lines are obtained.

3. Data Reduction Planes

The lines drawn on the leading edge as in Figure 6 from $\alpha = -70$ to $+70$ at every 5 -degree interval are used for data reduction. The spanwise averaged effectiveness discussed in the later sections is obtained by area weighted average of these lines. Wall-normal planes from the leading edge surface are also generated with respect to these lines.

4. Results and Discussion

4.1. Validation. The computational model is validated by comparing the static pressure and effectiveness distribution on the vane obtained computationally with experiments (Figures 7 and 8). The NGV used in the experiment has the properties of Material B. The static pressure is measured at $Re = 2.9 \times 10^5$. For validation, the coolant inlet condition is changed from velocity boundary condition at the impingement hole inlet to mass flow boundary condition at the impingement insert inlet to match the experimental condition. This coolant

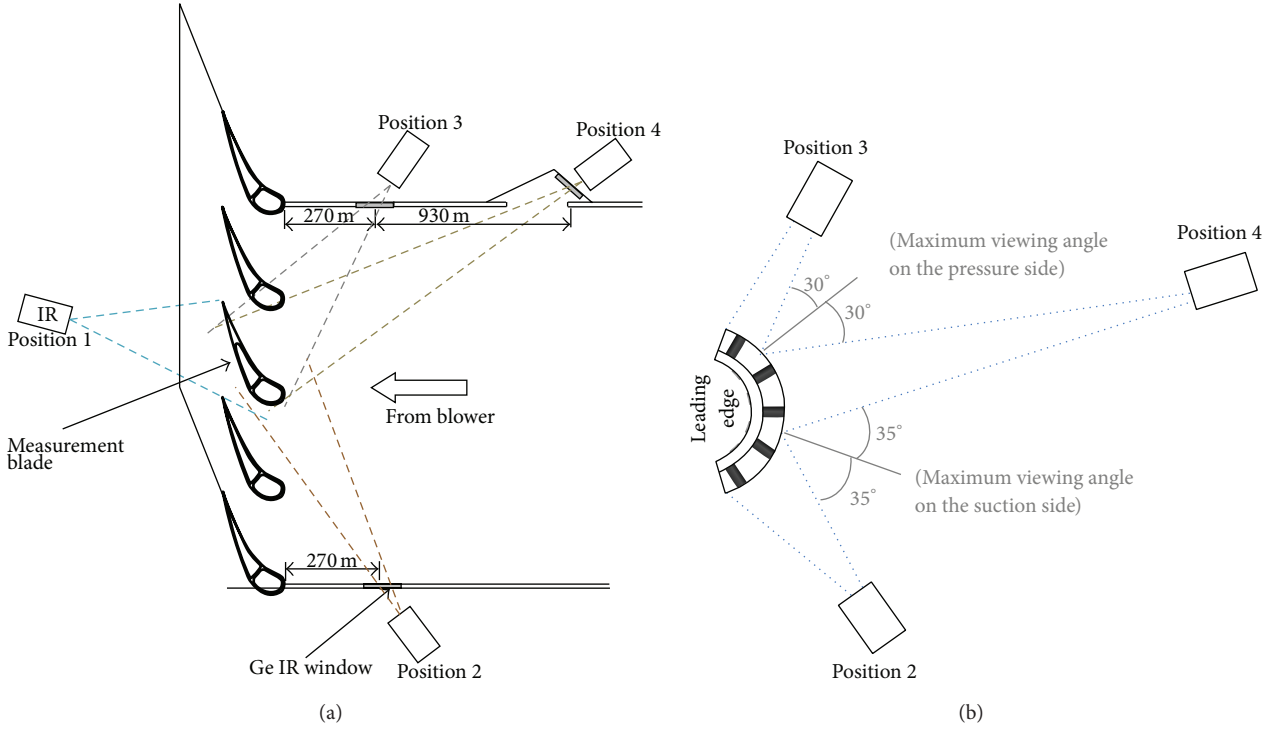


FIGURE 5: Surface temperature mapping using IR thermography: (a) general cascade setup and (b) focusing the leading edge.

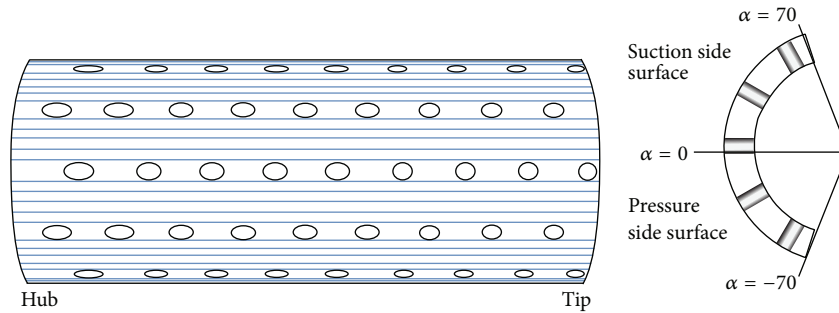


FIGURE 6: Data reduction planes.

mass flow distributed to the showerhead holes as well as four rows of film holes. Hence the minimum blowing ratio (M_{min}) corresponds to minimum mass flow rate at the inlet of impingement insert which is sufficient enough for the coolant to come out of all the showerhead and film holes. This value is found out computationally by trial and error. Later, while conducting experiments at this minimum coolant mass flow, it is ensured that the coolant comes out of all the film holes, by traversing a thermocouple probe.

Figures 7 and 8 show that a good correspondence exists between the experimental and computational results, thereby validating the computational methodology, including the mesh and the turbulence model adopted for the computations. Figure 8 shows the IR image at the leading edge and comparison of the experimental and computational values of the spanwise averaged effectiveness. The comparison made for three blowing ratios shows a good agreement between

the experimental and computational values with a maximum difference of about 6%, which is well within the acceptable range.

4.2. Flow and Temperature Patterns. The flow and heat transfer characteristics are different on the pressure and suction sides of the leading edge for different blowing ratios. Figure 9 shows the path lines coloured by nondimensional temperature emerging from all rows of holes.

Figure 9 shows the coolant emerging out of the five rows of showerhead holes located at the leading edge. These streamlines are coloured by nondimensional temperature, θ . At low blowing ratio ($M = 1$), the coolant coming out of the stagnation row of showerhead holes is getting equally distributed towards the pressure and suction sides. Symmetry is seen with respect to the stagnation row. But, as the blowing ratio increases, more coolant tends to flow

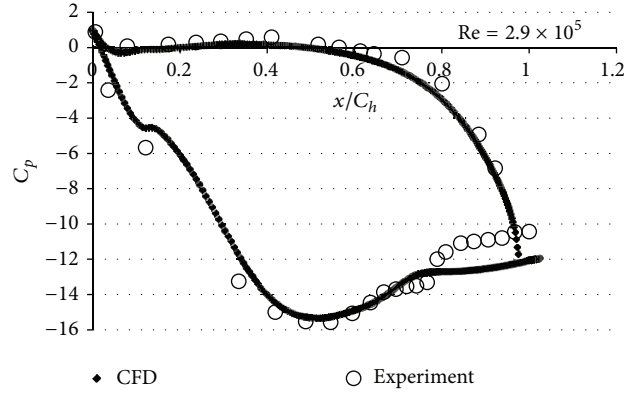


FIGURE 7: Comparison of static pressure.

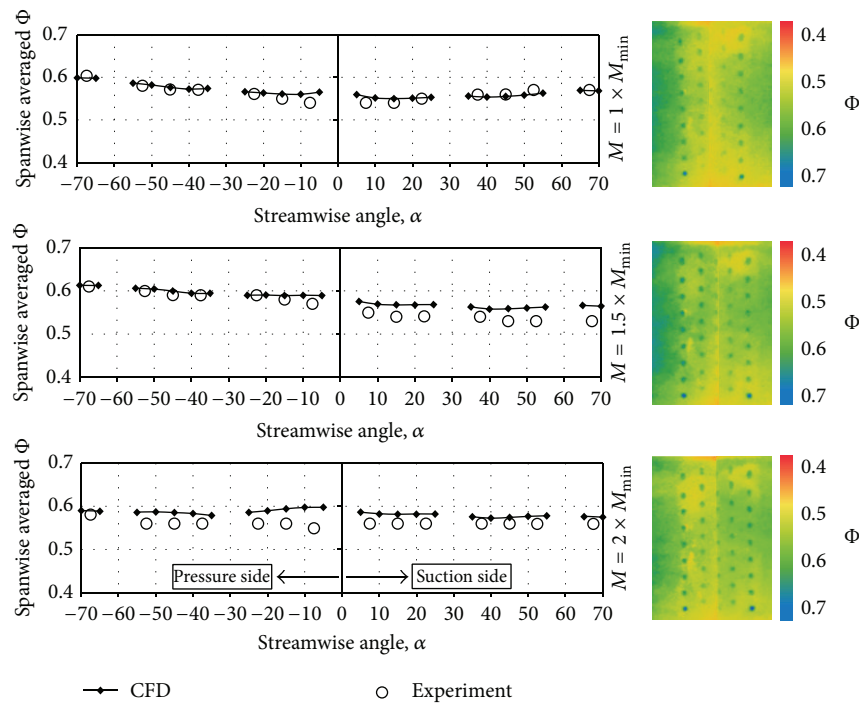


FIGURE 8: Comparison of spanwise averaged overall effectiveness and the IR images.

towards the pressure side compared to the suction side. This is prominent at the highest blowing ratio, $M = 2$. The areas not covered by the streamlines are the ones having the lowest effectiveness. Hence pressure side surface has better coolant spread at higher blowing ratios. The reason behind this is explained with the help of Figure 10.

Figure 10 shows the streamlines coloured by nondimensional temperature (θ) drawn in wall-normal planes L1, L2, and L3 (shown at the top) at different locations along the stagnation row. Planes are drawn just after the first hole, just before the second hole, and through the second hole of the SH row. It can be seen that, after hole 1, counter rotating vortex pair (CRVP) is formed for $M = 1.5$ and $M = 2$. In the case of $M = 1$, CRVP are not formed and this is characterized by an attached flow. The strength of the CRVP formed for $M = 2$ is

higher compared to $M = 1.5$. From the second plane which is just before the second hole, it is evident from the colour of the streamlines that the coolant from the 1st hole is not reaching the second hole for $M = 1$ case. Hence it is not affecting the coolant flow from the second hole. As a result the coolant streamlines from the 2nd hole are getting equally distributed to pressure and suction sides as shown in plane L3. But this is not the case for higher blowing ratios where the coolant from the 1st hole is affecting that from the 2nd hole. At $M = 1.5$, even though the coolant from the 1st hole reaches the 2nd hole, the strength of the CRVP developed from the 1st hole drastically reduces by the time it reaches the 2nd hole. Though weak, there is a small current towards the pressure side as can be seen from plane L2. Hence, it can be noticed from plane L3 that the coolant is flowing slightly more towards the pressure

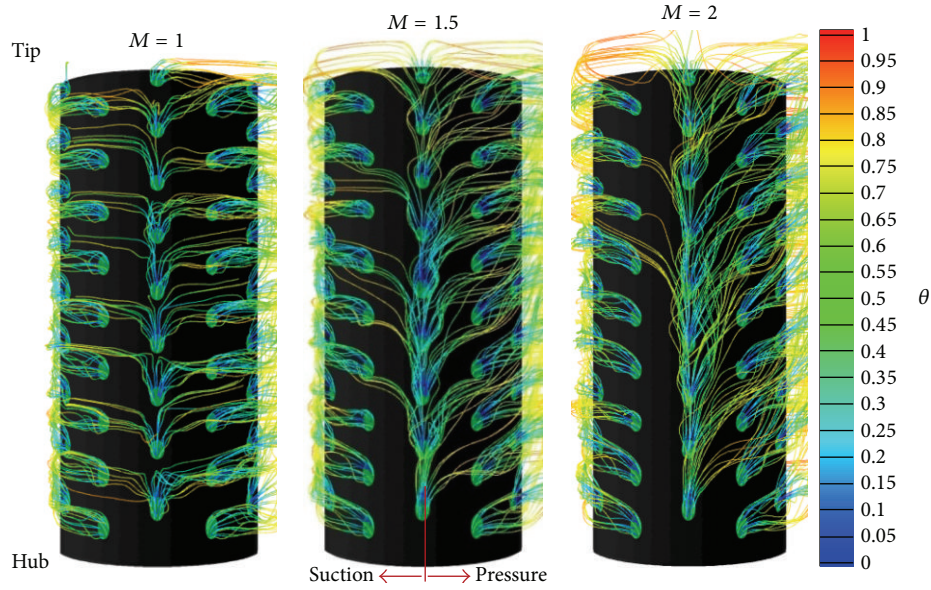


FIGURE 9: Pathlines coloured by nondimensional temperature emerging out of the showerhead holes.

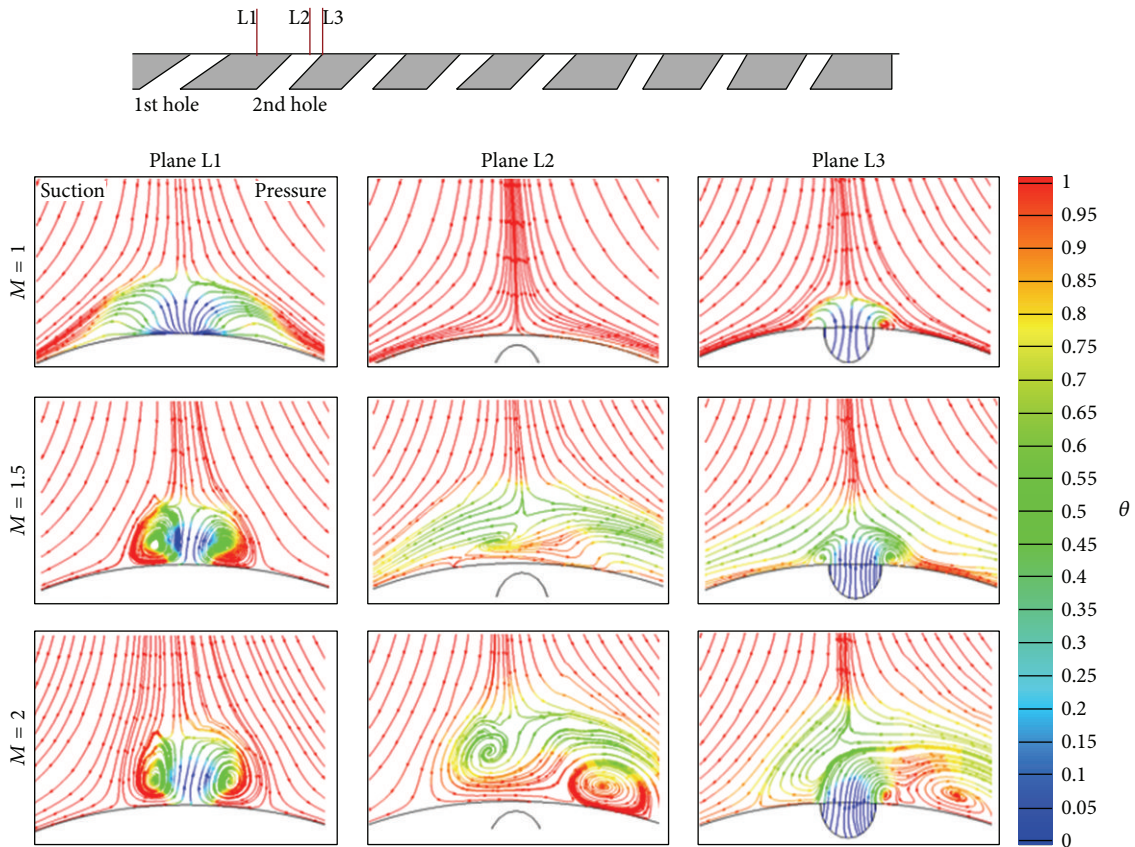


FIGURE 10: Stream lines coloured by θ drawn at wall-normal planes at various locations in the SH row of the leading edge.

side as compared to suction side. This phenomenon is even more prominent for the highest blowing ratio ($M = 2$). It can be seen from plane L2 that, for the flow approaching hole 2, CRVP has considerable strength. A strong vortex formation is

seen on the pressure side and it induces a low pressure in that region. This causes the coolant coming out of the 2nd hole to flow towards the pressure side as can be seen from plane L3. This is the reason why the coolant effusing out of SH row is

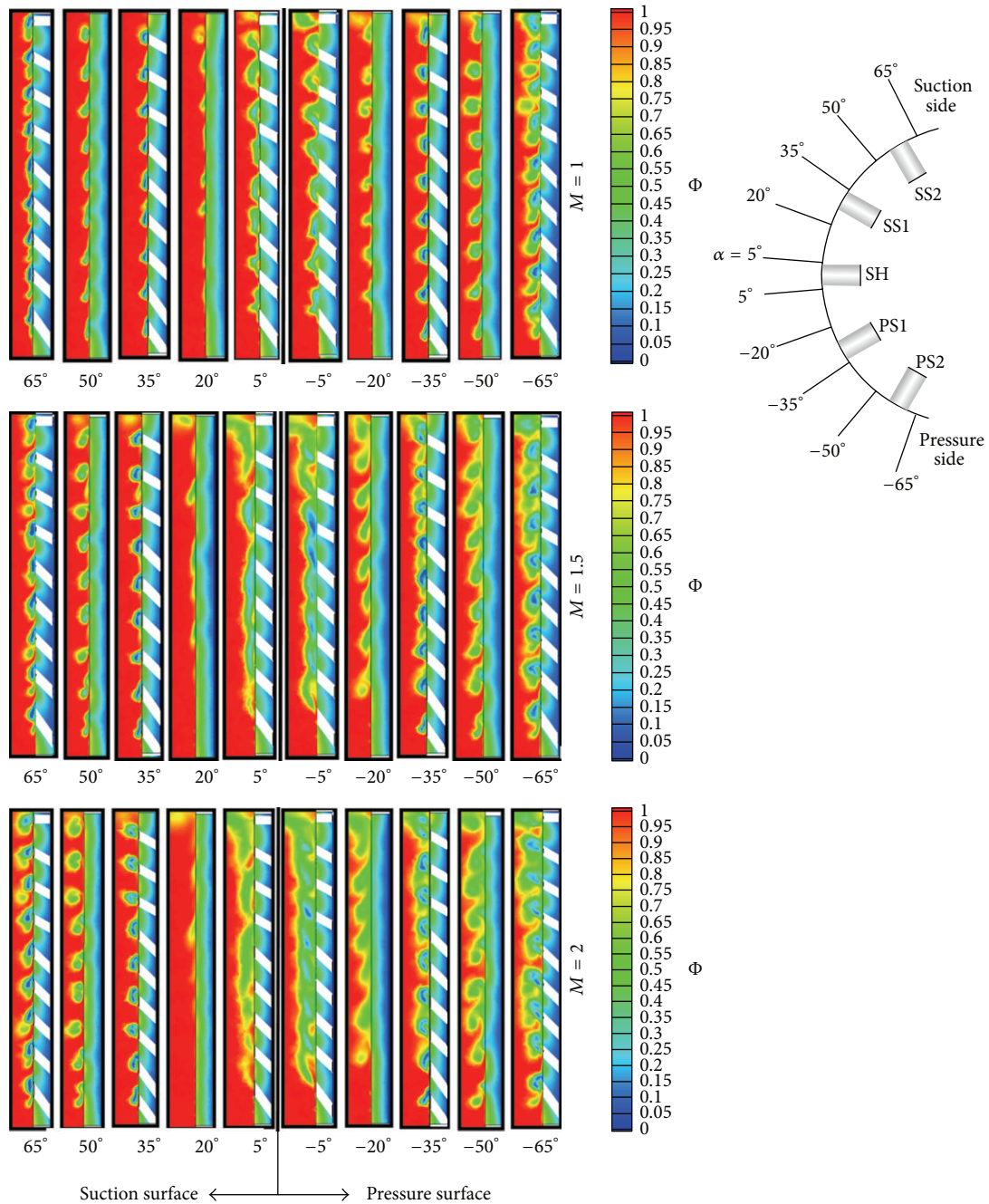


FIGURE 11: Contours of nondimensional temperature (θ) plotted on wall-normal planes at different streamwise locations for various blowing ratios at Re_1 .

distributed more towards the pressure side at higher blowing ratios.

Figure 11 shows the nondimensional temperature contour plotted at different wall-normal planes perpendicular to the leading edge (along the data reduction lines, Figure 6). As seen in the figure, the contours at $\pm 5^\circ$ and $\pm 20^\circ$ depict that the coolant coming out of SH spreads more on to the pressure side surface than the suction side. The contour at 35° and 50° on the suction surface shows the coolant flow downstream of the SS1 row and vividly shows that, with

increase in blowing ratio, the coolant jet gets lifted off more from the surface and in turn entraps the hot mainstream beneath it, whereas on to the pressure side, at 35° and 50° , plots depict an improvement in the concentration of coolant with increase in blowing ratio and a denser and thicker cover of coolant is observed. On the contrary, downstream of SS2 and PS2 rows, a better spread and attachment of coolant on to the surface are seen for $M = 1$. When the blowing ratio increases, the coolant is slightly getting detached and hot mainstream is seen penetrating the region between the film

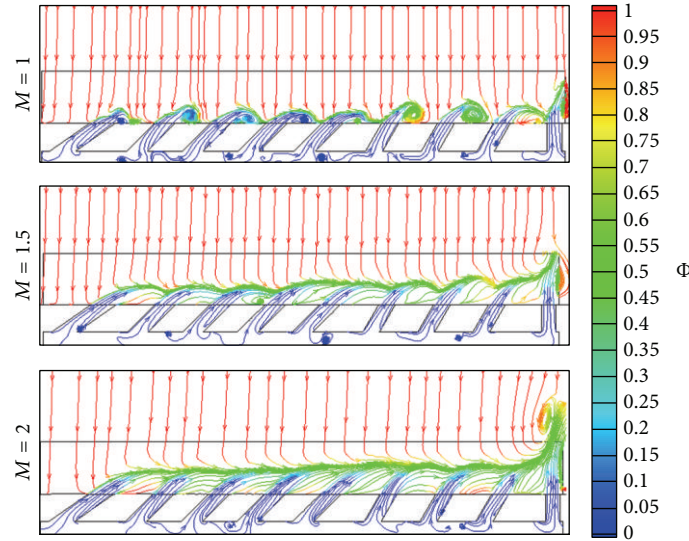


FIGURE 12: Streamlines coloured by nondimensional temperature (θ) showing coolant-mainstream interaction at the leading edge stagnation region ($\alpha = 0$) for blowing ratios: (a) $M = 1$, (b) $M = 1.5$, and (c) $M = 2$.

holes. Moreover, at higher blowing ratios, the coolant is seen to be gathering near the tip region while a meager amount of coolant is present near the hub. This is mainly due to the high spanwise inclination of showerhead holes near the hub. At higher blowing ratios, the coolant effusing out of these holes attains enough momentum to push the coolant coming out of adjacent holes towards the tip. This phenomenon can be better understood with the aid of Figure 12 which shows the coolant-mainstream interaction at the stagnation region ($\alpha = 0$). It is also observed that, for all rows of holes, the coolant effusing out of the holes closer to the tip region which are less inclined to the spanwise direction shows a higher tendency to liftoff from the surface. The tendency to liftoff also decreases when moved towards the hub region, as the holes gradually get more inclined to the spanwise direction.

4.3. Effect of Blowing Ratio on Effectiveness. The effect of blowing ratio on the overall effectiveness is different for suction and pressure side surface of the leading edge as can be seen from Figure 13. Whilst the effectiveness appears to improve with blowing ratio on the pressure side surface, it is seen to decrease on the suction side surface. The above qualitative explanation can be justified with the spanwise averaged effectiveness plot at various streamwise angles from the stagnation region as shown in Figure 14.

On the pressure side surface, downstream of SH and PS1 holes, the effectiveness is least for $M = 1$ for all three Reynolds numbers. Moreover the effectiveness gradient between two rows of holes is also highest for $M = 1$ whereas it is least for $M = 2$ especially downstream of SH row. This is due to the uniform and wide coverage of coolant in that region at $M = 2$, as discussed from Figure 11. At $M = 1.5$ and $M = 2$, the effectiveness curves are almost overlapping downstream of PS1 for all Reynolds numbers. After PS2, on the contrary, effectiveness is seen decreasing with increase

in blowing ratio. This is vivid from Re_1 , whereas, for higher Reynolds numbers, the effectiveness curves in this region are almost overlapping for $M = 1$ and 1.5.

On the suction side surface, the effectiveness is least for $M = 2$ throughout due to the coolant jet getting lifted off from the surface as explained in the previous section. The effectiveness gradient between two rows of holes is also found highest for $M = 2$ case and least for $M = 1$. Effectiveness distribution at $M = 1$ and $M = 1.5$ is almost overlapping downstream of SH and SS1 holes for Re_1 and Re_3 cases. For Re_2 case, the effectiveness values are slightly reduced at $M = 1.5$ and the distribution moves close to $M = 2$. Downstream of SS2, the effectiveness distribution is distinct and the trend is similar for all Reynolds numbers. The effectiveness is decreasing with increasing blowing ratio. The effectiveness distribution at $M = 1.5$ is in between that of $M = 1$ and $M = 2$ at almost throughout the leading edge region and at all Reynolds numbers. Hence, when area weighted average of the whole surface is taken, the overall effectiveness is higher for $M = 1.5$. But the gradient in effectiveness between the pressure and suction side is least for $M = 1$ case.

The averaged values of effectiveness are found quite high for Material B because the effect of impingement cooling is felt more due to the high conductivity of the material. From the effectiveness contours in Figure 13, it is very clear that the distribution is uniform throughout the leading edge region compared to Material A. Due to lateral conduction within the plate, gradients in the effectiveness between rows of holes are very small. Even though the variation is less, zones of relatively higher effectiveness can be found in the pressure side surface of the leading edge compared to the suction side surface. Further insight into this can be obtained from the plot of spanwise averaged effectiveness from Figure 14.

The effect of blowing ratio, though prevalent, is considerably smaller compared to the low conductivity material.

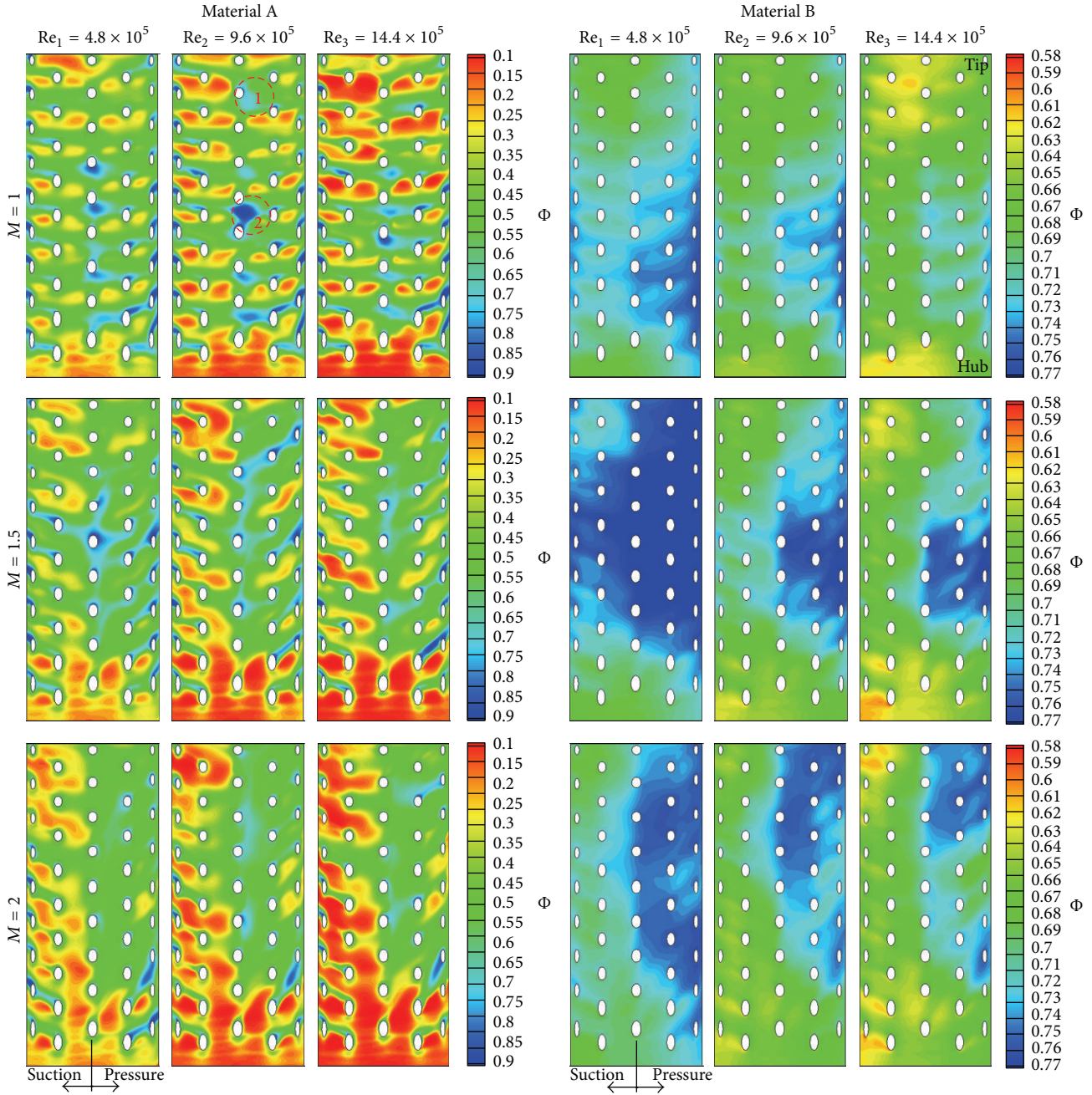


FIGURE 13: Overall effectiveness contours at all three blowing ratios and Reynolds numbers for Materials A and B.

At $M = 1.5$, the effectiveness values are relatively high compared to other blowing ratios and this difference is more distinct at Re_1 . At higher Reynolds numbers this difference in effectiveness values is found to be reduced. On the suction side surface downstream of the SH row, the effectiveness curves at all blowing ratios are overlapping at Re_2 and Re_3 and the same is found in the downstream region of SS1 at Re_3 . Downstream of PS2, the effectiveness is highest at $M = 1.5$ at all Reynolds numbers, whereas, downstream of SS2, the highest effectiveness found at $M = 1.5$ gradually changes to $M = 1$ as the Reynolds number increases. A close observation

of the plot reveals that the effectiveness values on the pressure side surface are least at $M = 1$ and those on the suction side surface are least at $M = 2$ at all Reynolds numbers. Hence effectiveness at $M = 1.5$ is comparatively more consistent and higher for $M = 1.5$. The same scenario was seen for low conductivity material too.

4.4. Effect of Reynolds Number on Effectiveness. For Material A, it can be seen from Figure 15 that effectiveness decreases with increase in Reynolds number for all blowing ratios at all regions of the leading edge except the region between SH and

TABLE 1: Area weighted averaged values of effectiveness at interaction and target surface.

	Material A		Material B	
	interaction surface	Target surface	interaction surface	Target surface
Re_1	0.475	0.923	0.719	0.737
Re_2	0.442	0.934	0.7	0.725
Re_3	0.405	0.94	0.678	0.709

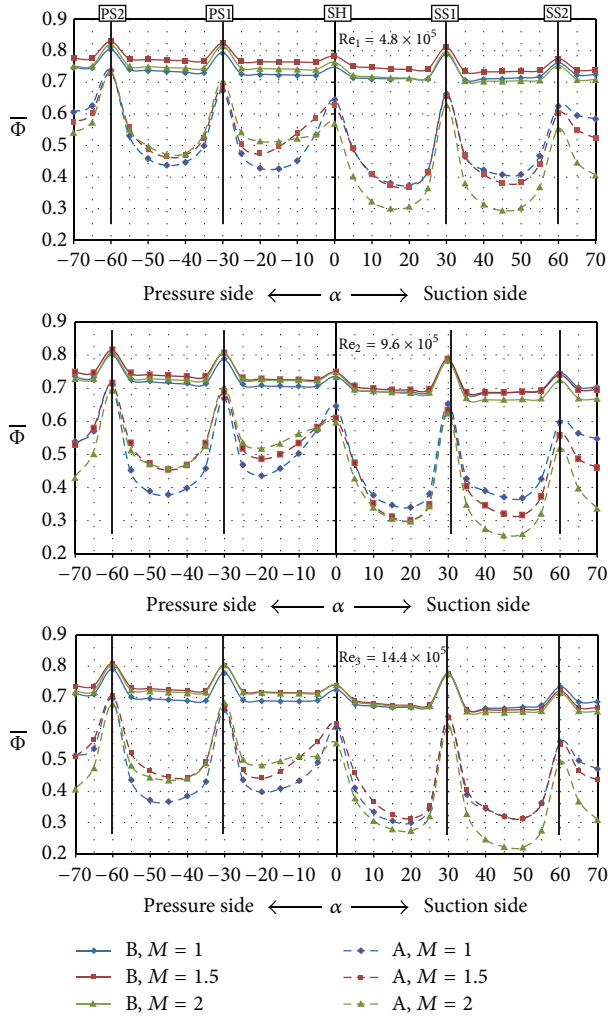


FIGURE 14: Spanwise averaged overall effectiveness at various streamwise angles, α .

PS1. In that region the value is higher for effectiveness at Re_2 and this is later explained with Figures 16 and 17. For Material B, the effectiveness is decreasing with increase in Reynolds number throughout the leading edge for all blowing ratios.

Table 1 shows the area weighted average of effectiveness at the outer and inner surface of the leading edge. Interaction surface is where the coolant, coming out of the film holes, interacts with the mainstream and target surface is where the coolant impinges. It can be clearly seen that as Reynolds number increases, effectiveness decreases at the interaction

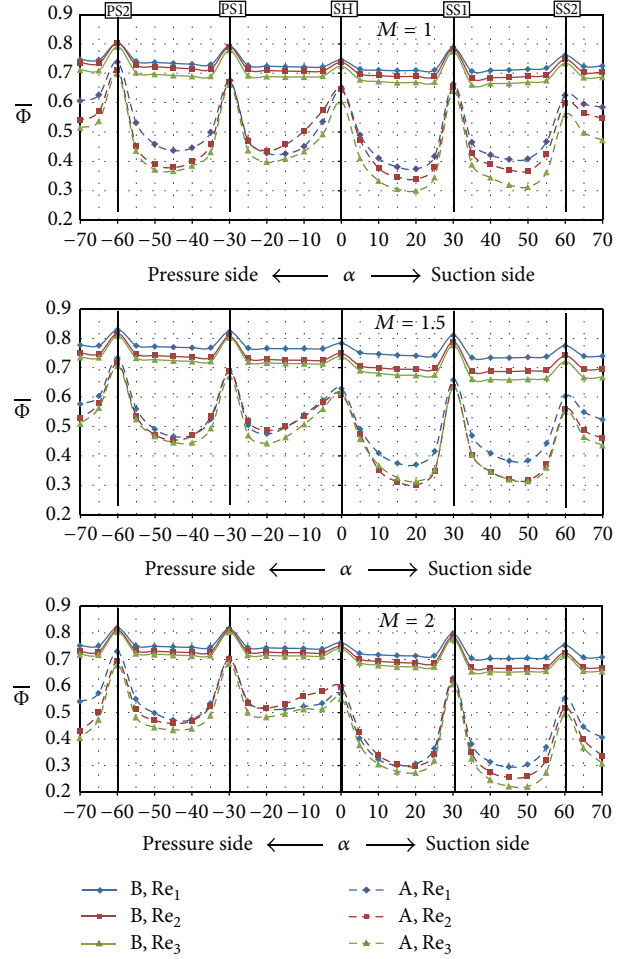


FIGURE 15: Spanwise averaged overall effectiveness at various streamwise angles, α .

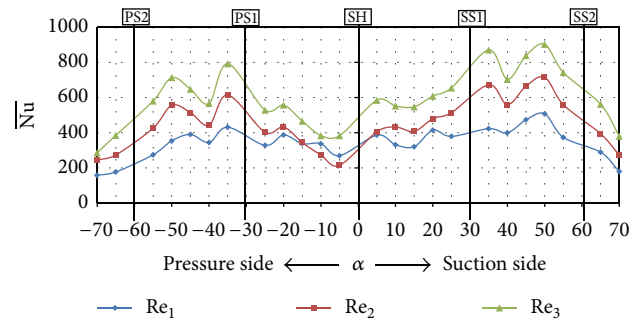


FIGURE 16: Spanwise averaged Nusselt number distribution at $M = 1$ for Material A.

surface whereas it increases at the target surface for Material A. This shows that, with increase in Reynolds number, the heat transfer at both interaction and target surfaces increases. The values for Material B however show a decrease in effectiveness at both the interaction and target surfaces with increase in Reynolds number. This shows that even though heat transfer rate increases at both the surfaces, the increase in heat transfer at the interaction surface is more dominant. This

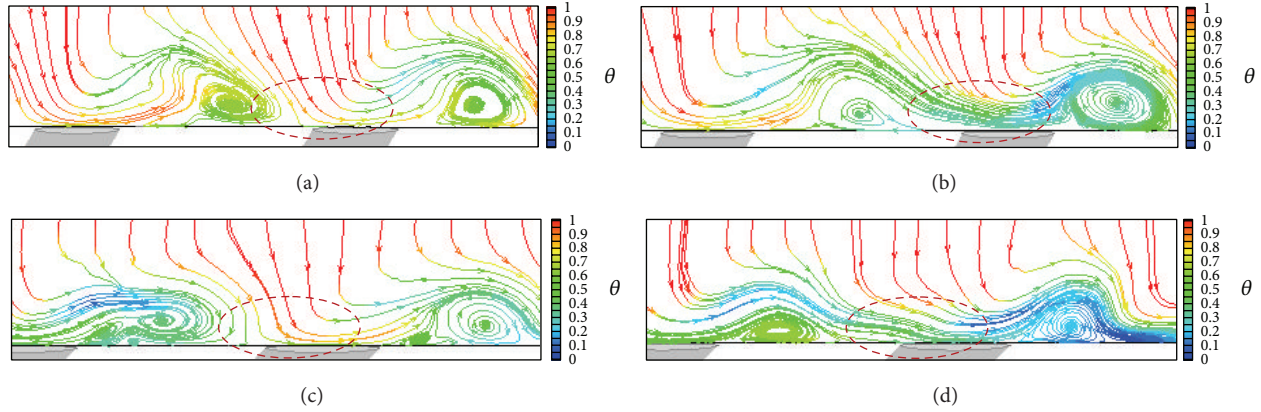


FIGURE 17: Streamlines coloured by nondimensional temperature at a wall-normal plane 5° downstream SH.

increase in heat transfer with Reynolds number is evident from the spanwise averaged Nusselt number plot shown in Figure 16.

An overlapping is seen in the graph in the immediate downstream region of SH row towards the pressure side where the heat transfer is found low for Re_2 . This is mainly attributed to the cold spots as indicated in Figure 13. Flow behavior in this region is studied for Re_1 and Re_2 by drawing pathlines (Figure 17) in a plane drawn 5 degrees downstream of SH row on the pressure side surface. Figures 17(a) and 17(b) correspond to the location of spot 1 of Figure 13 at Re_1 and Re_2 , respectively. Similarly Figures 17(c) and 17(d) correspond to the location of spot 2 on Figure 13 at Re_1 and Re_2 , respectively. It can be seen that the region between the two eddies is occupied by the mainstream in the cases of Re_1 , whereas, in the cases of Re_2 , that region is filled by the coolant effusing out of the adjacent hole and hence results in improved effectiveness.

5. Conclusions

A computational and experimental study is carried out on the leading edge of a typical gas turbine nozzle guide vane. The effect of blowing ratio and Reynolds number is studied by considering two materials: Material A ($k = 0.2$ W/mK) and Material B ($k = 14.9$ W/mK) of low and high thermal conductivity, respectively. The heat transfer and overall effectiveness distributions at the leading edge are extensively studied and reported. These results are explained with the aid of pathlines, nondimensional temperature contours, and Nusselt number distributions describing the mainstream-coolant interaction at the exit of film holes. The salient conclusions drawn from the study are as follows.

- (1) The computational turbine NGV cascade model is validated with the experimental data, as a close agreement in static pressure distribution and overall effectiveness distribution on the vane surface is obtained.
- (2) The overall effectiveness value of Material B is higher and its distribution in streamwise and spanwise directions is more uniform compared to Material A owing

to the high conductivity of the former. The sudden peaks and valleys appearing in the effectiveness distribution of Material A disappear in the case of Material B owing to the high lateral diffusion within the plate.

- (3) The effect of blowing ratio is different for the pressure side and suction side of the stagnation line. As the blowing ratio increases, the coolant tends to distribute more towards the pressure surface. Hence, with increase in blowing ratio, effectiveness increased on the pressure side and decreased on the suction side. For Material A, the effectiveness is higher on the pressure side at $M = 2$ and on the suction side at $M = 1$. When considering the whole blade, a more uniform distribution of overall effectiveness between pressure and suction side was noticed at $M = 1$, resulting in less thermal gradient whereas the averaged overall effectiveness value is higher at $M = 1.5$. For Material B, the overall effectiveness value is higher at $M = 1.5$ throughout the leading edge. For both Materials A and B, when blowing ratio was increased from $M = 1$ to $M = 2$, the region with higher effectiveness was seen getting shifted from hub to tip.
- (4) An increase in Reynolds number has showed an increase in heat transfer on both the external and internal sides of the leading edge even though external heat transfer is more dominant. An increase in Reynolds number at a particular blowing ratio results in a decrease in the overall effectiveness throughout the leading edge for Material B. While Material A also exhibits similar behavior at most of the leading edge, a slight disagreement is seen in the region between SH and PSI rows where the maximum effectiveness is at Re_2 owing to the formation of cold spots.

Nomenclature

- C_h : Chord length, m
 C_p : Coefficient of pressure $(p - p_m)/(0.5 * \rho * v_m^2)$
 h : Heat transfer coefficient, $Q''/(T_{aw} - T_w)$, W/m²-K
 k : Thermal conductivity (W/m-K)
 x : Streamwise direction, m

M : Blowing ratio ($\rho_c v_c / \rho_m v_m$)
 Nu : Nusselt number, hC_h/k
 \bar{Nu} : Spanwise averaged Nu
 p : Static pressure
 Q'' : Total surface heat flux, W/m^2
 Re : Reynolds number ($\rho v_e C_h / \mu$)
 T : Temperature (K)
 v : Velocity magnitude
 SST : Shear stress transport.

Greek

θ : Nondimensional temperature $(T - T_c)/(T_m - T_c)$
 η : Adiabatic effectiveness $(T_m - T_{aw})/(T_m - T_c)$
 Φ : Overall cooling effectiveness $(T_m - T_w)/(T_m - T_c)$
 $\bar{\Phi}$: Spanwise averaged Φ
 α : Streamwise angle with respect to stagnation line ($^\circ$)
 ρ : Fluid density
 κ : Turbulent kinetic energy, m^2/s^2
 ω : Specific dissipation rate, $1/sec$
 μ : Coefficient of viscosity, Ns/m^2 .

Subscript

aw : Adiabatic wall
 amb : Ambient
 c : Coolant
 e : Exit of cascade
 f : Fluid
 m : Mainstream
 min : Minimum
 s : Solid
 w : Wall.

Conflict of Interests

The authors declare that there is no conflict of interests regarding the publication of this paper.

Acknowledgment

The authors are grateful to Gas Turbine Research Establishment (GTRE), Bangalore, for supporting this project through GATET program.

References

- [1] A. B. Mehendale and H. Je-Chin, "Reynolds number effect on leading edge film effectiveness and heat transfer coefficient," *International Journal of Heat and Mass Transfer*, vol. 36, no. 15, pp. 3723–3730, 1993.
- [2] S. Ou and R. Rivir, "90° skew leading edge film cooling effectiveness, heat transfer, and discharge coefficients for cylindrical film holes at high free stream turbulence," in *Proceedings of the RTO AVT Symposium on "Advanced Flow Management: Part A—Vortex Flows and High Angle of Attack for Military Vehicles*, RTO-MP-069(I), Loen, Norway, May 2001.
- [3] S. Ou and R. B. Rivir, "Leading edge film cooling heat transfer with high free stream turbulence using a transient liquid crystal image method," *International Journal of Heat and Fluid Flow*, vol. 22, no. 6, pp. 614–623, 2001.
- [4] K. Funazaki, H. Kawabata, D. Takahashi, and Y. Okita, "Experimental and numerical studies on leading edge film cooling performance: effects of hole exit shape and freestream turbulence," in *Proceedings of ASME Turbine Technical Conference and Exposition*, GT2012-68217, Copenhagen, Denmark, 2012.
- [5] H. Reiss and A. Bölcs, "Experimental study of showerhead cooling on a cylinder comparing several configurations using cylindrical and shaped holes," *Journal of Turbomachinery*, vol. 122, no. 1, pp. 161–169, 2000.
- [6] W. D. York and J. H. Leylek, "Leading-edge film-colling physics. Part III. Diffused hole effectiveness," *ASME Journal of Turbomachinery*, vol. 125, no. 2, pp. 252–259, 2003.
- [7] Y. Lu, D. Allison, and S. V. Ekkad, "Turbine blade showerhead film cooling: Influence of hole angle and shaping," *International Journal of Heat and Fluid Flow*, vol. 28, no. 5, pp. 922–931, 2007.
- [8] A. Kassab, E. Divo, J. Heidmann, E. Steinthorsson, and F. Rodriguez, "BEM/FVM conjugate heat transfer analysis of a three-dimensional film cooled turbine blade," *International Journal of Numerical Methods for Heat and Fluid Flow*, vol. 13, no. 5-6, pp. 581–610, 2003.
- [9] L. Zhao and T. Wang, "An investigation of treating adiabatic wall temperature as the driving temperature in film cooling studies," *ASME Journal of Turbomachinery*, vol. 134, Article ID 061032, pp. 1–9, 2012.
- [10] F. Montomoli, M. Massini, H. Yang, and J. C. Han, "The benefit of high-conductivity materials in film cooled turbine nozzles," *International Journal of Heat and Fluid Flow*, vol. 34, pp. 107–116, 2012.
- [11] N. Moritz, K. Kusterer, D. Bohn, T. Sugimoto, R. Tanaka, and T. Taniguchi, "Conjugate calculation of a film-cooled blade for improvement of the leading edge cooling configuration," *Propulsion and Power Research*, vol. 2, pp. 1–9, 2013.
- [12] M. L. Nathan, T. E. Dyson, D. G. Bogard, and S. D. Bradshaw, "Adiabatic and overall effectiveness for the showerhead film cooling of a turbine vane," in *Proceedings of the ASME Turbo Expo: Turbine Technical Conference and Exposition (GT '12)*, pp. 1537–1547, Copenhagen, Denmark, June 2012.
- [13] R. K. Panda and B. V. S. S. Prasad, "Conjugate heat transfer from a flat plate with combined impingement and film cooling," in *Proceedings of the ASME Turbo Expo: Turbine Technical Conference and Exposition (GT '12)*, pp. 347–356, Copenhagen, Denmark, June 2012.
- [14] M. Vollmer and K. P. Mollmann, *Infrared Thermal Imaging: Fundamentals, Research and Applications*, Wiley-VCH, 2010.

Research Article

Experimental Investigation of Factors Influencing Operating Rotor Tip Clearance in Multistage Compressors

Reid A. Berdanier and Nicole L. Key

School of Mechanical Engineering, Purdue University, 500 Allison Road, West Lafayette, IN 47907, USA

Correspondence should be addressed to Reid A. Berdanier; rberdani@purdue.edu

Received 9 October 2014; Revised 3 January 2015; Accepted 4 January 2015

Academic Editor: Nekkanti Sitaram

Copyright © 2015 R. A. Berdanier and N. L. Key. This is an open access article distributed under the Creative Commons Attribution License, which permits unrestricted use, distribution, and reproduction in any medium, provided the original work is properly cited.

An analysis of compressor rotor tip clearance measurements using capacitance probe instrumentation is discussed for a three-stage axial compressor. Thermal variations and centrifugal effects related to rotational speed changes affect clearance heights relative to the assembled configuration. These two primary contributions to measured changes are discussed both independently and in combination. Emphasis is given to tip clearance changes due to changing loading condition and at several compressor operating speeds. Measurements show a tip clearance change approaching 0.1 mm (0.2% rotor span) when comparing a near-choke operating condition to a near-stall operating condition for the third stage. Additional consideration is given to environmental contributions such as ambient temperature, for which changes in tip clearance height on the order of 0.05 mm (0.1% rotor span) were noted for temperature variations of 15°C. Experimental compressor operating clearances are presented for several temperatures, operating speeds, and loading conditions, and comparisons are drawn between these measured variations and predicted changes under the same conditions.

1. Introduction

Rotor tip clearance height is known to be a significant contributor to overall compressor performance. In particular, previous studies have discussed its influence on total pressure rise, efficiency, and stall margin [1]. Current goals of increased efficiency and decreased fuel burn for gas turbine engines are focused toward more aggressive compressor designs featuring increased blade loadings and decreased blade heights in the rear block of high pressure engine cores. In these rear stages, blade aspect ratios are smaller, tip clearance heights are large relative to blade span, and endwall flows contribute to a more significant portion of the overall loss [2]. As a result, research focusing on the underlying flow physics for rotor tip leakage flows is growing in importance, particularly for tip clearance heights which are large as a percentage of overall blade span.

Ongoing research projects typically apply an extensive array of experimental techniques, but the ability to connect these experimental results to numerical models and validate computational tools is essential [3]. Although many

computational fluid dynamics models struggle to accurately model the fundamental flow physics of tip clearance flows [4], the overall performance deltas due to clearance changes are typically comparable to experimental results. Small tip clearance changes and the related performance changes which occur as a result of changes to ambient temperature are typically considered negligible [5]. However, recent research has shown the measurability of these small performance changes in a multistage compressor [6]. As a result, it is imperative that the tip clearance heights are known for the conditions at which the experimental performance data are collected so that the compressor system can be appropriately modeled in numerical simulations.

Static rotor tip clearances—sometimes referred to as “cold” clearances—do not typically represent the operating, or “hot” running, clearances. In general, thermal growth, pressure forces, and circumferential forces due to high-speed blade rotation contribute to blade growth which leads to a clearance height change at different operating conditions and for different ambient conditions. Mechanical touch probes and erodible rub sticks offer low-cost options for measuring

tip clearance during operation with easy implementation, but these methods only measure the tallest blade (i.e., the smallest clearance) during an entire test campaign [7], and no additional information is gained as a result of changes in operating condition or ambient temperature. Thus, non-contact clearance measurement systems, such as optical probes, eddy current sensors, or capacitive sensors, provide an alternative solution. Optical probes can be prone to failure if their line of sight is blocked by foreign objects, and thus the rugged design of capacitance sensors makes them a primary candidate for gas turbine applications [8].

The introduction of frequency modulated (FM) capacitance probe clearance measurement systems by Chivers [9] and Barranger [3] provided alternatives to earlier optical measurement systems. Continued component improvements have provided the ability to incorporate these high-accuracy systems in increasingly harsh environments. An overview of the advancement of capacitance probe measurements systems is given by Sheard [8].

Many authors have presented methods for modeling variations of tip clearances (e.g., Agarwal et al. [10], Kypuros and Melcher [11], and Dong et al. [12]). However, up to now, greater interest has been given to turbines, instead of compressors, due to the known benefits of active clearance control [13] and more significant thermal effects. Of the limited studies focused on predictive clearance modeling in compressors, Dong et al. discuss clearance changes due to loading condition at a fixed speed. Specifically, the authors noted changes of tip clearance approaching 0.5% span for the rear stages of a 10-stage compressor simulation. Further, simulations yielded misrepresentations of flow rate and efficiency when clearances corresponding to the static, or “cold,” assembled configuration were implemented in the solution instead of estimated operating clearances.

While the work of Dong et al. [12] provides an important step in predictive modeling development for compressor tip clearances, there is a lack of experimental data in the open literature to support this model and advance the state of the art. Thus, the work presented here aims to fill that void by experimentally validating the variations of clearance with operating condition that was predicted by Dong et al. Further discussion is given to environmental effects on rotor tip clearances, and comparisons are drawn between the operating clearances measured by a capacitance probe system and the predictive clearances using the model proposed by Dong et al. Several recommendations are given for consideration in future test campaigns since experimental tip clearance studies which also measure the operating tip clearance are largely absent in the open literature.

2. Experimental Methods

This research was performed in the three-stage axial compressor research facility at Purdue University. Extensive experimental compressor performance data have been collected for an advanced tip clearance study implementing three different rotor tip clearance heights. In support of this project, a recent facility upgrade has incorporated a

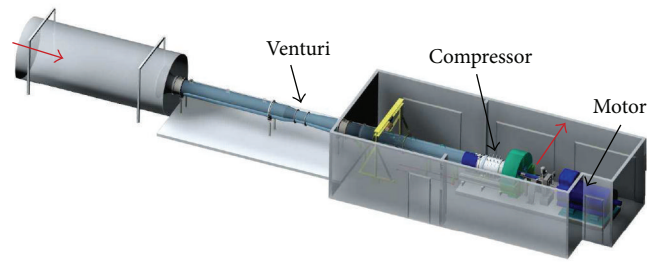


FIGURE 1: Purdue 3-stage axial compressor research facility.

capacitance-type tip clearance measurement system to measure the operating tip clearances in the compressor.

2.1. Compressor Facility. The Purdue three-stage axial compressor research facility is shown in Figure 1. The compressor draws unconditioned atmospheric air into a large settling chamber. A bell mouth directs the air into a long duct and through an ASME-standard long-form Venturi meter where the mass flow rate is measured. A nosecone directs the air into the 50.8 mm constant-annulus height (with a hub-to-tip ratio of 0.8333 throughout). Past the compressor exit, the air passes through a sliding-annulus throttle and is then directed out a scroll-type collector where the air exhausts to ambient conditions. The compressor is driven from the rear by a 1044 kW AC motor, and the driveline passes through a 5 : 1 speed-increasing gearbox to facilitate a corrected design speed of 5000 rpm. An encoder on the motor drive shaft and a proportional-integral-derivative control sequence maintain the rotational speed of the compressor within 0.01% of the desired set point. Aside from the motor control, an optical laser tachometer aimed at the high-speed shaft of the gearbox creates a transistor-transistor logic (TTL) signal which is used as a once-per-revolution (OPR) trigger for the high frequency response data acquisition systems.

The three-stage axial compressor features a 6061 aluminum casing and double-circular arc rotor blades made from 17-4 stainless steel. The rotor blade counts decrease through the compressor with 36 blades for Rotor 1, 33 blades for Rotor 2, and 30 blades for Rotor 3. The stator vanes in this facility are all shrouded without hub clearances. Additional information related to the airfoil geometry can be found in [14]. The compressor casing was machined with tight tolerances to create the best possible vehicle for tip leakage flow measurements. Specifically, the inner diameter of the casing was specified as 609.6 mm +0.025/-0.000 mm dimensionally, but additional geometric tolerances included a maximum 0.127 mm overall runout and a 0.051 mm surface profile shape. All dimensions were confirmed to be within tolerance using coordinate measuring machine (CMM) inspection techniques. Unless otherwise noted, the nominal rotor tip clearances for all data presented in this paper are 1.524 mm, representing 3.0% of the annulus height. For reference, Table 1 provides the aspect ratio of the rotor blades and the corresponding tip clearances as a function of average blade

TABLE 1: Rotor blade aspect ratios and clearance-to-chord values.

	Rotor 1	Rotor 2	Rotor 3
Blade aspect ratio	0.76	0.72	0.68
Clearance-to-chord value (1.5% span)	1.14%	1.08%	1.02%
Clearance-to-chord value (3.0% span)	2.28%	2.16%	2.04%

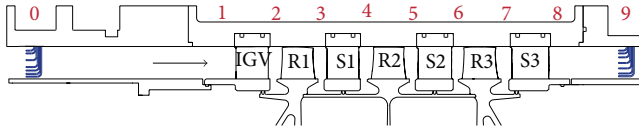


FIGURE 2: Compressor flow path and measurement plane locations.

chord for the two tip clearance configurations referenced in this document.

Steady pressure and temperature measurements throughout the compressor are standard for all operations. These data include a seven-element radial distribution of stagnation pressure and stagnation temperature at the inlet and exit planes of the compressor (locations 0 and 9 in Figure 2), a circumferential and axial distribution of static pressures at all axial positions 0 through 9, and a series of surface-mounted T-type thermocouples on the outside of the compressor casing. These surface-mounted thermocouples are positioned at the aerodynamic interface plane (AIP) (plane 0 in Figure 2) and over each of the seven blade rows at a circumferential position of 124 degrees from the top of the compressor in the direction of rotor rotation, as shown in Figure 3. Past studies have shown that one surface temperature measurement is sufficient since circumferential surface temperature variations are less than 1°C. For data sets requiring interstage flow information, seven-element rakes measuring stagnation pressure and stagnation temperature are also inserted at each of the axial positions labeled 1 through 8 in Figure 2. A careful design of the temperature measurement system has reduced the calculated uncertainty to less than 0.3°C for all channels, and the uncertainty of the measured absolute pressures is less than or equal to 50 Pa.

2.2. Capacitance Probe System. The capacitance probe system utilized for this study is a CapaciSense 5-series FM clearance measurement system produced by Pentair Thermal Management. There are nine channels available, allowing three probes to be implemented for each of the three compressor rotors. The three probes are equally spaced circumferentially, 120 degrees apart, at positions of 105 degrees, 225 degrees, and 345 degrees—all measured from the top of the compressor in the direction of rotor rotation. These locations are also marked in Figure 3. Each of the nine probes was individually calibrated using a custom-designed calibration disk which represents the tip geometry of the rotor blade through scaling techniques proven by the manufacturer. The probes were all calibrated for operation from a rub condition (0 mm clearance) to a maximum 5 mm clearance height.

The electronics chain for the FM tip clearance measurement system has several key components. The probes were

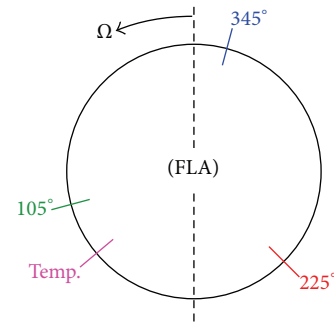


FIGURE 3: Circumferential instrumentation locations.

TABLE 2: Capacitance probe measurement system specifications.

Parameter	Value
Operating frequency	2 MHz nominal
Oscillator sensitivity	100 kHz per pF
Demodulator sensitivity	500 mV per kHz typical
Measurement range	5 mm calibrated
System resolution	<0.001 mm (at 0.7 mm clearance)
Signal-to-noise ratio	30–50 typical

designed and built for application in this specific facility; a triaxial cable is permanently attached to the probe and provides enhanced rejection of electromagnetic interference. The use of a non-mineral-insulated cable limits the maximum operating temperature of this system to 260°C. The oscillator drives the cable with an oscillating voltage (nominally 2 MHz). As the blade passes the probe, the measured capacitance modulates the driven frequency from the oscillator. This modulation is sensed by the carrier, and the demodulator converts the modulation frequency due to the blade passing event to a DC voltage. The DC voltage is correlated to a clearance height via the individual channel calibration. This proportionality between measured capacitance, frequency modulation, voltage, and tip clearance is the crux of the FM tip clearance measurement system.

The clearance measurement system is controlled from a set of “control and processing module” (CPM) computers. Each of these computers utilizes one Advantech PCI-I714UL data acquisition card capable of sampling at a rate of up to 10 MHz per channel, as well as an external trigger which is linked to the OPR signal from the TTL tachometer signal. For the measurements presented in this study, all data were collected using the full 10 MHz sampling capability of the data acquisition card. Other specifications for the capacitance probe measurement system are given in Table 2.

The clearance calculation process provides a blade-by-blade clearance output calculated from the peak-to-peak voltage for the typical blade pulse output signal (known as the blade passing signal (BPS)). As an alternative, the software applies a low-pass filter to the BPS output to create a DC voltage output signal which the manufacturer refers to as a “RMS” signal, although it should be noted that the low-pass filter mechanism does not represent a true root-mean-square

TABLE 3: Representative primary uncertainty analysis components for capacitance probe measurement system.

Parameter	Uncertainty value
System noise	5 mV
Oscillator temperature coefficient	0.2% per °C
Demodulator temperature coefficient	0.1% per °C
A/D card uncertainty	1 mV
Standard deviation of calibration	80 mV
Probe setback uncertainty	0.0125 mm

calculation procedure. This RMS signal serves as a representative average measurement of the tip clearance for all blades by a particular probe. A separate calibration was performed for both the BPS and RMS output signals. All data presented in this study were calculated using data output from the RMS calculation procedure, but a comparison of the RMS with an arithmetic mean of BPS results (not shown here) agrees well.

3. Uncertainty Analysis

The manufacturer of the capacitance probe measurement system claims an umbrella uncertainty on the measurement system of less than 0.01 mm. This value is based on historical comparisons with other measurement techniques, including laser measurements and rub sticks, as well as careful attention to the design, manufacture, and calibration processes to ensure minimal uncertainties. However, no formal uncertainty analysis had yet been performed to validate this claim, which represents more of a repeatability or comparability and does not consider uncertainty contributions from the electronics components.

Other authors have performed uncertainty analyses for capacitance probe measurement systems, including Satish et al. [15] and Müller et al. [16]. The calculations from Satish et al. are extremely thorough as a reference for overall uncertainty analysis, but the manufacturer of the system used for this study did not provide sufficient information to perform the calculations outlined by Satish et al. The uncertainty analysis included by Müller et al. was performed for a comparable FM capacitance probe system several years ago and therefore was used as a model for the calculations performed here. Table 3 outlines some of the representative contributing components of the uncertainty analysis for the electronics of the capacitance probe system used for this study. Using these components, a root-sum-squared (RSS) calculation technique was implemented to calculate the overall system uncertainty. Table 3 includes the temperature coefficients for the demodulator and oscillator, but these components were not considered in the uncertainty analysis for two reasons: (i) the demodulator is operated in a climate-controlled environment to reduce thermal effects and (ii) the data presented in this paper were collected within 7°C of the calibration temperature, and convective cooling around the oscillators helps to reduce thermal effects related to temperature increases.

The uncertainty of the electronics system is ultimately a function of the nominal clearance measured by the probe since the standard deviation of the calibration data varied inversely with increasing clearances. By calculating the representative uncertainty at each calibrated nominal clearance, a curve representing calculated system uncertainty versus nominal clearance was created for each of the nine probes, as shown in Figure 4(a). Because the probe-to-probe variability in Figure 4(a) is small (less than 0.005 mm) for nominal clearances of interest in this study (less than 2 mm), a representative average of the nine probes was calculated and a 4th-order polynomial fit was applied to those data, as shown in Figure 4(b).

To further quantify systematic errors, a typical compressor build may include measurement of the *static* tip clearance over each rotor at each of the nine tip clearance probe locations using a micrometer and a dial indicator, as described by Brossman [17]; these measurements are then compared with the clearances calculated from the capacitance probe system at a low-speed operation (200 rpm is a typical limit for low-speed measurement) at the start of a compressor measurement campaign. By measuring the operating clearances immediately after start-up and at a low operating speed, influences due to centrifugal effects and thermal gradients can be considered negligible.

4. Results

4.1. Rotational Speed. Figure 5 shows measured tip clearances as a function of the compressor operating speed during a typical startup process. These results are presented as a clearance difference with respect to the static clearance value:

$$\Delta\tau = \tau - \tau_{\text{static}}. \quad (1)$$

In Figure 5, the compressor is accelerated through a series of discrete mechanical speeds to allow the oil temperature in the gearbox manifold to increase to an appropriate level. During this process, the effect of tip clearance variation due to the increasing speed is apparent. However, tip clearance changes due to thermal effects are minimal since the temperature rise through the compressor is low at part speed, and the overall acceleration time is relatively small. As a result, the measured clearance changes in Figure 5 are largely due to the centrifugal effects imposed on the rotor as the rotor blades grow with increased operating speed. A minor exception to this is somewhat apparent for compressor operating speeds above 4500 rpm, when the measured clearances increase slightly during constant mechanical speed operation. At these higher-speed “plateaus,” small contributions due to temperature rise through the compressor are first noticeable. However, because the compressor operates at an open throttle condition (near-choke) during the startup process, the temperature rise remains very low. These changes in tip clearance with increasing rotational speed have been documented by other authors in the past [8, 9, 16].

4.2. Loading Condition. Once a steady operating speed has been reached, the loading of the compressor can be increased

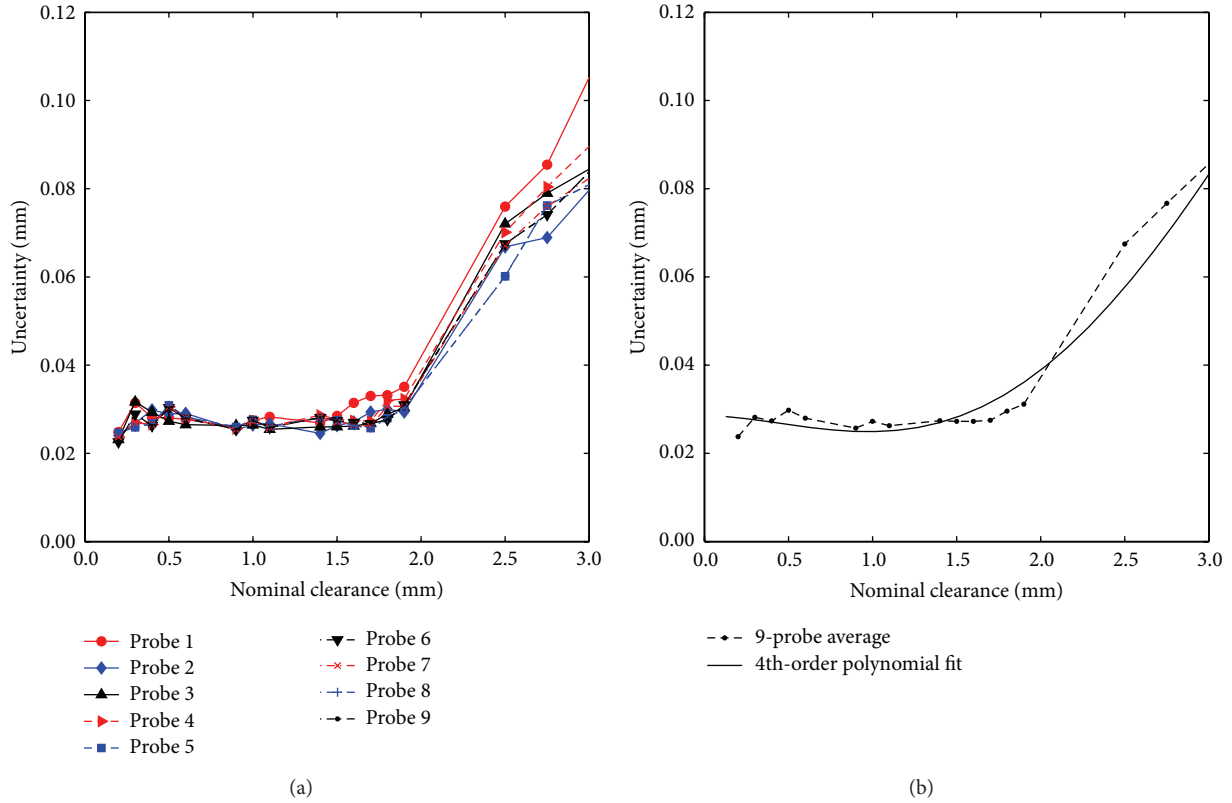


FIGURE 4: Uncertainty of tip clearance measurements. (a) All nine probes; (b) average.

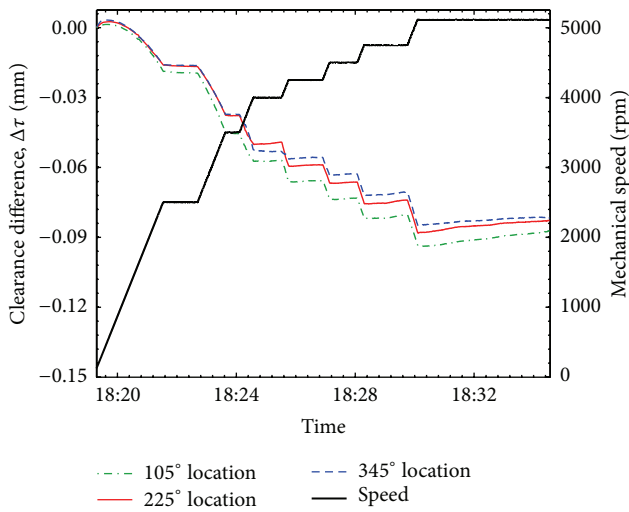


FIGURE 5: Clearance changes with speed for Rotor 2 during startup process at an open throttle operating condition.

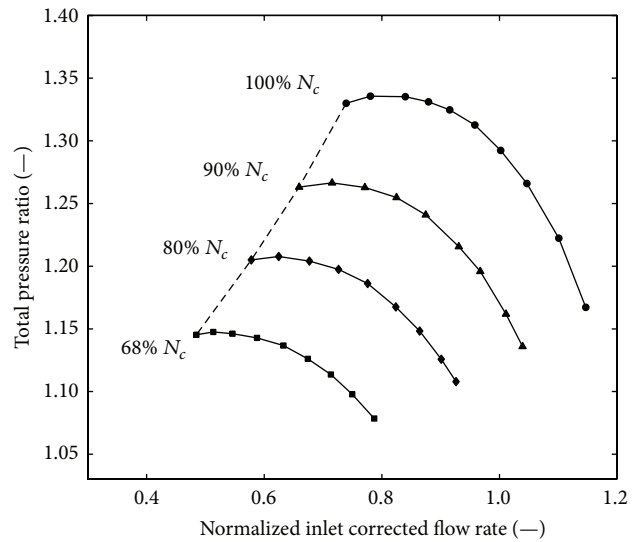


FIGURE 6: Overall compressor map at four operating speeds.

in the direction toward stall by closing the sliding-annulus throttle at the exit of the machine. The overall compressor total pressure ratio is shown in Figure 6 at each of the four corrected operating speeds. In Figure 6, the total pressure is presented as a function of normalized inlet corrected mass flow rate, for which a normalized inlet corrected mass flow rate of unity denotes a nominal loading condition near the

peak efficiency point. Each of the data points in Figure 6 represents a circumferential average of 20 vane positions with respect to measurement probes in order to remove variability due to stator wake effects. Each of the points in Figure 6 represents approximately one hour of compressor operating time.

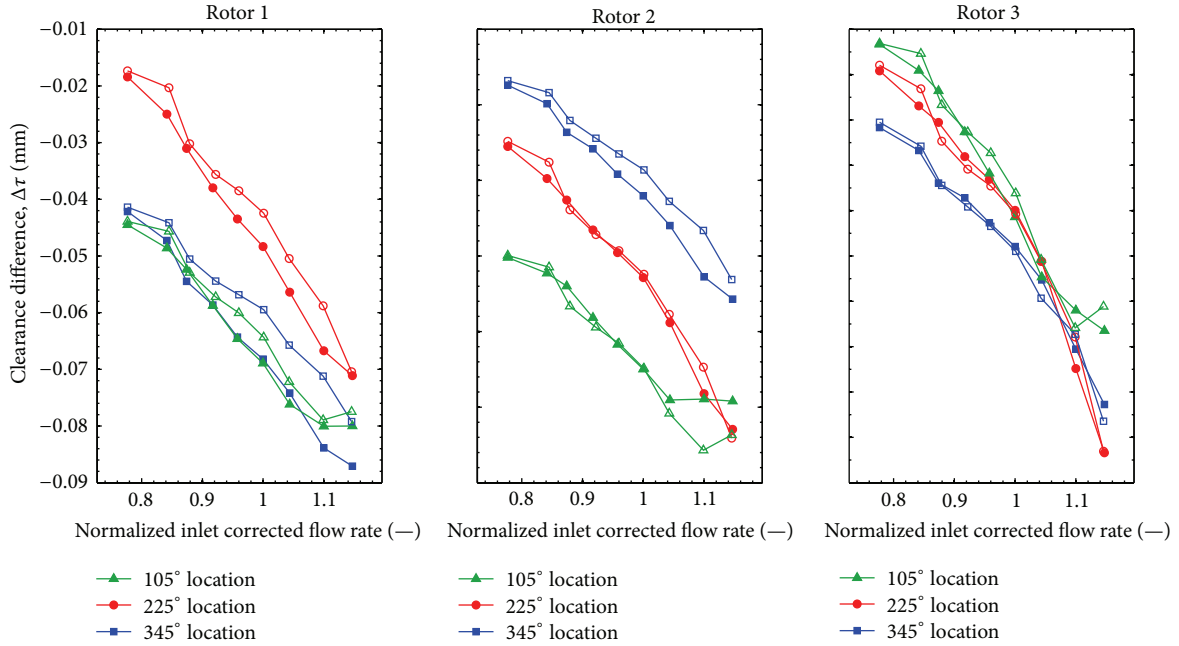


FIGURE 7: Clearance changes with compressor loading condition at a 100% corrected operating speed.

Understandably, the temperature rise through the compressor increases with increased loading. As this occurs, the thermal effects begin to have a greater impact on the outer casing of the compressor. Specifically, moving from the open throttle position to a near-stall operating condition has the effect of increasing the stagnation temperature rise at the exit of each rotor blade row due to the increased work done on the flow.

Figure 7 shows the measured tip clearances for each of the nine loading conditions on the 100% corrected speedline from the compressor map in Figure 6. During the measurement of the overall compressor performance map in Figure 6, the operating clearances were measured, but since each data point in Figure 6 corresponds to approximately one hour of compressor operation, there is a possibility that any observed trends in measured clearance with loading condition are affected by variations in ambient temperature. In an effort to avoid false conclusions due to this potential thermal affect, the rotor clearances shown in Figure 7 were measured at the same loading conditions corresponding to the 100% corrected speedline from Figure 6. However, the data in Figure 7 were collected with approximately ten minutes between adjacent points during a period of time when the ambient temperature was relatively constant (within 2°C). This time allows the machine to sufficiently reach a thermal equilibrium without allowing ambient temperatures to vary significantly. Furthermore, Figure 7 presents two series of measured clearances collected on separate occasions to represent the repeatability of the measurements as an alternative to the calculated electronic system uncertainty from Figure 4. With few exceptions, Figure 7 shows measurement repeatability of 0.01 mm or better, which is in agreement with the value reported by the system manufacturer.

The change in tip clearance with compressor loading condition has been predicted by Dong et al. [12] using a series of model equations for clearance change due to thermal and centrifugal effects. Predicted clearances calculated using this model were verified using experimental measurements collected from the General Electric E³ ten-stage compressor build. For a separate 11-stage compressor, Dong et al. predicted that increasing the loading condition from near choke to near-stall would affect the tip clearance by approximately 0.1% span for Rotor 4 but as much as 0.4% for Rotor 10 (due to an increase in temperature rise in the rear stages of the compressor).

The model presented by Dong et al. [12] utilizes a series of six calculated deformation contributions, each of which can be calculated using independent equations and combined to calculate the overall clearance. Specifically, the model calculates blade deformation due to thermal expansion and centrifugal forces, shroud deformation due to thermal expansion and pressure forces, and disc deformation due to thermal expansion and centrifugal forces. The six contributions are then combined with the static assembled clearance to determine the model clearance

$$\begin{aligned} \tau_{\text{model}} = & \tau_{\text{static}} - (u_{B,\text{thermal}} + u_{B,\text{centrif}}) \\ & + (u_{S,\text{thermal}} + u_{S,\text{pressure}}) - (u_{D,\text{thermal}} + u_{D,\text{centrif}}), \end{aligned} \quad (2)$$

where the subscripts *B*, *S*, and *D* represent the blade, shroud, and disc, respectively. The equations representing these six contributing deformations have been applied using pressure and temperature data corresponding to the compressor performance points presented in Figure 6 for comparison with

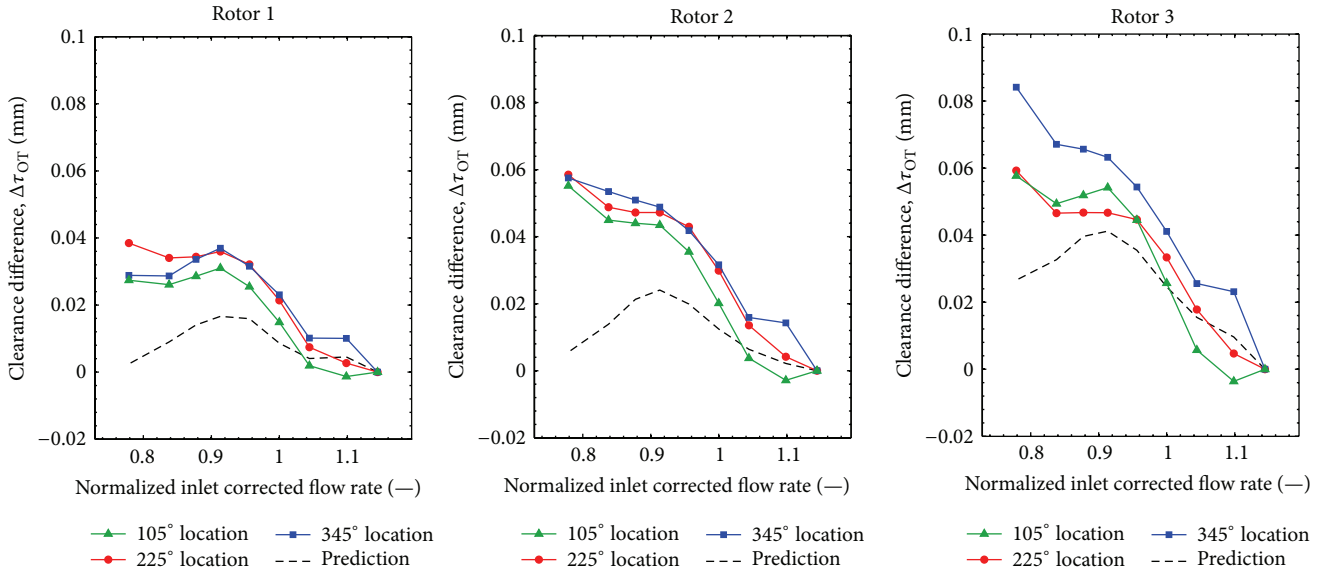


FIGURE 8: Predicted and measured clearance variations with loading condition, presented as a difference from the open throttle condition (100% N_c).

operating rotor tip clearances measured simultaneously with the capacitance probe system.

The equations for the blade and shroud deformations were applied exactly as suggested by Dong et al. [12]. However, the equation for the disc deformation due to thermal effects was simplified to accommodate information available from the experimental results. Specifically, there were insufficient experimental data to allow calculation of the radial temperature distribution on the disc. As a result, the equations were simplified to approximate the disc temperature distribution by a constant temperature measured at the inner diameter of the flow path. This approximation is based on two primary pieces of information: (i) radial temperature gradients in the disc are expected to be small for the front stages of axial compressors and (ii) the integrated-bladed-rotor (blisk) design of the Purdue three-stage axial compressor does not have air paths to facilitate convective cooling.

Using the series of stagnation pressures, stagnation temperatures, and static pressures in the flow path combined with temperatures measured on the outside of the casing, the six components required for the Dong et al. model were calculated. In the cases when static temperatures were required, the thermodynamic equation program REFPROP [18] was utilized in combination with measured parameters, allowing the application of high-accuracy equations to calculate thermodynamic properties including any pertinent humidity effects. Specifically, measured stagnation temperatures and pressures were combined with measured static pressure at the wall (assuming a constant radial distribution of static pressure due to a constant annulus height) to calculate the required static temperatures.

The results comparing the experimental data with the calculated model results are shown in Figures 8 and 9 for 100% and 90% corrected operating speeds. In this case,

the results are presented as a difference with respect to the open throttle loading condition, denoted by the subscript OT:

$$\Delta\tau_{OT} = \tau - \tau_{OT}. \quad (3)$$

Considering first the results of the 100% corrected speedline data shown in Figure 8, there is a noticeable lack of agreement between the measured clearances and the predicted clearances for normalized inlet corrected mass flow rates less than one. Specifically, for the results from Rotor 2 in Figure 8, the near-stall point (lowest mass flow rate) shows a discrepancy nearly two times the uncertainty presented in Figure 4 and at least five times the repeatability shown in Figure 7. On the other hand, the 90% corrected speedline data in Figure 9 show excellent agreement between the predicted and measured clearances. Similar agreement between predicted and measured clearances also exists for the 80% and 68% corrected speedlines (not shown here).

The model equation presented in (1) suggests that the discrepancy for the 100% corrected speedline results could come from an overprediction of blade and/or disk growth or an underprediction of shroud growth. To more closely consider the source of the errors, the individual components are presented in Figure 10. From this figure, the contributions to the predicted clearances are driven primarily by the thermal growth, which yield clearance differences several orders of magnitude larger than the pressure or centrifugal components.

4.3. Ambient Temperature Effects. Analysis of the data corresponding to the results in Figure 8 shows that a significant temporal variation of ambient temperature (on the order of 3°C) exists for the data at low inlet corrected mass flow rates. These variations of temperature are present throughout the data collection period due to changes of ambient conditions. Of course, the corrected parameters defining the operating

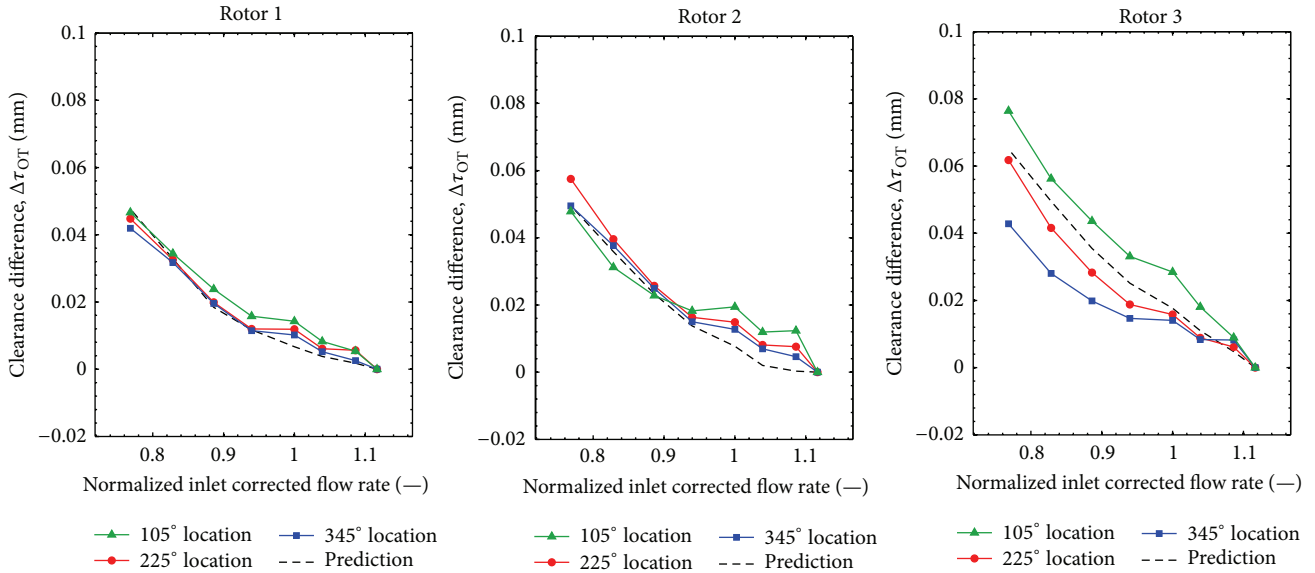


FIGURE 9: Predicted and measured clearance variations with loading condition, presented as a difference from the open throttle condition (90% N_c).

point (rotational speed, mass flow rate) appropriately account for these varying ambient conditions in overall performance, but the averaged data which were utilized to calculate the temperatures required for use in (2) do not appropriately represent the required parameters. Thus, an adjustment was made to the prediction calculations such that the temperature utilized for the thermal components of (2) represents the temperatures measured at the exact same time as the measured tip clearances. Figure 11 shows that the adjustment does not remedy the entire discrepancy, but it more closely represents the measured values on the order of the uncertainty of the measurements. No adjustments were made to the nonthermal components of (2) due to their relatively small contribution shown in Figure 10.

Careful consideration is always given to ensure that a thermal equilibrium is reached prior to collecting these data. However, the data presented thus far suggest that the clearance variations with loading condition can also depend on the ambient conditions. Figure 12 shows this by comparison of two different tip clearance cases corresponding to different ambient conditions. Specifically, the data presented previously for the 3.0% clearance was susceptible to variations of ambient temperature for the low flow rates (as discussed above), whereas the 1.5% tip clearance results were collected over a period of time when the ambient temperature was nearly constant, which leads to the increased clearance growth at the low flow rates. The change of nominal tip clearance between the two cases poses a potential source of variability, particularly in terms of temperatures, but these data were collected during periods of similar weather and previous studies have shown that the temperature rise through the compressor is nearly identical for these two tip clearance cases.

To further emphasize the effect of ambient temperature on measured rotor tip clearance, Figure 13 shows the results

of the 80% corrected speedline for one of the tip clearance configurations. It is important to note here that the lower rotational speed creates less temperature rise through the compressor. This lower temperature rise leads to clearance measurements which are less sensitive to loading condition. In other words, the measured and predicted clearances for adjacent operating points are nearly constant.

Considering the data in Figure 13, a stretch of severe weather forced a stop of the experimental campaign after the completion of the three points with the lowest flow rates, and the data collection process resumed on the following day. As shown in Figure 13, the discontinuity of ambient conditions for between the third and fourth points in the order of increasing flow rates caused a discernable discontinuity of rotor tip clearance (measured and predicted). This jump in clearance is approximately 0.06 mm, which represents an 8% change of operating tip clearance for the nominal tip clearance of 1.5% span (0.762 mm), and is attributable to a change in ambient temperature of approximately 15°C. Although there is no measureable change of performance parameters due to this difference of rotor tip clearance in this compressor, these results suggest that it is advisable to avoid a “stop and start” when a comparison of tip clearance information between adjacent data points is desired.

In these cases of varying ambient temperature and other environmental considerations, it is possible that the changing air composition could affect the dielectric properties enough to skew the capacitive effect, thereby artificially introducing the measured clearance changes shown here. Chivers [9] analyzed the relative permittivity of the dielectric material (for this study, air) at several temperatures and pressures representing a 220 kN thrust class gas turbine engine. From that analysis, Chivers showed that increases in pressure and temperature due to flow through the compressor would affect the relative permittivity of air by approximately 0.05%

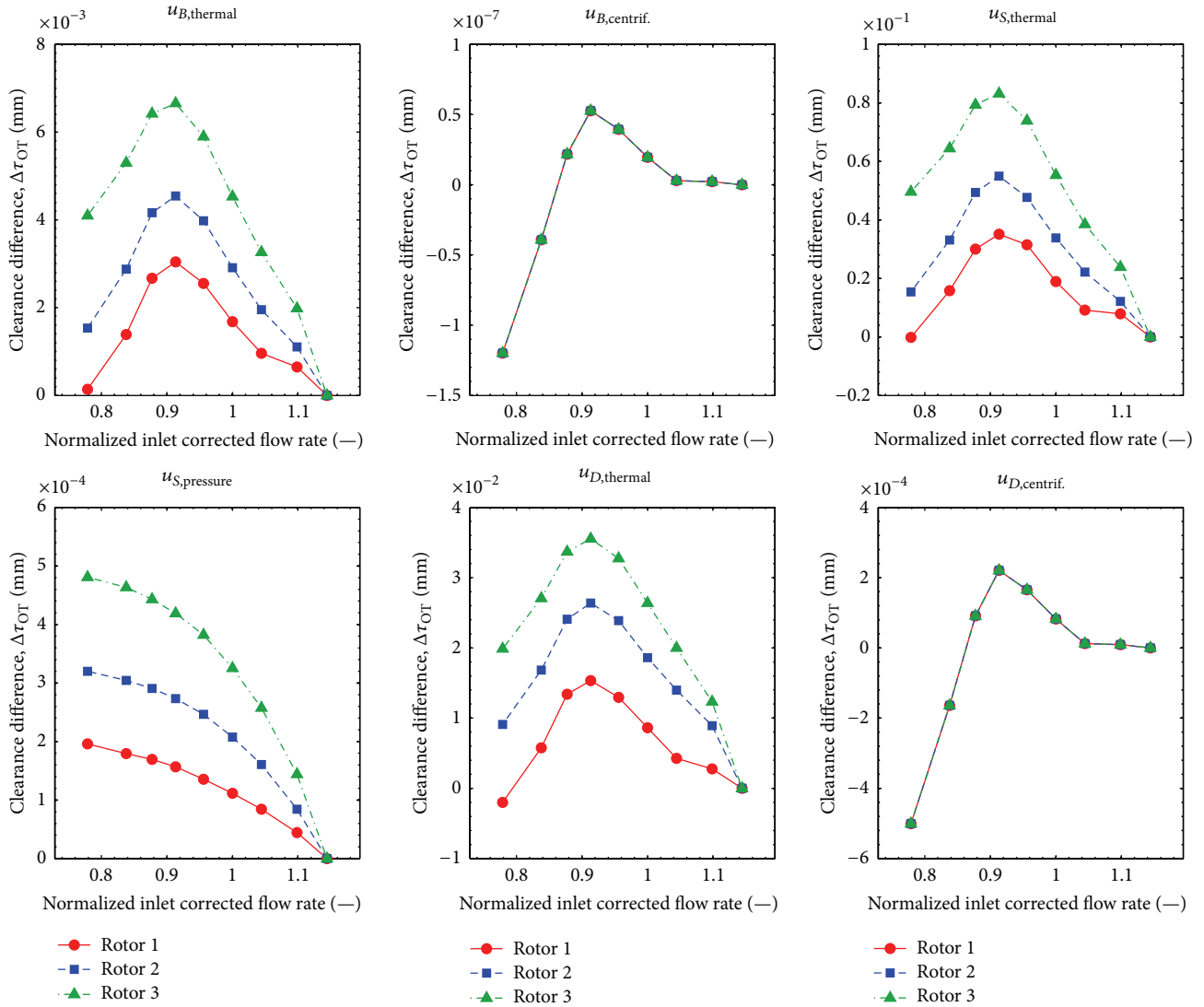


FIGURE 10: Components of predicted clearances from (2) corresponding to data for Figure 8.

compared to the same properties at the inlet of the machine. Further, Baxter [19] addresses the concern of humidity effects on relative permittivity. An increase of relative humidity from 40% to 90% at 20°C (a representative average for the data presented here) would affect the relative permittivity and, therefore, the measured capacitance on the order of 0.007%—an order of magnitude less than changes due to temperature alone. From these values, it is expected that the changes of dielectric properties do not have a significant effect on the measured clearances.

4.4. Thermal Equilibrium Considerations. To this point, analysis of rotor tip clearance effects due to rotational speed, loading condition, and ambient temperature has been considered. Allusion has been given to thermal equilibrium, but primarily in the framework of ambient temperature variations due to time of day. Thus, the time associated with approaching a condition of equilibrium based on measured clearances was also considered explicitly in the context of thermal equilibrium.

The compressor was operated at a steady rotational speed of 2500 rpm and was allowed to reach a state of equilibrium as determined from measured thermocouples and tip clearance measurements. At that point, the operating speed was increased to 5150 rpm (a mechanical speed relating to a 100% corrected rotational speed based on ambient conditions) at a linear rate of 1100 rpm per minute, and the corresponding response of measured clearances and shroud outer diameter temperatures was observed. In addition to the mechanical speed in Figure 14(d), the measured ambient temperature is also shown to verify that the measured temperature and clearance changes in Figures 14(a)–14(c) are not a result of changes in ambient temperature. These clearance results are shown in Figures 14(a)–14(c) as a difference with respect to the static clearance values.

Referring to Figure 14, immediately after the increase of speed, the measured clearances decrease in a nonlinear fashion. Throughout this speed change process, the surface

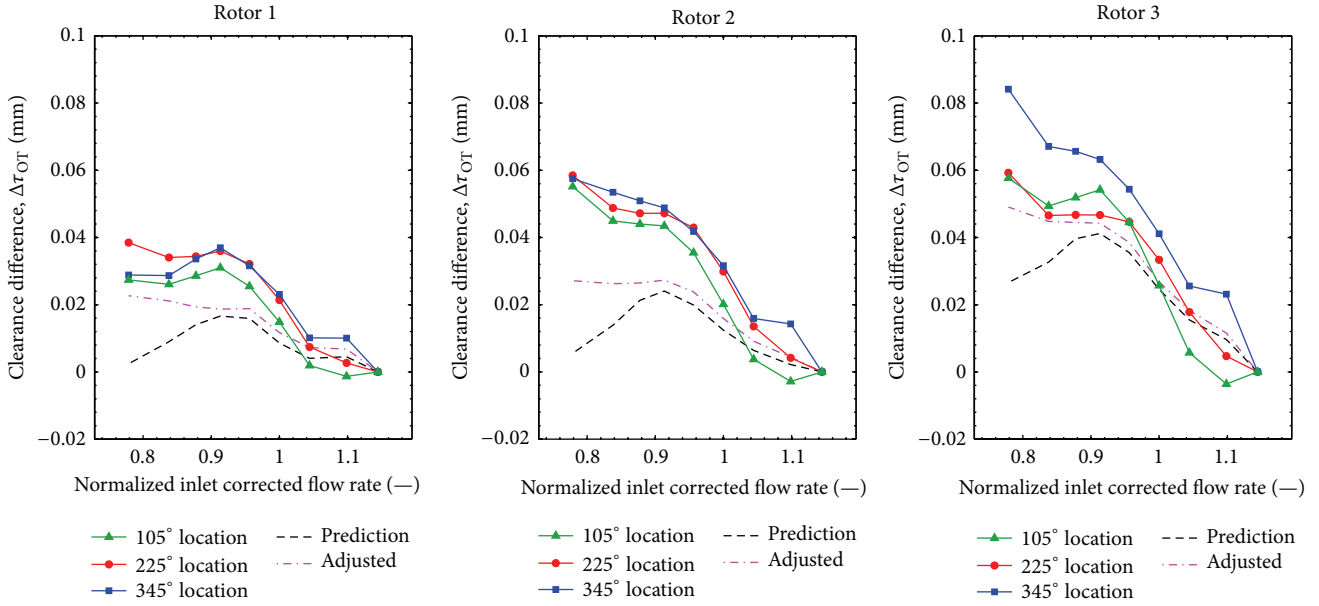


FIGURE 11: Predicted and measured clearance differences from the open throttle loading condition including a temperature adjustment for the predicted results (100% N_c).

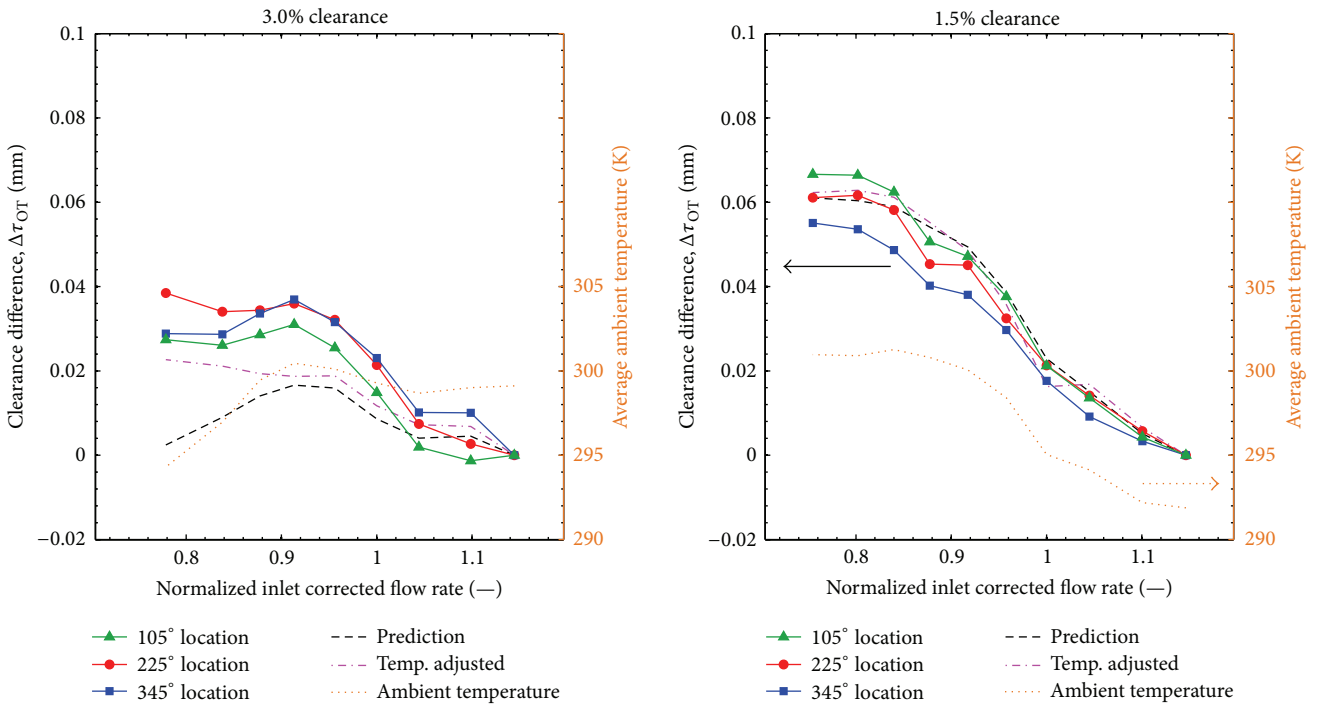


FIGURE 12: Predicted and measured clearance variations with loading condition, presented as a difference from the open throttle condition for different compressor tip clearance configurations with variations due to ambient conditions (100% N_c , Rotor 1).

temperatures measured at the outer diameter of the compressor shroud show no change. In this period (Region I; approximately 2-3 minutes), an increase of flow temperatures exists, but there is a definitive lag in the clearance response due to thermal growth. Over the course of the following 15 minutes (Region II), however, the temperature increase

measured at the outer diameter of the compressor shroud is observable for all three rotors following an asymptotic trend. During this same period, the measured clearances also show an increase, but the trends for the three rotors differ slightly.

Throughout the entirety of Region II, the clearance change over Rotor 1 is approximately linear. In contrast,

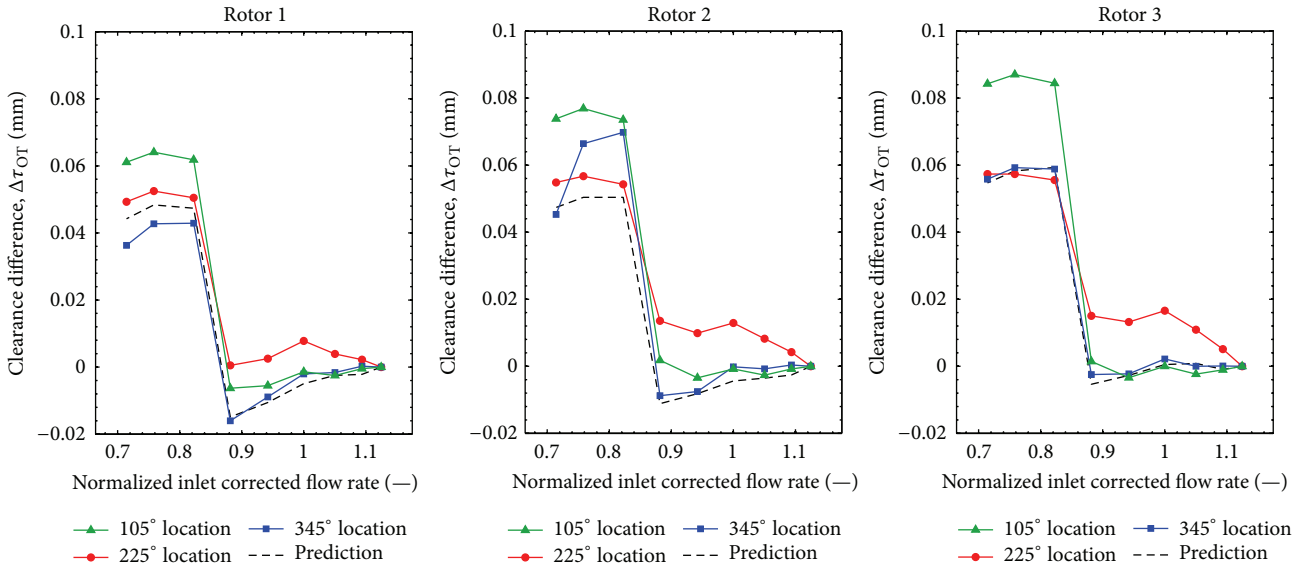


FIGURE 13: Predicted and measured clearance variations with loading condition, presented as a difference from the open throttle condition (80% N_c) for compressor testing with a “stop and start” (1.5% tip clearance).

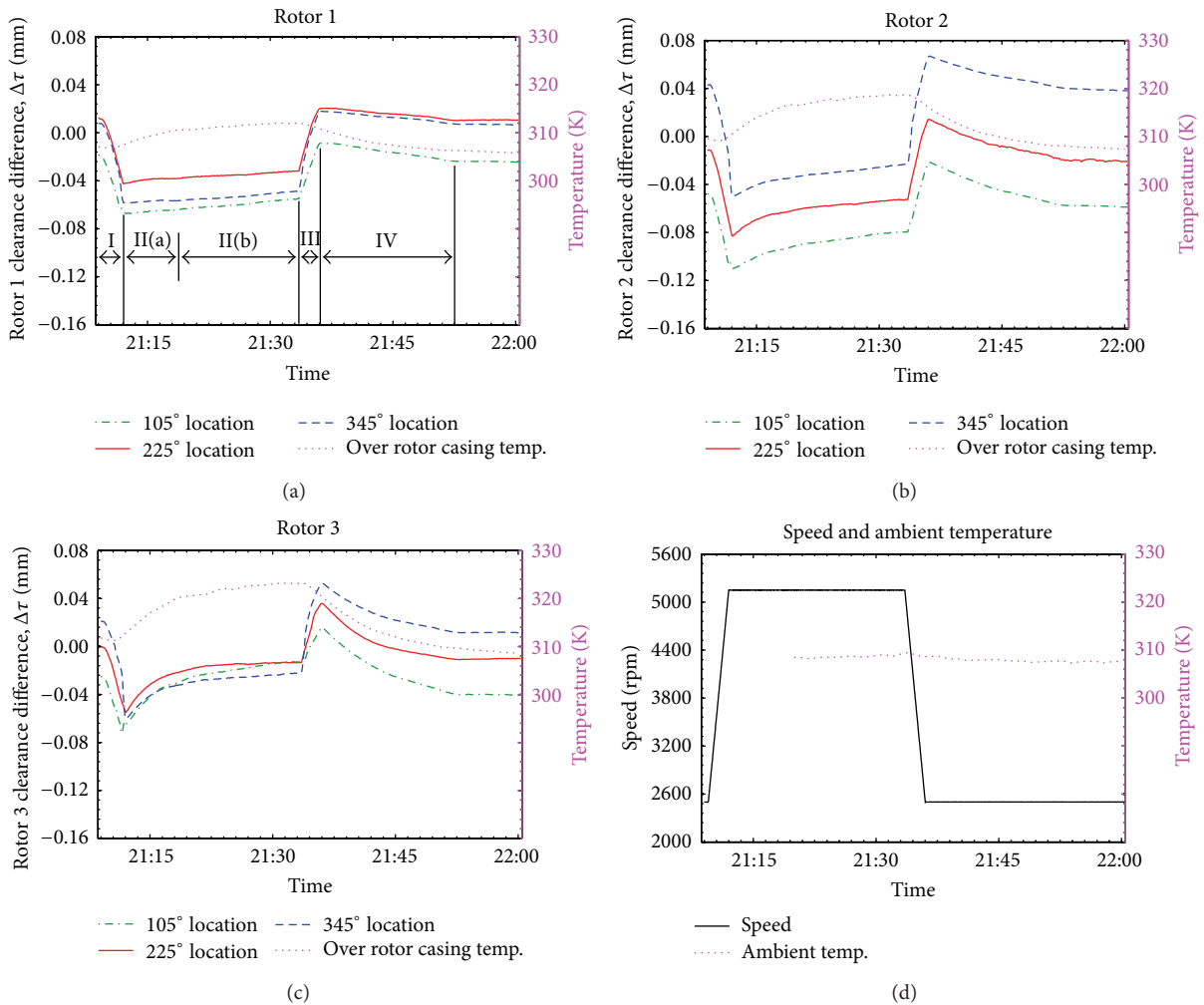


FIGURE 14: Clearance changes due to compressor speed changes and corresponding thermal variations at a nominal loading condition.

the clearance changes over Rotor 2 and Rotor 3 exhibit a nonlinear section, Region II(a), which extends across approximately the initial one-third of Region II. The nonlinear response of Region II(a) is expectedly due to the more immediate change of tip clearance due to temperature rise in the flow (e.g., the contribution $u_{B,thermal}$). For this reason, the clearance change in Region II(a) for Rotor 3 is more significant than that of Rotor 2, and the relatively small temperature rise across Rotor 1 leads to a nondiscernable Region II(a) for that blade row. Region II(b), on the other hand, is primarily a contribution due to the heat transfer through the compressor shroud contributing to the thermal growth term $u_{S,thermal}$.

Once the measured temperatures at the outer diameter of the shroud approached an asymptotic value, the rotational speed was decreased at the same rate of 1100 rpm per minute. Predictably, the trends of measured clearances show a sharp increase with the decreased rotational speed as the clearance contributions due to centrifugal forces respond (Region III). In contrast with Region II, the thermally dominated Region IV for the deceleration follows a more linear trend for all three rotors. This important difference is related to the cooling process imposed by decreasing speed as the temperature rise through the compressor decreases and the convective heat transfer to the air around the compressor increases. As a result, there is a less distinct separation of thermal contributions in Region IV. Although there is a slight asymptotic trend in the clearance variations of Region IV for Rotor 3, the trend is significantly less apparent than it was for Region II with the same blade row.

5. Summary and Conclusions

Operating rotor tip clearances have been measured using an FM capacitance probe measurement system with the Purdue three-stage axial compressor. Due to the large amount of experimental data available, this facility provides a unique opportunity to examine tip clearance variations due to several external factors. In particular, tip clearance changes due to rotational speed, loading condition, ambient temperature, and thermal equilibrium have been addressed. This study has experimentally validated the existence of measurable changes in tip clearance at several loading conditions and for several different compressor tip clearance heights. Many of these measured changes are well beyond the calculated uncertainty of the electronics system, and nearly all are beyond the repeatability of the measurements.

The results presented herein pose a very real problem for operating gas turbine engines that has not been presented previously through experimental data. Previous authors have discussed the potential variation of rotor tip clearance with changing loading condition, but this changing clearance is typically not implemented in computational models. These measurable changes of tip clearance with operating condition could be important for comparing experimental and computational performance. More importantly, these measured clearance changes with ambient operating conditions can also lead to measurable changes in overall total pressure ratio beyond the uncertainty of the measurements.

These results have focused on a machine which yields relatively low total temperature ratios. Thus, the thermally driven clearance changes could be considered small in comparison with larger multistage compressors. In particular, it has been shown that the largest clearance variations exist in the rear stages where the temperature rise is the greatest. For typical gas turbine compressor designs, this is the location at which the blade heights and the relative tip clearances are the smallest. As a result, the change of tip clearance with operating condition and ambient temperature is likely more significant than some may believe.

Ultimately, the results presented here motivate a need to incorporate tip clearance measurement systems with compressor test facilities desiring to accurately monitor compressor performance. Experimental data collected at different times of day, during different periods of the calendar year, or at different loading conditions can lead to significant variations of tip clearances which must be monitored for a best comparison with computational tools.

Nomenclature

FLA:	Forward looking aft
τ :	Operating tip clearance height
τ_{OT} :	Operating tip clearance height at open throttle
τ_{static} :	Static tip clearance height
u_B :	Clearance contribution due to blade deformation
u_D :	Clearance contribution due to disc deformation
u_S :	Clearance contribution due to shroud deformation.

Conflict of Interests

The authors declare that there is no conflict of interests regarding the publication of this paper.

Acknowledgments

This material is based upon work supported by NASA under the ROA-2010 NRA of the Subsonic Fixed Wing project and in part by the National Science Foundation Graduate Research Fellowship Program under Grant no. DGE-1333468. The authors are grateful to Reg Morton for providing technical information specific to the probe measurement system. The authors would also like to thank Rolls-Royce for the permission to publish this work.

References

- [1] D. C. Wisler, "Loss reduction in axial-flow compressors through low-speed model testing," *ASME Journal of Engineering for Gas Turbines and Power*, vol. 107, no. 2, pp. 354–363, 1985.
- [2] C. C. Koch and L. H. Smith Jr., "Loss sources and magnitudes in axial-flow compressors," *ASME Journal of Engineering for Gas Turbines and Power*, vol. 98, no. 3, pp. 411–424, 1976.
- [3] J. P. Barranger, "Recent advances in capacitance type of blade tip clearance measurements," NASA Technical Memorandum 101291, 1998.
- [4] J. D. Denton, "Some limitations of turbomachinery CFD," ASME Paper GT2010-22540, American Society of Mechanical Engineers, 2010.

- [5] P. P. Walsh and P. Fletcher, *Gas Turbine Performance*, Blackwell Science, Oxford, UK, 2008.
- [6] N. R. Smith, R. A. Berdanier, J. C. Fabian, and N. L. Key, "Reconciling compressor performance differences with varying ambient conditions," ASME Paper POWER2015-49102, American Society of Mechanical Engineers, 2015.
- [7] D. E. van Zante, A. J. Strazisar, J. R. Wood, M. D. Hathaway, and T. H. Okiishi, "Recommendations for achieving accurate numerical simulation of tip clearance flows in transonic compressor rotors," *ASME Journal of Turbomachinery*, vol. 122, no. 4, pp. 733–742, 2000.
- [8] A. G. Sheard, "Blade by blade tip clearance measurement," *International Journal of Rotating Machinery*, vol. 2011, Article ID 516128, 13 pages, 2011.
- [9] J. Chivers, "A technique for the measurement of blade tip clearance in a gas turbine," AIAA Paper 89-2916, AIAA, 1989.
- [10] H. Agarwal, S. Akkaram, S. Shetye, and A. McCallum, "Reduced order clearance models for gas turbine applications," AIAA Paper 2008-2177, AIAA, 2008.
- [11] J. A. Kypuros and K. J. Melcher, "A reduced model for prediction of thermal and rotational effects on turbine tip clearance," NASA Technical Memorandum 2003-212226, 2003.
- [12] Y. Dong, Z. Xinqian, and L. Qiushi, "An 11-stage axial compressor performance simulation considering the change of tip clearance in different operating conditions," *Proceedings of the Institution of Mechanical Engineers Part A: Journal of Power and Energy*, vol. 228, no. 6, pp. 614–625, 2014.
- [13] D. C. Ye, F. J. Duan, H. T. Guo, Y. Li, and K. Wang, "Turbine blade tip clearance measurement using a skewed dual-beam fiber optic sensor," *Optical Engineering*, vol. 51, no. 8, Article ID 081514, 2012.
- [14] N. L. Key, "Influence of upstream and downstream compressor stators on rotor exit flow field," *International Journal of Rotating Machinery*, vol. 2014, Article ID 392352, 10 pages, 2014.
- [15] T. N. Satish, R. Murthy, and A. K. Singh, "Analysis of uncertainties in measurement of rotor blade tip clearance in gas turbine engine under dynamic condition," *Proceedings of the Institution of Mechanical Engineers, Part G: Journal of Aerospace Engineering*, vol. 228, no. 5, pp. 652–670, 2014.
- [16] D. Müller, A. G. Sheard, S. Mozumdar, and E. Johann, "Capacitive measurement of compressor and turbine blade tip to casing running clearance," *ASME Journal of Engineering for Gas Turbines and Power*, vol. 119, no. 4, pp. 877–884, 1997.
- [17] J. R. Brossman, *An investigation of rotor tip leakage flows in the rear-block of a multistage compressor [Ph.D. thesis]*, Purdue University, West Lafayette, Ind, USA, 2012.
- [18] E. W. Lemmon, M. L. Huber, and M. O. McLinden, *NIST Standard Reference Database 23: Reference Fluid Thermodynamic and Transport Properties-REFPROP*, Version 9.1, National Institute of Standards and Technology, Standard Reference Data Program, Gaithersburg, Md, USA, 2013.
- [19] L. K. Baxter, *Capacitive Sensors: Design and Applications*, Wiley-IEEE Press, Hoboken, NJ, USA, 1996.

Review Article

Some Experimental Investigations on Gas Turbine Cooling Performed with Infrared Thermography at Federico II

T. Astarita, G. Cardone, L. de Luca, and G. M. Carlomagno

University of Naples Federico II, Piazzale le Tecchio 80, 80125 Napoli, Italy

Correspondence should be addressed to G. M. Carlomagno; carmagno@unina.it

Received 17 October 2014; Accepted 6 January 2015

Academic Editor: Tariq Iqbal

Copyright © 2015 T. Astarita et al. This is an open access article distributed under the Creative Commons Attribution License, which permits unrestricted use, distribution, and reproduction in any medium, provided the original work is properly cited.

This paper reviews some experimental measurements of convective heat transfer coefficient distributions which are connected with the cooling of gas turbines, performed by the authors' research group at the University of Naples Federico II with infrared thermography. Measurements concern impinging jets, cooling of rotating disks, and gas turbine blades, which are either stationary or rotating. The heated thin foil sensor, associated with the detection of surface temperature by means of infrared thermography, is exploited to accurately measure detailed convective heat transfer coefficient maps. The paper also intends to show how to correctly apply the infrared technique in a variety of gas turbines cooling problems.

1. Introduction

The establishment of gas turbine engines dates back to the forties and, since then, the gas highest absolute temperature more than doubled, going from around 1000 K to over 2000 K. This temperature increase was required by the need to improve the efficiency of the engine thermodynamic cycle and, consequently, of the overall engine performance [1].

Currently, the temperatures reached are well in excess of those at which creeping (as well as thermal oxidation, melting, spallation, crack formation, etc.) of the leading nickel base superalloys, from which some components are generally made, occurs. Whilst some of the increase of the turbine entry temperature was made possible through the use of more sophisticated materials, a great part of it was made possible because of the developments in turbine component cooling technology. In fact, to reduce the temperature of these components, a certain amount of air is extracted from the HP compressor and used to cool HP turbine nozzle guide vanes and rotating blades, seal segments, and disks the blades are attached to.

The use of turbine cooling flows may appear to be quite a restricted strategy since cooling flows basically represent losses in the thermodynamic cycle and increasing them may eventually lead to thermal efficiency deficits. Nevertheless,

cooling will be essential until the introduction of new materials, such as ceramics, will become a major reality. However, a lot more research is required before this goal is fully achieved.

In [1] of 2011, it is reported that, despite the relatively low improvement rate in turbine material technology (which can be roughly estimated to be approximately 3 K/year), engine designs have undergone substantial increases of the turbine entry temperature over the past 60 years (of the order of 10 K/year). This is illustrated in Figure 1 for engines designed for long-haul applications. The main reasons behind this temperature increase are, firstly, the introduction of cooling, which produced an initial abrupt rise, and secondly to improve cooling efficiency not to mention the introduction of thermal barrier coatings and single crystal blade castings.

Because of cycle efficiency reasons, the maximum temperature increase is accompanied by a growth in the engine compression ratio which, consequently, leads to an increase in the initial temperature of the cooling air (up to about 700°C). In addition, due to their common origin in the final stage of the HP compressor, this air is at a pressure which is not much higher than that of the hot gas stream at the turbine initial stage. The pressure margin of the cooling air is, therefore, relatively small and cooling must necessarily be performed by means of enhanced heat transfer.

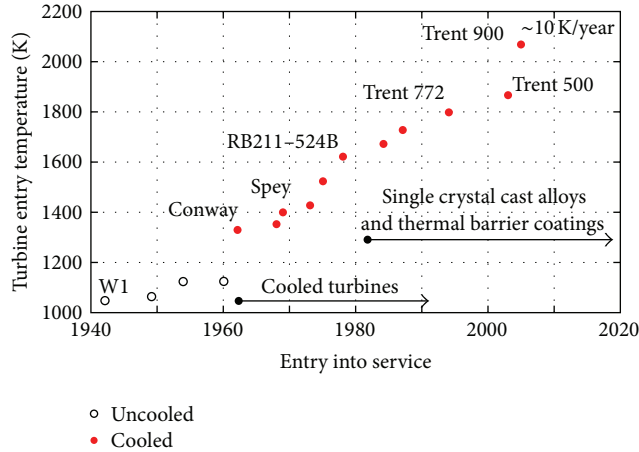


FIGURE 1: Turbine entry temperature versus date of entry into service. Adapted from Kyprianidis [1].

Several methods of gas turbines cooling have been considered in the past and the most efficient of them are still in use in modern engines. Typically, the critical components are cooled internally and externally by using the cooling air extracted from the compressor final stage. For example, high-pressure turbine rotor blades have internal serpentine labyrinths of passages through which the cooling air goes before being vented to the external blade surface. Often, this latter occurs via an array of tiny holes along and around its hottest areas. In this way, the air, emerging with velocity, of the order of the mainstream flow, forms a film of colder fluid around the blade surface (film cooling), thereby insulating it from the hot gases.

From a basic engineering point of view, the parameters the designer has to face are basically the stress levels, due to both mechanical and thermal loads, and the fatigue life of each component. However, these parameters can be only dealt with on the basis of a detailed evaluation of the local temperature distribution in the component under scrutiny which, in turn, requires the knowledge of the local convective heat transfer coefficients (internal and external) for different operating conditions.

Of course, research on gas turbine engines is also extensively oriented towards the reduction of noise and emissions produced by the ever increasing global air traffic although this is not of interest within the present context.

Following on from and developing on a previous article on the same subject [2], this paper describes some detailed measurements of the convective heat transfer coefficient distribution, performed by the authors' research group, in some complex fluid flows related to the cooling of both stationary and rotating gas turbine components. The *heated thin foil* sensor, together with detection of surface temperature by means of infrared (IR) thermography, is exploited to accurately measure such a coefficient. After educating the basic principles that make IR thermography work and of the employed heat flux sensor, several applications, mainly dedicated to gas turbine cooling, are presented and discussed.

2. Experimental Technique

2.1. Infrared Thermography. Infrared thermography is based on radiation heat transfer, which is an energy transport mechanism that occurs under the form of electromagnetic waves. By way of this heat transfer mode, energy can also travel in vacuum and may partially be absorbed and reflected by a body or even pass through it [3]. If the intensity of radiation is put at equal to unity and by denoting by $\alpha_r(\lambda)$ the fraction being absorbed by the body, with $\rho_r(\lambda)$ the fraction being reflected by it and with $\tau_r(\lambda)$ the fraction which is being transmitted (which passes through the body), energy conservation requires

$$\alpha_r(\lambda) + \rho_r(\lambda) + \tau_r(\lambda) = 1, \quad (1)$$

where α_r , ρ_r , and τ_r are, respectively, called *absorptivity*, *reflectivity*, and *transmissivity coefficients* of the body under consideration. These coefficients may depend on both radiation wavelength (*spectral*) and propagation direction (*directional*).

Radiation is emitted by all bodies at an absolute temperature $T > 0$ and, for nontransparent bodies (*opaque*, $\tau_r = 0$), it originates only from their surface. The body which emits the greatest amount of energy at a given temperature is called *black body*.

The law prescribing the energy flux (energy rate per unit area) per wavelength (*spectral hemispherical emissive power*) emitted by a black body $I_b(\lambda)$ (W/m^3) is the *Planck law of radiation*:

$$I_b(\lambda) = \frac{C_1}{\lambda^5 (e^{C_2/\lambda T} - 1)}, \quad (2)$$

where λ is the radiation wavelength (m), T is the absolute black body temperature (K), and C_1 and C_2 are the *first* and the *second universal radiation constants*, equal, respectively, to $3.7418 \times 10^{-16} \text{ Wm}^2$ and $1.4388 \times 10^{-2} \text{ Km}$. Equation (2) shows that I_b goes to zero for both $\lambda \rightarrow 0$ and $\lambda \rightarrow \infty$.

The electromagnetic spectrum is roughly divided into a number of wavelength *bands*. The infrared spectral band, of interest within the present context, is generally subdivided into four lesser bands with arbitrarily chosen boundaries: *near infrared* ($0.75 \div 3 \mu\text{m}$), *middle infrared* ($3 \div 6 \mu\text{m}$), *far* (or *long infrared*) ($6 \div 15 \mu\text{m}$), and *extreme infrared* ($15 \div 1000 \mu\text{m}$). Most of currently used IR cameras are sensitive in the middle (MWIR) and the far (LWIR) spectral bands.

By deriving and integrating it with respect to λ , Planck law leads to the following two laws.

(i) *Wien Displacement Law.* The wavelength λ^m at which the black body emits its maximum spectral emissive power is a function of the absolute black body temperature T according to

$$\lambda^m T = 2897.8 \mu\text{m-K}; \quad (3)$$

that is, the maximum value of I_b moves towards shorter wavelengths as the temperature increases.

(ii) *Stefan-Boltzmann Law*. The total (overall wavelengths) hemispherical emissive power E_b (W/m^2) also depends on the absolute black body temperature alone:

$$E_b = \sigma T^4, \quad (4)$$

where σ is the *Stefan-Boltzmann constant*, which is equal to $5.6704 \times 10^{-8} \text{ W}/(\text{m}^2\text{K}^4)$.

Since infrared camera detectors capture only a relatively narrow band of the whole electromagnetic spectrum, Planck law (2), rather than Stefan-Boltzmann law (4), has to be applied in IR thermography.

Real objects almost never comply with the above described laws even if they may approach black body behaviour in certain spectral bands and conditions. A real object generally emits only fraction $I(\lambda)$ of the radiation emitted by the black body $I_b(\lambda)$, at the same temperature and wavelength, by introducing the *spectral emissivity coefficient*, defined as

$$\varepsilon(\lambda) = \frac{I(\lambda)}{I_b(\lambda)}. \quad (5)$$

Equation (2) can be rewritten for real bodies by simply multiplying its second term by $\varepsilon(\lambda)$:

$$I(\lambda) = \varepsilon(\lambda) \frac{C_1}{\lambda^5 (e^{C_2/\lambda T} - 1)}. \quad (6)$$

Kirchhoff law states that the spectral emissivity coefficient $\varepsilon(\lambda)$, which is the fraction of radiation at wavelength λ emitted by a body, is equal to the *spectral absorptivity coefficient* $\alpha_r(\lambda)$ at the same wavelength. So, for nontransparent bodies, such as those which are mainly used in infrared thermography, (1) becomes

$$\varepsilon(\lambda) + \rho_r(\lambda) = 1. \quad (7)$$

Therefore, materials with low emissivity ε (such as shining metallic materials) not only emit less energy, but also reflect a large amount of the radiation coming from the ambient and impinging on them. Whenever possible, they should not be employed in IR thermography or, if it is necessary to use them, they have to be lightly sandblasted or else, if transient heat transfer is not implied, covered with a thin layer of thermally black paint (such as white dull enamel).

Besides $I(\lambda)$ being dependent on λ , real objects almost never emit in a *diffuse* (isotropic) way, the emissivity coefficient ε being also dependent on the angle between the direction of emission and the normal to the emitting surface (*viewing angle*) [3].

Measurement of convective heat fluxes must be performed by means of a *heat flux sensor*, where proper temperatures have to be measured. By correctly choosing the heat flux sensor, IR thermography can be successfully exploited to resolve convective heat transfer distributions with both steady and transient techniques. When compared to standard

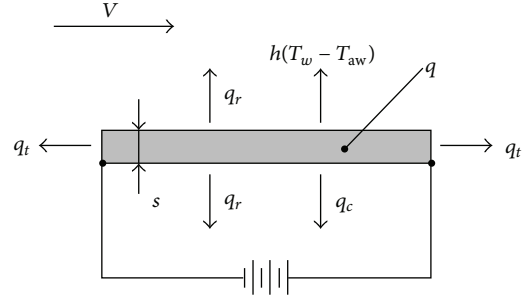


FIGURE 2: Sketch of the heated thin foil sensor with the considered heat fluxes.

transducers, the IR camera appears very valuable because (i) it is nonintrusive, (ii) it has a high sensitivity (down to 20 mK) and low response time (down to 20 μs), and (iii) it is fully two-dimensional (from 300 k up to 1 M pixels) and so allows for better evaluation of errors, for example, due to tangential conduction within the sensor.

2.2. Steady-State Heated Thin Foil Sensor. Measurement of the local convective heat transfer coefficient can be performed by means of the steady-state *heated thin foil sensor* associated with the detection of wall temperature by means of an infrared camera [3, 4].

The heated thin foil sensor method consists of uniformly heating by Joule effect a thin metallic foil (or a printed circuit board) and of measuring the convective heat transfer coefficient h between the foil and the stream flowing on it by means of the relationship (*Newton law*):

$$h = \frac{q - q_l}{T_w - T_r}, \quad (8)$$

where q is the known Joule heating flux (W/m^2); $q_l = q_t + q_c + q_r$ represents heat flux losses which are mainly due to tangential conduction along the foil q_t , natural convection at the foil back side q_c , and radiation q_r (see Figure 2); T_w is the wall temperature which is measured by the IR camera when the foil is heated (*hot image*); T_r is a reference temperature. For example, for channel flows, T_r coincides with the local bulk temperature or, for relatively high Mach number flows, is the so-called *adiabatic wall temperature* T_{aw} [3]. It being possible to neglect q_l , T_{aw} may be detected by measuring the wall temperature of the foil when this latter is not being heated ($q = 0$, *cold image*).

Generally, the foil should be thermally insulated at its back face, that is, the face opposite to that which the stream is flowing over with velocity V . When insulation cannot be accomplished, for example, to measure the temperature distribution over this face, additional thermal losses, such as natural convection and radiation, have also to be taken into account. In fact, it can be readily understood that, if the Biot number, $\text{Bi} = h_t s / k_s$, is relatively small, the foil can be considered isothermal across its thickness and measurements can be performed on either of the foil's faces.

Often ignored tangential conduction, which modulates the thermal signal, can be evaluated by means of the Laplacian

of the wall temperature [3]. In principle, this seems relatively easy to perform by considering that the camera provides a very large number of measurement points. However, it has to be stressed that spurious effects, linked to spatial noise, must be avoided by carefully filtering, and/or splining, the temperature signal. Since the sensor is a steady-state one, averaging a large number of thermal images can consistently reduce the temporal noise.

If the heated thin foil is made of a printed circuit board, the bulk tangential thermal conductance along the foil is nonisotropic. In fact, if the circuit is obtained with several electrical conducting tracks arranged in a Greek fret mode, due to the very high thermal conductivity coefficient of copper, the thermal conductance along the tracks is usually significantly higher than that perpendicular to them. This anisotropy may be taken into account by allowing for two different bulk tangential thermal conductances, one along the tracks and the other one perpendicular to them. Further details on the correction of the nonisotropic heated thin foil can be found in Astarita and Carlomagno [3].

The infrared systems used herein are either AGEMA Thermovision 900LW or CEDIP Jade III. In the first, the field of view is scanned by a single detector in the LWIR infrared window; nominal sensitivity (expressed in terms of noise equivalent temperature difference) is 0.07 K and each thermal image is digitised at 12 bits in a frame of 136×272 pixels. The second has a MWIR FPA, 320×240 pixels, with sensitivity of 0.02 K. For each image, dedicated software is employed which normally involves noise reduction by numerical filtering, computation of temperature maps, and evaluation of radiation and tangential conduction losses as well as heat transfer correlations.

3. Applications

In the following, several experimental applications of infrared thermography, regarding gas turbines cooling, are reported. Average data accuracy is of the order of at most $\pm 7\%$.

3.1. Rotating Disk. The authors apply IR thermography to heat transfer measurements in different rotating disk configurations [5–7] and illustrate the importance of the adiabatic wall temperature T_{aw} in relatively high Mach number flows.

The experimental apparatus is sketched in Figure 3 and consists of a 450 mm diameter shallow steel cup (disk), rotating in still air, filled with a 20 mm thick layer of polyurethane foam on which a printed circuit board is glued. The latter has copper tracks, with a double spiral shape, $35 \mu\text{m}$ thick, 2 mm wide, and with a 2.5 mm pitch. The board's overall thickness is about 0.2 mm. Electric power from a stabilized power supply is provided to the tracks via a mercury rotating contact. The disk's angular speed ω can be varied in the range 100–4400 rpm and is precisely monitored by an optical transducer, speed fluctuations resulting less than 1%. For this section, the nozzle is not present.

The thermogram of Figure 4(a) presents the temperature map of the disk rotating in still air ($T_a = 21.4^\circ\text{C}$) at 576 rpm with an imposed Joule heat flux $q = 515 \text{ W/m}^2$. Due to disk

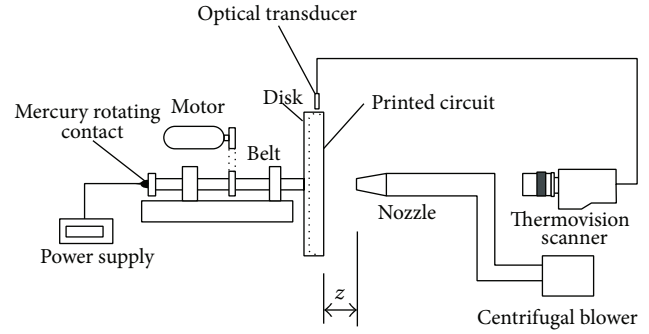


FIGURE 3: Apparatus to study the rotating disk heat transfer with, and without, a centred impinging jet.

rotation, the reported map is practically an azimuthal average of the local wall temperature (this explains its almost perfect symmetry) and, as shown by (8), this map can be interpreted with the inverse proportionality between temperature difference ($T_w - T_{aw}$) and convective heat transfer coefficient. Most of the thermogram of Figure 4(a) indicates constant temperature T_w over the disk of about 45.6°C and this is because, given the relatively low rotating speed, the flow there is laminar.

In fact, it has to be remembered that, for a disk rotating at angular speed ω , the heat transfer solution of Millsaps and Pohlhausen [8] for the heat transfer coefficient in laminar flow is

$$h = ak\sqrt{\frac{\omega}{\nu}}, \quad (9)$$

where ν and k are the air kinematic viscosity and thermal conductivity coefficients, respectively, and a is a constant, which for air at ambient temperature ($\text{Pr} \approx 0.71$) turns out to be equal to about 0.33. Equation (9) shows that h does not depend on the disk radial coordinate r . Given that the convective heat transfer coefficient is constant over the central region of the disk surface, from (8) it follows that, for a constant heat flux boundary condition and constant reference temperature $T_r = T_{aw}$ (which in this case is the ambient air temperature T_a), the wall temperature T_w also has to be constant. Towards the disk edge, temperature varies rapidly because, as will be shown, h increases rapidly there.

On the other hand, the thermogram of Figure 4(b) shows the temperature map of the same disk rotating at a much higher speed, 4390 rpm, with an imposed Joule heat flux $q = 871 \text{ W/m}^2$. It will be evidenced that, for the present case, the adiabatic wall temperature plays a significant role in the thermal behaviour of the flow because; if it is not considered, an inconsistency is found.

In fact, in Figure 4(b), a relatively small region ($\approx 16\%$ of the disk surface), near the disk centre where the flow is still laminar, shows constant temperature T_w of about 38.5°C . Actually, in this central part of the disk, the local tangential speed is relatively small and consequently the flow regime is practically hypersonic (very low Mach number M), so that the adiabatic wall temperature T_{aw} essentially coincides with the ambient air temperature $T_a \approx 21.4^\circ\text{C}$. This is shown in

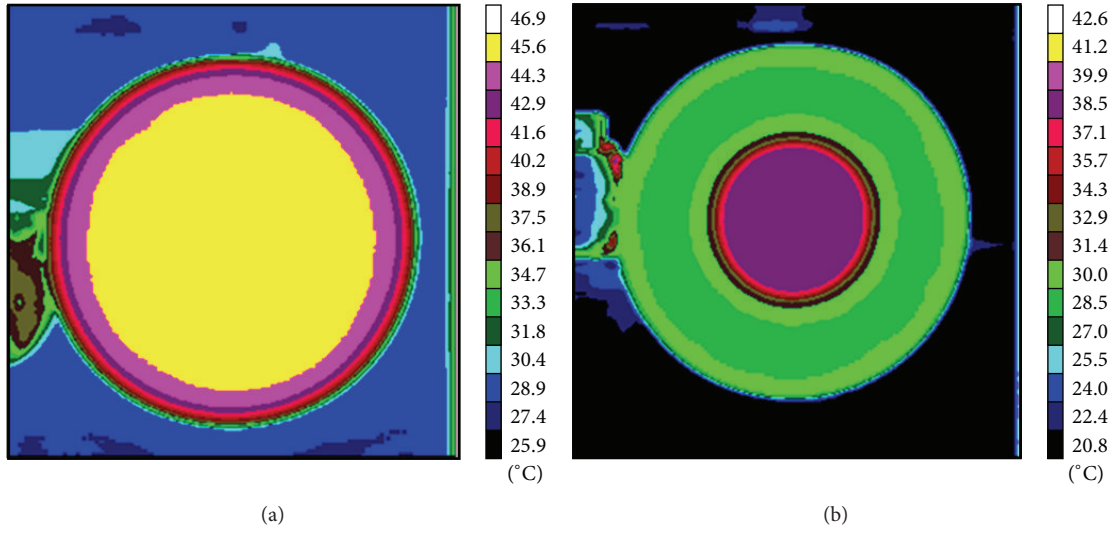


FIGURE 4: Temperature map ($^{\circ}\text{C}$) of the rotating disk for $T_a = 21.4^{\circ}\text{C}$: (a) $\omega = 576$ rpm, $q = 515$ W/m^2 ; (b) $\omega = 4390$ rpm, $q = 871$ W/m^2 .

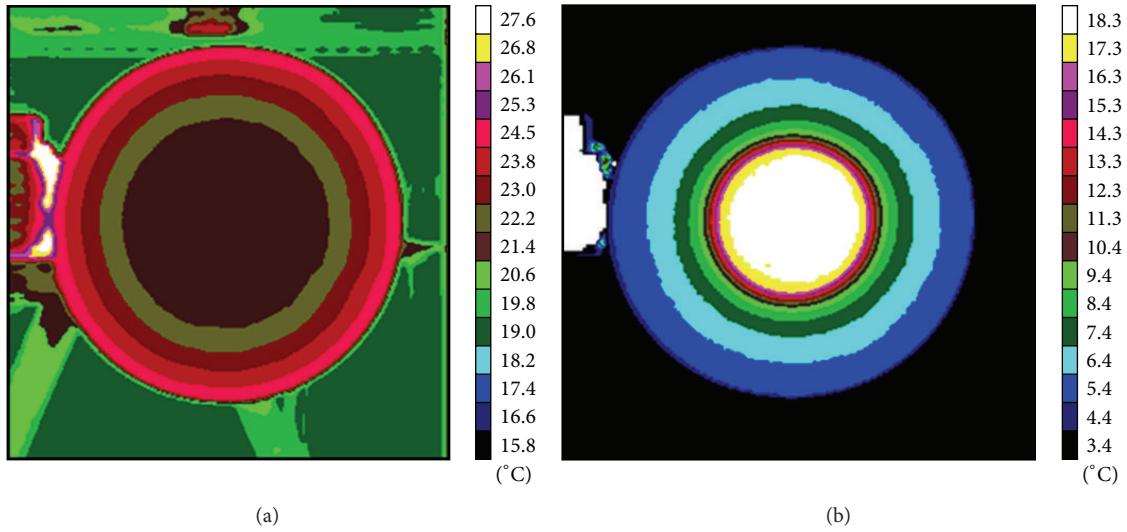


FIGURE 5: Disk rotating at 4390 rpm: (a) adiabatic wall temperature T_{aw} ($^{\circ}\text{C}$), $q = 0$ W/m^2 ; (b) temperature difference $T_w - T_{aw}$ ($^{\circ}\text{C}$), $q = 515$ W/m^2 .

the central part of the thermogram of Figure 5(a), which is obtained by simply making $q = 0$ at the same angular speed practically giving, therefore, T_{aw} as mentioned above. Afterwards, in Figure 4(b), the wall temperature decreases, at first, rapidly and then more slowly. Immediately after, besides some edge effects at disk periphery, the wall temperature trend is reversed as T_w slowly rises (medium to light green).

Actually, this temperature increase is explained by looking at the adiabatic wall temperature map of the thermogram of Figure 5(a). In this map, T_{aw} is practically constant (equal to the ambient air temperature) only within the circumference whose radius is about 60% of the disk radius. Then, T_{aw} exhibits quite an increase (about 3°C near the disk edge).

Since, for the tested conditions, $T_w - T_{aw}$ is of the same order of magnitude as $T_{aw} - T_a$, (8) explains the T_w increase

in Figure 4(b). It has to be pointed out that, in the case of much higher Joule heating, the effect of the T_{aw} would become less important and a monotonically decreasing wall temperature, towards the disk limb, would be observed. As Figure 5(b) shows, going from the disk centre to its periphery, the difference $T_w - T_{aw}$ monotonically decreases because the corresponding convective heat transfer coefficient increases.

The use of T_{aw} allowed very accurate data for the Nusselt number dependence on the Reynolds number to be obtained and they are reported in Figure 6, where the laminar, transitional, and turbulent regimes are easily recognizable.

3.2. Rotating Disk with an Impinging Jet. The line scan facility of the Agema 900 infrared camera is exploited by Astarita and Cardone [9] who measure the convective heat transfer

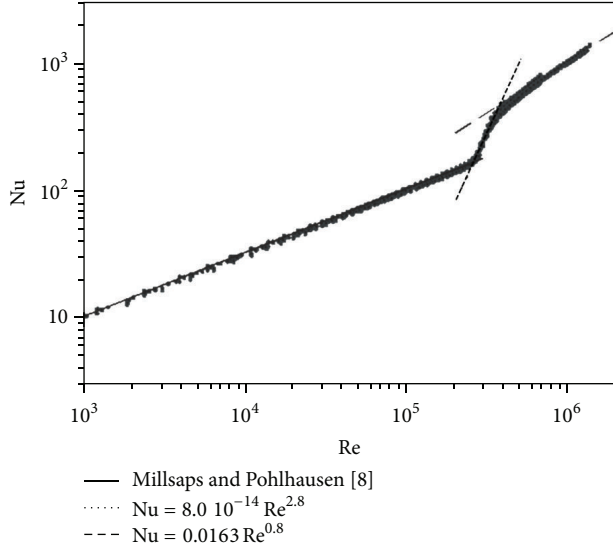


FIGURE 6: Nusselt number Nu versus Reynolds number Re for a rotating disk. From Cardone et al. [6].

coefficient on a rotating disk with a jet impinging at its centre. For each test, about 16,000 radial temperature profiles are acquired to reconstruct the main temperature profile and compute the Nusselt number profile azimuthal average. The authors use the same experimental apparatus described before (Figure 3) with the presence of the centred jet that is produced by air passing through a heat exchanger and a rotameter and finally exhausting from a nozzle. The heat exchanger ensures a jet bulk temperature practically equal ($\pm 0.1^\circ\text{C}$) to the temperature of the ambient air the jet mixes with to avoid mixing of two fluids (jet and ambient air) at different temperatures. Three nozzles with exit diameter D from 4 to 8 mm are in turn used during the tests and the nozzle-exit-to-disk distance z is varied between $3D$ and $75D$. The jet is always impinging perpendicularly at the disk centre.

In order to reduce the number of governing parameters and because of the lack of a theoretical analysis, it is essential to find a rational way to evaluate the relative importance of jet influence compared to that due to disk rotation. On the assumption that the heat transfer coefficient depends on the flow momentum rate, a reasonable dimensionless parameter is the ratio between the two momentum rates (one of the jet and the other one due to the disk rotation). By assuming a jet width proportional to the distance from the nozzle (the nozzle-to-disk distance should be relatively high as compared to D) and in the simplest case of laminar flow over the disk, such a parameter can be put in the form [9]

$$\Phi = \frac{DV}{\nu} \left(\frac{\nu}{\omega z^2} \right)^{3/4}, \quad (10)$$

where ν and ω are the air kinematic viscosity coefficient and disk angular velocity, respectively.

Only convective heat transfer coefficients at the jet stagnation point h_o are reported. By considering only the disk rotation (i.e., without jet), the flow is always laminar at the disk centre and h_o can be evaluated from (9).

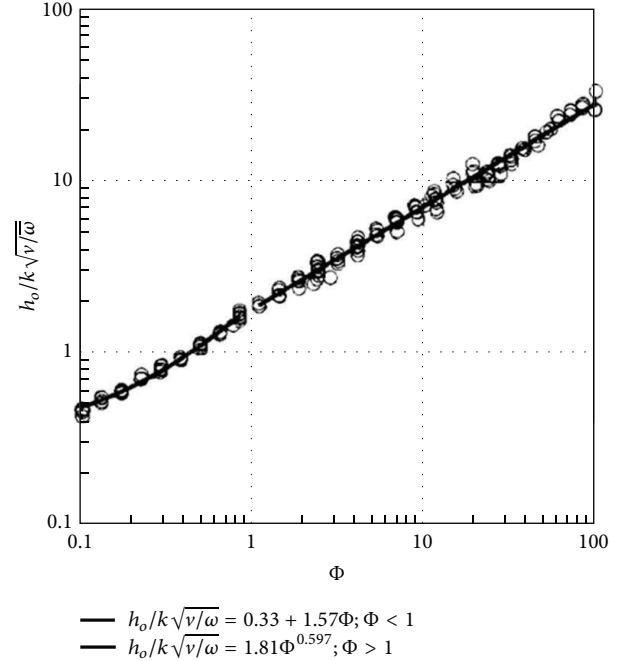


FIGURE 7: Convective heat transfer coefficient at the flow stagnation point of a jet perpendicularly impinging on the centre of a rotating disk. Adapted from Astarita and Cardone [9].

On the other hand, if one also considers the jet effect, the h_o departure from the value predicted by (9) should be a function of Φ only. Therefore, the dimensionless quantity $(h_o/k)\sqrt{\nu/\omega}$ is plotted in Figure 7 as a function of Φ , which refers to about 160 tests, carried out by randomly varying disk angular speed, nozzle diameter, jet flow rate, and nozzle-to-disk distance z . Since Φ holds only for high values of the z/D ratio, z always fulfills the condition $z/D > 14$. Data, for $\Phi > 1$, appears well correlated, in the log-log plane, by a straight line, while the same is not true for smaller Φ values where a linear regression (11) shows a more satisfactory data fitting.

The two best correlation curves, which are also represented in Figure 7 with solid lines, are found to be

$$\frac{h_o}{k} \sqrt{\frac{\nu}{\omega}} = 0.33 + 1.57\Phi; \quad \text{for } \Phi < 1, \quad (11)$$

$$\frac{h_o}{k} \sqrt{\frac{\nu}{\omega}} = 1.81\Phi^{0.597}; \quad \text{for } \Phi > 1. \quad (12)$$

The two correlations (11) and (12) are obtained by using correspondingly a set of 42 and 122 data points and their square correlation factors turn out to be 0.988 and 0.989, respectively. Equation (11) shows the initial linear dependence of h_o on Φ and, for $\Phi \rightarrow 0$, clearly recovers (9).

3.3. 180° Turn and Channels. As stated before, in order to cool a blade or vane, air from the HP compressor stage goes through the hub section into its interior and, after flowing through serpentine passages, is discharged into the main

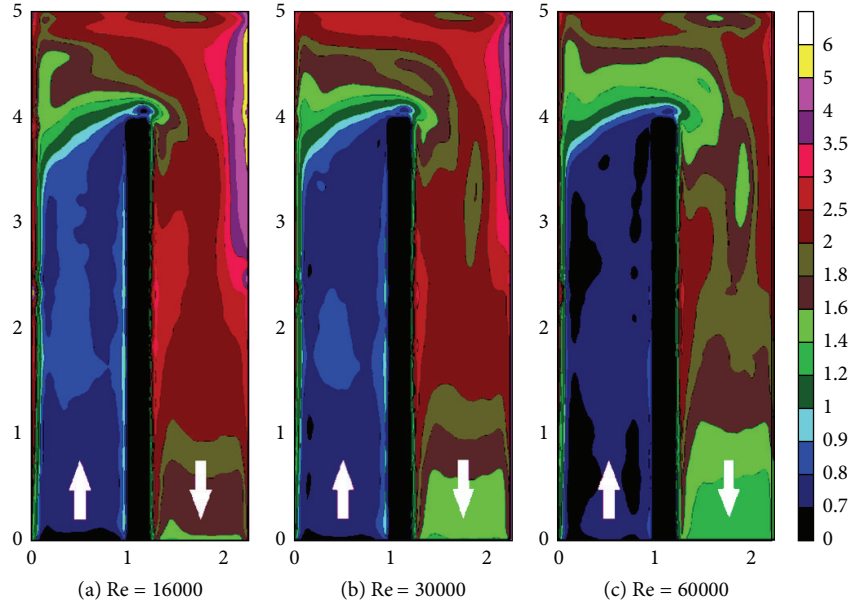


FIGURE 8: Normalised Nusselt number Nu/Nu^* , distribution for the smooth channel. Adapted from Astarita and Cardone [10].

flow to provide film cooling as well. These passages are mostly made of several adjacent straight ducts, spanwise aligned along the blade and connected by 180° turns (also called *U turns*). Turns cause flow separation/reattachment and induce secondary flows so convective heat transfer coefficients exhibit high local variations with consequently increased wall thermal stresses.

By using a heated thin foil made of three joined printed circuit boards (each 600 mm long and total length 1800 mm), Astarita and Cardone [10] obtain local heat transfer measurements in a 180° sharp turn of a square channel (side, $D = 80$ mm). The Reynolds number Re , based on the fluid bulk velocity and hydraulic diameter D , ranges from 16,000 to 60,000 and the ratio between D and the thickness of the partition wall between the two adjacent ducts is equal to 5. The quite large channel side is justified for two reasons, that is, to have a high data spatial resolution and to reduce the contribution of tangential conduction within the sensor. The reference temperature chosen for (8) is the local flow bulk temperature which is evaluated by measuring the inlet temperature and by making a one-dimensional energy balance along the channel, that is, along the channel main axis, with considered triangular heating sections in the turning zones.

Heat transfer coefficients are obtained from IR measurements and (8) for the channel heated from both sides and presented in terms of the normalised local Nusselt number Nu/Nu^* (which can be considered also as h/h^*). Nu^* and h^* are, respectively, the Nusselt number and the convective heat transfer coefficient values predicted by the Dittus and Bölder correlation for fully developed channel flows as interpreted by Kakac et al. [11]:

$$Nu^* = 0.024Re^{0.8}Pr^{0.4}. \quad (13)$$

Because of the low value of the pertinent Biot number (which, in the worst case, is appraised to be less than 0.01), the wall temperature is measured on the back side of the sensor where copper tracks are placed. Raw data is corrected for radiation, anisotropic tangential conduction [3], and natural convection at the back of the sensor, which is evaluated with an accurate calibration.

The normalised local Nusselt number distributions for three values of the Reynolds number Re are presented in Figure 8. The flow enters the duct from the left channel (inlet) and exits from the right one (outlet). In the inlet channel, the flow is quasifull/developed dynamically and thermally, so the heat transfer coefficient is slightly lower than that predicted by the Dittus and Bölder correlation. The flow field in the turn region, and downstream from it, appears to be highly three-dimensional and the Nu maps show zones with a relatively low heat transfer coefficient, corresponding to recirculation bubbles, as well as zones with high heat transfer coefficient, which are due to flow reattachment and/or to an increase in the flow's mean turbulence level, as well as flow impingement after turning.

A first recirculation bubble is located just before the first outer corner (upper left) and attached to the external wall. Two other regions with relatively low heat transfer coefficient may be noticed, the first near the tip of the partition wall and the second by the end wall at about the outlet channel axis. It is also possible to notice three high heat transfer zones: the first situated near the end wall; the second located below the second outer corner and extending for about 3 diameters; the third situated at about 2 diameters after the second inner corner and attached to the partition wall. They are due to the jet effect of the flow through the bend.

At the two higher Reynolds numbers (30,000 and 60,000), the Nusselt number distributions in the outlet channel and just after the turn show a region, about 1 diameter in length

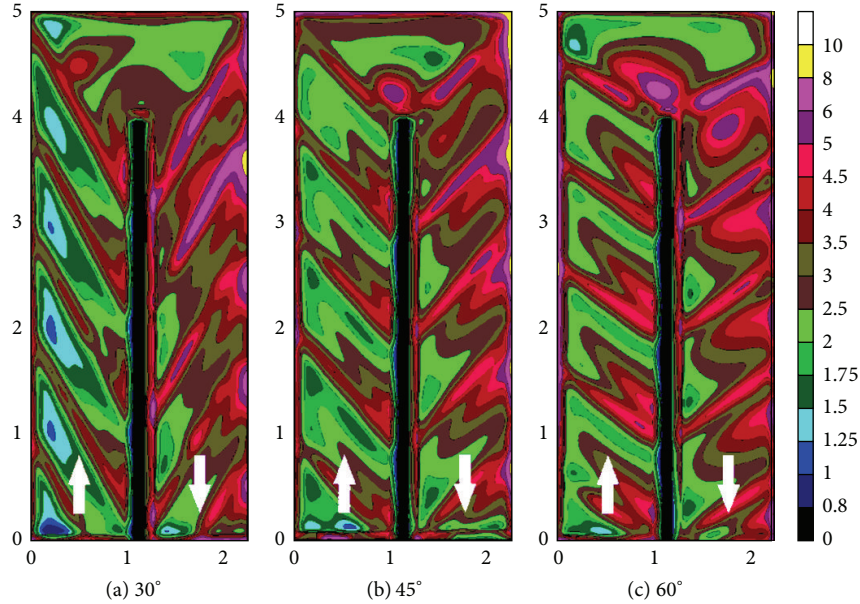


FIGURE 9: Nu/Nu^* distribution for a channel with superimposed ribs, $Re = 30,000$, symmetric heating, $p/e = 10$, and various rib angles δ ; adapted from Astarita et al. [13].

and very slim, of relatively low local convective heat transfer. This is attributed by the authors to the formation, just after the turn, of four vortices, clearly shifted towards the external wall. However, the highest Nu/Nu^* enhancement, which is present downstream of the second outer corner, occurs at the lowest Re because of the higher relative importance of the turbulence induced by the turn.

Rib turbulators, often attached to the blade heat exchanging walls, enhance the convective heat transfer efficiency and completely modify the channel flow field as well as the heat transfer distribution. With a single rib normal to the flow, the mainstream first separates, generating a recirculation zone ahead of the rib, and then reattaches over the rib itself. The further separation, occurring just after the rib, creates a second recirculation zone followed by another reattachment at the duct wall. If several ribs exist and their pitch is sufficiently large with respect to the rib height, these main flow features do not change and reoccur along the duct. Naturally, the presence of the ribs enhances the overall convective heat transfer coefficient both for the increased turbulent level they induce and for the effects associated with the reattachments.

For the channel described above, Carlomagno et al. [12], Astarita et al. [13, 14], and Astarita and Cardone [15] present detailed quantitative maps of the heat transfer distribution obtained with linear angled and V-shaped rib turbulators. Ribs are made of aluminium and have a square cross section 8 mm on a side (i.e., with a ratio between the duct side and rib height $D/e = 10$), joined to the heat exchanging walls at an angle between 30° and 60° with respect to the duct axis. For reasons reported later, orthogonal ribs are less efficient and not tested. Two rib pitches p , two rib arrangements (superimposed or staggered), two heating conditions (from one or both channel sides), and three values of the Reynolds

number, varying from 16,000 to 60,000, are investigated, but only data relative to superimposed ribs and heating from both channel sides are herein reported. Raw data is corrected as indicated above.

The two-dimensional maps of the local normalised Nusselt number Nu/Nu^* , for the superimposed rib arrangement, $p/e = 10$, symmetrical heating, and rib angle δ equal to either 30° or 45° or 60° are shown in Figure 9 for $Re = 30,000$ [13]. In the normalised Nu maps, ribs are clearly visible due to the higher heat transfer rate occurring over them. Indeed, the higher value of the normalised Nusselt number over the ribs is a consequence of their higher effective heat transfer surface (i.e., fin effect) and of the flow reattachment there.

Owing to the high local thermal stresses which are difficult to avoid, there is a partial detachment of the ribs glued to the wall resulting in lower local Nu/Nu^* value. For example, this effect is clear on both the last rib of the inlet duct and the first rib of the outlet duct, near the partition wall, for $\delta = 45^\circ$ and 60° (Figures 9(b) and 9(c)). The authors believe that this has a little influence on the local nearby data but highlight that the reported event is easily revealed by IR thermography. Upstream of the turn, the thermal pattern in the inlet duct appears to be recurring (a kind of thermally fully developed flow) except for some edge effects at duct entrance (which are found also at channel exit), linked to strong tangential conduction due to dissimilar nearby zones, there. The maps also show that the sharp turn already induces a slight change in the shape of the contour lines just before the last rib of the inlet duct.

The rib angle causes secondary flows under the form of two counterrotating vortices in the channel cross section; see also Figure 12 relative to a rotating channel, where, for the present case, the trailing wall has to be regarded as the external wall and the leading one as the partition wall. In

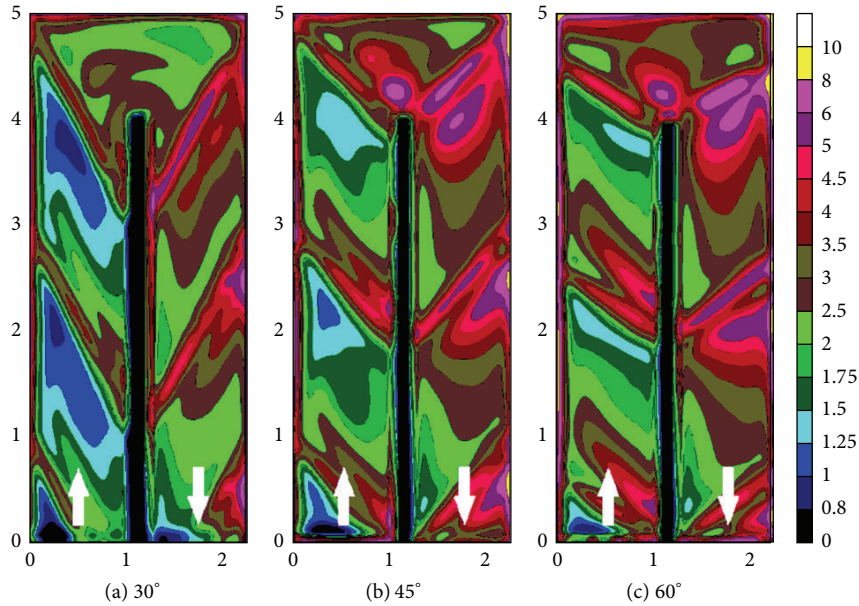


FIGURE 10: Nu/Nu^* distribution for a channel with superimposed ribs, $Re = 30,000$, $p/e = 20$, and various rib angles δ ; adapted from Astarita et al. [13].

the inlet duct, the main flow nearby both the bottom and top walls, entrapped by the ribs, is accelerated towards the external wall (left side of the figure). The two secondary flows after licking this wall merge and go back, via the duct central zone, to the partition wall so as to practically generate a jet which impinges onto the latter. This explains the ribwise Nu/Nu^* asymmetry. In fact, the jet presence tends to increase heat transfer near the partition wall with respect to that at the external one. So, colder fluid is pumped from the channel centre towards the heat exchanging walls. By increasing δ , both the asymmetry of Nusselt number distribution and the averaged Nu/Nu^* value become more evident, due to the increased strength of the secondary flows. Naturally, the latter ones do not exist for ribs normal to the channel axis. The maps show also that, towards channel exit, secondary flows (that are reversed) enhance heat transfer near the external wall (right side of the figure) with respect to that near the partition wall.

In the inlet duct, the reattachment downstream of the ribs can be identified as the locus of the normalised Nusselt number local maxima when moving in streamwise direction. The increase of reattachment distance by moving towards the external wall is most likely due to the interaction of the main flow with the secondary one. For the lowest δ value, going towards the left wall of the inlet channel, the reattachment line between ribs appears to vanish and a relatively large low heat transfer zone completely fills the wall leftmost part. Most probably towards the channel left side, owing to the relatively small distance between two successive ribs, the main flow, interacting with the secondary one, is not able to reattach in the zone between them so that it reattaches directly over the top of the following rib. The separation zone after each rib is strongly influenced by the secondary flow impingement towards the partition wall. On the other hand, the separation zone ahead of each rib remains clearly visible and it is not

much affected by the secondary flow, its width remaining practically constant along the rib. The separation zone after each rib, which should be confined between the rib and the reattachment line, has an indeterminate shape because of the asymmetry of the normalised Nusselt number contours. Towards the right wall, the reattachment line is very close to the preceding rib; thus the separation zone is small; moving towards the left wall, its size increases and for $\delta = 30^\circ$, as already mentioned, tends to occupy the whole zone between ribs. For $\delta = 60^\circ$, the separation zone ahead of each rib is quite clearly visible and does not appear to be strongly influenced by the secondary flow while, for $\delta = 45^\circ$, it splits in two different low Nu/Nu^* zones, becoming practically indistinguishable for $\delta = 30^\circ$.

In the turn, the low heat transfer zone attached to the external wall just before the first outer corner, already seen at the smooth channel, is again visible for $\delta = 30^\circ$ and $\delta = 60^\circ$, while, for $\delta = 45^\circ$, the rib presence does not allow its formation. For $\delta = 30^\circ$, the interaction between the secondary flow and the sharp turn produces two high heat transfer zones and, between them, a local minimum just after the last rib, while, for the two larger angles, only one high heat transfer zone is found near the partition wall. At the outlet channel exit, the recurring flow is not completely recovered and the normalised Nusselt number mean values are yet larger compared to those in the inlet channel.

By increasing the rib pitch ($p/e = 20$), the Nusselt number distributions presented in Figure 10 are found. Because of the absence of some ribs in the channel, the secondary flow has a less important effect on the spanwise distribution of the heat transfer coefficient, but the previously discussed main features of the flow are substantially retained.

In the inlet duct downstream of the ribs, the reattachment line shows itself to be moved slightly forward compared to

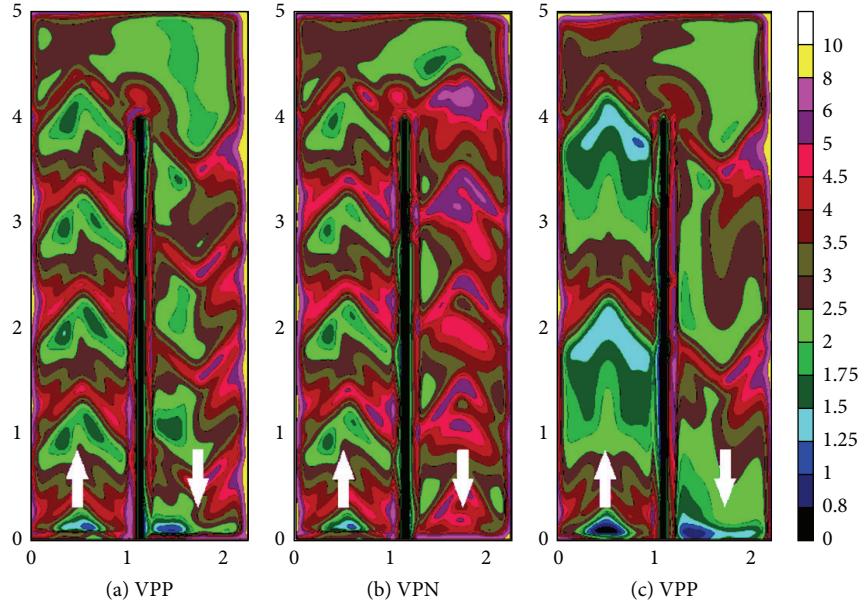


FIGURE 11: Nu/Nu^* distribution for a channel with superimposed ribs, $Re = 30,000$: (a) VPP, $p/e = 10$; (b) VPN, $p/e = 10$; (c) VPP, $p/e = 20$; adapted from Astarita et al. [14].

previous case, although in this configuration too the reattachment distance increases moving towards the external wall. For $\delta = 30^\circ$, the reattachment line does not disappear towards the external wall, as found for $p/e = 10$. The separation zone after the ribs again seems more evident towards the left wall, where a well-defined low heat transfer zone is found. The development of the boundary layer after the reattachment is shown by the downstream decrease of the normalised Nusselt number.

For the two smaller angles, the separation zone ahead of each rib is not easily identified but, towards the left wall, a triangular low heat transfer zone appears, while, for $\delta = 60^\circ$, again an easily detectable separation zone is found.

In the turn zone and outlet channel, the distribution of the normalised Nusselt number, already found for the smaller pitch, is confirmed even if some differences are present and the mean value decreases.

Typical normalised Nusselt number distributions for the V-shaped rib configurations are presented in Figure 11. As it is evident from the Nu/Nu^* maps, ribs have a V shape (with an angle of 45° with respect to the duct axis), their apex always pointing downstream for the VPP configuration (Figures 11(a) and 11(c)), while, only in the outlet duct, for the VPN configuration (Figure 11(b)), the ribs point upstream. For the VPP configuration, two rib pitches are shown in the figure.

In these cases, the secondary flows due to the V-shaped ribs have the form of two pairs of counterrotating cells, which, in the inlet channel for all configurations, produce variations in the spanwise Nusselt number distribution by decreasing heat transfer near the channel axis compared to that towards the side walls. In the outlet channel, the same occurs for the VPP rib configuration while, for the VPN one, the behaviour is obviously reversed.

Again, especially in the inlet duct, the reattachment line downstream of the ribs can be identified by the locus of the normalised Nusselt local maxima. The reattachment distance, which increases for the higher rib pitch, also appears to increase going from the walls towards the channel axis and this is most likely due to the interaction of the main flow with the secondary ones.

In the proximity of the first external corner, it is possible to notice a low heat transfer zone, due to a recirculation bubble as already observed for the previous configurations. Just after the last rib near the partition wall, the interaction between the secondary flow and the sharp turn produces a high heat transfer zone that tends to shift downstream with increasing pitch. For the VPN configuration, the presence of the rib in the turn zone reduces the zone of relatively low convective heat transfer.

3.4. Rotating Channels. The rotation of a channel gives rise to Coriolis forces in the flow and enhances buoyancy forces, which both completely change the flow and the local heat transfer coefficient distribution, as described previously for a static channel. As schematically indicated in Figure 12 [16], in a rotating channel, it is usual to call the wall that goes ahead *leading* and the one that follows *trailing*.

For a radially outward flow, the Coriolis force produces a secondary flow, in the plane perpendicular to the main flow direction, in the form of a pair of counterrotating vortices. The sketch of Figure 12 shows that the secondary flow pushes the fluid particle in the centre of the channel towards the trailing wall, then along the sidewalls, and finally to the leading wall. As regards the static case, these secondary flows enhance heat transfer at the trailing wall compared to that at the leading wall. When the flow is reversed, that is, radially

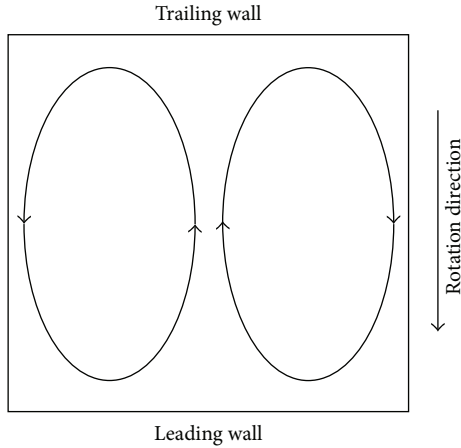


FIGURE 12: Secondary flows in a rotating channel with radially outward flow; adapted from Gallo et al. [16].

inward flow, one has only to change the role played by the leading wall for that of the trailing one and vice versa.

Furthermore, since heat exchange at the wall causes a density difference between the fluid core and that near the wall, the strong centripetal acceleration, which may occur due to rotation, gives rise to a radial buoyant effect. This magnifies the influence of the Coriolis force in the radially outward flow and reduces it (or changes its sign) in the opposite case. Therefore, the velocity gradient at the wall changes and, consequently, the heat transfer coefficient also modifies.

One of the first attempts to measure convective heat transfer coefficients in a rotating air channel with IR thermography is reported by Cardone et al. [17]. The utilized apparatus is a direct consequence of the used heated thin foil sensor. Since the sensor's back surface (which is to be viewed by the IR camera) cannot be thermally insulated, the only way to prevent high external thermal losses by forced convection over this surface is to have the channel rotating in a vacuum chamber. Really, for turbulent flow, the convective heat transfer coefficient from a rotating channel to the ambient fluid is also proportional (with an exponent smaller than unity) to the ambient fluid density. Therefore, a strong reduction of the ambient pressure causes a decrease of the fluid density and, consequently, of the external convective heat transfer coefficient.

The apparatus, represented in Figure 13, consists of a confinement circular chamber (vacuum tank) which contains an arm mounted on a rotating shaft. The tank is 750 mm in diameter and its structure and seals are designed so as to have the tank operating at an absolute pressure below 100 Pa. The rotating arm includes a two-pass square channel, with side of 22 mm and length of 330 mm, which is balanced by a counterweight and fed through the hollow shaft which also provides the air exhaust. To reduce the rotating mass as well as the wall thermal conductance, the walls of the two-pass channel are made of composite material (about 1 mm thick): epoxy resin and Kevlar mat. The thickness of the channel frontal cover, which also constitutes the heated thin foil heat flux sensor, is chosen so as to maintain the deformation

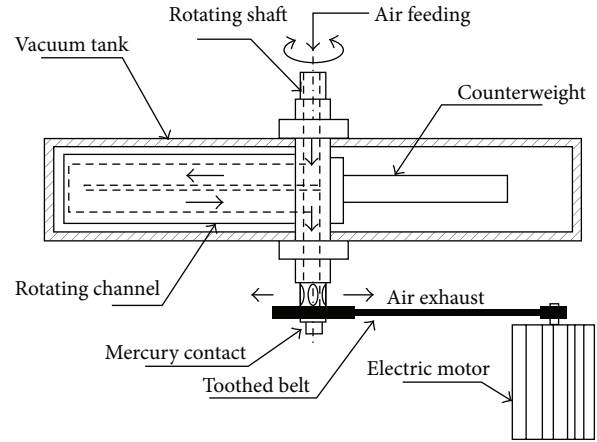


FIGURE 13: Experimental apparatus for a rotating channel of Cardone et al. [17].

(under the effect of the pressure difference between the inside of the channel and the vacuum tank) at less than 0.1 mm. A printed circuit board is used to generate the uniform heating prescribed by the chosen heat flux sensor and it is connected to a stabilized DC power supply via a mercury rotating contact attached to the shaft.

At the time of testing, practically all of the IR cameras commercially available were based on a single thermal detector with an optical scanning mechanism so that the complete frame acquisition frequency was relatively low. Since the channel rotates during the tests and since the frame acquisition frequency of the used infrared system was 15 Hz, it was not possible to take the whole thermal picture in one single shot. For example, at 2,000 rpm, during the time needed for the acquisition of a full frame, the channel would make more than two revolutions around its axis of rotation. To solve this problem, Cardone et al. [17] used the line scan facility of the AGEMA 900 infrared system to take advantage of the much higher acquisition frequency of a line (2,551 Hz). Therefore, adhoc software was developed to reconstruct an averaged (in time) image from multiple line scan acquisitions.

Details of this procedure can be found in the Ph.D. degree thesis by Astarita [18]. In this pioneering work, the spatial resolution of the results turned out to be relatively poor on account of the strong influence of the tangential conduction heat fluxes which are due to the small dimension of the channel ($22 \times 22 \text{ mm}^2$). Therefore, the measured results were not the detailed ones that can be obtained with IR thermography, but this work is reported because it offers a useful option in order to study flows into moving bodies with IR thermography.

A different approach, in order to reduce the relative importance of the external convection with respect to the internal one, was chosen by Gallo et al. [16] to obtain more detailed convective heat transfer coefficient h maps near a 180° sharp turn of a rotating U channel with the heated thin foil sensor. The authors decided to significantly increase h at the sensor's front surface by using water as a working fluid as well as to use a much larger channel in order to reduce

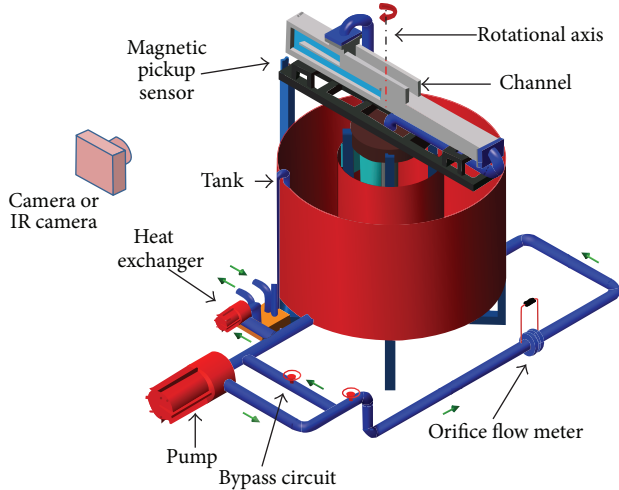


FIGURE 14: Experimental apparatus for a rotating channel of Gallo et al. [16].

its rotational speed and, therefore, q_i at the back surface. In this way, they were able to obtain quite a good spatial resolution and low tangential conduction in the acquired measurements.

The experimental apparatus, represented in Figure 14, consists of a Perspex two-pass water channel with a sharp 180° turn, mounted on a revolving platform whose rotational speed ω can be continuously varied and precisely monitored in the range of $0 \div 60$ rpm. The channel has a square cross section of 60 mm on a side and length of 1200 mm ahead of the 180° , which provides a hydro-/thermodynamically fully developed flow before the turn. The central partition wall dividing two adjacent ducts is 12 mm thick. Water from a tank is pumped through an orifice meter and a rotating hydraulic coupling and, after flowing in the test channel, is discharged back into the tank. Mass flow rate can be varied with a bypass circuit and the inlet to channel water temperature is kept constant with a heat exchanger. A magnetic pick-up allows the synchronization of the IR image acquisition.

The apparatus is capable of simulating both Reynolds number Re and Rotation number $Ro = \omega D/V$ (where ω is the angular speed of the channel) values typical of turbine blades. The D increase and the V decrease (to maintain a given Re) allow a drastic reduction in ω by keeping a constant Ro . Results relative to the static channel (no rotation) well agree with the measurements performed with air by Astarita and Cardone [10], already presented in Figure 8.

In Figure 15(a), the normalised Nusselt number Nu/Nu^* (as earlier defined) distribution over the leading wall, for $Re = 20,000$ and Ro equal to 0.3, is represented. In the inlet duct, the flow appears to be fully developed, also from the thermal point of view, since the normalised Nusselt number is practically constant. The Nu/Nu^* values are lower than those relative to the static case and, following Gallo et al. [16], decrease with the increasing of the rotation number.

In the first half of the first corner, it is possible to notice a high heat transfer zone that is caused by the inversion of the Coriolis force in the turn zone. Really, in the turn

zone, the radial velocity component suddenly decreases and changes sign with a consequent decrease and inversion of the Coriolis force. This inversion makes the flow separate on the trailing side and abruptly reattach towards the leading one, with a strong increase of the normalised Nusselt number at the reattachment point. Other low and high heat transfer zones are clearly visible in the normalised Nusselt number map and their cause is explained in detail by flow field measurements made with particle image velocimetry in the work of Gallo et al. [19].

As it is possible to see from Figure 15(b), the normalised Nusselt number distribution over the trailing wall appears to be completely different from that on the leading wall. In the inlet channel, the Nu/Nu^* values are again uniform but much higher than those for the static case and for the leading wall; besides, as reported by Gallo et al. [16], they tend to increase for increasing rotation number Ro .

In the turn region, it is possible to note that the iso-Nusselt number zone tends to advance into the first corner of the turn and to insinuate in the first half of the second corner. On the second outer corner, it is possible to note a high heat transfer zone that, near the frontal wall, results as being adjacent to a relatively lower heat transfer zone. In the outlet duct, the Nusselt number distribution relative to the trailing wall exhibits two high heat transfer coefficient zones located on the centre and downstream near the partition wall, respectively. Again, the reason for such behaviour can be found in the paper by Gallo et al. [19].

It should be noted that the measurements by Gallo et al. [16] are performed at relatively high Biot number because of the presence of water in the channel and that the heated tracks of the printed circuit are placed on the sensor's back surface for electrical insulation reasons. Therefore, data are reduced according to a special procedure.

3.5. Spray Tubes. Sometimes, to cool leading edges of turbine vanes, a spray tube inside and parallel to them (in aeronautics sometimes called *piccolo tube*), with an array of aligned holes, generates a row of jets which blow cold air to maintain the blade surface temperature below critical values [21]. Piccolo tubes are also amongst the most widely used anti-icing devices for wings and engine nacelles of commercial aircraft [22]. In such devices, hot air is extracted from the compressor and blown on the inner surface of the leading edge through small holes drilled in a pipe. The aim is to supply enough energy to keep the surface at a temperature above the freezing point of water and to liquefy impinging ice crystals. In these devices, the impingement distance is relatively short, this problem being addressed for single jets by Carlomagno and Ianiro [23].

A piccolo tube is experimentally analysed by Imbriale et al. [20]. The test article includes the leading edge of a NACA 0012 wing profile with 1.50 m chord c , with a spray tube located inside at 4% of the chord profile. The profile is 0.20 m spanwise long and it is stopped at about 1/10 of the chord with an open side to facilitate discharge of injected gas so as to avoid recirculation effects. To allow measurements with the heated thin foil sensor, the leading edge section consists

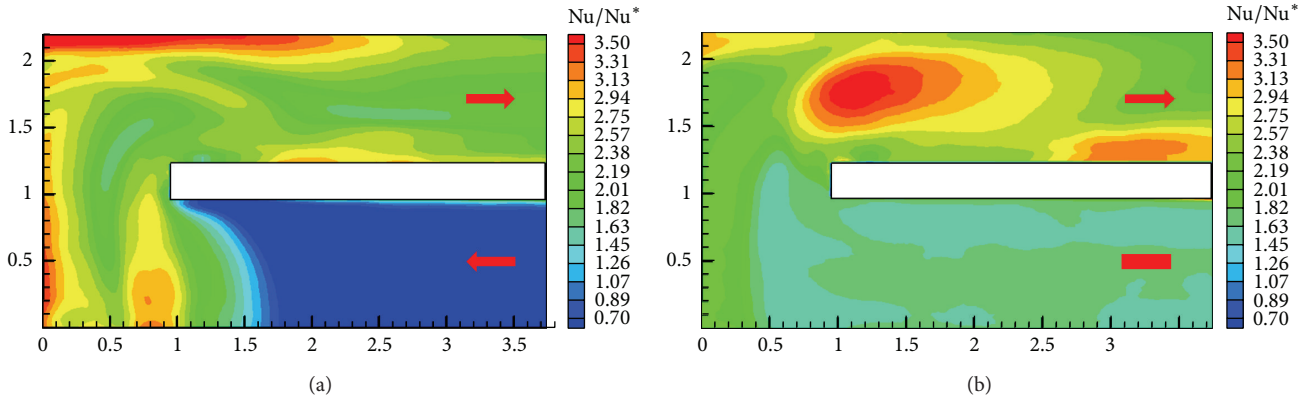


FIGURE 15: Normalised Nusselt number Nu/Nu^* distributions for a smooth rotating channel: (a) leading wall and (b) trailing wall; adapted from Gallo et al. [19].

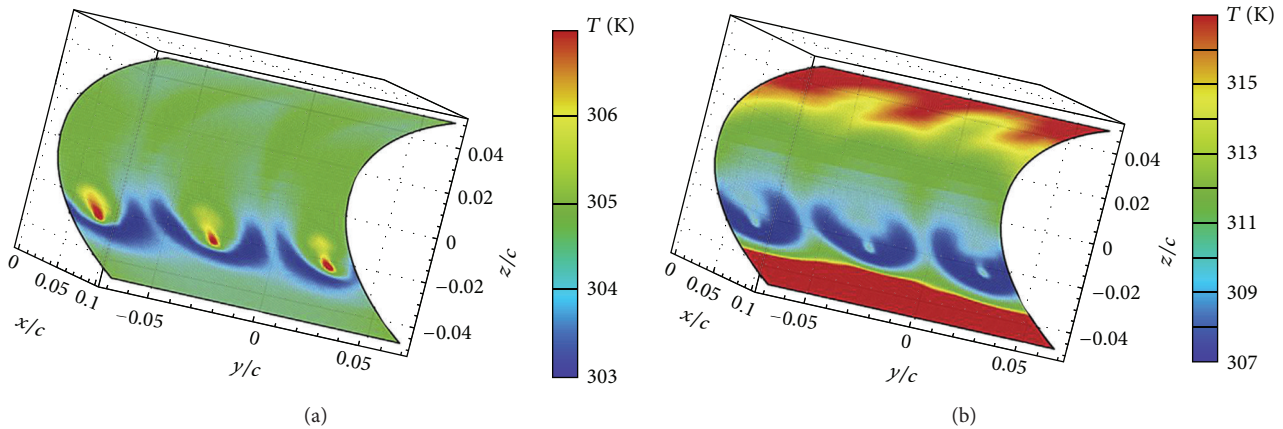


FIGURE 16: 3D temperature reconstruction for $d = 4$ mm, $\phi = 30^\circ$, $M = 1.0$, and $p/d = 15$: (a) adiabatic wall temperature (foil not heated) and (b) wall temperature (heated foil); adapted from Imbriale et al. [20].

of a thin stainless steel sheet ($40 \mu\text{m}$ thick) lodged inside an ad hoc fixture. In particular, different spray tubes are used with a different number of holes from 3 to 5, orifice diameter D from 2 mm to 4 mm, and holes pitch-to-diameter ratio p/D between 5 and 15. In addition, the jet inclination ϕ with respect to airfoil chord is varied from 0° to 50° by rotating the spray tube around its axis. The exit Mach number M is varied from 0.6 to 1.0 and the Reynolds number ($Re = VD/\nu$) is based on the ideal jet exit velocity V . In order to avoid measurement errors due to the surface directional emissivity decay, the camera viewing angle is kept lower than 55° . Raw data is corrected for radiation, tangential conduction within the sensor, and natural convection at the foil viewed side.

Due to the curvature of the viewed surface, to obtain the temperature distribution over the entire leading edge surface, at least two images must be acquired; temperature maps are reconstructed on the object mesh grid according to Cardone et al. [24]. This involves not only a different data reduction, but primarily a geometrical calibration of the IR camera. Then, before performing calculation with (8), the temperature maps of T_w and T_{aw} have to be reconstructed on a 3D mesh grid from the 2D IR images.

An example of such a map reconstruction is presented in Figure 16 for the adiabatic wall temperature T_{aw} (Figure 16(a), foil not heated) and for the wall temperature T_w (Figure 16(b), heated foil), taken for three aligned holes, $d = 4$ mm, inclination angle $\phi = 30^\circ$, $M = 1.0$, and orifice pitch-to-diameter ratio $p/d = 15$. Maps clearly exhibit the jet impingement zones which are not centred with respect to the chord due to the 30° jet inclination and, again, the influence of the relatively high Mach number on the adiabatic wall temperature distribution is recognized.

A typical heat transfer (Nu) distribution, for the same testing conditions of Figure 16, is shown in Figure 17. The impinging jets entail very high Nusselt number values with local peaks in a small region matching with the jets centres; so, these peaks clearly locate the area of jet impingement on the front-side surface. Even though the holes are perfectly circular, the high Nu region somehow stretches in a chordwise direction. This behaviour is due to the jets' inclination with respect to the foil surface. In fact, only jets with inclination ϕ equal to either 0° or 65° are perpendicular to the foil; for other ϕ values, the impingement is affected by inclination effects.

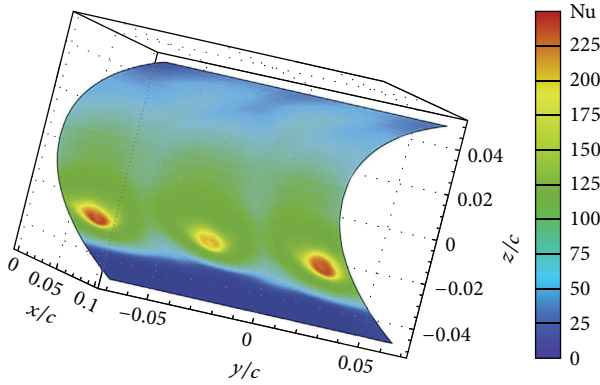


FIGURE 17: Nusselt number reconstruction for $d = 4$ mm, $\phi = 30^\circ$, $M = 1.0$, and $p/d = 15$; adapted from Imbriale et al. [20].

In addition, variations of the Nusselt number distribution are present at the upper back region ($z/c > 0.2$). In particular, it is possible to recognize local Nu increase in the spanwise direction between two contiguous jets, at the same locations where the two green streaks are visible in the wall temperature map of Figure 16(b). This behaviour resembles the fountain effect, already described in literature [25]. However, some fundamental differences regarding position and appearance of such local maxima exist. In fact, the fountain effect, described in literature, is exactly localized between contiguous jets, while, in the present case, local heat transfer maxima seem to originate between jets but they extend and strengthen on the backside region, far from the impingement.

4. Conclusions

The heated-thin-foil technique, associated with the detection of surface temperature by means of infrared thermography, is used to measure the convective heat transfer coefficient in several fluid flow configurations which are relevant to the cooling of gas turbine components, namely, a rotating disk with, or without, a centred impinging jet; the flow in a two-pass smooth (with, or without, rotation), or ribbed, channel with a 180° sharp turn; a spray tube placed inside the leading edge of a turbine blade.

For all the applications shown, the infrared technique adopted has proved its capability to accurately measure the convective heat transfer coefficient distributions in the fluid flows generated by the examined complex geometries and to be a very effective investigation tool for thermo-fluid-dynamic experimental research.

When compared to standard techniques, the use of an infrared camera as a temperature transducer in convective heat transfer measurements appears advantageous from several points of view. In fact, since the IR camera is fully two-dimensional (nowadays, up to more than 1 M pixels per frame), besides producing a whole temperature map, it allows an easier evaluation of errors due to radiation and tangential conduction. Furthermore, the camera is nonintrusive (i.e., it does not disturb the measuring process and allows avoiding conduction through thermocouple or RTD wires). It also

has high sensitivity (down to 10 mK) and low response time (down to 20 ms). As such, IR thermography can be effectively exploited to measure convective heat fluxes even in circumstances where they undergo drastic variations.

Finally, it has to be pointed out that the concurrent use of infrared thermography with the particle image velocimetry (PIV) technique is of great help in the understanding of a thermo-fluid-dynamic phenomenon, especially when exploiting tomographic PIV [23].

The potential of tomographic PIV already allows for quite detailed inspection and characterization of flow physics. In fact, time resolved tomographic PIV has been already applied to water jets [26] and some technical developments may also permit relatively inexpensive exploitation of instrumentation [27]. At the same time, the application of high speed measurements to air flows is limited by the laser power and speed, even if solutions for high speed volumetric measurements in air have been proposed and are being improved [28]. However, it has to be pointed out that tomographic PIV is far from having reached its final development and assessment stage. Researchers are working on the enhancement of spatial resolution and measurement accuracy [29] which could undoubtedly also produce further comprehensive benchmarks for computational methods. Some thermographic measurements, concurrently performed with standard PIV, have already appeared in [19].

Symbols

Roman Letters

- a : Constant (9)
- c : Airfoil chord
- c_p : Fluid specific heat at constant pressure
- C_1 : First radiation constant
- C_2 : Second radiation constant
- D : Channel side, Nozzle diameter
- e : Rib height
- E_b : Emissive power of black body
- I : Spectral emissive power
- h : Convective heat transfer coefficient
- k : Fluid thermal conductivity coefficient
- p : Pitch
- q : Heat flux
- r : Radial coordinate
- s : Sensor thickness
- T : Temperature
- V : Fluid velocity
- x : Coordinate
- y : Coordinate
- z : Coordinate, Nozzle-to-plate distance.

Greek Letters

- α_p : Absorptivity coefficient
- δ : Rib Angle
- ε : Emissivity coefficient

Φ : Dimensionless parameter (10)
 λ : Wavelength of electromagnetic wave
 ν : Fluid kinematic viscosity coefficient
 ρ_r : Reflectivity coefficient
 σ : Stefan-Boltzmann constant
 τ_r : Transmissivity coefficient
 ϕ : Jet inclination to airfoil chord
 ω : Angular speed.

Subscripts

a : Ambient
 aw : Adiabatic wall
 b : Black body
 c : Convective
 l : Loss
 o : At disk centre
 r : Radiative, reference
 t : Tangential
 w : Wall.

Apices

m : At maximum emissive power
 $*$: As per Dittus and B lter correlation.

Dimensionless Groups

Bi : Biot number, hs/k_s
 M : Mach number
 Nu : Nusselt number, hD/k
 Nu_r : Local Nusselt number on the disk, hr/k
 Pr : Prandtl number, $c_p\mu/k$
 Re : Reynolds number, VD/ν
 Re_r : Local Reynolds number on the disk, Vr/ν
 Ro : Rotational number, $\omega D/V$.

Conflict of Interests

The authors declare that there is no conflict of interests regarding the publication of this paper.

References

- [1] K. G. Kyprianidis, "Future aero engine designs: an evolving vision," in *Advances in Gas Turbine Technology*, E. Benini, Ed., chapter 1, pp. 3–24, InTech, Rijeka, Croatia, 2011.
- [2] T. Astarita, G. Cardone, and G. M. Carlomagno, "On the cooling of gas turbines," *Journal of Flow Visualization and Image Processing*, vol. 8, no. 2-3, pp. 287–302, 2001.
- [3] T. Astarita and G. M. Carlomagno, *Infrared Thermography for Thermo-Fluid-Dynamics*, Springer, Berlin, Germany, 2013.
- [4] G. Carlomagno, L. de Luca, G. Cardone, and T. Astarita, "Heat flux sensors for infrared thermography in convective heat transfer," *Sensors*, vol. 14, no. 11, pp. 21065–21116, 2014.
- [5] G. Cardone, T. Astarita, and G. M. Carlomagno, "Infrared heat transfer measurements on a rotating disk," *Optical Diagnostics in Engineering*, vol. 1, pp. 1–7, 1996.
- [6] G. Cardone, T. Astarita, and G. M. Carlomagno, "Heat transfer measurements on a rotating disk," *International Journal of Rotating Machinery*, vol. 3, no. 1, pp. 1–9, 1997.
- [7] T. Astarita, G. Cardone, and G. M. Carlomagno, "Spiral vortices detection on a rotating disk," in *Proceedings of the 23rd Congress of the International Council of the Aeronautical Sciences (ICAS '02)*, Paper no. ICAS2002-3.6.4, 2002.
- [8] K. Millsaps and K. Pohlhausen, "Heat transfer by laminar flow from a rotating-plate," *Journal of the Aeronautical Sciences*, vol. 19, pp. 120–126, 1952.
- [9] T. Astarita and G. Cardone, "Convective heat transfer on a rotating disk with a centred impinging round jet," *International Journal of Heat and Mass Transfer*, vol. 51, no. 7-8, pp. 1562–1572, 2008.
- [10] T. Astarita and G. Cardone, "Thermofluidynamic analysis of the flow in a sharp 180° turn channel," *Experimental Thermal and Fluid Science*, vol. 20, no. 3-4, pp. 188–200, 2000.
- [11] S. Kakac, R. K. Shah, and W. Aung, *Handbook of Single Phase Flow Convective Heat Transfer*, Wiley, New York, NY, USA, 1987.
- [12] G. M. Carlomagno, T. Astarita, and G. Cardone, "Convective heat transfer and infrared thermography," *Annals of the New York Academy of Sciences*, vol. 972, pp. 177–186, 2002.
- [13] T. Astarita, G. Cardone, and G. M. Carlomagno, "Convective heat transfer in ribbed channels with a 180° turn," *Experiments in Fluids*, vol. 33, no. 1, pp. 90–100, 2002.
- [14] T. Astarita, G. Cardone, and G. M. Carlomagno, "Infrared thermography: an optical method in heat transfer and fluid flow visualisation," *Optics and Lasers in Engineering*, vol. 44, no. 3-4, pp. 261–281, 2006.
- [15] T. Astarita and G. Cardone, "Convective heat transfer in a square channel with angled ribs on two opposite walls," *Experiments in Fluids*, vol. 34, no. 5, pp. 625–634, 2003.
- [16] M. Gallo, T. Astarita, and G. M. Carlomagno, "Heat transfer measurements in a rotating two-pass square channel," *Quantitative InfraRed Thermography Journal*, vol. 4, no. 1, pp. 41–62, 2007.
- [17] G. Cardone, T. Astarita, and G. M. Carlomagno, "Wall heat transfer in static and rotating 180° turn channels by quantitative infrared thermography," *Revue G n rale de Thermique*, vol. 37, no. 8, pp. 644–652, 1998.
- [18] T. Astarita, *Alcuni aspetti di scambio termico nelle turbine a gas [Ph.D. thesis]*, Universita di Napoli, Naples, Italy, 1996, (Italian).
- [19] M. Gallo, T. Astarita, and G. M. Carlomagno, "Thermo-fluid-dynamic analysis of the flow in a rotating channel with a sharp 'u' turn," *Experiments in Fluids*, vol. 53, no. 1, pp. 201–219, 2012.
- [20] M. Imbriale, A. Ianiro, C. Meola, and G. Cardone, "Convective heat transfer by a row of jets impinging on a concave surface," *International Journal of Thermal Sciences*, vol. 75, pp. 153–163, 2014.
- [21] H. Iacovides and B. E. Launder, "Internal blade cooling: the Cinderella of computational and experimental fluid dynamics research in gas turbines," *Proceedings of the Institution of Mechanical Engineers, Part A: Journal of Power and Energy*, vol. 221, no. 3, pp. 265–290, 2007.
- [22] T. Cebeci and F. Kafyke, "Aircraft icing," *Annual Review of Fluid Mechanics*, vol. 35, pp. 11–21, 2003.
- [23] G. M. Carlomagno and A. Ianiro, "Thermo-fluid-dynamics of submerged jets impinging at short nozzle-to-plate distance:

- a review,” *Experimental Thermal and Fluid Science*, vol. 58, pp. 15–35, 2014.
- [24] G. Cardone, A. Ianiro, G. dello Ioio, and A. Passaro, “Temperature maps measurements on 3D surfaces with infrared thermography,” *Experiments in Fluids*, vol. 52, no. 2, pp. 375–385, 2012.
- [25] H. Iacovides, D. Kounadis, B. E. Launder, J. Li, and Z. Xu, “Experimental study of the flow and thermal development of a row cooling jets impinging on a rotating concave surface,” *Journal of Turbomachinery, Transactions of ASME*, vol. 127, no. 1, pp. 222–229, 2005.
- [26] D. Violato, A. Ianiro, G. Cardone, and F. Scarano, “Three-dimensional vortex dynamics and convective heat transfer in circular and chevron impinging jets,” *International Journal of Heat and Fluid Flow*, vol. 37, pp. 22–36, 2012.
- [27] S. Discetti, A. Ianiro, T. Astarita, and G. Cardone, “On a novel low cost high accuracy experimental setup for tomographic particle image velocimetry,” *Measurement Science and Technology*, vol. 24, no. 7, Article ID 075302, 2013.
- [28] S. Ghaemi and F. Scarano, “Multi-pass light amplification for tomographic particle image velocimetry applications,” *Measurement Science and Technology*, vol. 21, no. 12, Article ID 127002, 2010.
- [29] F. Scarano, “Tomographic PIV: principles and practice,” *Measurement Science and Technology*, vol. 24, no. 1, Article ID 012001, 2013.

Research Article

Effect of Chamfer Angle on the Calibration Curves of Five Hole Probes

Nekkanti Sitaram and Kancherla Srikanth

Thermal Turbomachines Laboratory, Department of Mechanical Engineering, IIT Madras, Chennai 600 036, India

Correspondence should be addressed to Nekkanti Sitaram; nsitaram.iitm@gmail.com

Received 30 May 2014; Accepted 28 August 2014; Published 15 September 2014

Academic Editor: Takayuki Matsunuma

Copyright © 2014 N. Sitaram and K. Srikanth. This is an open access article distributed under the Creative Commons Attribution License, which permits unrestricted use, distribution, and reproduction in any medium, provided the original work is properly cited.

Five hole probes are extensively used for measurement of total and static pressures, flow angles, velocity and its components in turbomachinery, and other aerodynamic flows. Their operating range is usually limited to 30–40° depending on the type of the probe head. The chamfer angle of the probe is usually taken around 45°. Recent studies on three hole probes have shown that 30° chamfer angle is desirable for unsteady flow measurements. Hence the present investigation is undertaken to find the optimum chamfer angle of five-hole probes. A special five-hole probe of 9.6 mm head diameter and 3 mm diameter pressure take off tubes was designed and fabricated. The large size of the probe was chosen to minimize machining inaccuracies. The probe chamfer angle was varied from 30° to 60° in 5° steps. For each of the chamfer angles, the probe was calibrated in the range of –30° to +30° in 5° interval and the calibration curves are presented. In addition the sensitivities of the calibration coefficients are determined. It is concluded that five-hole probe with a chamfer angle 30° has large operating range, while five-hole probe with a chamfer angle of 50° has good sensitivity.

1. Introduction

In general flow can be analysed by three techniques, namely, flow visualization, computational methods, and measurements of flow parameters. Computational methods are expensive to develop and use. Flow visualization techniques serve only to locate flow regions of interest. Obtaining quantitative data often requires direct measurement of the flow. One such method of direct measurement is by inserting multihole pressure probes into the flow.

Multihole pressure probes have been conveniently used to determine static and total pressures and flow angles in two mutually perpendicular planes (named yaw and pitch planes) in three-dimensional flow fields with suitable calibrations. From these four flow parameters, flow velocity and its three components can be determined. Multihole pressure probes thus combine the means for simultaneous measurement of total, static, and dynamic pressures and flow directions with one instrument. When designing a pneumatic probe that is to be used for flow measurements, the effects of blockage, frequency response, pressure hole size and geometry, the local

Mach and Reynolds numbers, and the relative scale of the phenomenon under investigation must be specified.

For measuring three-dimensional flows, multihole probes with four, five, seven, or even higher number of pressure holes strategically placed on aerodynamic bodies such as sphere, hemisphere, and prism can be used. In principle a four-hole probe can measure the four quantities that are required to completely define the flow. However for the sake of symmetry in both yaw and pitch planes, five hole probes are usually employed. When the yaw and pitch angles of the flow exceed the usual operating range of five hole probes, seven hole probes or probes with larger number of holes are employed.

Five hole probes Treaster and Yocum [1] are extensively used for measurement of total and static pressures, flow angles, velocity and its three components in highly complex and three-dimensional turbomachinery, and other aerodynamic probes. Five hole probes also find applications in other flows (automotive wheel arch flow, Malviya et al. [2], supersonic flow measurements, Naughton et al. [3] and Milanovic and Kalkhoran [4]). Five hole probes also find novel applications, such as measurement of skin friction in

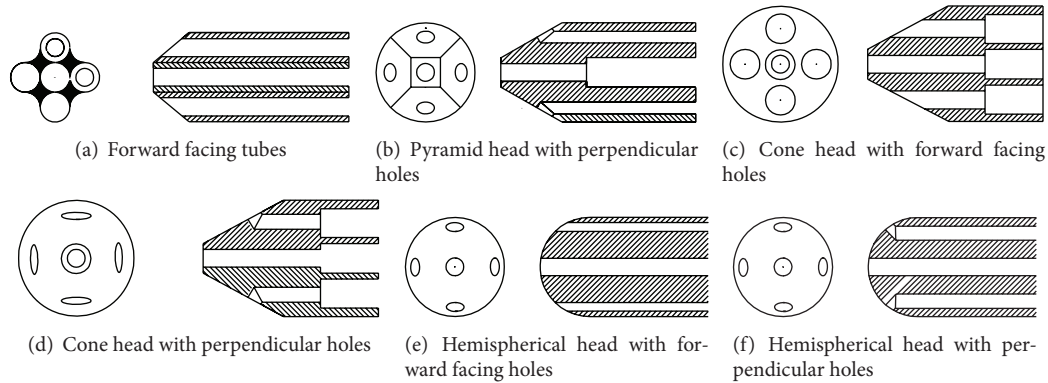


FIGURE 1: Geometry of five-hole probe heads Dominy and Hodson [10].

complex two- and three-dimensional flows Lien and Ahmed [5]. Recently Telionis et al. [6] had made a comprehensive survey of multihole pressure probes for flow measurements.

The shape of the head of the five-hole probe can vary widely as shown in Figure 1. Probes with forward facing tubes are usually inexpensive and can be fabricated in miniature size (about 1.22 mm diameter tip, Ligrani et al. [7]). However their operating angle is usually limited to 30° , while the operating range of probes with perpendicular holes is limited to 40° Pisasale and Ahmed [8]. The limitation is due to the value of denominator, D , becoming very small, zero or negative, when yaw or pitch angle exceeds a certain value. In such case, the calibration coefficients become very large or singular or changes sign. The chamfer angle of the probe is usually taken as 45° (or in the range of $40\text{--}50^\circ$). But recent studies on three hole probes Díaz et al. [9] have shown that 30° chamfer angle is desirable for unsteady flow measurements. Hence the present investigation is undertaken with the objective of determining the effect of chamfer angle on the calibration curves of five hole probes to find the optimum chamfer angle. To the best of the knowledge of the authors, no such systematic investigations are undertaken. Dominy and Hodson [10] had calibrated three conical probes with perpendicular holes. The cone angles of the probes were 45, 60, and 90° , respectively, corresponding to chamfer angles of 67.5, 60, and 45° . However they had not examined the effect of chamfer angle on the calibration coefficients and their sensitivity.

2. Design and Fabrication of Five-Hole Probe

2.1. Five-Hole Probe. A 9.6 mm diameter five-hole probe was fabricated with the tip of the probe shaped as truncated cone. The probe was made of a 9.6 mm brass rod with five holes of 3 mm diameter drilled in a + format with a clearance of 0.15 mm between the holes and outer circumference. Five 3 mm diameter stainless steel tubes were fitted tightly into these holes. The diameter of the tubes was reduced slightly by grinding, so that the tubes would fit into the holes. The tubes were silver brazed to the brass body at the rear end with 10–15 mm of the tubes exposed. Plastic tubes were fitted to the exposed ends of the tubes. Among the five tubes, one

forward-facing tube was at the centre, two chamfered side tubes were on the horizontal axis, and remaining two side tubes were on the vertical axis as shown in Figure 2. The tubes and the brass body were integral and machined together to change the chamfer angle of the probe. The design deviated from the usual design of integral probe head and stem to facilitate easy machining of the probe head to the required chamfer angle.

2.2. Probe Holder and Support. The probe support was made up of stainless steel (SS) material. The probe support consisted of a 9.6 mm diameter SS tube of 400 cm long is attached to a 12.7 mm hexagonal rod. A hole of 9.6 mm diameter was centrally drilled in the hexagonal rod. A small tube was perpendicularly silver brazed to the hexagonal rod. A M3 tapped hole was drilled in the center of the small tube to position the probe and to hold the probe tightly. The probe holder and support are shown in Figure 3.

3. Calibration Tunnel and Calibration Device

3.1. Calibration Tunnel. The probe was calibrated in the calibration tunnel available in Thermal Turbomachines Laboratory of Department of Mechanical Engineering. The probe was fixed so that its head is at the center of calibration section to minimise boundary layer and duct wall effects. A photo of the calibration tunnel is shown in Figure 4.

3.2. Calibration Device. The calibration device was mounted on the calibration section of the calibration tunnel. The probe was mounted in the central hole of the calibration device with the probe tip at the centre of the axis of the calibration tunnel. The calibration device has provisions to change the yaw angle in the range of $\pm 180^\circ$, at an interval of 1° , and pitch angle of the probe in the range of $\pm 30^\circ$, at an interval of 1° . The probe can be rotated in both clockwise and anticlockwise directions to change the yaw angle with the help of a rotating mechanism fitted onto the calibration device. It is desirable to carry out the calibrations in the yaw and pitch angle range of -60° to $+60^\circ$. However the pitch angle can be varied only in the range of -30° to $+30^\circ$. Hence the probe was calibrated at a velocity of 25 m/s in yaw and pitch angle range of -30° to

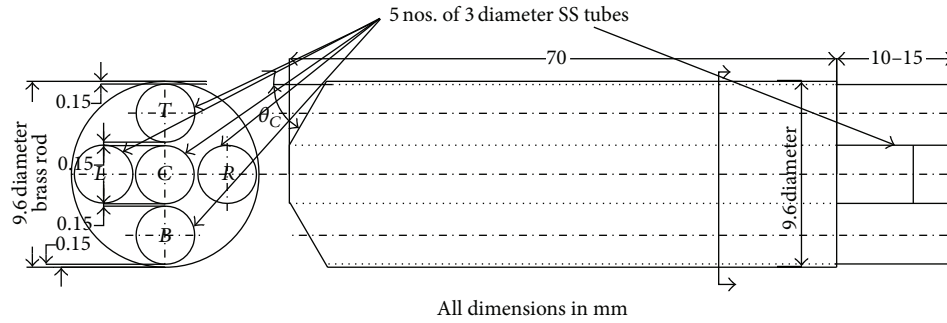


FIGURE 2: AutoCAD drawing of Five-hole probe.

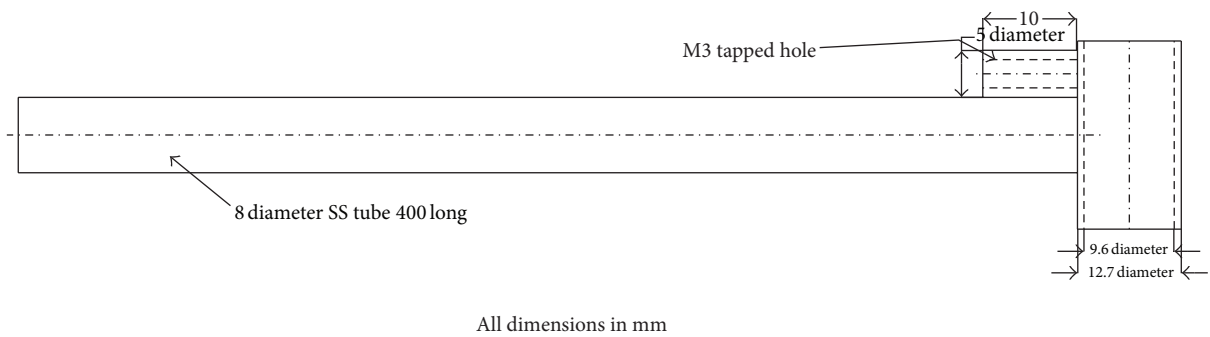


FIGURE 3: Probe holder and support.



FIGURE 4: Calibration tunnel.

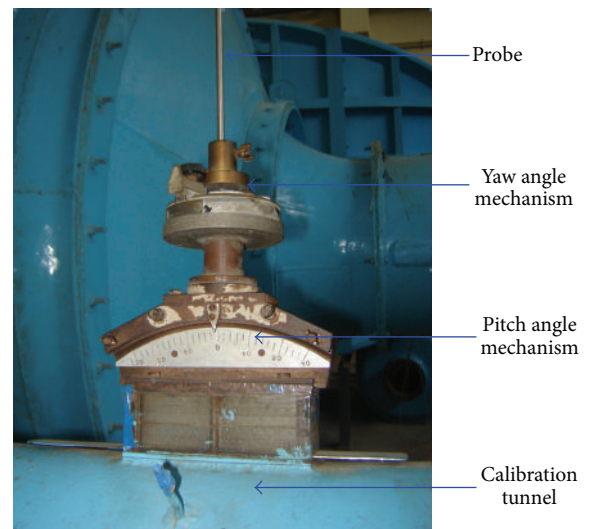


FIGURE 5: Calibration device.

+30° at an interval of 5°. The calibration device is shown in Figure 5.

3.3. *Instrumentation.* The twenty-channel single selection scanning box (model no. FCO 91-3) and FC012 digital micro manometer manufactured by Furness control Ltd., Bexhill, London were used to measure probe pressure. The scanning box has twenty channels, which were numbered sequentially. The pressures to be measured were connected to the numbered inputs. The outlet channel was connected to the micromanometer. A particular channel was selected manually in the scanning box and its corresponding pressure was read from the micromanometer. The micromanometer used has a resolution of 0.1 mm with a range of ±200 mm

of water gauge. The accuracy of the micromanometer is ±0.1 mm of the water column. The output of the scanning box was connected to the micromanometer and it gave reading directly in terms of velocity in m/s or pressure in mm of water gauge. Time constant potentiometer was used to get time averaged pressures.

4. Experimental Procedure and Programme

4.1. Experimental Procedure. The calibration of the five-hole probe for the present experimental investigation was carried out in the low-speed calibration tunnel. Free stream velocity of air was maintained at 25 m/s determined from the settling chamber pressure and calibration section wall static pressure. The five pressure tubes of the probe along with the settling chamber wall static pressure and calibration section wall static pressure taps were connected to a scanning box, which enabled to measure multipressures using just one pressure measuring instrument (digital micromanometer in this case). The fluctuating pressure signals were typically averaged over a period of 5 seconds time to allow for conditions to reach steady-state. Using the calibration device, the pitch and yaw angles of the probe were changed by 5° increment in range of ±30°, respectively. After calibration of the probe at one chamfer angle, the probe was removed from the calibration device and the chamfer angle was changed by machining the probe in a lathe by using the tool bit at the desired angle.

4.2. Experimental Programme. The chamfer angle of the probe was varied systematically from 30 to 60 deg, with gradually increasing chamfer angle at an increment of 5 deg.

This range covers most of the usually used chamfer angles. After completing calibration of the probe with a chamfer angle, the probe chamfer angle was changed by machining the probe in a lathe. The accuracy of the probe chamfer angle is checked in Metrology Laboratory, Department of Mechanical engineering, IIT Madras and was found to be within an accuracy of ±0.2 deg.

5. Results and Discussion

5.1. Sample Data. The pressures measured by the five tubes of the five-hole probe with a chamfer angle of 30° are presented in Figure 6. The pressures are nondimensionalised with the total pressure and are plotted against the pitch angle. The static pressure measured on the wall of the settling chamber was taken as the total pressure as the magnitude of the dynamic pressure in the settling chamber was very small.

For the sake of clarity, only pressures at three values of yaw angles, namely, -30°, 0°, and 30° are presented. The data are presented to see that the data is following the expected trends. Such data for all chamfer angles are plotted to validate the data. However the data are not presented for the sake of brevity.

As expected pressures measured by the central, left, and right holes show parabolic variation with the pitch angle. At $\alpha = -30^\circ$, P_L is always more than P_C , but P_R always shows the lowest pressure, as this hole is inclined at a large angle to the flow. At $\alpha = 30^\circ$, P_R is always more than P_C , but P_L always shows the lowest pressure, as this hole is inclined at a large angle to the flow. At $\alpha = 0^\circ$, pressures measured by the left and right holes are almost equal at all the pitch angles. Similarly at $\alpha = -30^\circ$ and 30° , pressures measured by the top hole are almost equal at all the pitch angles and these pressures are lower than the corresponding pressures at $\alpha = 0^\circ$. Similar observation is made for pressures measured by the bottom

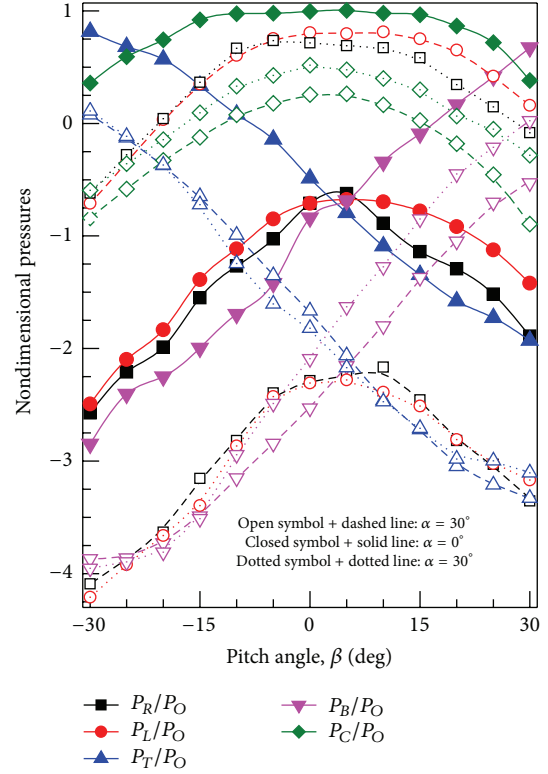


FIGURE 6: Nondimensional probe pressures for chamfer angle of 30°.

hole. Similar observations are made for the probe heads with different chamfer angles, confirming that the chamfer angle is nearly the same for the side pressure tubes.

5.2. Calibration Coefficients of Five-Hole Probe. The pressures measured by the five holes, the calibration tunnel settling chamber pressure, and calibration section wall static pressure at different values of yaw and pitch angle are used to define nondimensional calibration coefficient as follows:

$$\begin{aligned} \underline{P} &= \frac{(P_B + P_T + P_L + P_R)}{4}, \\ D &= P_C - \underline{P}, \\ C_{PYAW} &= \frac{(P_L - P_R)}{D}, \\ C_{PPITCH} &= \frac{(P_T - P_B)}{D}, \\ C_{PTOTAL} &= \frac{(P_O - P_C)}{D}, \\ C_{PSTATIC} &= \frac{(P_S - \underline{P})}{D}. \end{aligned} \quad (1)$$

5.3. Calibration Curves of Five-Hole Probe. The calibration curves are presented as follows for the probe with different chamfer angles:

TABLE 1: Minimum and maximum values and sensitivity of C_{PYAW} .

Chamfer angle	30°	40°	50°	60°
Minimum value	-4.050	-6.00	-16.200	-7.500
Normalized value	1.000	1.481	4.000	1.852
Maximum value	2.380	3.000	6.200	10.700
Normalized value	1.000	1.261	2.605	4.496
Total difference	6.430	9.00	22.400	18.200
Normalized value	1.000	1.400	3.484	2.830
Sensitivity at $\beta = -30^\circ$	0.083	0.140	0.293	0.293
Normalized value	1.000	1.687	3.530	3.530
Sensitivity at $\beta = 0^\circ$	0.058	0.083	0.121	0.107
Normalized value	1.000	1.431	2.086	1.845
Sensitivity at $\beta = 30^\circ$	0.104	0.134	0.362	0.021
Normalized value	1.000	1.288	3.481	0.202

TABLE 2: Minimum and maximum values and sensitivity of C_{PPITCH} .

Chamfer angle	30°	40°	50°	60°
Minimum value	-3.220	-5.800	-12.100	-5.200
Normalized value	1.000	1.801	3.758	1.615
Maximum value	3.020	5.400	15.000	8.000
Normalized value	1.000	1.788	4.967	2.649
Total difference	6.240	11.200	27.100	13.200
Normalized value	1.000	1.795	4.343	2.115
Sensitivity at $\alpha = -30^\circ$	0.081	0.108	0.211	0.140
Normalized value	1.000	1.333	2.605	1.728
Sensitivity at $\alpha = 0^\circ$	0.057	0.077	0.090	0.099
Normalized value	1.000	1.351	1.579	1.737
Sensitivity at $\alpha = 30^\circ$	0.107	0.179	0.438	0.120
Normalized value	1.000	1.673	4.093	1.121

- (1) C_{PYAW} versus C_{PPITCH} for various values of pitch and yaw angles,
- (2) C_{PTOTAL} versus pitch angle for various yaw angles,
- (3) $C_{PSTATIC}$ versus pitch angle for various yaw angles.

These calibration curves are presented and discussed in the following sections.

5.4. Effect of Chamfer Angle on C_{PYAW} versus C_{PPITCH} Calibration Curve of Five Hole Probe. The C_{PYAW} versus C_{PPITCH} calibration curves of the five hole probes with different chamfer angles are presented in Figure 7. The corresponding values of yaw and pitch angles are also shown in the figures. All figures are drawn to the same scale. For the sake of clarity only calibration curves at alternate values of yaw angles are shown. The minimum and maximum values of C_{PYAW} and C_{PPITCH} for different chamfer angles are presented in Tables 1 and 2, respectively. Also the sensitivity values at three yaw and pitch angles, namely, -30 , 0 , and 30 deg, are given. In addition, normalized values of all parameters with respect to the values for the probe with a chamfer angle of 30° are given in Tables 1 and 2.

From Figure 7 and Tables 1 and 2, it is evident that both C_{PYAW} and C_{PPITCH} increase as the probe chamfer angle

increases. As the chamfer angle increases, one of the side tubes measure pressure higher than that of the centre tube at some of the yaw and pitch angles. Hence the value of D becomes smaller, causing the values of C_{PYAW} and C_{PPITCH} to increase rapidly. In fact the value of D can become negative at large values of yaw and pitch angles, limiting the useful range of the probe. For lower values of probe chamfer angles, the values of C_{PYAW} and C_{PPITCH} are comparatively lower. Hence the useful range of yaw and pitch angles for probes with smaller chamfer angle can be more than that for probes with larger chamfer angle. The difference between the minimum and maximum values is also shown in Tables 1 and 2. Again the same trend is observed. As the chamfer angle increases, the side holes sense less of total pressure and more of static pressure. Hence the pressures measured by the side holes will be lesser as the chamfer angle increases. This is a desirable trend. As can be seen from the calibration curves, the range of C_{PYAW} and C_{PPITCH} curves increases as the chamfer angle increases. Hence the change in C_{PYAW} and C_{PPITCH} is higher as the chamfer angle increases. Hence the sensitivity of C_{PYAW} and C_{PPITCH} with yaw and pitch angle increases, giving more accurate interpolated values of yaw and pitch angles as the chamfer angle increases. However this trend is broken when chamfer angle is 55 deg. For this and higher chamfer angles,

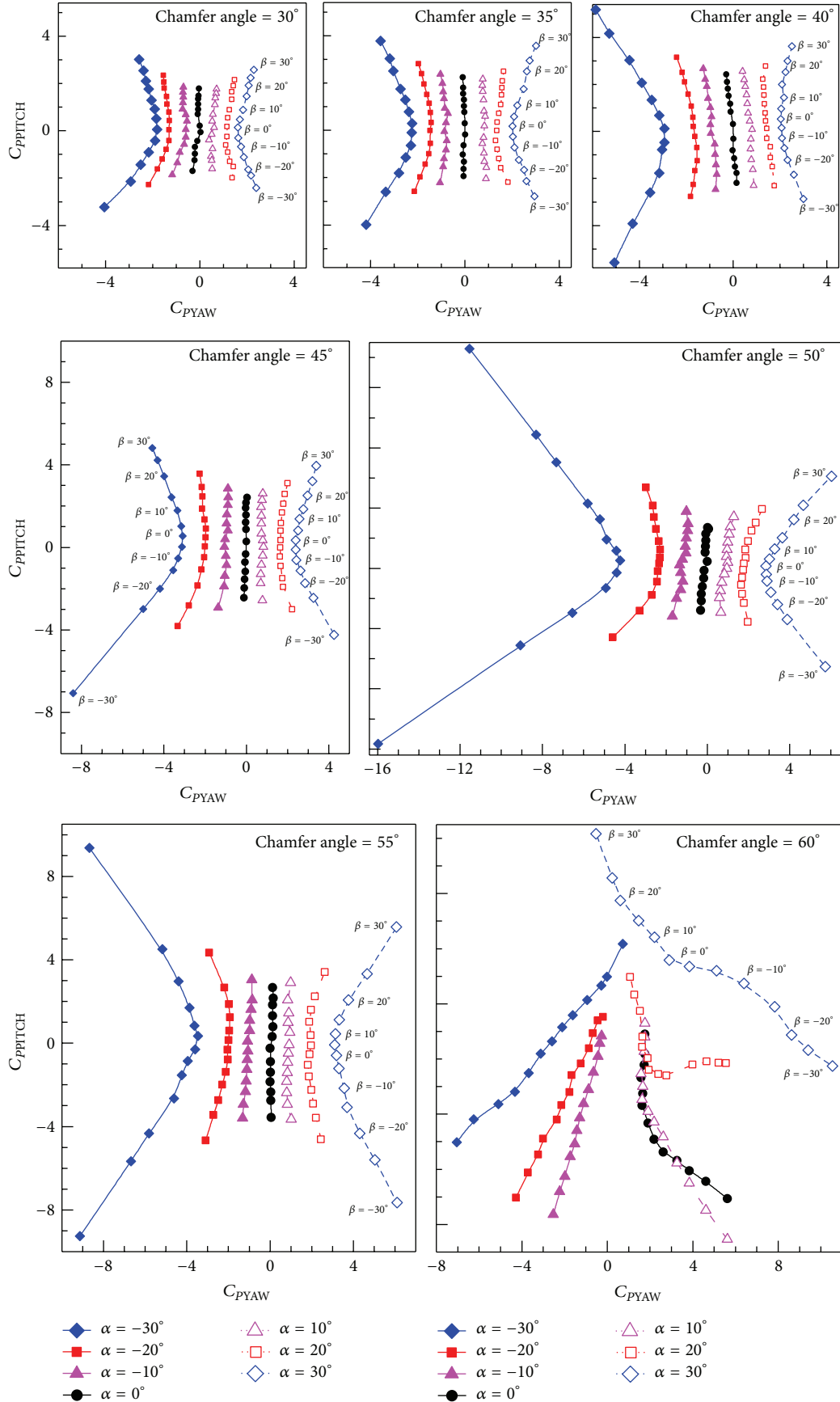


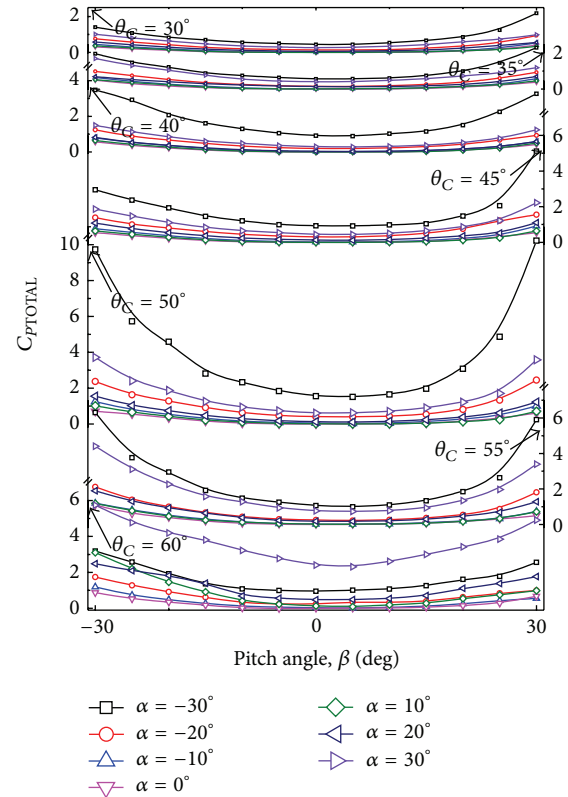
FIGURE 7: Calibration curves: C_{PPITCH} versus C_{PYAW} .

TABLE 3: Minimum and maximum values and sensitivity of C_{PTOTAL} .

Chamfer angle	30°	40°	50°	60°
Minimum value	0.000	0.000	0.000	0.000
Maximum value	2.180	3.500	10.000	6.000
Normalized value	1.000	1.606	4.587	2.752
Total difference	2.180	3.500	10.000	6.000
Normalized value	1.000	1.606	4.587	2.752
Sensitivity at $\beta = -30^\circ$	0.025	0.097	0.301	0.162
Normalized value	1.000	3.880	12.040	6.480
Sensitivity at $\beta = 0^\circ$	0.014	0.030	0.052	0.080
Normalized value	1.000	2.143	3.714	5.714
Sensitivity at $\beta = 30^\circ$	0.058	0.095	0.321	0.141
Normalized value	1.000	1.638	5.534	2.431
Sensitivity at $\alpha = -30^\circ$	0.037	0.040	0.104	0.111
Normalized value	1.000	1.081	2.811	3.000
Sensitivity at $\alpha = 0^\circ$	0.015	0.019	0.023	0.029
Normalized value	1.000	1.267	1.533	1.933
Sensitivity at $\alpha = 30^\circ$	0.059	0.086	0.289	0.074
Normalized value	1.000	1.458	4.898	1.254

the side holes are more parallel to the streamlines. Hence they sense more static pressure. Also the variation of the side hole pressures may not be much as the yaw and pitch angles increase beyond a certain range. Examination of raw pressure data for probes with these chamfer angles shows that one of the side holes is showing flow separation even when the yaw and pitch angles are low. It is quite likely that different definitions of yaw and pitch coefficients are needed for these chamfer angles. Or zonal method developed by Sitaram and Govardhan [11] may be used. This zonal method is similar to the zonal method used for seven hole probes Venkateswara Babu et al. [12] and Everett et al. [13]. The calibration space is divided into five zones. In each of the zones, one of the five pressures is maximum and this pressure is taken as the representative total pressure. Calibration coefficients are defined differently in each of the zones. The zones are extended so that no calibration space is left without calibration coefficients. The measured pressures are examined to find out the maximum pressure and the calibration curves corresponding to this zone are used to determine the four unknowns, namely, static and total pressures and flow angles. Alternatively the definition of D may be changed following Pisasale and Ahmed [8], Pisasale and Ahmed [14], and Pisasale and Ahmed [15].

5.5. Effect of Chamfer Angle on C_{PTOTAL} versus Pitch Angle Calibration Curve of Five-Hole Probe. The C_{PTOTAL} versus pitch angle calibration curves of the five-hole probe with different chamfer angles are presented in Figure 8. These calibration curves are drawn for constant yaw angles. For the sake of clarity only calibration curves at alternate values of yaw angles are shown. All figures are drawn to the same scale. The minimum and maximum values of C_{PTOTAL} for different chamfer angles are presented in Table 3. Also the sensitivity values at three yaw and pitch angles are given. In addition,

FIGURE 8: Calibration curves: C_{PTOTAL} versus β .

normalized values of all parameters with respect to the values for the probe with a chamfer angle of 30° are given in Table 4. The minimum value of C_{PTOTAL} is close to zero, indicating that the central hole is measuring total pressure when the yaw and pitch angles are close to zero.

TABLE 4: Minimum and maximum values and sensitivity of $C_{PSTATIC}$.

Chamfer angle	30°	40°	50°	60°
Minimum value	-0.620	-0.900	-1.500	-2.800
Normalized value	1.000	1.452	2.419	4.516
Maximum value	0.480	0.700	0.900	0.500
Normalized value	1.000	1.458	1.875	1.042
Total difference	1.100	1.600	2.400	3.300
Normalized value	1.000	1.455	2.182	3.000
Sensitivity at $\beta = -30^\circ$	0.017	0.025	0.033	0.043
Normalized value	1.000	1.471	1.941	2.529
Sensitivity at $\beta = 0^\circ$	0.018	0.018	0.03	0.011
Normalized value	1.000	1.000	1.667	0.611
Sensitivity at $\beta = 30^\circ$	0.018	0.019	0.008	0.003
Normalized value	1.000	1.056	0.444	0.167
Sensitivity at $\alpha = -30^\circ$	0.016	0.017	0.022	0.062
Normalized value	1.000	1.063	1.375	3.875
Sensitivity at $\alpha = 0^\circ$	0.016	0.023	0.041	0.031
Normalized value	1.000	1.438	2.563	1.938
Sensitivity at $\alpha = 30^\circ$	0.019	0.031	0.050	0.047
Normalized value	1.000	1.632	2.632	2.474

From Figure 8 and Table 3, it is evident that C_{PTOTAL} increases as the probe chamfer angle increases. The difference between the minimum and maximum values is also shown in Table 3. Again the same trend is observed. The central hole always senses more or less the same pressure for the probes with different chamfer angles. However it is normalized with the dynamic pressure based on the probe pressures. As this value gets reduced the value of C_{PTOTAL} increases as the chamfer angle increases. As the chamfer angle increases, the side holes sense less of total pressure and more of static pressure. Hence the pressures measured by the side holes will be lesser as the chamfer angle increases. This is a desirable trend. As can be seen from the calibration curves, the range of C_{PTOTAL} curves increases as the chamfer angle increases. Hence the change in C_{PTOTAL} is higher as the chamfer angle increases. Hence the sensitivity of C_{PTOTAL} curves with yaw and pitch angle increases, giving more accurate interpolated values of total pressure as chamfer angle increases.

However this trend is broken when chamfer angle is 55 deg. For this and higher chamfer angles, the side holes are more parallel to the streamlines. Hence they sense more static pressure. Also the variation of the side hole pressures may not be much as the yaw and pitch angles increase beyond a certain range. It is quite likely that different definition of C_{PTOTAL} is needed for these chamfer angles. Or alternate techniques described in Section 5.4 may be employed.

5.6. Effect of Chamfer Angle on $C_{PSTATIC}$ versus Pitch Angle Calibration Curve of Five-Hole Probe. The $C_{PSTATIC}$ versus pitch angle calibration curves of the five-hole probe with different chamfer angles are presented in Figure 9. These calibration curves are drawn for constant yaw angles. For the sake of clarity only calibration curves at alternate values of

yaw angles are shown. All figures are drawn to the same scale. The minimum and maximum values of $C_{PSTATIC}$ for different chamfer angles are presented in Table 4. Also the sensitivity values at three yaw and pitch angles are given. In addition, normalized values of all parameters with respect to the values for the probe with a chamfer angle of 30° are given in Table 3.

From Figure 9 and Table 4, it is evident that $C_{PSTATIC}$ increases as the probe chamfer angle increases. The difference between the minimum and maximum values is also shown in Table 4. Again the same trend is observed. The central hole always senses more or less the same pressure for the probes with different chamfer angles. However it is normalized with the dynamic pressure based on the probe pressures. The value of $C_{PSTATIC}$ depends on the average value of side hole pressures which occurs both in the numerator and denominator. As the chamfer angle increases, the side holes sense less of total pressure and more of static pressure. Hence the pressures measured by the side holes will be lesser as the chamfer angle increases. This is a desirable trend. As can be seen from the calibration curves, the range of $C_{PSTATIC}$ curves increases as the chamfer angle increases. Hence the change in $C_{PSTATIC}$ is higher as the chamfer angle increases. Hence the sensitivity of $C_{PSTATIC}$ curves with yaw and pitch angle increases, giving more accurate interpolated values of static pressures as chamfer angle increases. However this trend is broken when chamfer angle is 55 deg. For this and higher chamfer angles, the side holes are more parallel to the streamlines. Hence they sense more static pressure. Also the variation of the side hole pressures may not be much as the yaw and pitch angles increase beyond a certain range. It is quite likely that different definition of $C_{PSTATIC}$ is needed for these chamfer angle. Or alternate techniques described in Section 5.4 may be employed.

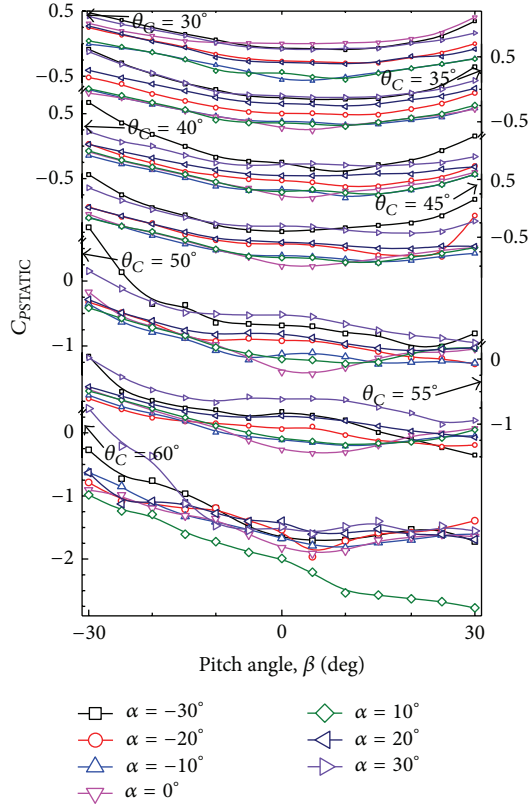


FIGURE 9: Calibration curves: $C_{PSTATIC}$ versus β .

5.7. Effect of Chamfer Angle on Sensitivity of Calibration Coefficients of Five-Hole Probe. The pressure probes used for fluid flow measurements should satisfy two conflicting requirements. They are sensitivity of the probe and operating range of the probe. These conflicting requirements depend on the chamfer angle of the probe head. The present section examines the sensitivity of the probe measurements with yaw and pitch angles. This can be done in two ways: one by examining the sensitivity of the pressures measured by the probe with yaw and pitch angles and the other by examining the sensitivity of the calibration coefficients of the probe with yaw and pitch angles. The second approach is taken in the paper. Ideally the sensitivity has to be determined at all combinations of yaw and pitch angles. While this is possible, it is cumbersome to present and interpret. Hence the sensitivity of various coefficients are examined at three values of yaw and pitch angles, namely, -30° , 0° , and 30° . These values are presented in Tables 1 to 4. However, for the sake of better visibility, they are plotted in Figure 10. The sensitivities of various coefficients are defined as follows:

$$C_{PYAW} : \frac{(C_{PYAW} \text{ at } \alpha = 30^\circ - C_{PYAW} \text{ at } \alpha = -30^\circ)}{60}$$

at constant value of pitch angle,

$$C_{PPITCH} : \frac{(C_{PPITCH} \text{ at } \beta = 30^\circ - C_{PPITCH} \text{ at } \beta = -30^\circ)}{60}$$

at constant value of yaw angle,

$$C_{PTOTAL} : \frac{(C_{PTOTAL} \text{ at } \beta = \pm 30^\circ - C_{PTOTAL} \text{ at } \beta = 0^\circ)}{30}$$

at constant value of yaw angle,

$$C_{PSTATIC} : \frac{(C_{PSTATIC} \text{ at } \beta = \pm 30^\circ - C_{PSTATIC} \text{ at } \beta = 0^\circ)}{30}$$

at constant value of yaw angle,

$$C_{PTOTAL} : \frac{(C_{PTOTAL} \text{ at } \alpha = \pm 30^\circ - C_{PTOTAL} \text{ at } \alpha = 0^\circ)}{30}$$

at constant value of pitch angle,

$$C_{PSTATIC} : \frac{(C_{PSTATIC} \text{ at } \alpha = \pm 30^\circ - C_{PSTATIC} \text{ at } \alpha = 0^\circ)}{30}$$

at constant value of pitch angle.

(2)

Larger value of sensitivity of C_{PTOTAL} and $C_{PSTATIC}$ is used at yaw and pitch angles of -30° or 30° .

From Figure 10, it can be seen that the sensitivity of C_{PYAW} , C_{PPITCH} , and C_{PTOTAL} gradually increases with probe chamfer angle and the maximum value occurs for the probe with a chamfer angle of 50° . As the chamfer angle further increases, the sensitivity of these coefficients decreases. The static pressure coefficient has very low value of sensitivity and its value is nearly independent of probe chamfer angle.

6. Conclusions

The following major conclusions are drawn from the present experimental investigation on the effect of chamfer angle on the calibration curves of five hole probes.

- (1) The value of the calibration coefficients increases as the chamfer angle increases. This trend is observable up to the chamfer angle of 50° . For this chamfer angle, the calibration coefficients show maximum values. This is a desirable trend, as the sensitivity of the calibration coefficients increases, more accurate values of interpolated values of yaw and pitch angles and total and static pressures can be obtained. However the useful range of the probe is limited to about 30° .
- (2) If the flow to be measured is expected to have large changes in yaw and pitch angles, probe with a chamfer angle of about 30° is desirable. Probe with this chamfer angle has large useful range.
- (3) Sensitivity of static pressure coefficient is nearly independent of probe chamfer angle.
- (4) For the chamfer angles of 55° and higher values, alternate techniques given at the end of Section 5.4 may be used.

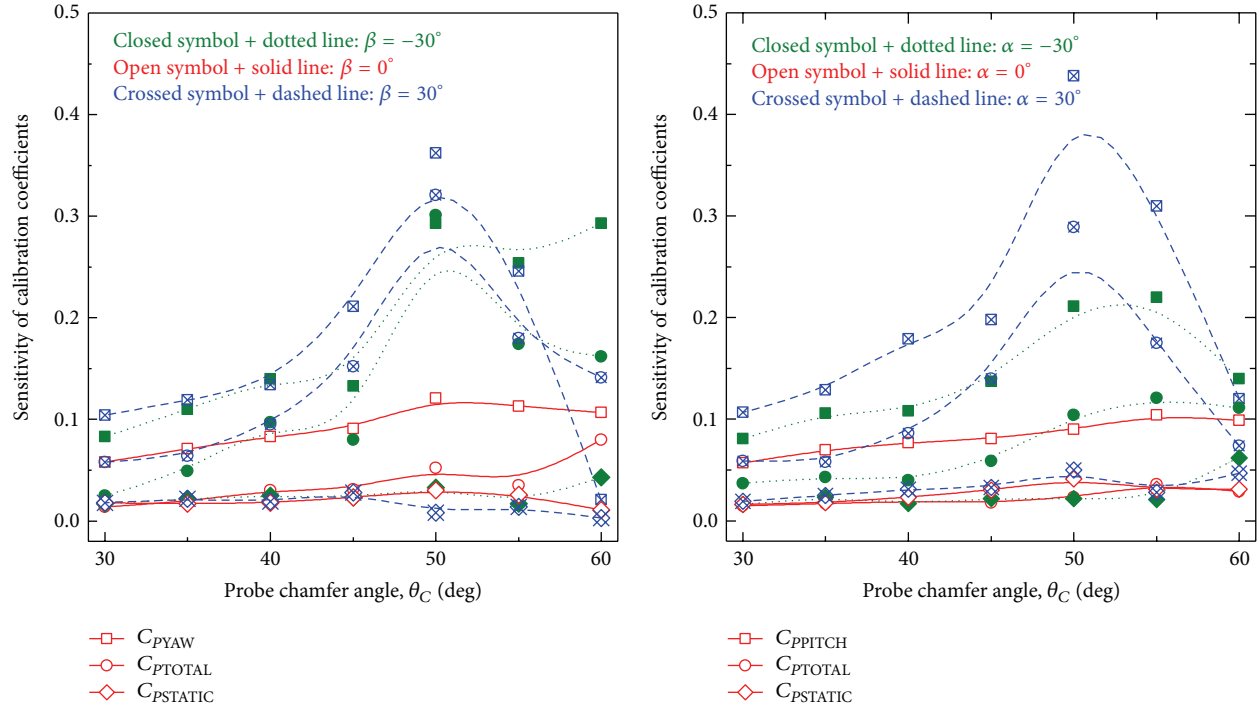


FIGURE 10: Sensitivity of calibration coefficients.

Nomenclature

C_{PPITCH} :	Pitch coefficient (defined in text)
$C_{PSTATIC}$:	Static pressure coefficient (defined in text)
C_{PYAW} :	Yaw coefficient (defined in text)
C_{PTOTAL} :	Total pressure coefficient (defined in text)
D :	Probe dynamic head (Pa) (defined in text)
P :	Mean pressure (Pa) (defined in text)
P_B, P_C, P_L, P_R, P_T :	Pressures measured by bottom, centre, left, right and top holes of the probe (please see Figure 2 for identification of holes)
P_O :	Total pressure (Pa)
P_S :	Static pressure (Pa)
α :	Yaw Angle (deg.)
β :	Pitch Angle (deg.)
θ_C :	Chamfer Angle (deg.).

Conflict of Interests

The authors declare that there is no conflict of interests regarding the publication of this paper.

Acknowledgments

The authors would like to thank Mr. P. Perumal of Thermal Turbomachines Laboratory for fabricating the probe and other technical and administrative staff of Thermal Turbomachines Laboratory, Department of Mechanical Engineering,

IIT Madras, for their help. The authors would like to thank the reviewers for their suggestions, which improved the quality of the paper substantially.

References

- [1] A. L. Treaster and A. M. Yocum, "The calibration and application of five-hole probes," *ISA Transactions*, vol. 18, no. 3, pp. 23–34, 1979.
- [2] V. Malviya, R. Mishra, and E. Palmer, "CFD investigation on 3-dimensional interference of a five-hole probe in an automotive wheel arch," *Advances in Mechanical Engineering*, vol. 2010, Article ID 763718, 19 pages, 2010.
- [3] J. W. Naughton, L. N. Cattafesta III, and G. S. Settles, "Miniature, fast-response five-hole conical probe for supersonic flowfield measurements," *AIAA Journal*, vol. 31, no. 3, pp. 453–458, 1993.
- [4] I. M. Milanovic and I. M. Kalkhoran, "Numerical calibration of a conical five-hole probe for supersonic measurements," *Measurement Science and Technology*, vol. 11, no. 12, pp. 1812–1818, 2000.
- [5] S. J. Lien and N. A. Ahmed, "An examination of suitability of multi-hole pressure probe technique for skin friction measurement in turbulent flow," *Flow Measurement and Instrumentation*, vol. 22, no. 3, pp. 215–224, 2011.
- [6] D. Telionis, Y. Yang, and O. Rediniotis, "Recent developments in multi-hole probe technology," in *Proceedings of the 20th International Congress of Mechanical Engineering (COBEM '09)*, Gramado, Brazil, November 2009.
- [7] P. M. Ligrani, B. A. Singer, and L. R. Baun, "Miniature five-hole pressure probe for measurement of three mean velocity components in low-speed flows," *Journal of Physics E: Scientific Instruments*, vol. 22, no. 10, pp. 868–876, 1989.

- [8] A. J. Pisasale and N. A. Ahmed, "A novel method for extending the calibration range of five-hole probe for highly three-dimensional flows," *Flow Measurement and Instrumentation*, vol. 13, no. 1-2, pp. 23–30, 2002.
- [9] K. M. A. Díaz, J. M. F. Oro, and E. B. Marigorta, "Direct calibration framework of triple-hole pressure probes for incompressible flow," *Measurement Science and Technology*, vol. 19, no. 7, Article ID 075401, 2008.
- [10] R. G. Dominy and H. P. Hodson, "An investigation of factors influencing the calibration of five-hole probes for three-dimensional flow measurements," *Journal of Turbomachinery*, vol. 115, no. 3, pp. 513–519, 1993.
- [11] N. Sitaram and M. Govardhan, "Large angle calibration of five hole probes," *Journal of the Aeronautical Society of India*, vol. 54, no. 3, pp. 265–272, 2002.
- [12] C. Venkateswara Babu, M. Govardhan, and N. Sitaram, "A method of calibration of a seven-hole pressure probe for measuring highly three-dimensional flows," *Measurement Science and Technology*, vol. 9, no. 3, pp. 468–476, 1998.
- [13] K. N. Everett, A. A. Gerner, and D. A. Durston, "Seven-hole probe for high angle flow measurement: theory and calibration," *AIAA Journal*, vol. 21, no. 7, pp. 992–998, 1983.
- [14] A. Pissasale and N. A. Ahmed, "Theoretical calibration of a five hole probe for highly three dimensional flow," *Measurement Science and Technology*, vol. 13, pp. 1100–1107, 2002.
- [15] A. J. Pisasale and N. A. Ahmed, "Development of a functional relationship between port pressures and flow properties for the calibration and application of multihole probes to highly three-dimensional flows," *Experiments in Fluids*, vol. 36, no. 3, pp. 422–436, 2004.

Research Article

A Miniature Four-Hole Probe for Measurement of Three-Dimensional Flow with Large Gradients

Ravirai Jangir, Nekkanti Sitaram, and Ct Gajanan

Thermal Turbomachines Laboratory, Department of Mechanical Engineering, IIT Madras, Chennai 600 036, India

Correspondence should be addressed to Ravirai Jangir; raviraijangir90@gmail.com

Received 28 May 2014; Revised 11 August 2014; Accepted 12 August 2014; Published 2 September 2014

Academic Editor: Mark McQuilling

Copyright © 2014 Ravirai Jangir et al. This is an open access article distributed under the Creative Commons Attribution License, which permits unrestricted use, distribution, and reproduction in any medium, provided the original work is properly cited.

A miniature four-hole probe with a sensing area of 1.284 mm^2 to minimise the measurement errors due to the large pressure and velocity gradients that occur in highly three-dimensional turbomachinery flows is designed, fabricated, calibrated, and validated. The probe has good spatial resolution in two directions, thus minimising spatial and flow gradient errors. The probe is calibrated in an open jet calibration tunnel at a velocity of 50 m/s in yaw and pitch angles range of ± 40 degrees with an interval of 5 degrees. The calibration coefficients are defined, determined, and presented. Sensitivity coefficients are also calculated and presented. A lookup table method is used to determine the four unknown quantities, namely, total and static pressures and flow angles. The maximum absolute errors in yaw and pitch angles are 2.4 and 1.3 deg., respectively. The maximum absolute errors in total, static, and dynamic pressures are 3.4, 3.9, and 4.9% of the dynamic pressures, respectively. Measurements made with this probe, a conventional five-hole probe and a miniature Pitot probe across a calibration section, demonstrated that the errors due to gradient and surface proximity for this probe are considerably reduced compared to the five-hole probe.

1. Introduction

The use of the multihole pressure probes has become common to determine total and static pressures, flow velocity, and flow directions in three-dimensional flow fields with suitable calibrations. Multihole pressure probes make accurate and simultaneous measurement of total and static pressures and flow direction when pressure and velocity gradients are small. Pressure probes have some advantages over other methods as their maintenance, relatively low cost, and simplicity in operation. Hence these are preferred in research and industrial purposes. In principle, any aerodynamic body such as cylinder, sphere, wedge, or prism, with a number of holes can be used to measure three-dimensional flows. A minimum of four holes on an aerodynamic body is required to measure the four unknowns, namely, total and static pressures and two angles in mutually perpendicular planes, in three-dimensional flows. However for the sake of symmetry and extended range of measurement capability, five-hole and seven-hole probes are preferred.

Because of their simplicity in operation and low cost, extensive investigations are carried out on multihole probes, particularly on five-hole probes, on their calibration and data reduction methods and their application to complex three-dimensional flow measurements. Treaster and Yocum [1] reported on calibration of different types of five-hole probes and their errors due to Reynolds number variation and surface proximity effects. Pissasale and Ahmed [2] had developed a method to extend the useful operating range for highly three-dimensional flows by replacing the conventionally defined denominator in the calibration coefficients with a more complex denominator. Pissasale and Ahmed [3, 4] developed theoretical relationship based on potential flow for calibration and application of five-hole flows. Yasa and Paniagua [5] developed a robust method for five-hole probe calibration. This technique demonstrates that the five-hole probe can be used even if one of the side holes is blocked. Dominy and Hodson [6] investigated the effect of various factors including head shape and Reynolds number on the calibration of five-hole probes. Lee and Jun [7] calibrated a

commercial five-hole probe at different Reynolds numbers. They found that the effect of Reynolds number on the calibration coefficients is different at different yaw and pitch angles. A comprehensive review of recent developments in multihole probe technology is presented by Telionis et al. [8]. Recently Lien and Ahmed [9] have used a five-hole probe to measure skin friction coefficient in complex two and three-dimensional flows. This technique avoids the necessity of aligning a Preston probe with the flow direction and the necessity of a wall static tap.

But in three-dimensional flows with large pressure and velocity gradients, in flows such as tip clearance vortex and other complicated flow phenomena that occur in turbomachinery, these probes make erroneous measurements due to their relatively large size.

Spatial errors can be minimized in two ways first by minimizing the probe head dimensions and second by applying corrections. Earlier, work was done on the miniaturization of multihole probes. To characterize Dean's vortices, Ligrani et al. [10] developed a miniature five-hole probe (diameter 1.22 mm) and used in low speed channel flow and they applied a correction method to account for spatial errors. However this method has limitations on the size of the pressure tubes that are used to make the probes. Smaller diameter tubes have longer response time. Also the small tubes may be easily blocked by dirt and may give erroneous measurements or may not give any measurements.

The other alternative is to develop methods to correct the measurements for the errors due to pressure and velocity gradients and surface proximity. This approach was adopted by Chernoray and Hjärne [11], Town et al. [12], and Honen et al. [13]. However these methods may require larger number of measurements. For the minimum errors due to pressure and velocity gradients and surface proximity effects, it will be necessary to combine both the techniques.

The probe size is relatively large in the above cases. However the pressure and velocity gradients are large in tip clearance vortex, end wall flows, flow in corner of blades, and other complex flows that occur in turbomachinery. Hence there is a strong requirement of further miniaturisation of the probe head for highly three-dimensional flow measurements. For three-dimensional flow measurements a four-hole probe which can measure four independent pressures can be used.

Four-hole probes have some advantages over five- and seven-hole probes as fewer measurements and reduced instrumentation are required during calibration and application. The measuring volume of the probe head is small compared with the five-hole probe. Hence the spatial errors caused by large pressure and velocity gradients and errors due to the surface proximity effects and shear gradients effects are reduced.

Four-hole probes come in many configurations and are used for many applications. The simple and earliest four-hole probe was obtained by modifying a three-hole cylindrical probe. An additional hole which is mainly sensitive to the flow in the pitch plane is added to the end of a three-hole probe. This type of probe is known as cantilevered four-hole cylindrical probe and used in many measurement applications in turbomachinery (Erwin, [14]) and other

flows (Maheshwari et al., [15]). Similar four-hole probe with wedge configuration is commercially available from AC-flow Corporation [16]. Heneka [17] and Ainsworth et al. [18] developed similar four-hole wedge probes with fast response pressure transducers to measure periodic total and static pressures, velocity and its three components, and flow angles. These probes are usually large about 3 mm in diameter and the measuring errors due to pressure and velocity gradients and surface proximity are usually large. However it has to be mentioned that Schlienger [19] developed a cantilever cylindrical probe of 1.2 mm tip diameter with a spatial resolution of about 1 mm. This type of probe is very useful to measure the flows in diffusers of centrifugal compressors and in labyrinth seals of axial turbines, where the spanwise flow angles are usually small. However for many turbomachinery flow measurements, pressure probes with very small measurement volumes and capability to measure large spanwise angles are needed. The available literature on such probes is presented below.

A four-hole probe which satisfies partially the above requirements was developed by Shepherd [20] for the three-dimensional flow measurements. The main feature of the probe is a tip shaped like the frustrum of a pyramid, with three-side holes equispaced around a central hole. This probe was calibrated in yaw and pitch angle range of $\pm 40^\circ$ and the calibration space is divided into six zones, making the use of this probe somewhat complicated. Sitaram and Treaster [21] have developed and presented two miniature four-hole probes. The probe heads were fabricated from 0.55 mm outer diameter and 0.30 mm inner diameter stainless steel hypodermic tubes. The probe heads are machined to a 50 degree half angle cone and located approximately four local support diameters upstream to reduce support interference effects. These probes have slightly less measuring volumes and higher spatial resolution compared to the probe developed by Shepherd. The probe with pyramid head was extensively used in many flow measurement applications.

Based on the above literature the commonly used four-hole probes can be divided into three designs, namely, modified cylindrical/hemi spherical probe, wedge/pyramid probe, and forward facing tube probe. These probes are presented in Figure 1. Both modified cylindrical/hemi spherical probe and wedge/pyramid probe can be used when the measurement space is limited, such as in diffuser passages of centrifugal compressors and turbomachinery seals. But the pitch angle range of these probes is limited and cannot be increased. A properly designed forward facing tube four-hole probe can be used to measure highly three-dimensional flows with large variations in both yaw and pitch angle ranges.

The forward facing tube probe 2 shown in Figure 1 can be used both in the four-hole and five-hole probe modes. In the four-hole probe mode, tube 5 was not used. Tube 5 could be eliminated or used to mount a thermocouple. This probe has a smaller error due to velocity gradient effect, as the probe height in the pitch plane is equal to two-tube diameters only. The four-hole probe 1 shown in 1 and five-hole probe have larger errors due to velocity gradient effect, as their heights in the pitch plane are two and one-half times tube diameters and three times tube diameters, respectively. It should be

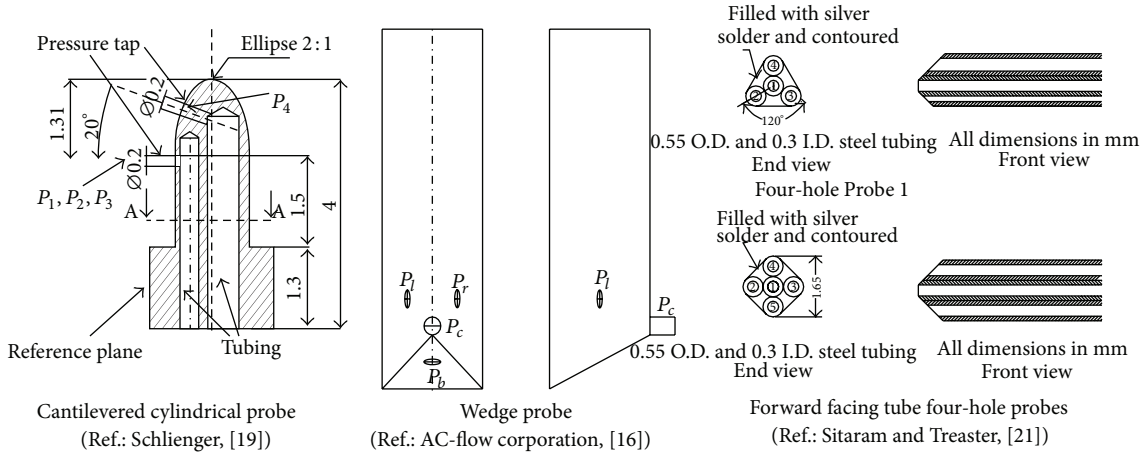


FIGURE 1: Commonly used four-hole probe configurations.

noted that these probes are smaller than any commercially available probes, so that spatial and velocity gradient effects are minimized.

The probes described above have small errors due to pressure and velocity gradients and surface proximity errors. However these errors are still large in many turbomachinery flows. Hence it is necessary to develop methods to further reduce the spatial and surface proximity errors.

The four independent pressures can be related to determine the four unknowns, namely, total and static pressures and two flow angles in mutually perpendicular planes. From the total and static pressures, velocity can be calculated. Using the flow angles, the three velocity components can be calculated. Hence a four-hole probe is chosen for development. Probe tip design can vary diversely depending on the particular application. A pressure probe must be designed for particular application where it is used. Four-hole probes are used by Sitaram and Treaster [21] and other researchers. However the configuration used by these researchers has good spatial resolution in one direction only. A four-hole probe with good spatial resolution in two directions for highly three-dimensional flow measurement is developed in this paper.

2. Objective

The objective of the present investigation is to design, fabricate, calibrate, and validate a miniature four-hole probe with minimum spatial error for accurate three-dimensional flow measurement with large pressure and velocity gradients as in cases of tip clearance vortex, flows in corner of blades, end wall flows, and other complex flows that occur in turbomachinery.

3. Design and Fabrication of Four-Hole Probe

For three-dimensional flow, four (at least) or more holes strategically located on a probe head are necessary to determine the flow. Design of any multihole probe is a compromise

between many conflicting requirements, such as small probe tip versus good response and large yaw and pitch angle measurement capability versus sensitivity of the calibration coefficients. As the size of the probe tip is reduced, by using smaller tubes, the response of the pressure measuring time increases. Hence more time is required for data acquisition. Smaller chamfer angle of the probe gives larger yaw and pitch angle measurement capability at the expense of reduced sensitivity of the calibration coefficients. The present probe is designed to optimise these conflicting requirements. In the present investigation, the four holes correspond to the centre hole, one yaw hole and two pitch holes of a five-hole probe. This design deviates from the design of earlier four-hole probes, which use one centre hole, two yaw holes, and one pitch hole of a five-hole probe. The commonly used five-hole probes are symmetric about both yaw and pitch axes, while the commonly used four-hole probes are symmetric about the yaw axis. The commonly used four-hole probes have more yaw angle range and better sensitivity of calibration coefficients in the yaw plane. The advantage of the present design is that the pitch angle range can be increased, although the yaw angle range is reduced. This is not a major disadvantage as the probe can be easily change its yaw angle when the flow exceeds the calibration yaw angle range. However a new technique needs to be developed to determine reference yaw angle. The centre hole with a chamfer angle of 90° to the tube gives a measure of total pressure and is denoted by P_C . The side hole is chamfered at an angle of about 35° to the yaw plane and is noted as P_S and is mainly sensitive to the yaw angle variation. The bottom and top holes are chamfered at an angle of about 35° to the pitch plane and are noted as P_B and P_T , respectively, and are mainly sensitive to the pitch angle variation. Hence four independent pressures can be measured, which are sufficient to define the three-dimensional flow. It has been already demonstrated that small chamfer angle gives higher calibration angle range. Hence small chamfer angle is chosen for the present design.

The probe head design is chosen so as it has good spatial resolution in both yaw and pitch directions. Assuming the tube size is the same, five-hole and seven-hole probes have a

TABLE 1

Measuring tube diameter (mm)	Holding tube diameter (mm)	Probe size		Measuring area (mm ²)
		W (mm)	T (mm)	
0.414	0.719	1.133	1.133	1.284

small diameter tubes are made using Araldite. The 0.719 mm diameter tubes are bent at an angle of 90° with a radius of curvature of about 5 mm.

Stem Section. The stem section consists of four 1.27 mm diameter tubes of about 500 mm length which are inserted into the other ends of the 0.719 mm diameter tubes. To keep the four tubes in the proper plane they are brazed at different positions along its length. To maintain the position of the inner tubes fixed with respect to the stem, the outer tube of 3.175 mm inner diameter is also brazed with these tubes. This tube of 4 mm outer diameter acts as the probe holder.

4. Calibration Tunnel, Device, Procedure, and Program

An open jet low speed calibration tunnel facility of Thermal Turbomachines Laboratory, Department of Mechanical Engineering, IIT Madras, is used for calibration of the miniature four-hole probe as shown in Figure 3.

Calibration device is made of base plate, *c* clamp, protractors, and pointers for measurement of pitch (β) and yaw (α) angles. The twenty-channel selection box and the FC012 digital micromanometer with a range of 1–200 mm of water and sensitivity of 0.1 mm of differential air pressure are used to measure the probe pressures. The micromanometer uses the output signals from the selection box to get the velocity and pressure readings.

Calibration of the probe is carried out at a velocity of 50 m/s. The probe is mounted on the probe holder with the help of sleeve such that the pressure sensing holes of the probe are to face the flow. The assembly of the probe and probe holder is kept 100 mm away from the exit of the nozzle.

At first the zeroing of probe is done by setting up the pitch angle (β) to zero degree. Initially, by changing the yaw angle (α), set the position of the probe such that the pressure sensed by centre hole is maximum and the yaw angle corresponding to the maximum pressure sensed by centre hole is noted down and then the probe is rotated on both positive and negative sides of the yaw angle until the pressure at the centre hole is equal to the half of the maximum pressure sensed and the corresponding yaw angles are noted down. The mean of these yaw angles is taken as zero reference yaw angle.

After fixing the zero reference position the probe is calibrated by changing α and β in the range of -40° to 40° with an interval of 5° . The calibration is done by keeping α constant and by varying β . For every combination of α and β , the probe pressures are recorded.

5. Results and Discussion

5.1. Sample Data. To determine the qualitative accuracy of the measurements, the measured pressure data is nondimensionalised with dynamic pressure and variation of various

nondimensional probe pressures presented against yaw and pitch angles in Figure 4. Pressure measured by the central hole, P_C , is maximum at smaller yaw and pitch angles and varies more or less symmetrically about both yaw and pitch angles. Pressure measured by the side hole, P_S , seems to be mainly sensitive to yaw angle. Pressures measured by the bottom hole, P_B , and top hole, P_T , are mainly sensitive to pitch angle. The graphs show the expected trends of measured pressures without any abnormal values. Hence the data is found satisfactory and is used to determine calibration coefficients.

5.2. Calibration Coefficients. The calibration coefficients are defined as follows:

$$\begin{aligned}
 P_{\text{BAR}} &= \frac{(P_S + P_B + P_T)}{3}, \\
 D &= P_C - P_{\text{BAR}}, \\
 C_{\text{PYAW}} &= \frac{(P_C - P_S)}{D}, \\
 C_{\text{PPITCH}} &= \frac{(P_T - P_B)}{D}, \\
 C_{\text{PTOTAL}} &= \frac{(P_C - P_O)}{Q}, \\
 C_{\text{PSTATIC}} &= \frac{(P_{\text{BAR}} - P_{\text{ST}})}{Q}, \\
 Q &= P_O - P_{\text{ST}} = P_O \quad (\text{as } P_{\text{ST}} = 0) \\
 &= \frac{(P_C - P_O)}{P_O} \\
 &= \frac{P_{\text{BAR}}}{P_O}.
 \end{aligned} \tag{1}$$

Calibration Curves. The following calibration curves are presented in Figure 4. For the sake of clarity, calibration curves are shown at 10° intervals only.

- (1) C_{PYAW} versus C_{PPITCH} for different pitch and yaw angles.
- (2) C_{PTOTAL} and C_{PSTATIC} contours with C_{PPITCH} and C_{PYAW} along the axis.

In Figure 4, calibration coefficients at $\alpha = -40^\circ$ and $\beta = -40^\circ$ are not presented. The value of probe dynamic pressure, D is very small and the magnitude of the calibration coefficients is very large.

For an ideal five-hole probe, C_{PYAW} versus C_{PPITCH} calibration curves at constant yaw angles will be horizontal



FIGURE 3: Calibration tunnel, calibration device, probe, and instrumentation.

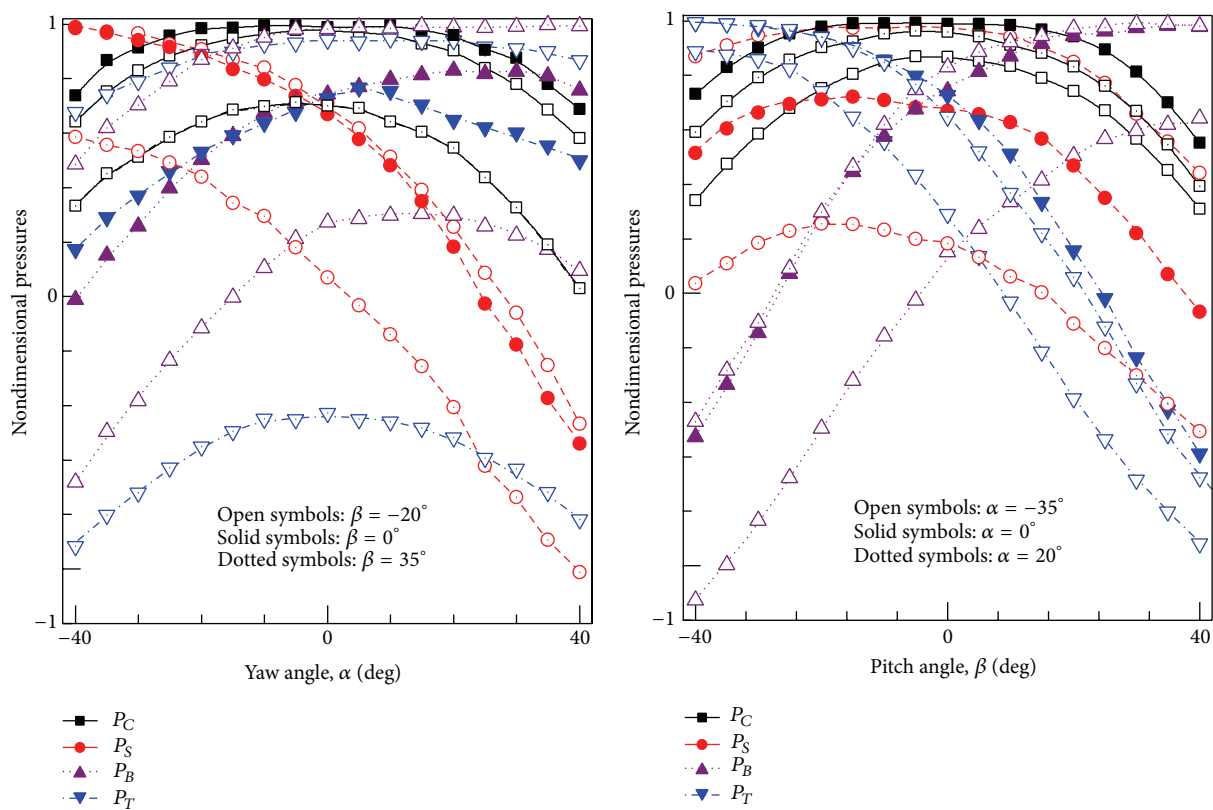


FIGURE 4: Sample data.

and symmetrical about zero yaw angle. C_{PYAW} versus C_{PPITCH} calibration curves at constant pitch angles will be vertical and symmetrical about zero pitch angle. Because of nonlinearity in the behaviour of static pressure, these calibration curves will be curved. For a four-hole probe, the calibration curves will be asymmetric about both yaw and pitch angles at zero

value. In C_{PYAW} versus C_{PPITCH} curves for $\beta = 20^\circ$, 30° , and 40° , C_{PPITCH} is minimum at $\alpha = 0^\circ$ and increases nonlinearly on both sides of the zero yaw angle. For $\beta = -20^\circ$, -10° , 0° , and 10° , C_{PPITCH} is found to vary nonlinearly for different values of yaw angles. For $\beta = -30^\circ$ and -40° , C_{PPITCH} is maximum at $\alpha = 0^\circ$ and decreases nonlinearly on both sides

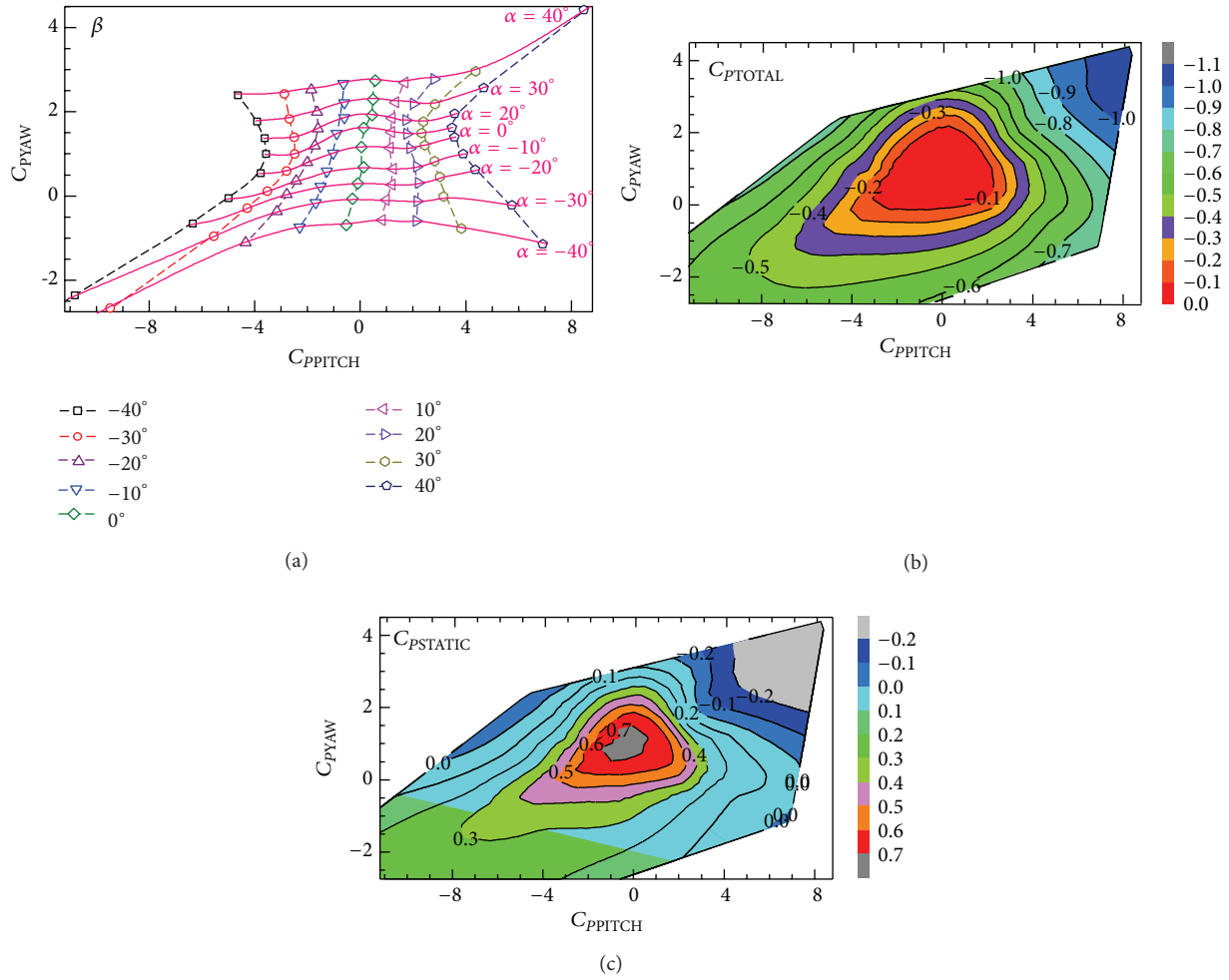


FIGURE 5: Calibration curves of miniature four-hole probe.

of the yaw angles. At $\alpha = 0^\circ$, C_{PYAW} is almost a straight line for various pitch angles and as α increases on both sides C_{PYAW} varies nonlinearly for different values of pitch angles as shown in Figure 4. From Figure 4, it is evident that the pitch coefficient, C_{PPITCH} , has larger sensitivity with pitch angle compared to C_{PYAW} sensitivity with yaw angle. This is expected as C_{PPITCH} depends on two pitch holes compared to C_{PYAW} which depends on one yaw hole only.

In the C_{PTOTAL} and $C_{PSTATIC}$ contours (Figure 5), the minimum C_{PTOTAL} contour is 0 at zero yaw and pitch angles. By definition of the C_{PTOTAL} , as the pressure sensed by the centre hole is always less than the total pressure, C_{PTOTAL} can be either zero or negative. At pitch and yaw angles away from zero values, C_{PTOTAL} becomes more negative.

The minimum $C_{PSTATIC}$ contour is 0.7 at small yaw and pitch angles because it depends on P_{BAR} and P_{BAR} is average pressure sensed by side, bottom, and top holes. Hence the value of $C_{PSTATIC}$ decreases at higher yaw and pitch angles because P_{BAR} decreases rapidly at higher yaw and pitch angles.

5.3. Sensitivity Analysis of Calibration Coefficients. To define the accuracy of the measurements, sensitivity analysis of

calibration data is carried out. The sensitivity coefficients are defined as a function of yaw or pitch angle while keeping pitch or yaw angle constant. The sensitivity coefficients are shown in Figure 6.

Sensitivity coefficients are defined as

$$\Delta C_{P_i} = \frac{(C_{P_{(i+1)}} - C_{P_{(i-1)}})}{(\text{Angle}(i+1) - \text{Angle}(i-1))}, \quad (2)$$

where C_P is the one of the four calibration coefficients, namely C_{PYAW} , C_{PPITCH} , C_{PTOTAL} , and $C_{PSTATIC}$, and i is the yaw or pitch angle where the calibration data is taken.

The probe pressures change rapidly at large yaw and pitch angles. Therefore calibration coefficients at large values of yaw and pitch angles have higher sensitivity. Although higher sensitivity implies more accurate measurements but operating range of the probe will be less. It is to be kept in mind that small error in pressures results in large errors in calibration coefficients and their sensitivity. At low values of yaw and pitch angles, sensitivity coefficients are low. The probe hole chamfered angles are small, about 35° . It is already demonstrated that small chamfer angles result in

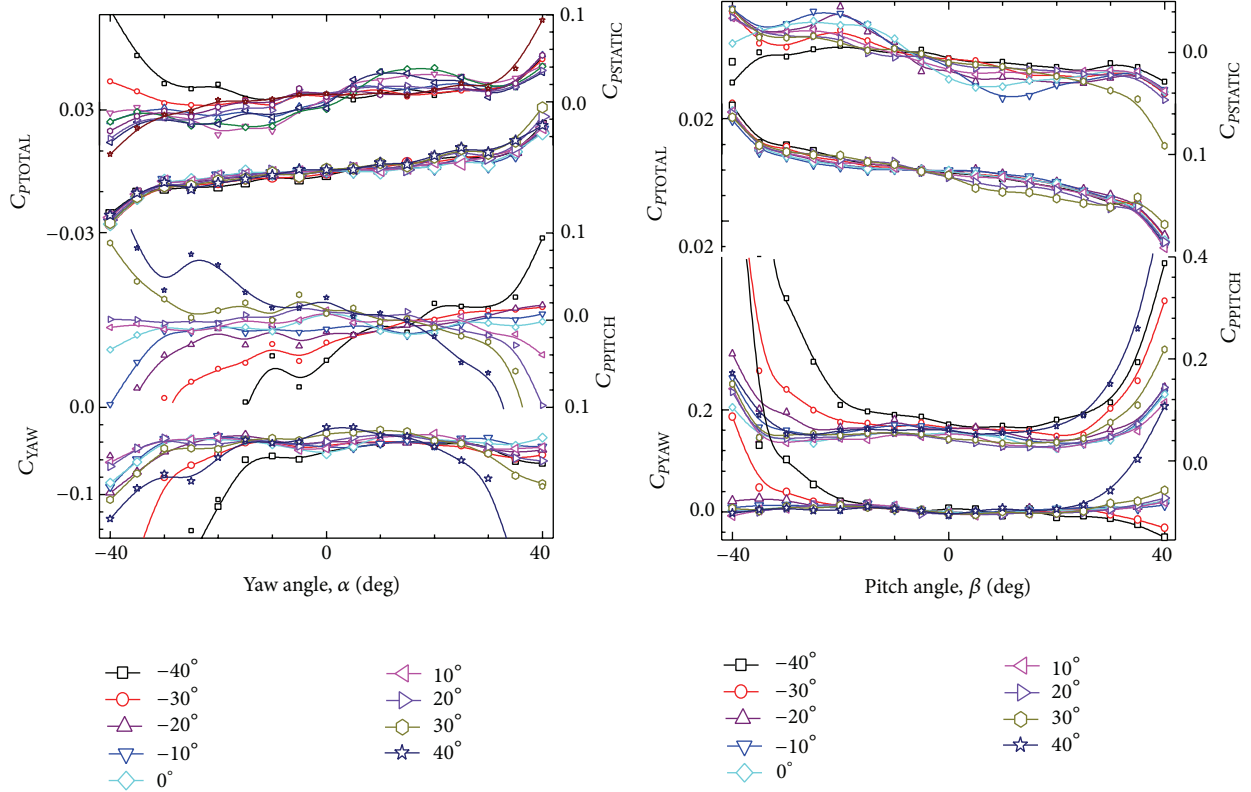


FIGURE 6: Sensitivity curves of calibration coefficients.

lower sensitivity and large chamfer angles result in higher sensitivity [22].

5.4. Validation of Calibration Data. Sitaram and Kumar [23] developed a look up table method to determine the four unknown quantities, namely, yaw and pitch angles and static and total pressure coefficients from the calculated yaw and pitch coefficients of a five-hole probe. The yaw and pitch coefficients are calculated from the measured pressure data. The same method is utilised for determining the flow quantities from the present four-hole probe measurements. No additional data is taken for interpolation during the calibration of the probe. However the calibration data at intervals of 10° rather than 5° are used. All the calibration data are used as measured data. A calibration interval of 10° is large. Sumner [24] recommended that this is the largest calibration interval that can be used with a seven-hole probe.

The interpolated values are compared with those obtained during calibration. Histograms of errors in yaw and pitch angles are presented in Figure 7. The errors at the extremes of the calibration range, that is, $\pm 40^\circ$ of yaw and pitch angles, are omitted from these graphs. Most of the errors in yaw and pitch angles are within $\pm 1^\circ$ and most of the errors in total, static, and dynamic pressures are within -0.005 to 0.01% of the dynamic head.

The maximum absolute, average, and rms values of errors in yaw and pitch angles and total, static, and dynamic pressures are also presented in Table 2.

Except for yaw angle and dynamic pressure, the errors are very small. The large values of error occur near the extreme range of calibration. The errors are due to the data reduction program only. All other measurement errors such as instrumentation errors, errors due calibration (zero angle settings, pitch and yaw angle measurements during calibration, etc.), are not included. The calibration data is given in 10° interval. The calibration data in 5° interval (excluding the data at 10° interval) are given as measured data. The errors are almost negligible when both calibration data and measured data are given in 5° interval. The errors presented by Lee and Jun [7], who used a calibration interval of 5° in their data reduction program, have similar magnitude.

5.5. Comparison of Measurements in a Calibration Duct.

The four-hole probe along with a conventional truncated conical head with perpendicular holes (3 mm dia. head) and an extremely small Pitot tube is used to measure the flow across the calibration section of the calibration tunnel available at Thermal Turbomachines Laboratory, Department of Mechanical engineering, IIT Madras (0.5 mm tip dia. of 5 mm length; this tube is extended to 0.8 mm dia. tube, followed by 1.27 mm dia. tube to reduce the response time). A schematic of the calibration tunnel is shown in Figure 8.

The circumferentially averaged wall static pressure of the settling chamber is equal to the total pressure in the calibration section. The static pressure at the measurement station is measured by means of four circumferentially

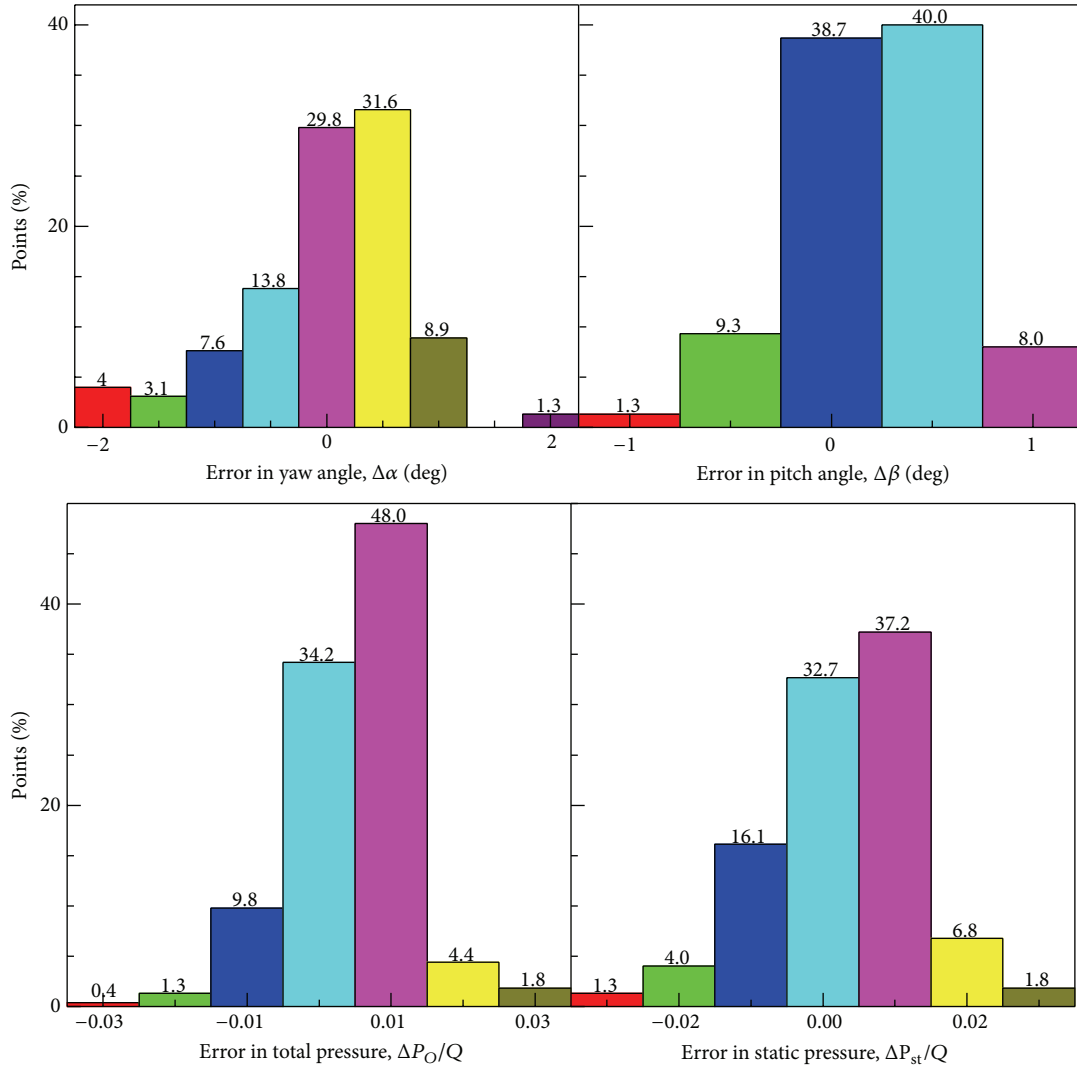


FIGURE 7: Histograms of interpolated errors in percentages.

TABLE 2

Parameter	Maximum error	Minimum error	Average value	RMS value
$\Delta\alpha$	1.7°	-2.4°	-0.26°	0.80°
$\Delta\beta$	1.3°	-1.1°	0.01°	0.42°
$\Delta P_{O}/Q$	0.034	-0.031	-0.001	0.008
$\Delta P_{ST}/Q$	0.026	-0.034	-0.002	0.012
$\Delta Q/Q$	0.029	-0.049	0.003	0.011

averaged wall static pressure taps. The probes are traversed from the centre of the calibration section to the end of the opposite wall. A manual traversing mechanism with 1 mm measurement resolution along the radial direction and 1° measurement resolution in the yaw plane is used to traverse the probes. The three probes are nulled at the centre of the calibration section and traversed in large intervals (10 mm) near the centre. As the probes approach the opposite wall, the intervals are reduced to 5 mm, 2 mm, and 1 mm. The results of these measurements are presented in Figure 9.

From Figure 9, it is evident that the nondimensional total pressure and velocity measured by all the three probes are in good agreement at the centre and away from the centre up to a distance of 0.2 times radius from the calibration section wall. For the Pitot tube, wall static pressure is used to calculate velocity. The flow is uniform in this region. The thickness of the boundary layer is about 0.2 times the radius of the calibration section. The nondimensional static pressures measured by the four-hole and five-hole probes are in good agreement with the nondimensional static pressure

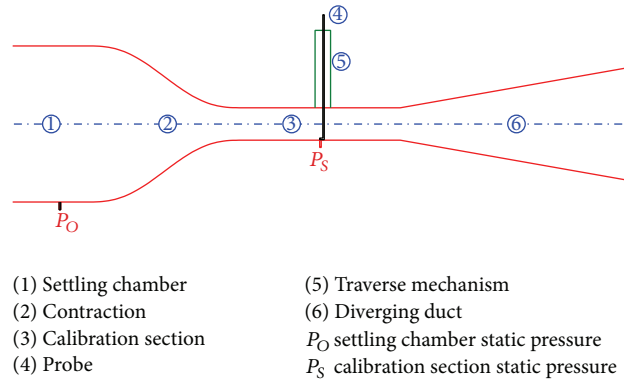


FIGURE 8: Schematic of calibration tunnel.

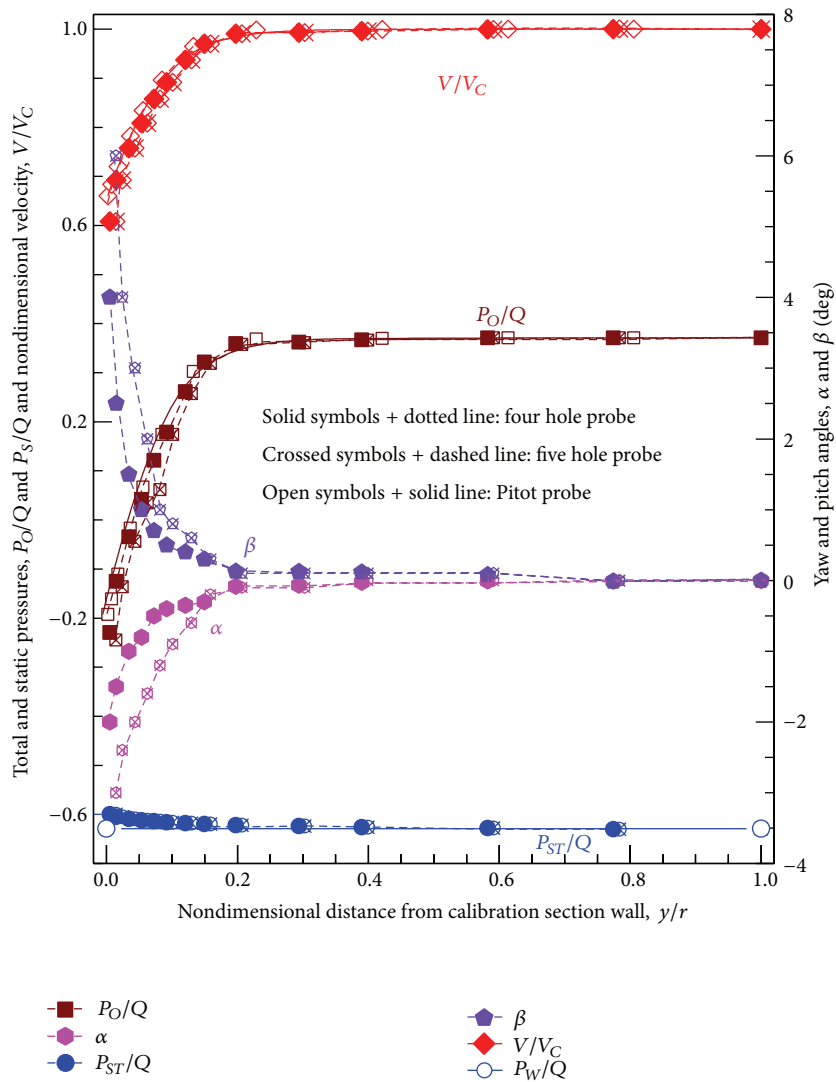


FIGURE 9: Comparison of probe measurements in the calibration section of the calibration tunnel.

measured by the wall static pressure taps. Only very near the wall of the calibration section, the static pressures measured by the probes are slightly higher than that measured by the wall static pressure taps.

Near the wall, pressure probes suffer from two major sources of errors, namely, pressure or velocity gradients and surface proximity errors. In addition, the turbulence intensity increases as the probes approach the walls. Recent investigations [25] have shown that the turbulence intensity affects the calibration characteristics of multihole probes and suggested that the multihole probes should be calibrated at the same turbulence intensity of the flow to be measured. Sitaram et al. [26] have discussed these and other sources of errors in the application of five-hole probes and they gave estimates of their magnitudes. Near the wall, the flow is modified due to the presence of the probe and the probe gives erroneous results. These erroneous results are usually confined to a distance of about twice the diameter of the probe. All the parameters that are measured, namely, total and static pressures, flow angles, and velocity and its three components, are affected due to the surface proximity. However, usually static pressure and pitch angle show larger errors. As the tip diameter of the Pitot tube is only 0.5 mm, it can measure total pressure accurately 1 mm away from the wall. The nominal sizes of the four-hole and five-hole probes are 1.1 mm and 3 mm, respectively, and the errors measured by these probes extend up to distances of about 2 and 6 mm, respectively. This can be clearly demonstrated by examination of the radial distribution of yaw and pitch angles.

The radial distribution of yaw and pitch angles measured by the four-hole and five-hole probes is also presented in Figure 9. At the centre of the calibration section, both yaw and pitch angles are zero as the flow is one-dimensional and aligned with the axis of the calibration section. These angles are close to zero up to very close to the wall. The small discrepancies can be attributed to the interpolation errors. As expected, the angles measured by the four-hole probe are nonzero very close to the wall ($y/r \leq 0.02$). For the five-hole probe, the angles measured are nonzero and are up to $y/r = 0.06$. The maximum values of yaw angles are -2 and -3 , for the four-hole and five-hole probes, respectively. The maximum values of pitch angles are 4 and 6 , respectively, for the four-hole and five-hole probes.

6. Conclusions

A miniature four-hole probe with minimum spatial error is designed and fabricated. The probe can be used to analyze three-dimensional flows with large pressure and velocity gradients in all directions as in cases of tip clearance vortex, flows in corner of blades, end wall flows, and other complex flows that occur in turbomachinery. The probe is calibrated in the range of -40° to 40° in both yaw and pitch planes with an interval of 5° . Calibration coefficients are defined, determined, and plotted. Sensitivity analysis of the calibration data is also performed. A lookup table method is used to interpolate the four unknown quantities, namely, total and static pressures and flow angles. The maximum absolute

errors in yaw and pitch angles are 2.4 and 1.3 deg. respectively. The maximum absolute errors in total, static and dynamic pressures are 3.4 , 3.9 and 4.9% of the dynamic pressures respectively. Measurements made with this probe, a conventional five-hole probe and a miniature Pitot probe across a calibration section, demonstrated that the errors due to gradient and surface proximity for this probe are considerably reduced compared to the five-hole probe. Hence, this probe is more suitable to measure three-dimensional flows with large pressure and velocity gradients as in cases of tip clearance vortex, flows in corner of blades, end wall flows, and other complex flows that occur in turbomachinery.

Nomenclature

C_{PPITCH} :	Pitch coefficient
$C_{PSTATIC}$:	Static pressure coefficient
C_{PTOTAL} :	Total pressure coefficient
C_{PYAW} :	Yaw coefficient
D :	Probe dynamic pressure (Pa)
P_B :	Pressure sensed by bottom hole (Pa)
P_C :	Pressure sensed by centre hole (Pa)
P_{BAR} :	Average pressure sensed by chamfered holes (defined in text)
P_O :	Total Pressure (Pa)
P_S :	Pressure sensed by side hole (Pa)
P_{ST} :	Static Pressure (Pa)
P_T :	Pressure sensed by top hole (Pa)
P_w :	Static pressure measured by wall taps of the calibration section (Pa)
Q :	Dynamic pressure (Pa)
r :	Radius of calibration section (m)
V :	Velocity in the calibration section (m/s)
V_C :	Velocity at the centre of the calibration section (m/s)
y :	Distance from the wall of the calibration section (m)
α :	Yaw angle (deg.)
β :	Pitch angle (deg.)
$\Delta\alpha, \Delta\beta$:	Errors in interpolated values of yaw and pitch angles (deg.)
$\Delta P_O, \Delta P_{ST}$:	Errors in interpolated values of total and static pressures (Pa)
C :	Value at the centre of the calibration section.

Conflict of Interests

The authors declare that there is no conflict of interests regarding the publication of this paper.

Acknowledgments

The authors would like to thank Mr. M. Veeraraghavan and Mr. N. Giri of Thermal Turbomachines Laboratory, Department of Mechanical Engineering, IIT Madras, for fabrication of the miniature four-hole probe. The authors

would like to thank Mr. R. Bharath Viswanath, Project Associate, Thermal Turbomachines Laboratory, Department of Mechanical Engineering, IIT Madras, for his help in running lookup table method program. The authors would like to thank the reviewers for their suggestions, which improved the quality of the paper substantially.

References

- [1] A. L. Treaster and A. M. Yocum, "The calibration and application of five-hole probes," *Instrumentation Society of America Transactions*, vol. 18, no. 3, pp. 23–34, 1979.
- [2] A. J. Pissasale and N. A. Ahmed, "A novel method for extending the calibration range of five-hole probe for highly three-dimensional flows," *Flow Measurement and Instrumentation*, vol. 13, no. 1-2, pp. 23–30, 2002.
- [3] A. Pissasale and N. A. Ahmed, "Theoretical calibration for highly three-dimensional low-speed flows of a five-hole probe," *Measurement Science and Technology*, vol. 13, no. 7, pp. 1100–1107, 2002.
- [4] A. Pissasale and N. A. Ahmed, "Development of a functional relationship between port pressures and flow properties for the calibration and application of multihole probes to highly three-dimensional flows," *Experiments in Fluids*, vol. 36, no. 3, pp. 422–436, 2004.
- [5] T. Yasa and G. Paniagua, "Robust procedure for multi-hole probe data processing," *Flow Measurement and Instrumentation*, vol. 26, pp. 46–54, 2012.
- [6] R. G. Dominy and H. P. Hodson, "Investigation of factors influencing the calibration of five-hole probes for three-dimensional flow measurements," *Journal of Turbomachinery*, vol. 115, no. 3, pp. 513–519, 1993.
- [7] S. W. Lee and S. B. Jun, "Reynolds number effects on the non-nulling calibration of a cone-type five-hole probe for turbomachinery applications," *Journal of Mechanical Science and Technology*, vol. 19, no. 8, pp. 1632–1648, 2005.
- [8] D. Telionis, Y. Yang, and O. Rediniotis, "Recent developments in multi-hole probe technology," in *Proceedings of 20th International Congress of Mechanical Engineering (COBEM '09)*, Gramado, Brazil, November 2009.
- [9] S. J. Lien and N. A. Ahmed, "An examination of suitability of multi-hole pressure probe technique for skin friction measurement in turbulent flow," *Flow Measurement and Instrumentation*, vol. 22, no. 3, pp. 153–164, 2011.
- [10] P. M. Ligrani, B. A. Singer, and L. R. Baun, "Miniature five-hole pressure probe for measurement of three mean velocity components in low-speed flows," *Journal of Physics E: Scientific Instruments*, vol. 22, no. 10, pp. 868–876, 1989.
- [11] V. Chernoray and J. Hjärne, "Improving the accuracy of multi-hole probe measurements in velocity gradients," in *Proceedings of the ASME Turbo Expo*, pp. 125–134, Berlin, Germany, June 2008.
- [12] J. Town, A. Akturk, and C. Camci, "Total pressure correction of a sub-miniature five-hole probe in areas of pressure gradients," in *Proceedings of the ASME Turbo Expo 2012: Turbine Technical Conference and Exposition (GT '12)*, pp. 855–861, Copenhagen, Denmark, June 2012.
- [13] H. T. Hoenen, R. Kunte, P. Waniczek, and P. Jeschke, "Measuring failures and correction methods for pneumatic multihole probes," in *Proceedings of the ASME Turbo Expo : Turbine Technical Conference and Exposition (GT'12)*, pp. 721–729, Copenhagen, Denmark, June 2012.
- [14] J. R. Erwin, "Experimental techniques: instrumentation," in *High Speed Aerodynamics and Jet Propulsion*, vol. 5 of *Aerodynamics of Turbines and Compressors*, p. 173, 1964.
- [15] N. K. Maheshwari, D. Saha, R. K. Sinha, and V. Venkat Raj, *Velocity Measurement in the Three Dimensional Flow Fluid in a Nuclear Reactor Calandria Using Four Hole Probe*, Reactor Engineering Division, Bhabha Atomic Research Centre, Mumbai, India, 1998.
- [16] AC-flow, <http://ac-flow.com/upload/files/4-hole%20wedge%20type%20probe.pdf>.
- [17] A. Heneka, "Instantaneous three dimensional flow measurements with a four hole wedge probe," in *Proceedings of the 7th Symposium on Measuring Techniques for Transonic and Supersonic Flow in Cascades and Turbomachines*, Aachen, Germany, 1983.
- [18] R. W. Ainsworth, J. L. Allen, and J. J. M. Batt, "The development of fast response aerodynamic probes for flow measurements in turbomachinery," *ASME Journal of Turbomachinery*, vol. 117, no. 4, pp. 625–634, 1995.
- [19] J. P. Schlienger, *Evolution of unsteady secondary flows in a multistage shrouded axial turbine [dissertation]*, ETH, Zürich, Switzerland, 2003, ETH no. 15230.
- [20] I. C. Shepherd, "A four hole pressure probe for fluid flow measurements in three dimensions," *Journal of Fluids Engineering*, vol. 103, no. 4, pp. 590–594, 1981.
- [21] N. Sitaram and A. L. Treaster, "A simplified method of using four-hole probes to measure three dimensional flow fields," *Journal of Fluids Engineering, Transactions of the ASME*, vol. 107, no. 1, pp. 31–35, 1985.
- [22] N. Sitaram and K. Srikanth, "Effect of chamfer angle on the calibration curves of five hole probes," in *Proceedings of the 39th National Conference on Fluid Mechanics and Fluid Power*, Paper No. FMFP2012-240, p. 10, SVNIT, Surat, India, December 2012.
- [23] N. Sitaram and S. Kumar, "Look up table method for five hole probe data reduction," in *Proceedings of the 38th National Conference on Fluid Mechanics and Fluid Power*, vol. 8 of *Paper No. EM05*, MANIT, Bhopal, India, December 2011.
- [24] D. Sumner, "A comparison of data-reduction methods for a seven-hole probe," *Journal of Fluids Engineering*, vol. 124, no. 2, pp. 523–527, 2002.
- [25] C. Crowley, I. I. Shinder, and M. R. Moldover, "The effect of turbulence on a multi-hole Pitot calibration," *Flow Measurement and Instrumentation*, vol. 33, pp. 106–109, 2013.
- [26] N. Sitaram, B. Lakshminarayana, and A. Ravindranath, "Conventional probes for the relative flow measurement in a turbomachinery rotor blade passage," *ASME Journal of Engineering for Gas Turbines and Power*, vol. 103, no. 2, pp. 406–414, 1981.